

Institute for Polymer Research

Celebrating 30 years of Official Institute Status

Thirty-Sixth Annual Symposium on Polymer Science/Engineering

Wednesday, May 21, 2014

Conrad Grebel University

University of Waterloo

Presentations (5-minute)

Ryan Amos Waterloo Institute for Nanotechnology (WIN), Waterloo	Hydrophobic Modification of Starch Nanoparticles
Remi Casier Chemistry, Waterloo	Using Visible Light to Probe Interparticle Diffusion in Latex Films
Li Chen Chemistry, Waterloo	Synthesis of β -cyclodextrin modified cellulose nanocrystals (CNCs)@Fe ₃ O ₄ @SiO ₂ superparamagnetic nanorods
Shiva Farhangi Chemistry, Waterloo	A Four-Atom Linker to Label Macromolecules with a Pyrene Derivative that Responds to Local Polarity
Dina Hamad Chemical Engineering, Waterloo	Experimental Study of Polyvinyl Alcohol Degradation in Aqueous Solution by UV/ H ₂ O ₂ Process
Yifeng Huang Chemical Engineering, Waterloo	Polyvinylamine-enhanced Ultrafiltration for Removal of Heavy Metals from Wastewater
Nicholas Lanigan Chemistry, Waterloo	A Novel Metal-Containing Supramolecular Polymer
Solmaz Pirouz Chemistry, Waterloo	Using Pyrene Fluorescence to Probe the Behaviour of Semicrystalline Polyolefins in Solution
Marzieh Riahinezhad Chemical Engineering, Waterloo	Some Special Factors Influencing Copolymerization Kinetics of a Polyelectrolyte System
Ankita Saikia Chemical Engineering, Waterloo	Modelling the Vulcanization Reaction of Devulcanized Rubber
Bingqing Yang Chemistry, Waterloo	Preparation and Characterization of Temperature-Responsive Polymeric Surfactants
Wei Yi Chemistry, Waterloo	Probing Hydrophobic Collapse of Starch Nanoparticles by Pyrene Fluorescence and Transmission Electron Microscopy

Institute for Polymer Research

Celebrating 30 years of Official Institute Status

Symposium documents for

Ryan Amos

Hydrophobic Modification of Starch Nanoparticles

Ryan Amos, Dr. Mario Gauthier

IPR Symposium

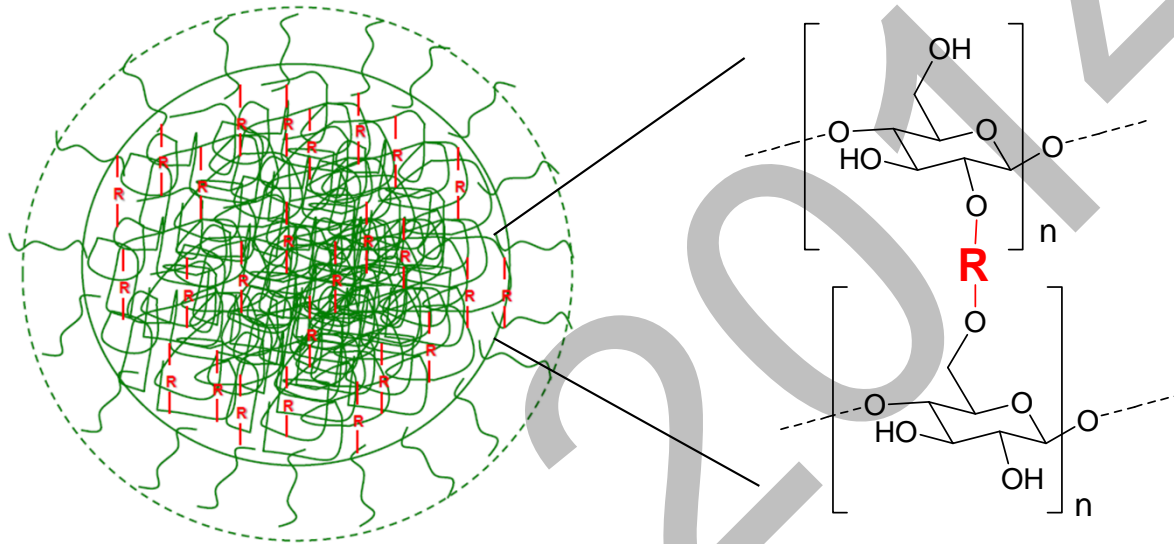
May 21, 2014



Research Goals

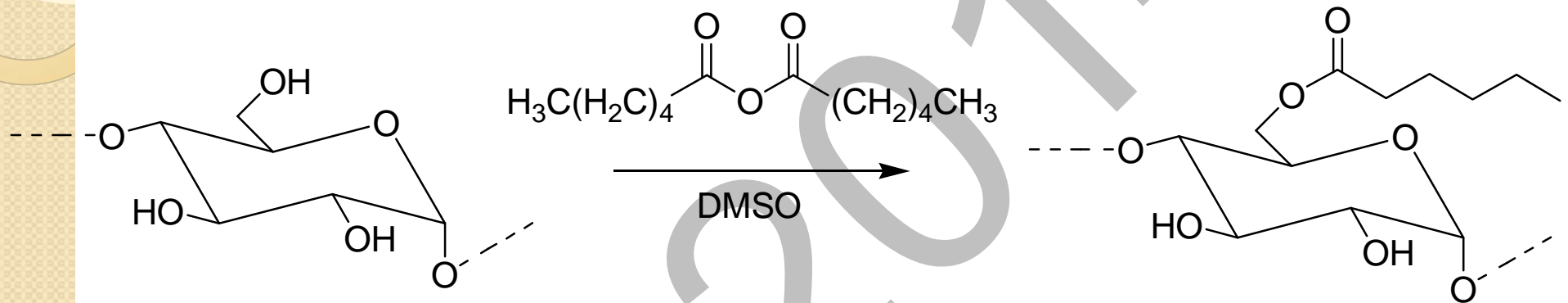
- Preparation of ester-modified research grade starch nanoparticle samples provided by EcoSynthetix by different methods
- Control the hydrophilic-lipophilic balance of the particles
- Perform detailed characterization of these new starch-based materials

Background



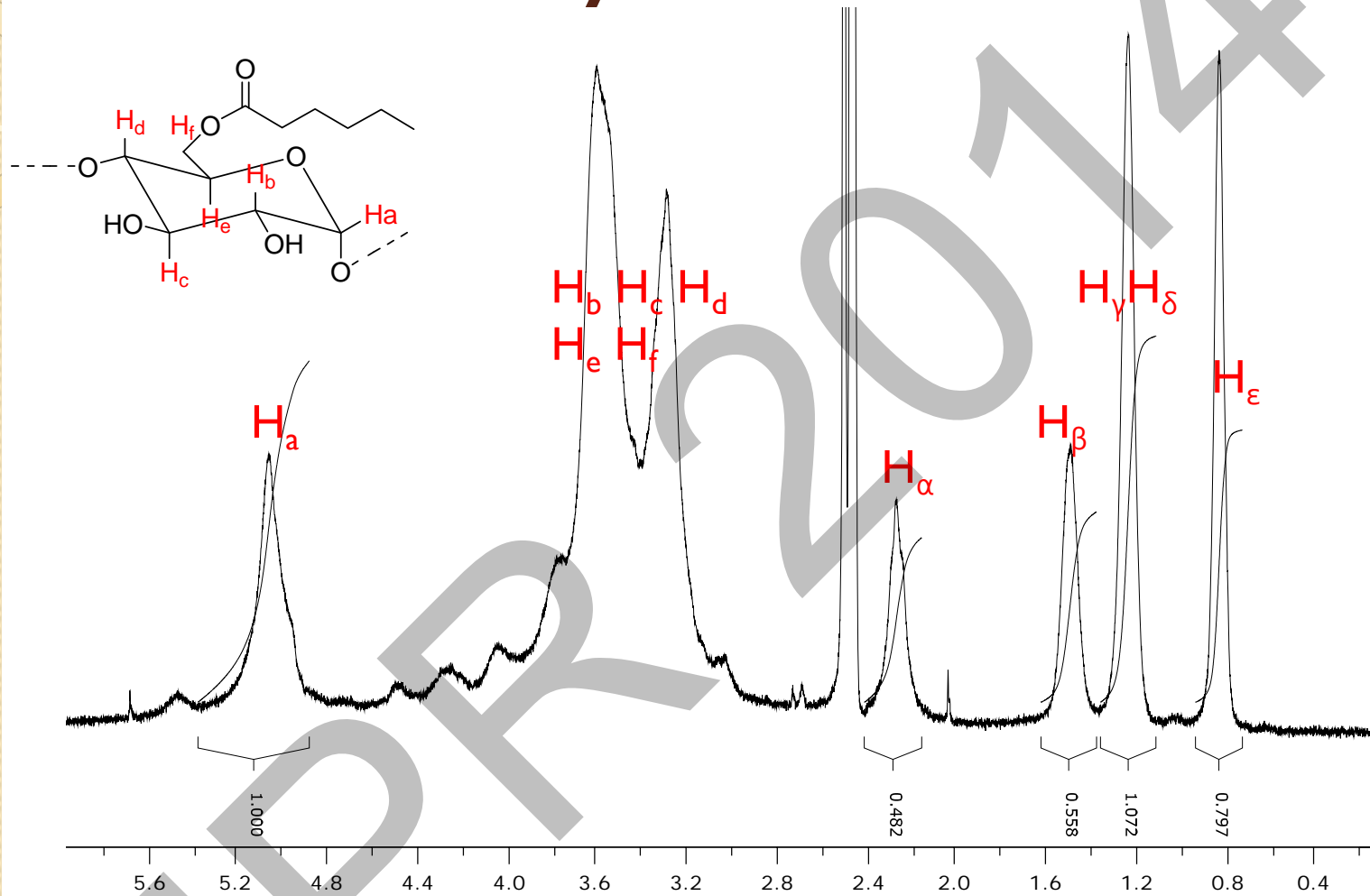
- EcoSynthetix produces starch nanoparticles for use as binder in paper coating, to replace styrene-butadiene latex
- The modification of starch nanoparticles could lead to other applications such as coatings or adhesives, to replace other non-biodegradable emulsion polymers

Experimental Procedure



- Approach minimizes the hydrolysis of the anhydride because no water is added
- Can control the DS by the amount of anhydride added
- Purified by precipitation in ethanol or water, depending on the DS
- Procedure not limited to hexanoic anhydride

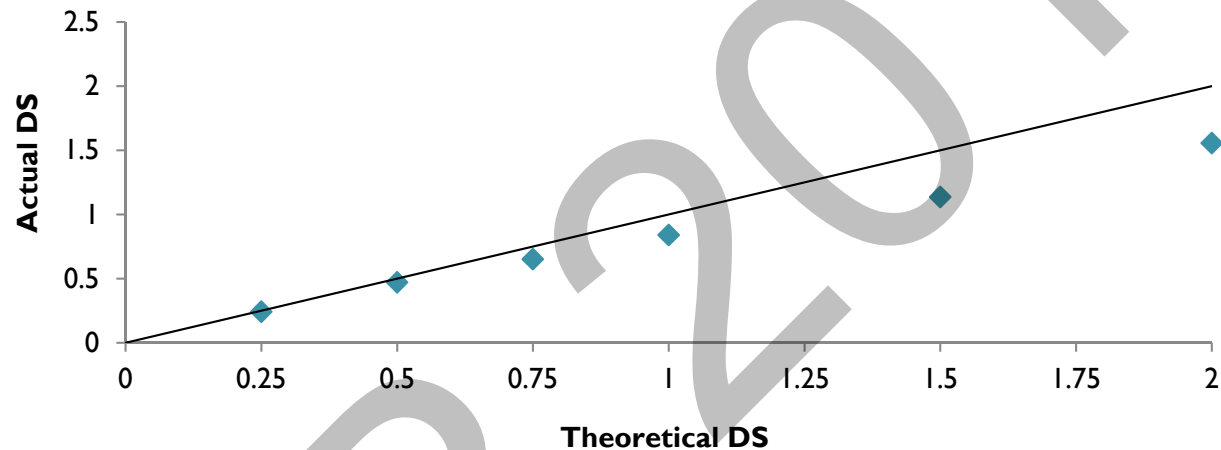
Preliminary Results



- 0.25 eq of anhydride added
- DS = 0.24

Preliminary Results

Degree of Substitution of Modified ENPs



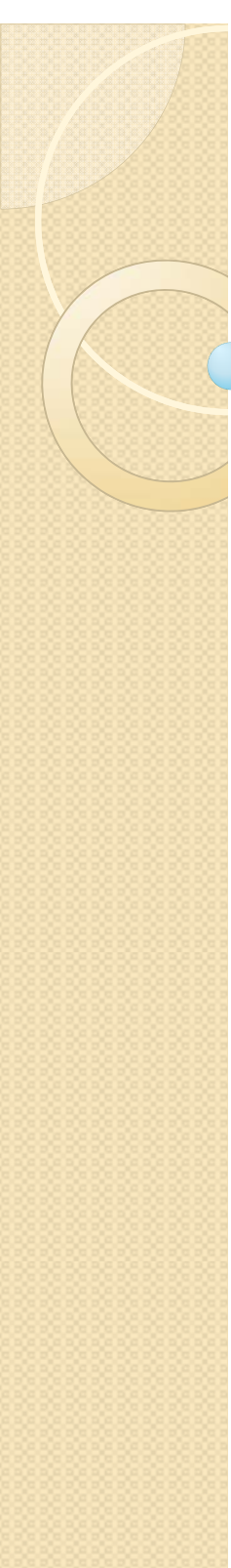
- Control of substitution level achieved for hexanoic anhydride
- For $DS > 0.5$, the nanoparticles are no longer water-dispersible
- Samples with low DS currently being analyzed in the Duhamel group to characterize the hydrophobic domains

Acknowledgements

- Committee members: Dr. Duhamel, Dr. Liu and Dr. Simon
- EcoSynthetix: Julien Mesnager, Steven Bloembergen
- Lab members: Gauthier Group, Duhamel Group
- Project colleagues: Dr. Taylor, Joanne Fernandez, Lu Li, Magda Karski, Duncan Li, Ziyi Sun, Howard Tsai, Wei Yi



NSERC
CRSNG



Thank You

Questions

IPR 2014

Institute for Polymer Research

Celebrating 30 years of Official Institute Status

Symposium documents for

Remi Casier

Using Visible Light to Probe Interparticle Diffusion in Latex Films

University of
Waterloo



Remi Casier

Supervisors: Prof. Jean Duhamel

Prof. Mario Gauthier

University of Waterloo

IPR

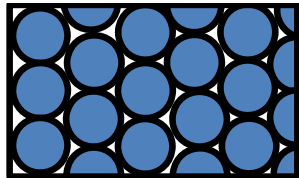
Institute for Polymer Research

Latex Film Formation

Latex: A stable dispersion of polymer particles in an aqueous solution

Stage 1:

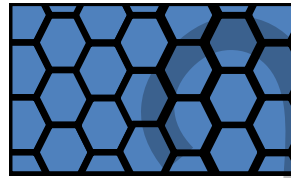
Water Evaporation



$T > MFT$

Stage 2:

Particle Deformation



$T > MFT$

Stage 3:

Coalescence

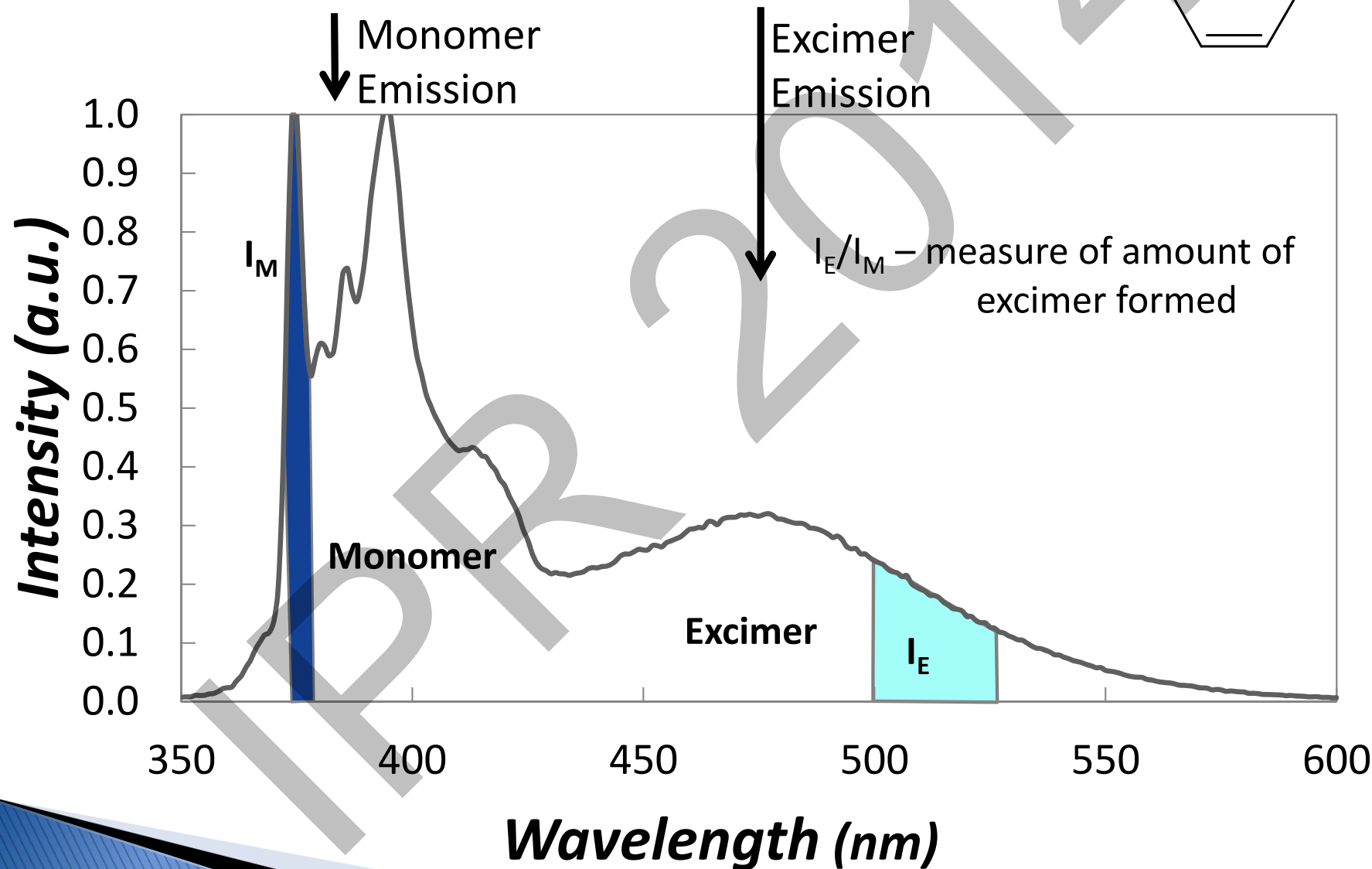
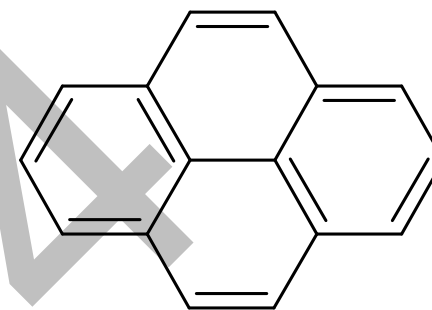
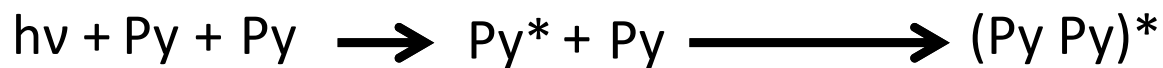


- Brittle
- Water Permeable

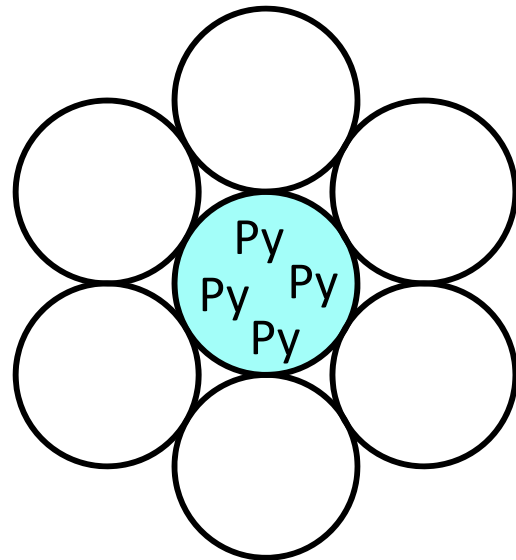
- Tough
- Water Resistant

- ▶ A minimum film formation temperature (MFT) must be reached before polymer chains can interdiffuse ($MFT \approx T_g$)¹
- ▶ Interparticle polymer diffusion (IPD) during coalescence produces a homogeneous film

Pyrene

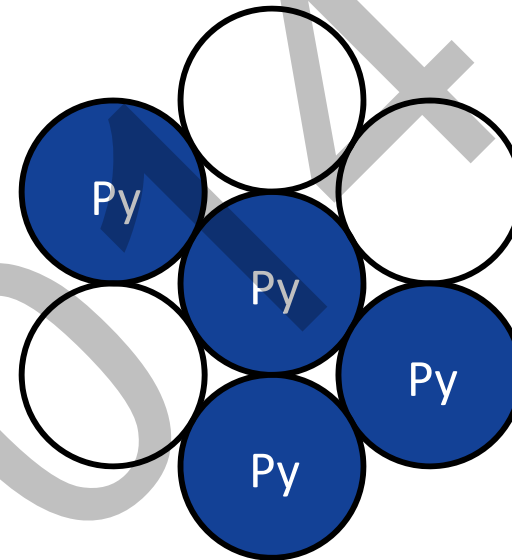


Interparticle Polymer Diffusion



$t=0$

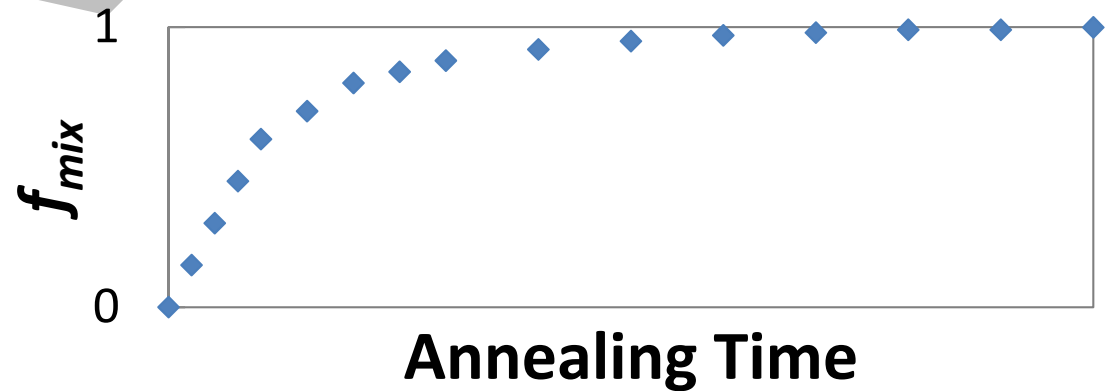
- ▶ High I_E/I_M
- ▶ $f_{mix} = 0$



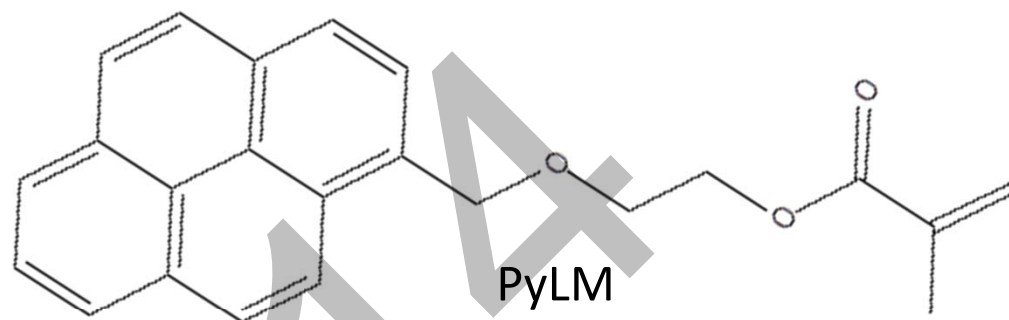
$t > 0$

- ▶ Low I_E/I_M
- ▶ $0 < f_{mix} \leq 1$

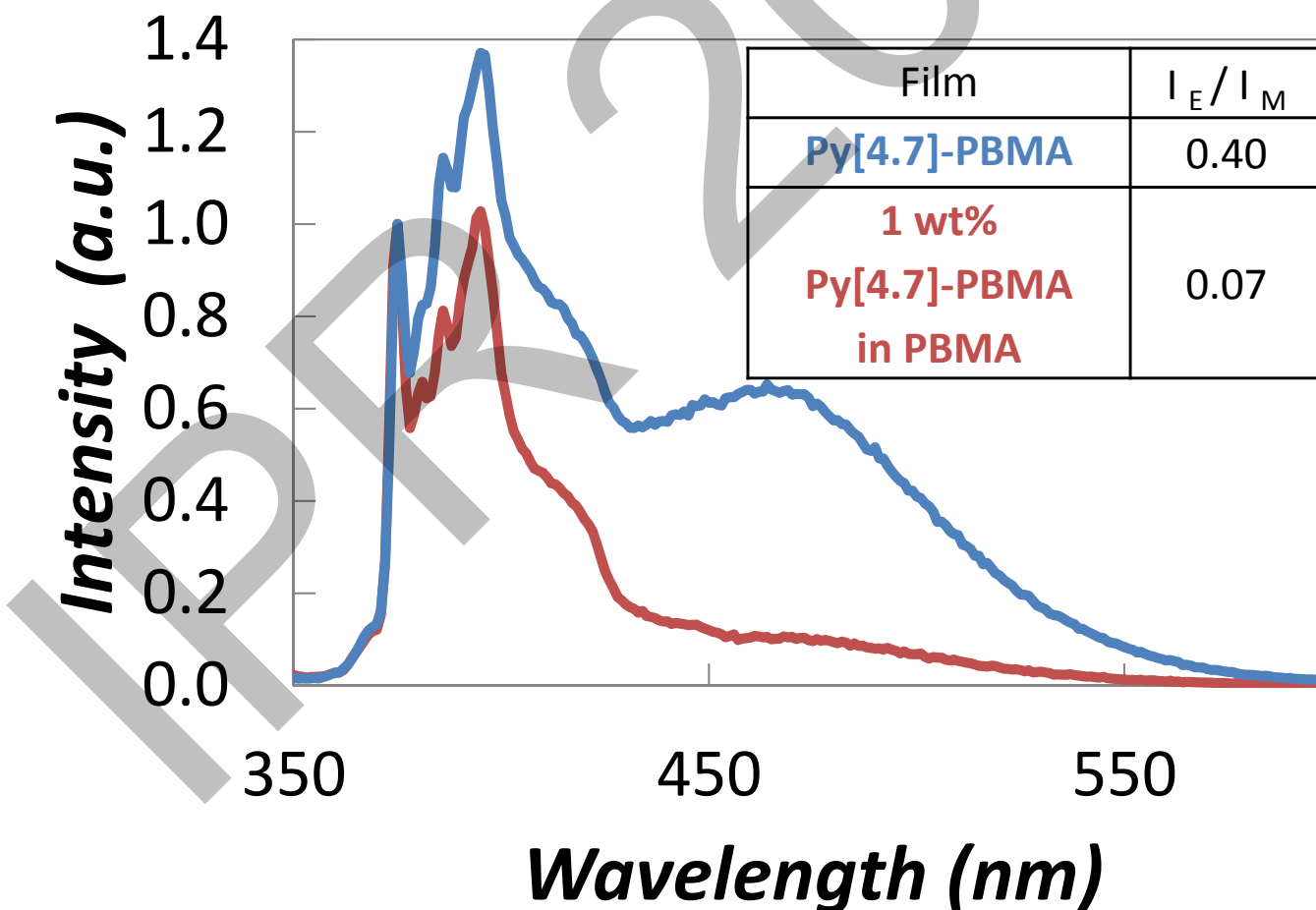
$$f_{mix}(t) = \frac{\left(\frac{I_E}{I_M}\right)_{(t)} - \left(\frac{I_E}{I_M}\right)_{(t=0)}}{\left(\frac{I_E}{I_M}\right)_{(t=\infty)} - \left(\frac{I_E}{I_M}\right)_{(t=0)}}$$



Preliminary Results



- ▶ A pyrene labeled monomer (PyLM) was synthesised and copolymerized with *n*-butyl methacrylate to yield a pyrene labeled copolymer with 4.7 mol% of the PyLM incorporated into the polymer (Py[4.7]-PBMA)



Acknowledgements



The Chemical Company

Xiaozhou Chen

Supervisors:

Prof. Jean Duhamel

Prof. Mario Gauthier

All members of the Duhamel and Gauthier groups



NSERC
CRSNG

IPR 2014

Institute for Polymer Research

Celebrating 30 years of Official Institute Status

Symposium documents for

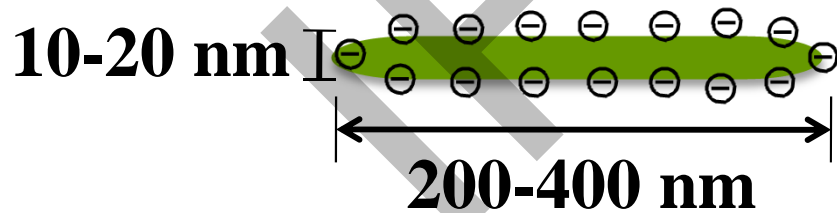
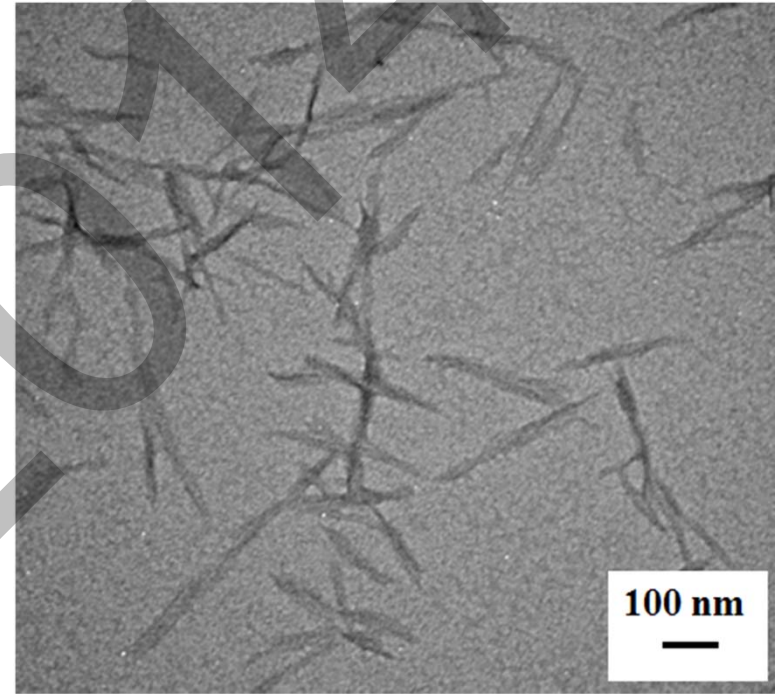
Li Chen

**Synthesis of β -cyclodextrin modified
cellulose nanocrystals (CNCs)@Fe₃O₄@SiO₂
superparamagnetic nanorods.**

Li Chen

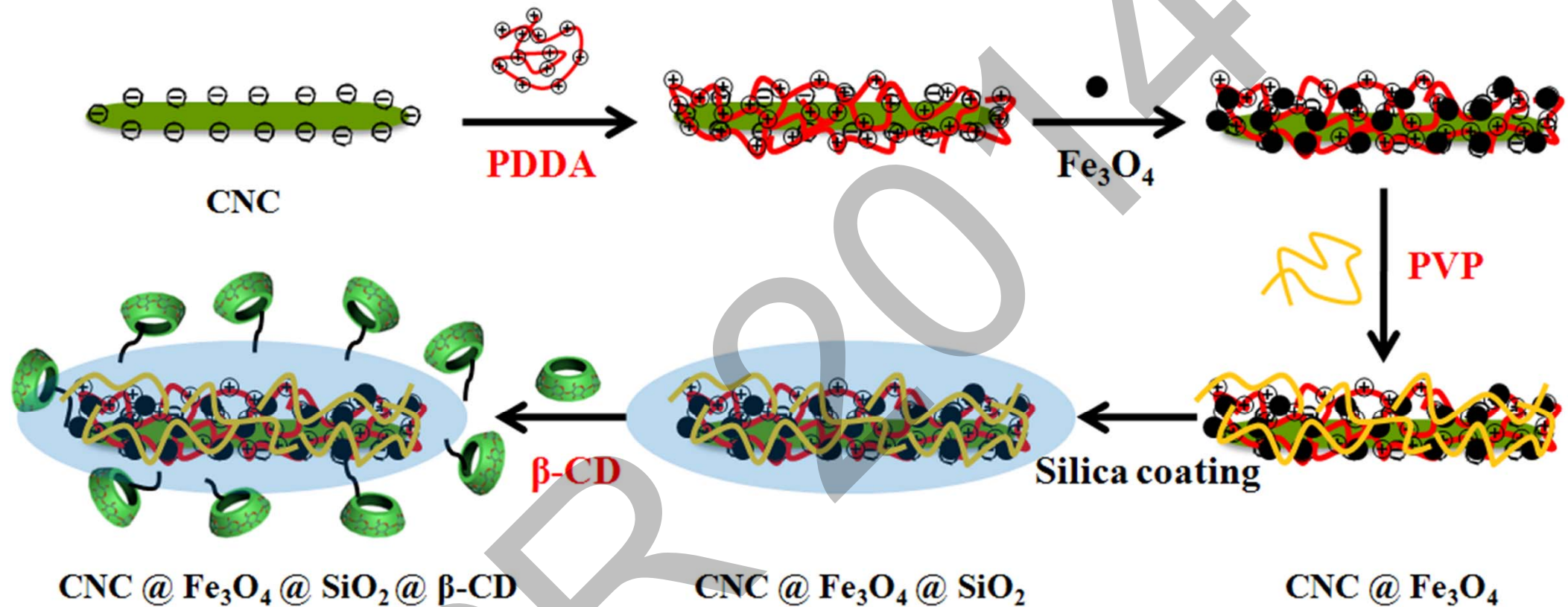
Supervisor: Prof. Michael Tam

Introduction



- Good mechanical strength**
- Regular rod-like structure**
- Sustainability**
- Environmentally friendly**
- Commercial availability**

Schematic pattern

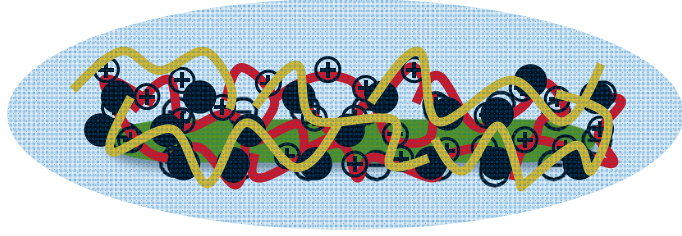


PDDA: poly(diallyldimethylammonium chloride).

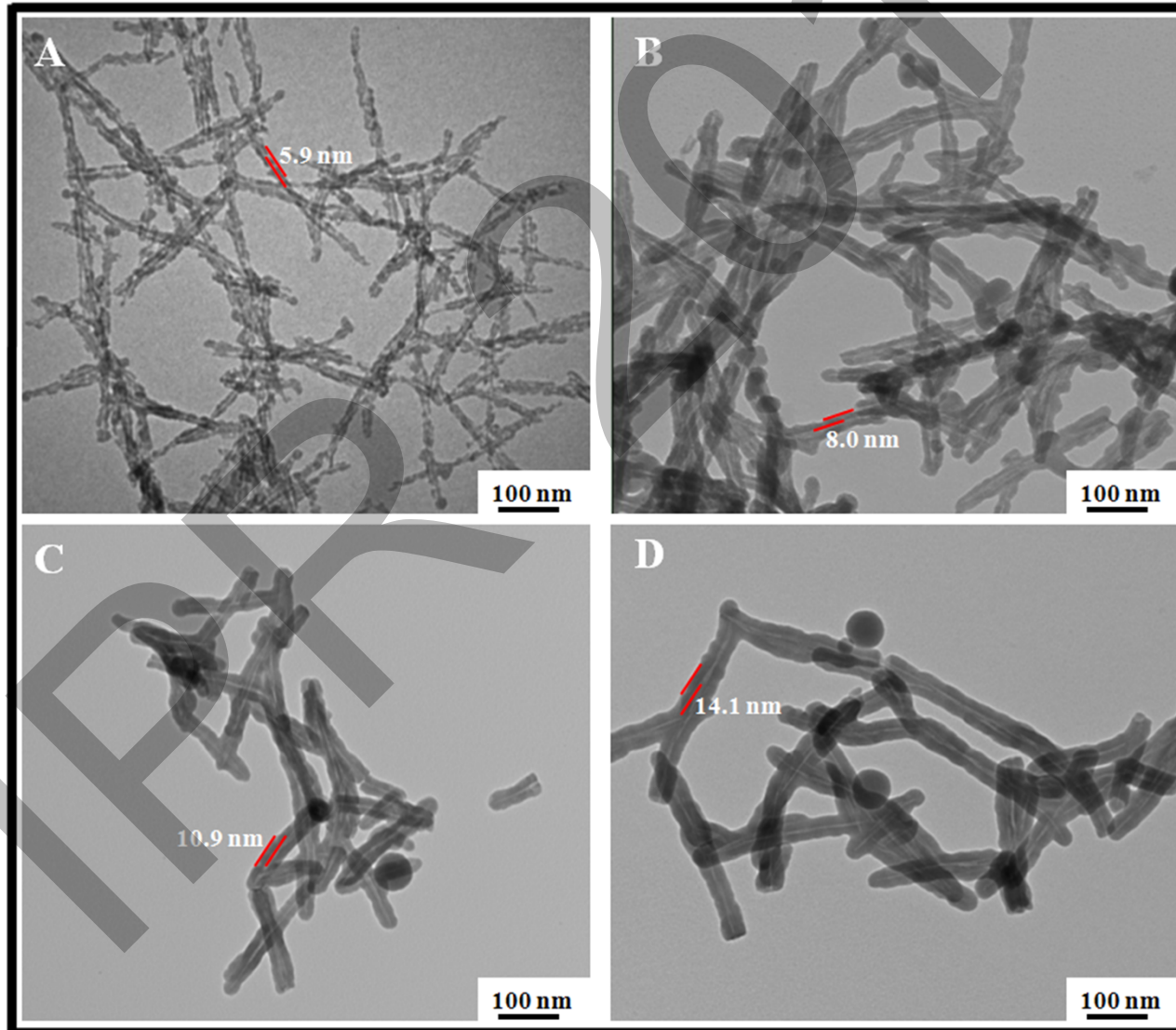
PVP: polyvinylpyrrolidone.

β-CD: β-cyclodextrin.

TEM



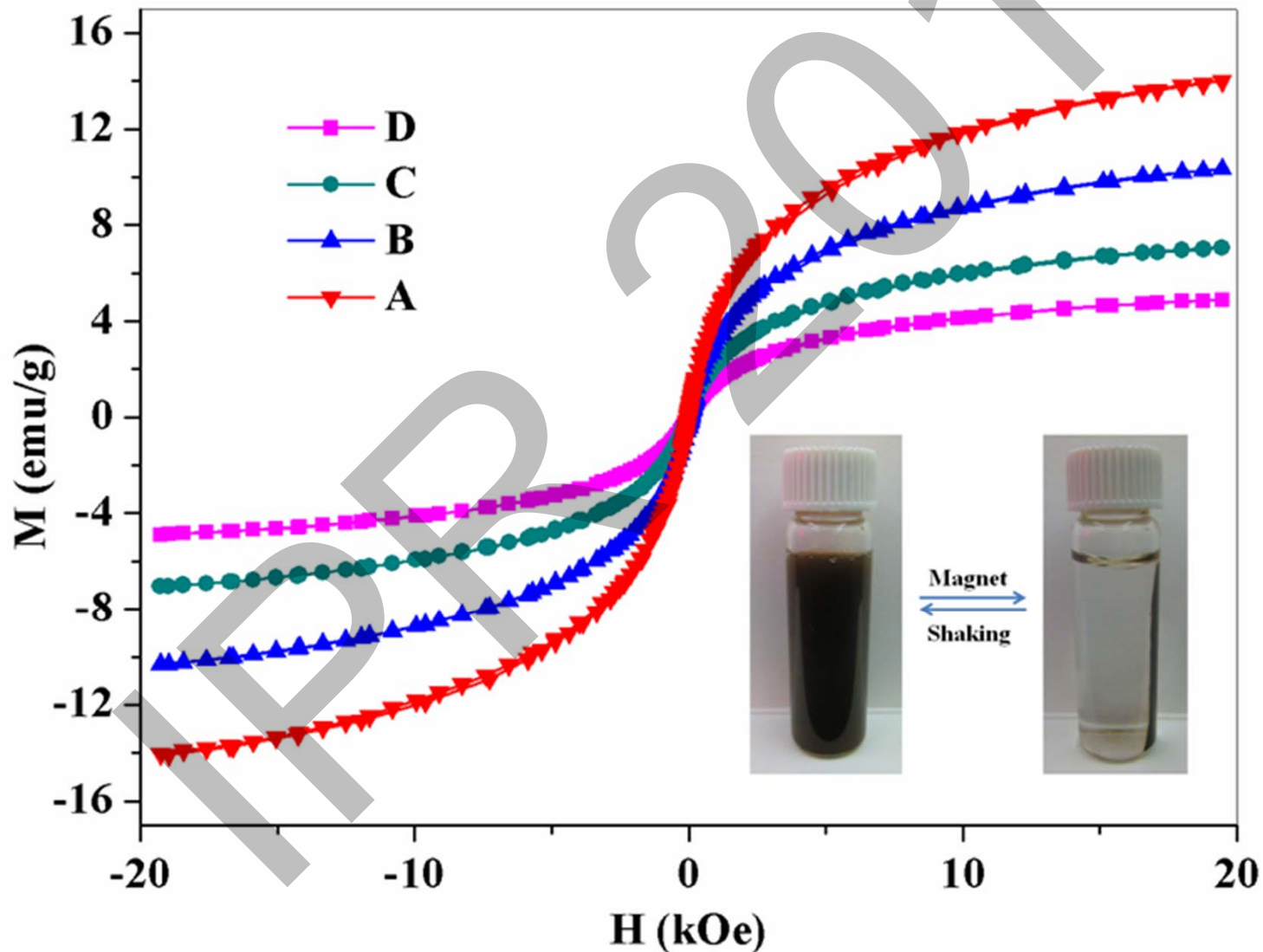
CNC @ Fe₃O₄ @ SiO₂



Magnetic hysteresis loops



CNC @ Fe₃O₄ @ SiO₂



Thanks!

Q & A

Institute for Polymer Research

Celebrating 30 years of Official Institute Status

Symposium documents for

Shiva Farhangi

UNIVERSITY OF
WATERLOO



A Four-Atom Linker to Label Macromolecules with a Pyrene Derivative that Responds to Local Polarity

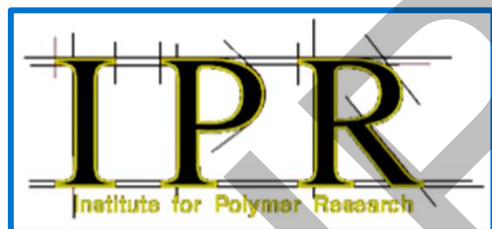
Shiva Farhangi

Supervisor: Jean Duhamel

36th Annual IPR Symposium

University of Waterloo

May 21, 2014

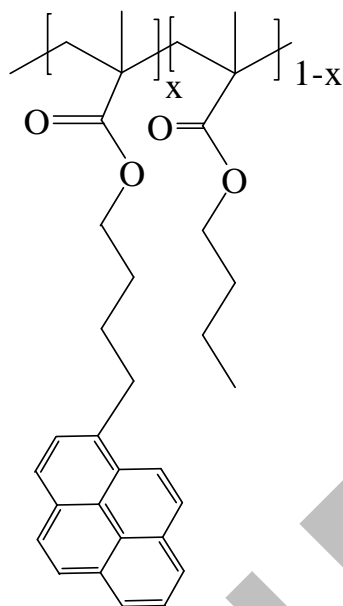


UNIVERSITY OF
WATERLOO

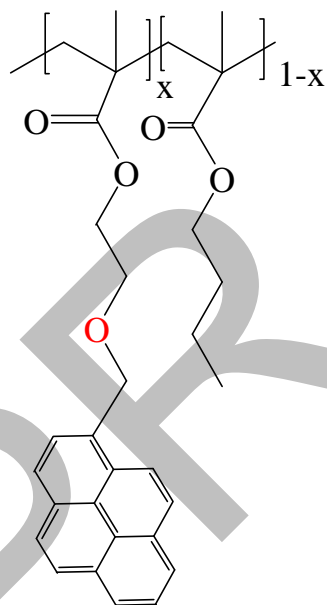
Sample Preparation

Poly(methacrylates) were randomly labeled with pyrene via radical copolymerization

PyBut-PC4MA



PyMeOEtO-PC4MA



✓ NMR :

- ✓ Determine the degree of conversion.

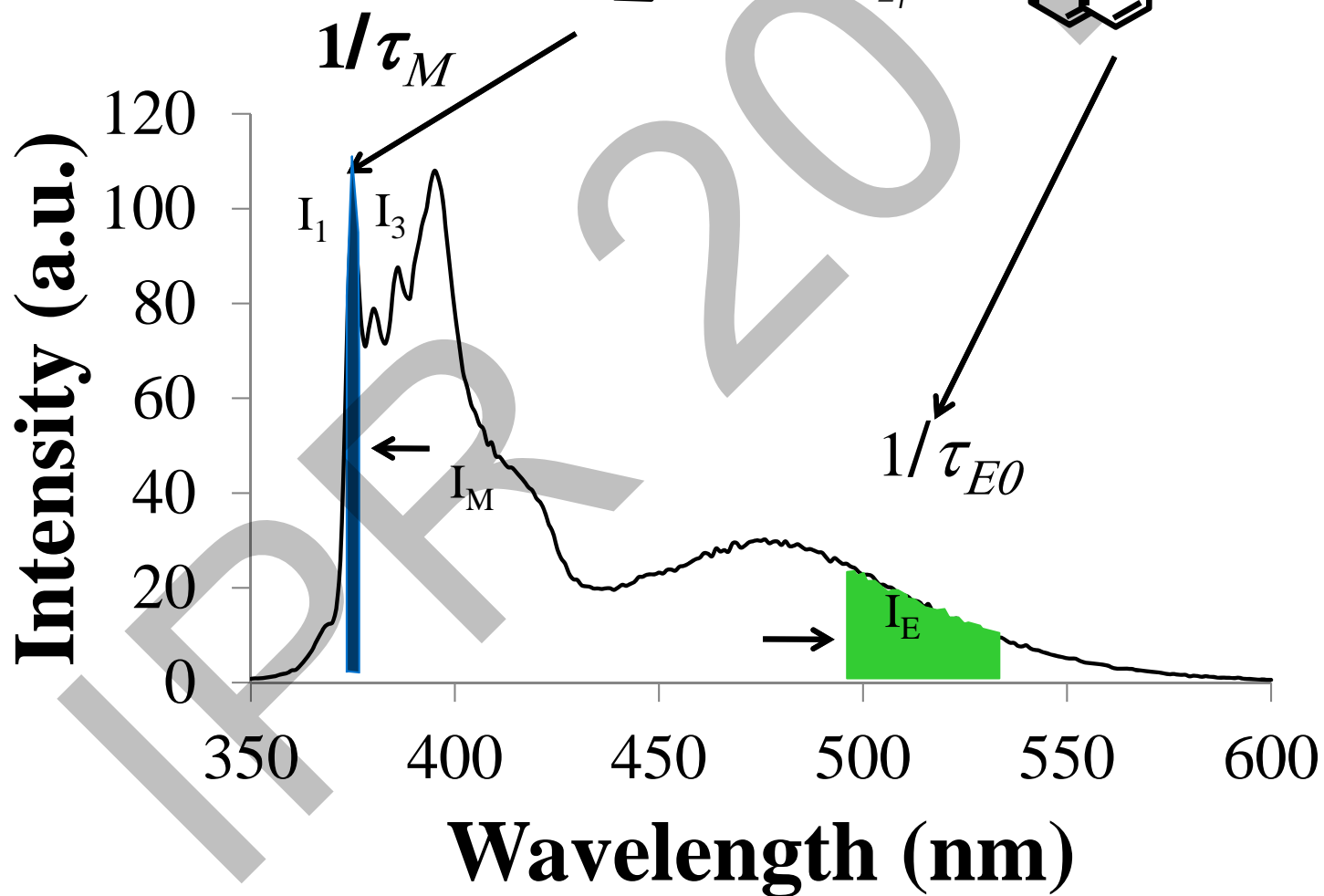
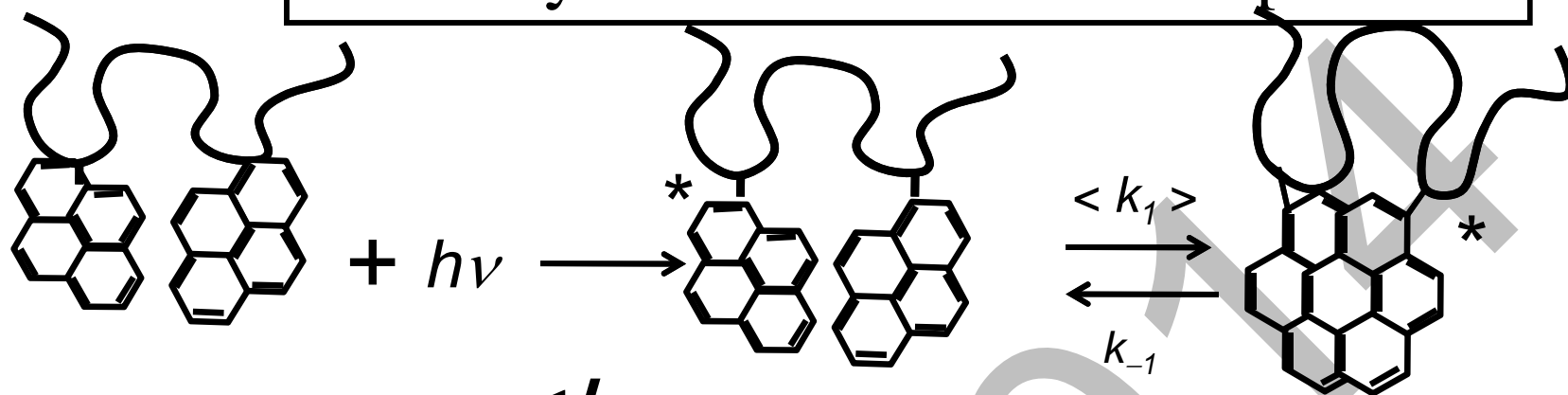
✓ GPC:

- ✓ Check for unreacted pyrene monomer using UV-Vis absorption detector.
- ✓ Determine molecular weight.

✓ Absorption spectroscopy:

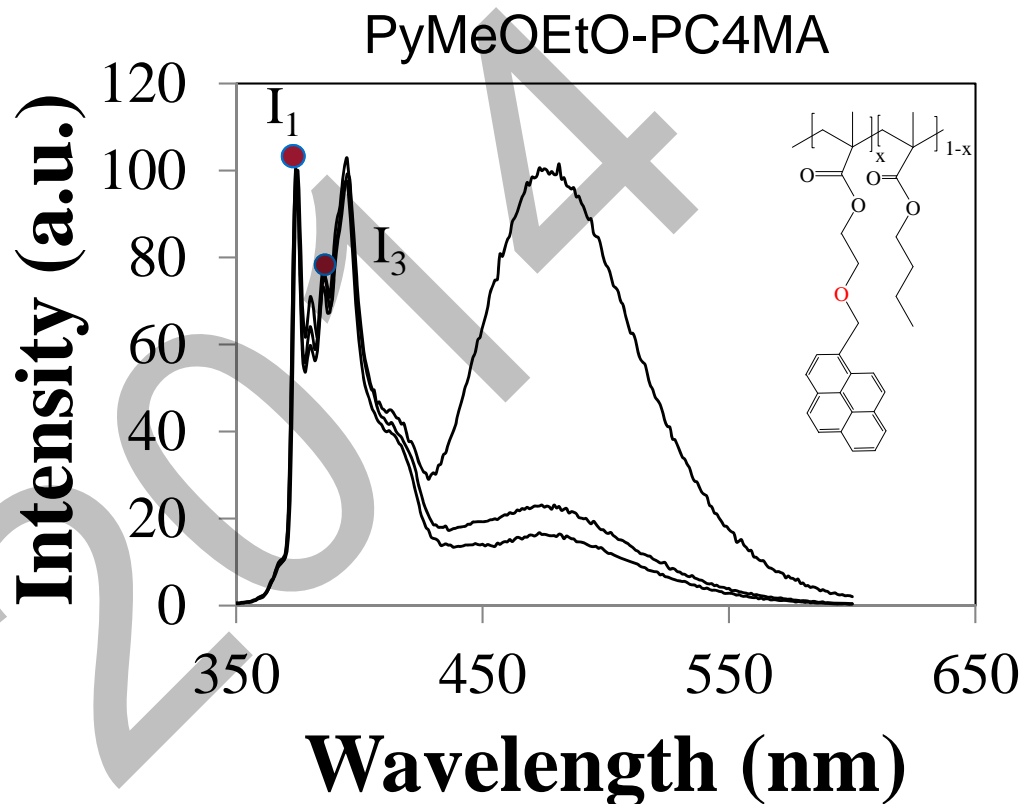
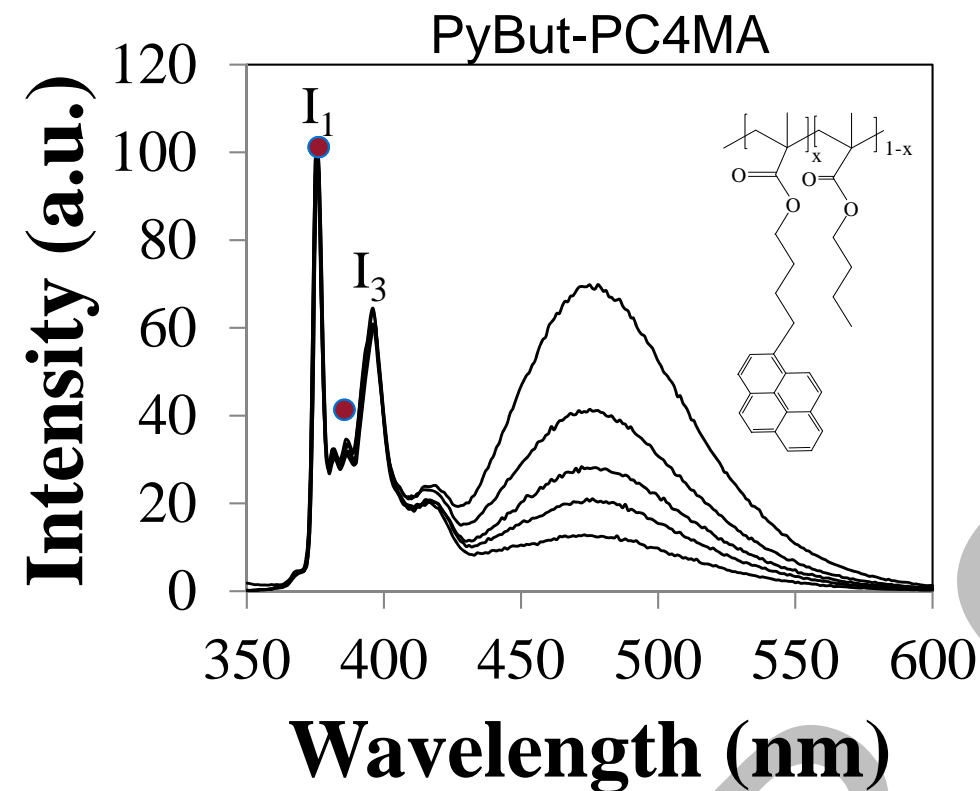
- ✓ Pyrene content was determined for all polymer samples.

Steady-State Fluorescence Spectra



(I_1/I_3) of pyrene emission was used to monitor the local environment of the pyrene molecules

I_1/I_3 Ratios in THF Using Steady-State Fluorescence Spectra

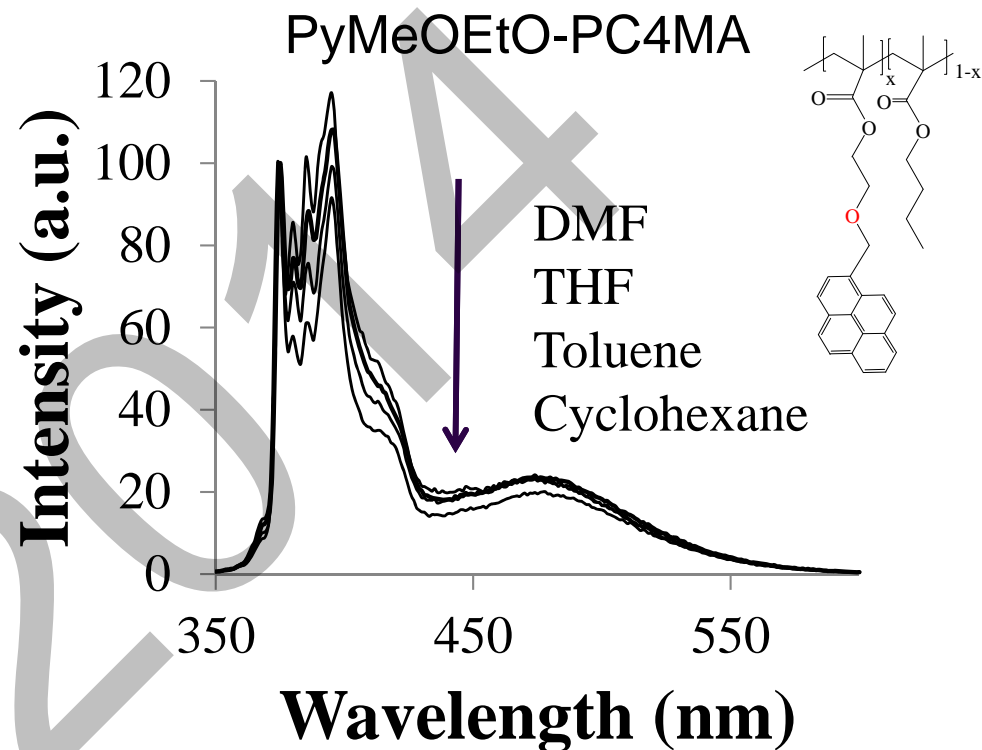
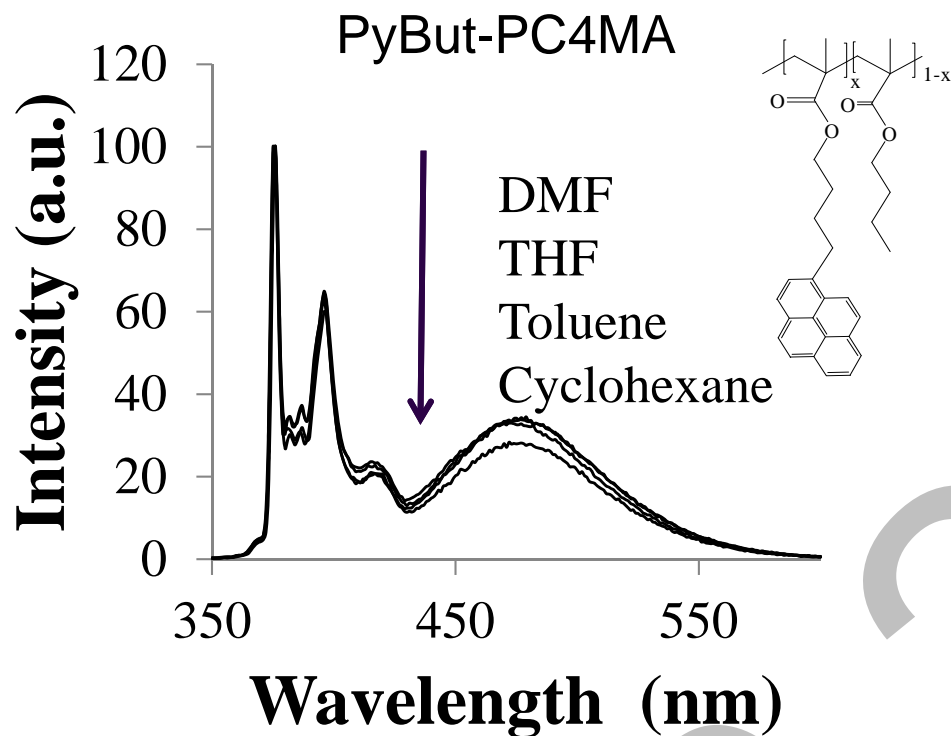


Pyrene Content mol%	I_1/I_3 Ratio (THF)
2.20	3.18
2.90	3.00
3.60	3.13
5.20	2.90
7.20	3.00

Pyrene Content mol%	I_1/I_3 Ratio (THF)
1.3*	1.37
1.8	1.32
4.7*	1.30

Samples with (*) has been prepared by Remi Casier
(Prof. JD lab)

I_1/I_3 Ratios Using Steady-State Fluorescence Spectra



Solvent	Polarity index	I_1/I_3 Ratio
DMF	6.4	3.24
THF	4.0	3.13
Toluene	2.4	2.75
Cyclohexane	0.2	2.61

Solvent	Polarity index	I_1/I_3 Ratio
DMF	6.4	1.64
THF	4.0	1.32
Toluene	2.4	1.13
Cyclohexane	0.2	1.00

Acknowledgements

- **Remi Casier**
- **Prof. Mario Gauthier**
- **Duhamel and Gauthier Group**
- **Funding provided by NSERC**



Institute for Polymer Research

Celebrating 30 years of Official Institute Status

Symposium documents for

Dina Hamad

Experimental Study of Polyvinyl Alcohol Degradation in Aqueous Solution by UV/ H₂O₂ Process

Dina Hamad, Ramdhane Dhib, Mehrab Mehrvar
Chemical Engineering Department
Ryerson University

36th Annual Symposium on Polymer Science/Engineering
Institute for Polymer Research, Waterloo University
May 21, 2014

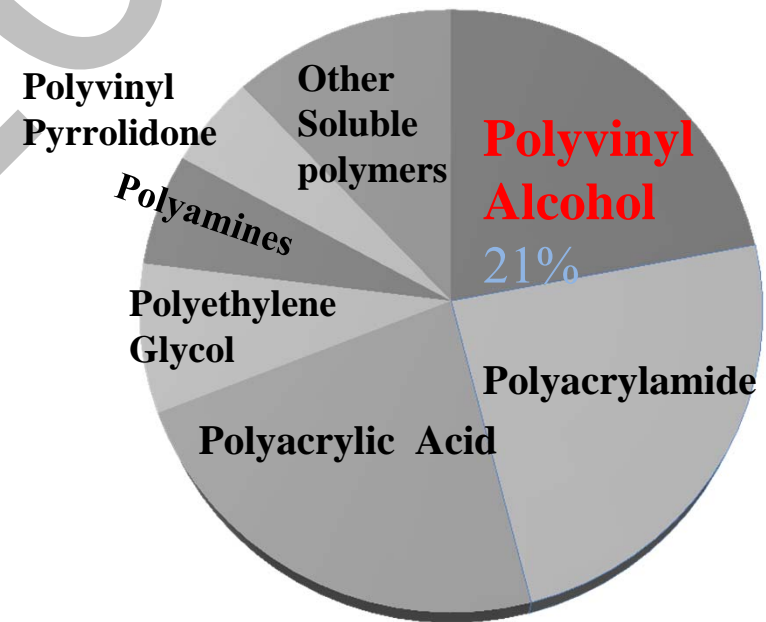
Outline

- Introduction
- Objectives
- Experimental Setup
- Results and Discussion
- Concluding Remarks

Water Soluble Polymers: PVA, PAA, PEG, PAM,....

Synthetic polymers that can dissolve, disperse or swell in **water**.

- Large scale production
- Wide spectrum of applications
- Considerable amounts of PVA-containing wastewater: production, use, and disposal
- Released into the aqueous environment



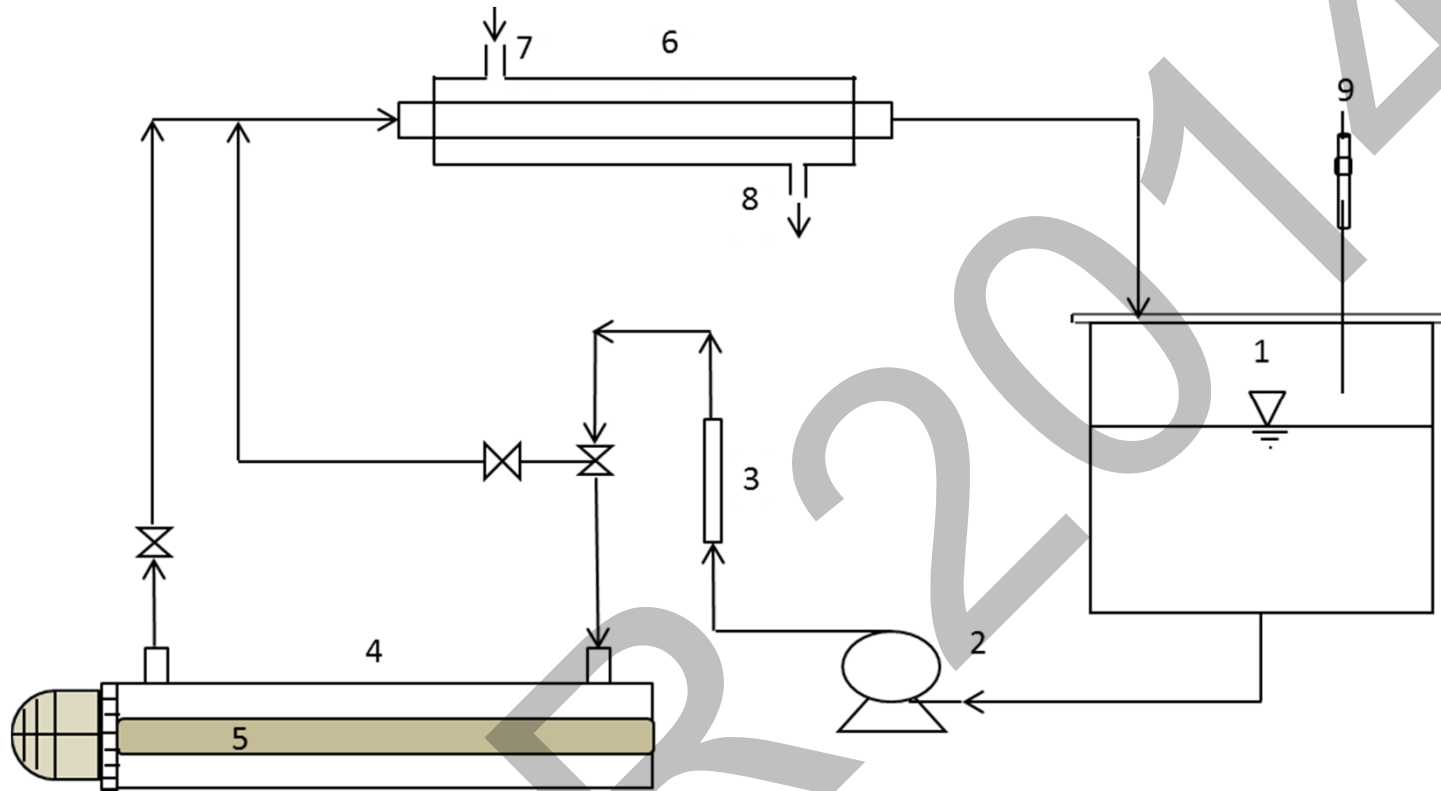
World Consumption of Water-Soluble Polymers

Powerful technologies to transform organic contaminants into water and carbon dioxide

- ❑ Formation of hydroxyl radicals (strong oxidants)
- ❑ Reaction of these radicals with polymers soluble in water

- *PVA degradation by batch and fed-batch advanced oxidation (UV/ H₂O₂) process*
- *Investigate the effects of H₂O₂ feeding strategy on polymer degradation rate*

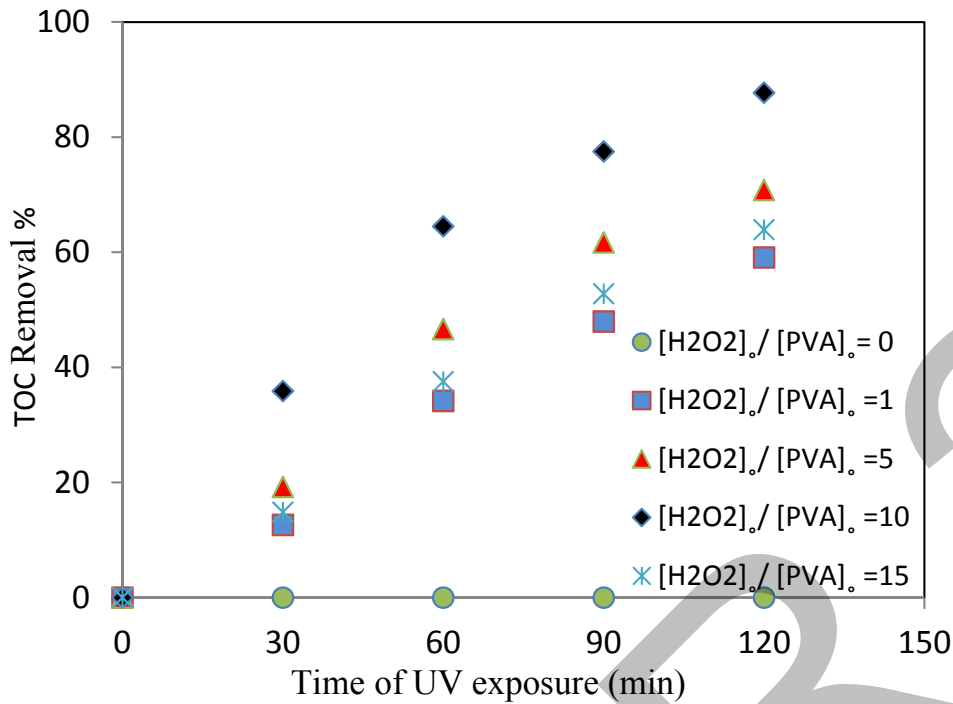
Experimental Photoreactor Setup



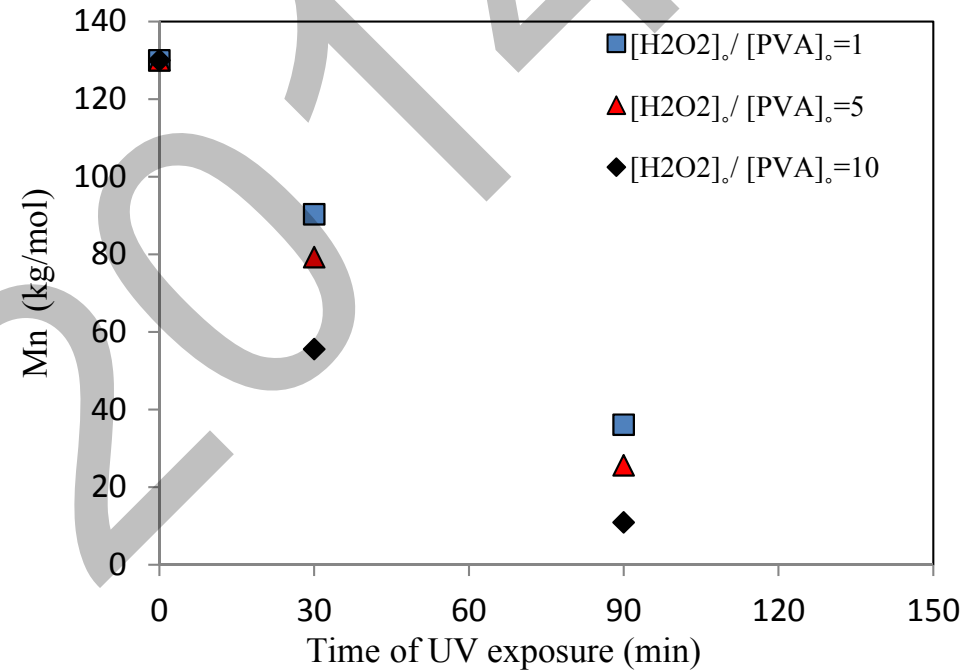
Schematic diagram of the laboratory scale batch and fed-batch system

1. Reservoir and collection tank, 2. Centrifugal pump, 3. Flow meter, 4. Annular photoreactor, 5. UV-C lamp, 6. Heat exchanger, 7. Cooling water inlet, 8. Cooling water outlet, 9. Syringe for H_2O_2 injection

Results and Discussion

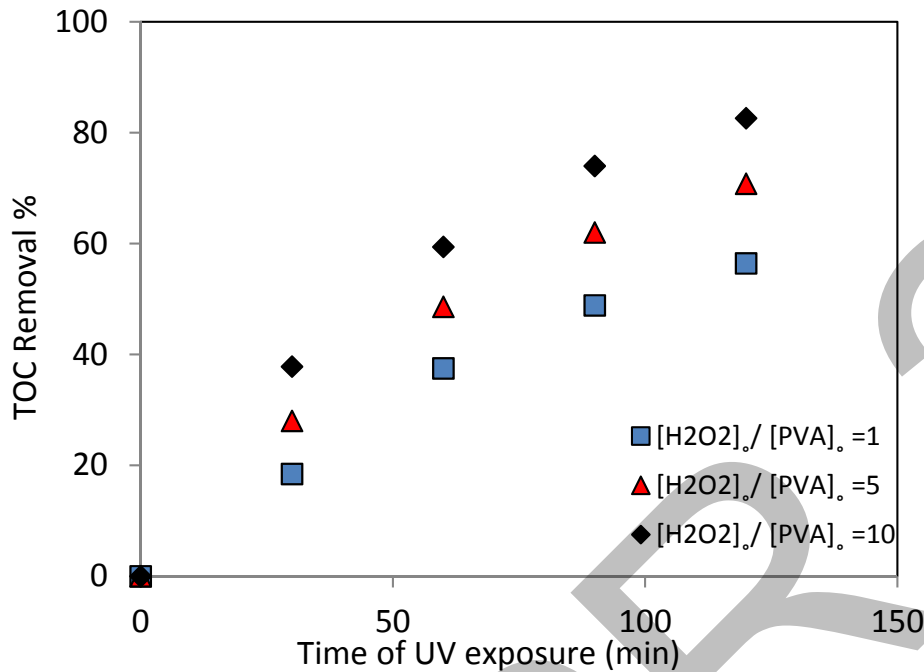


The effect of H₂O₂ dosage on the TOC removal during fed-batch UV/H₂O₂ process, [PVA]₀ = 500 mg/L, [H₂O₂]₀/[PVA]₀ mass ratio of 0, 1, 5, 10, 15, H₂O₂ dripped into the system in stepwise manner

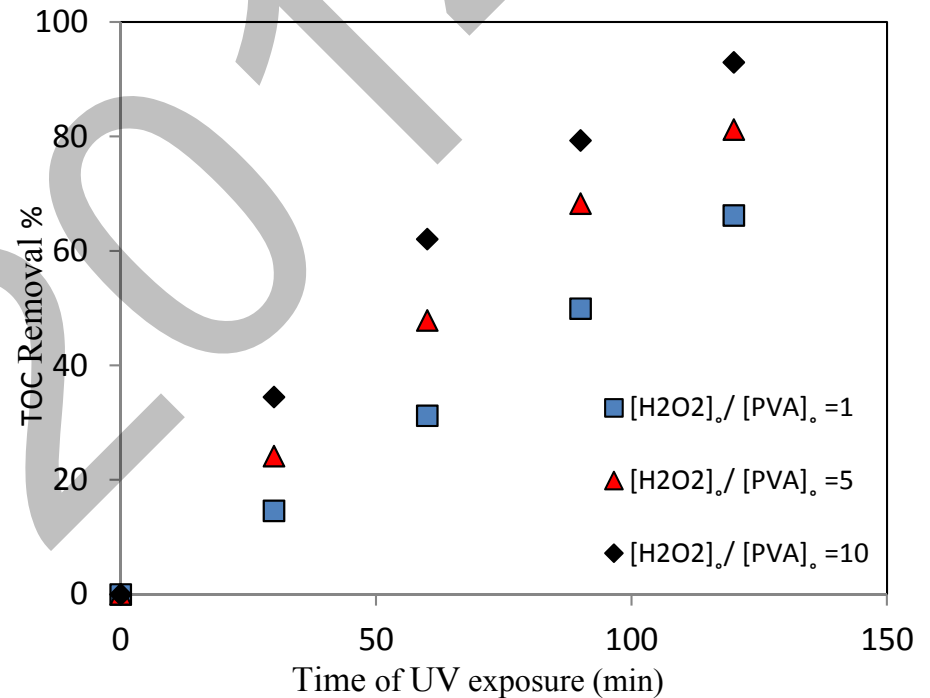


Molecular weight variation during fed-batch UV/H₂O₂ process, [PVA]₀ = 500 mg/L, [H₂O₂]₀/[PVA]₀ mass ratio of 1, 5, 10, H₂O₂ dripped into the system in stepwise manner

Results and Discussion



(a)



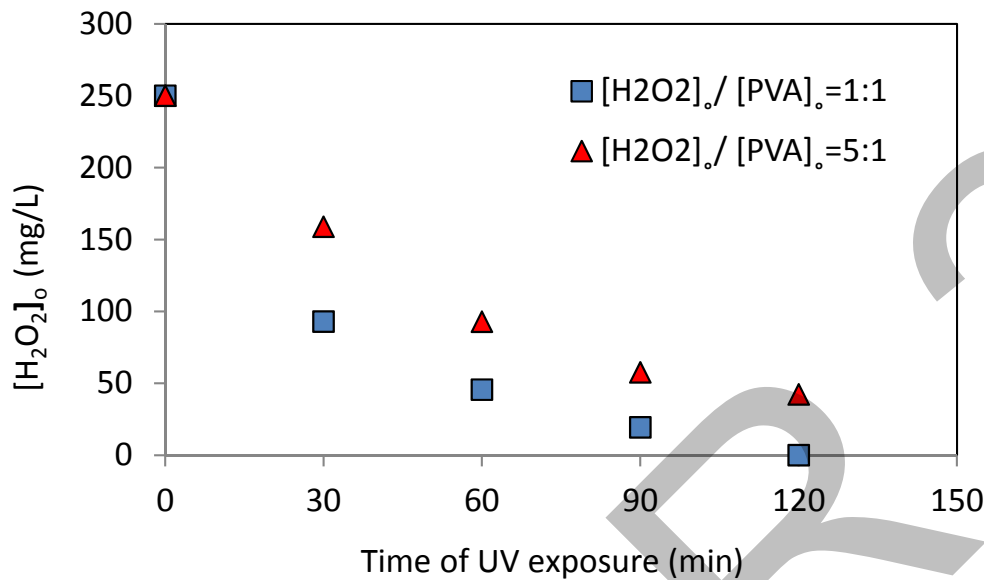
(b)

The effect of H₂O₂ feeding strategy on the TOC removal during batch and fed-batch UV/H₂O₂ process, [PVA]₀ = 50 mg/L, [H₂O₂]₀/[PVA]₀ mass ratio of 1,5,10.

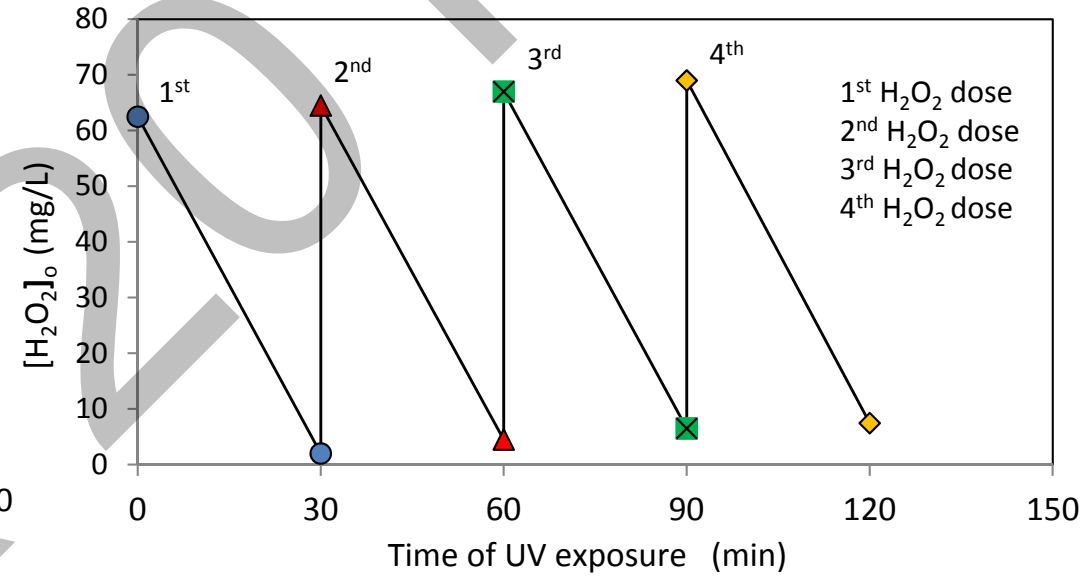
(a) one shot of H₂O₂ poured at the beginning of the experiment

(b) H₂O₂ dripped into the system in stepwise manner

Results and Discussion



a)



b)

H₂O₂ variation during batch and fed-batch UV/H₂O₂ process, [PVA]_o = 50 mg/L, [H₂O₂]_o/[PVA]_o mass ratio of 1,5.

(a) one shot of H₂O₂ poured at the beginning of the experiment

(b) H₂O₂ dripped into the system in stepwise manner

Concluding Remarks

- It is technically feasible to degrade PVA in aqueous solution by UV /H₂O₂ process.
- For aqueous solution of 500mg/L PVA (Mn=130,000 g/mol), H₂O₂/PVA mass ratio of 10, 87 % TOC removal was achieved. Accordingly, 91% decrease in the number average molecular weight.
- H₂O₂ feeding strategy has a great effect on polymer degradation and TOC removal.
- 92% TOC removal of 50mg/L PVA solution for dripping H₂O₂ compared to 83% TOC removal for dumping one single shot.

Acknowledgements

- Supervisors: Dr. Ramdhane Dhib and Dr. Mehrab Mehrvar.
- Chemical Engineering Department, Ryerson University
- Natural Science and Engineering Research Council of Canada (NSERC)

Thank You.

IPRR 2014

Institute for Polymer Research

Celebrating 30 years of Official Institute Status

Symposium documents for

Yifeng Huang



University of Waterloo

*Department of Chemical Engineering
Membrane & Separations Laboratory*

Polyvinylamine-enhanced Ultrafiltration for Removal of Heavy Metals from Wastewater

Yifeng Huang, and Xianshe Feng

IPR Symposium 2014

21 May 2014, Waterloo, ON



Introduction

Contamination of heavy metals

Heavy metals

hydrogen 1 H 1.0079	helium 2 He 4.0026																	boron 5 B 10.811	carbon 6 C 12.011	nitrogen 7 N 14.007	oxygen 8 O 15.999	fluorine 9 F 18.998	neon 10 Ne 20.180										
lithium 3 Li 6.941	beryllium 4 Be 9.0122																	aluminum 13 Al 26.982	silicon 14 Si 28.086	phosphorus 15 P 30.974	sulfur 16 S 32.065	chlorine 17 Cl 35.453	argon 18 Ar 39.948										
sodium 11 Na 22.990	magnesium 12 Mg 24.305																	gallium 31 Ga 69.723	germanium 32 Ge 72.61	arsenic 33 As 74.922	seelenium 34 Se 78.96	bromine 35 Br 79.904	krypton 36 Kr 83.80										
potassium 19 K 39.098	calcium 20 Ca 40.078	scandium 21 Sc 44.956	titanium 22 Ti 47.867	vanadium 23 V 50.942	chromium 24 Cr 51.996	manganese 25 Mn 54.938	iron 26 Fe 55.845	cobalt 27 Co 58.933	nickel 28 Ni 58.693	copper 29 Cu 63.546	zinc 30 Zn 65.39	cadmium 48 Cd 112.41	mercury 80 Hg 200.59	thallium 81 Tl 204.38	lead 82 Pb 207.2	bismuth 83 Bi 208.98	polonium 84 Po [209]	astatine 85 At [210]	radon 86 Rn [222]														
rubidium 37 Rb 85.468	strontium 38 Sr 87.62	yttrium 39 Y 88.906	zirconium 40 Zr 91.224	niobium 41 Nb 92.906	niobium 42 Nb 92.906	technetium 43 Tc [98]	ruthenium 44 Ru 101.07	rhodium 45 Rh 102.91	silver 47 Ag 107.87	gold 79 Au 196.97	platinum 78 Pt 195.08	uranium 92 U 238.03	neptunium 93 Np [237]	plutonium 94 Pu [244]	americium 95 Am [243]	curium 96 Cm [247]	berkelium 97 Bk [247]	californium 98 Cf [251]	einsteinium 99 Es [252]	fermium 100 Fm [257]	mendelevium 101 Md [258]	nobelium 102 No [259]											
cesium 55 Cs 132.91	barium 56 Ba 137.33	lanthanum 57 La 138.91	cerium 58 Ce 140.12	praseodymium 59 Pr 140.91	neodymium 60 Nd 144.24	promethium 61 Pm [145]	samarium 62 Sm 150.36	europium 63 Eu 151.96	gadolinium 64 Gd 157.25	terbium 65 Tb 158.93	dysprosium 66 Dy 162.50	holmium 67 Ho 164.93	erbium 68 Er 167.26	thulium 69 Tm 168.93	ytterbium 70 Yb 173.04	lutetium 71 Lu 174.967	hafnium 72 Hf 178.49	tantalum 73 Ta 180.95	wolfram 74 W 183.84	reynoldsium 75 Re 186.21	osmium 76 Os 190.23	iridium 77 Ir 192.22	platinum 78 Pt 195.08	gold 79 Au 196.97	mercury 80 Hg 200.59	thallium 81 Tl 204.38	lead 82 Pb 207.2	bismuth 83 Bi 208.98	polonium 84 Po [209]	astatine 85 At [210]	radon 86 Rn [222]		
francium 87 Fr [223]	radium 88 Ra [226]	actinium 89 Ac [227]	thorium 90 Th 232.04	protactinium 91 Pa 231.04	uranium 92 U 238.03	neptunium 93 Np [237]	plutonium 94 Pu [244]	americium 95 Am [243]	curium 96 Cm [247]	berkelium 97 Bk [247]	californium 98 Cf [251]	einsteinium 99 Es [252]	fermium 100 Fm [257]	mendelevium 101 Md [258]	nobelium 102 No [259]	bohrium 103 Bh [264]	hassium 104 Hs [265]	meitnerium 105 Mt [266]	darmstadtium 106 Ds [267]	roentgenium 107 Rg [268]	copernicium 108 Cn [269]	nihonium 109 Nh [270]	flerovium 110 Fl [271]	tennessine 111 Ts [272]	oganesson 112 Og [273]	unbinilium 113 Uub [274]	ununilium 114 Uuq [275]	ununnilium 115 Uuu [276]	unununium 116 Uub [277]	ununnium 117 Uuq [278]	ununseptium 118 Uus [279]	ununoctium 119 Uuo [280]	unbihexium 120 Uub [281]



* Lanthanide series

lanthanum 57 La 138.91	cerium 58 Ce 140.12	praseodymium 59 Pr 140.91	neodymium 60 Nd 144.24	promethium 61 Pm [145]	samarium 62 Sm 150.36	europium 63 Eu 151.96	gadolinium 64 Gd 157.25	terbium 65 Tb 158.93	dysprosium 66 Dy 162.50	holmium 67 Ho 164.93	erbium 68 Er 167.26	thulium 69 Tm 168.93	ytterbium 70 Yb 173.04	lutetium 71 Lu 174.967
actinium 89 Ac [227]	thorium 90 Th 232.04	protactinium 91 Pa 231.04	uranium 92 U 238.03	neptunium 93 Np [237]	plutonium 94 Pu [244]	americium 95 Am [243]	curium 96 Cm [247]	berkelium 97 Bk [247]	californium 98 Cf [251]	einsteinium 99 Es [252]	fermium 100 Fm [257]	mendelevium 101 Md [258]	nobelium 102 No [259]	bohrium 103 Bh [264]

** Actinide series

Contaminants (Total amount)	^a Maximum Allowable Discharge Conc. (mg/L)	^b Drinking Water Regulations (mg/L)	^b Public Health Goal (mg/L)
Lead (Pb)	1	0.015	Zero
Copper (Cu)	Not defined	1.3	1.3
Nickel (Ni)	1	Not defined	Not defined
Mercury (Hg)	0.05	0.002	0.002
Cadmium (Cd)	0.1	0.005	0.005
Chromium (Cr)	1.5	0.1	0.1
Arsenic (As)	0.5	0.01	zero

a: National Standard of the P.R.China Integrated Wastewater Discharge Standard

b: National Primary Drinking Water Regulations from USEPA

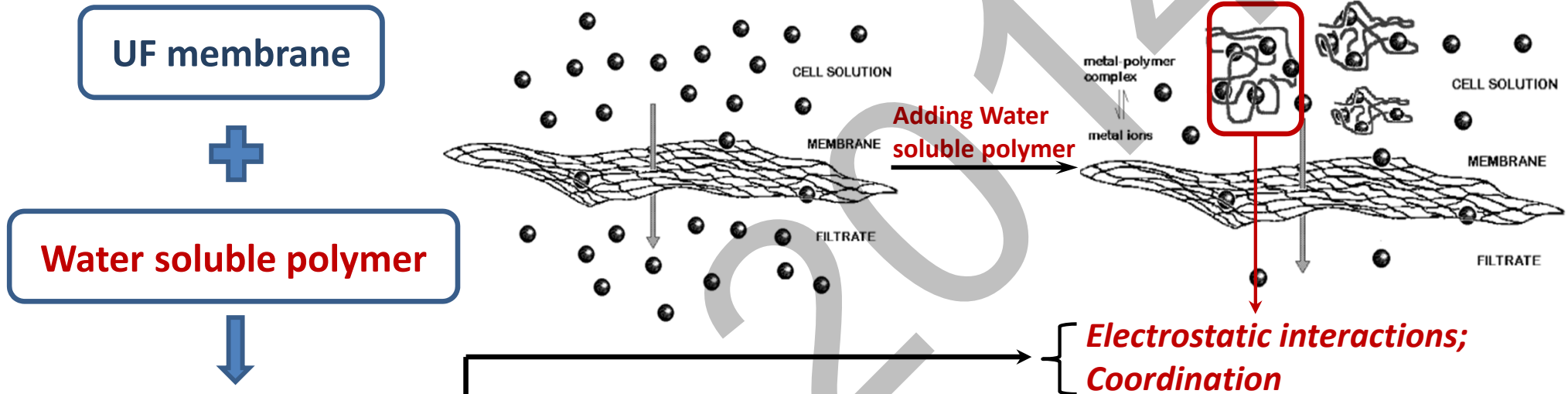
Sources to wastewater:

- Batteries
- Mining industry
- Petrochemical industry
- Manufacture



Introduction

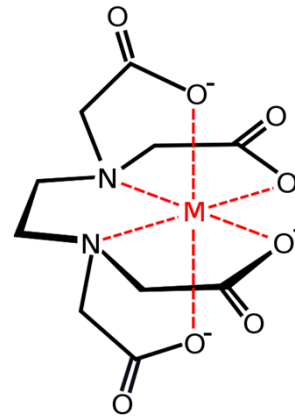
Polymer-enhanced ultrafiltration (PEUF)



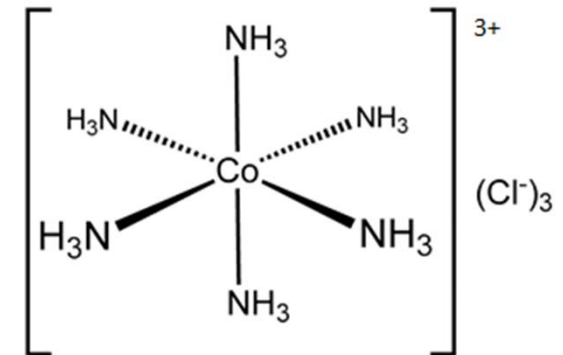
- High content of **Functional Groups**
- Molecular weight greater than the MWCO of UF membranes
- Sufficient solubility in aqueous solution

MWCO: Molecular Weight Cut-Off;
EDTA: Ethylenediaminetetraacetic acid

Coordination examples:



Metal-EDTA complex



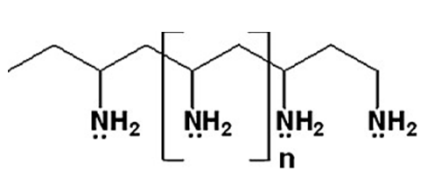
Cobalt(III) complex



Results and discussion

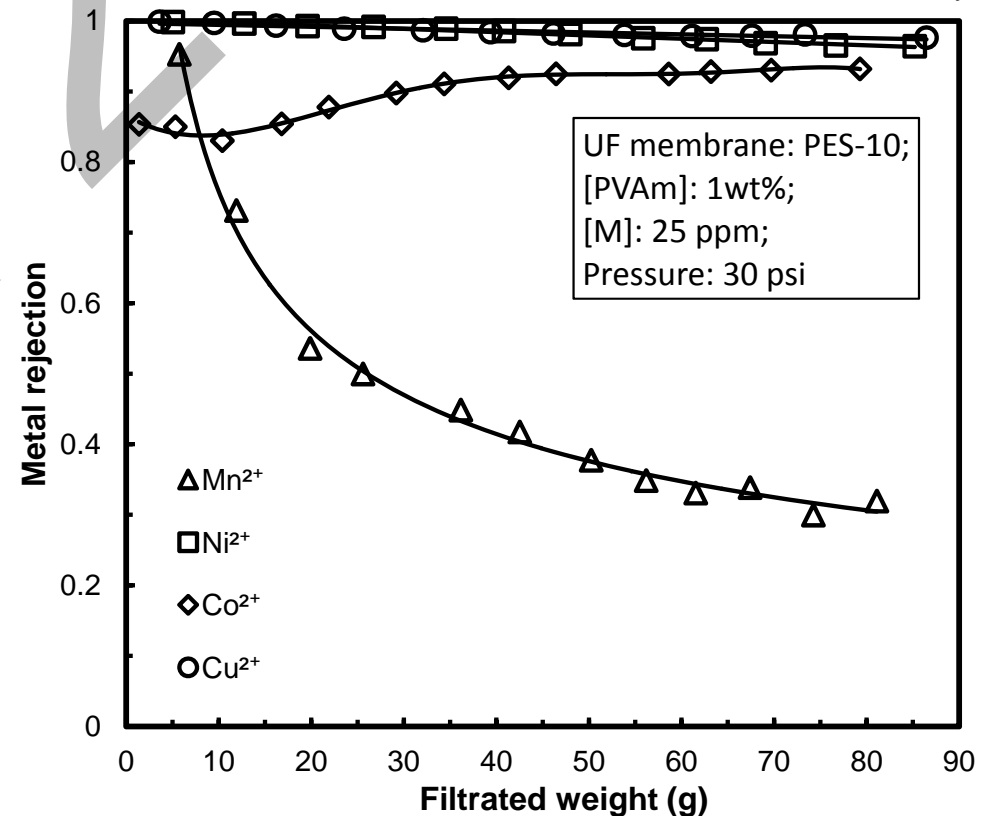
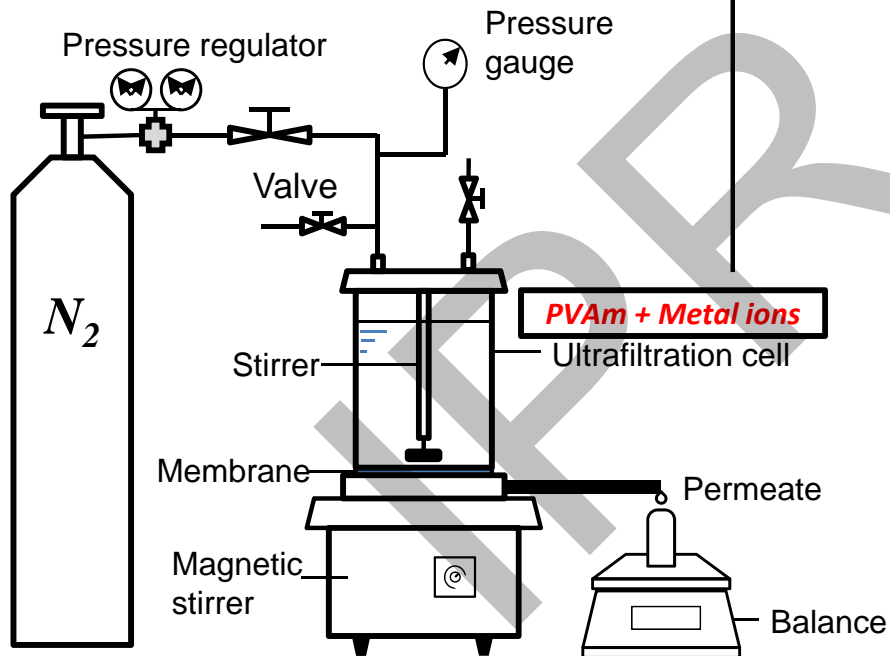
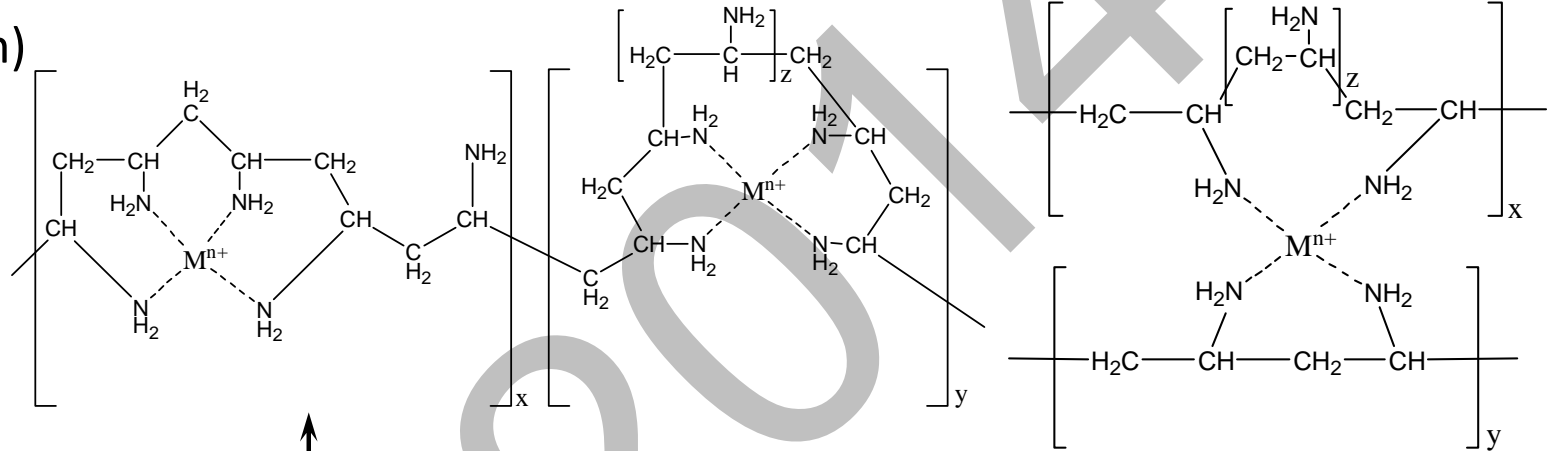
Metal removal by PVAm-enhanced UF

Polyvinylamine (PVAm)



Lupamin 9095 (BASF);

\overline{M}_n : 340,000





Summary

- Polyvinylamine is proved to work for heavy metal removal using PEUF
 - Metal rejection, Co²⁺: 89.0%, Cu²⁺: 99.3%, Ni²⁺: 98.8%, Mn²⁺: 40% ([PVAm]: 1wt%, [metals]: 25ppm)
- The metal rejections in PEUF are highly related to the coordination interactions between PVAm and heavy metals
- Potential application in the separation of mercury and arsenic from wastewater



Thank you !

IPR 2014

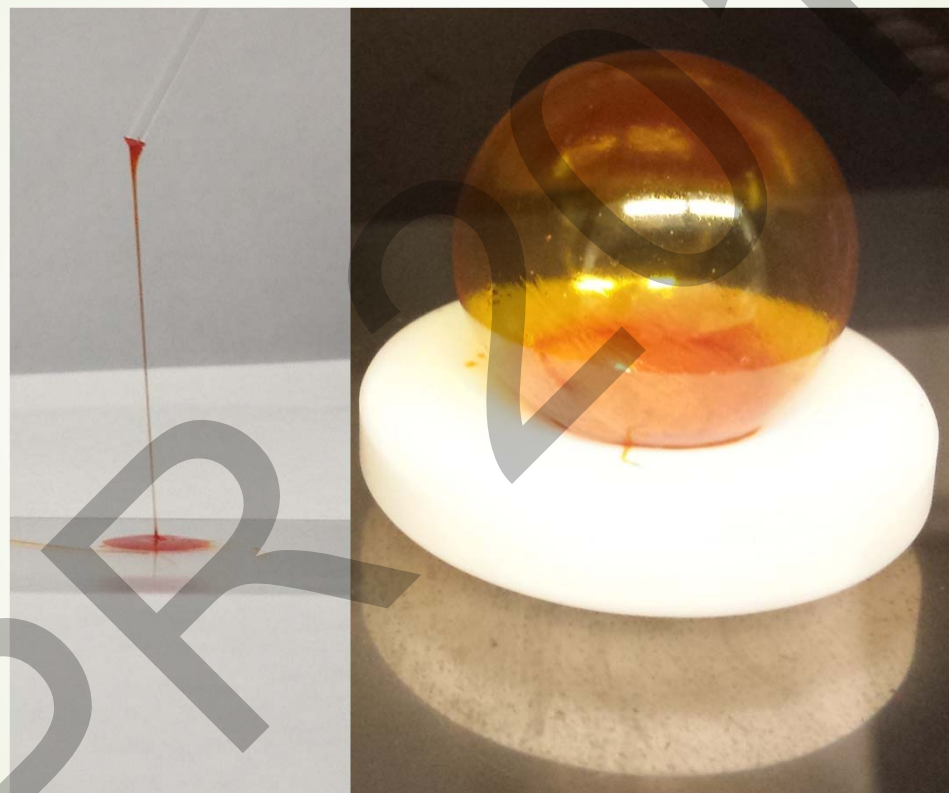
Institute for Polymer Research

Celebrating 30 years of Official Institute Status

Symposium documents for

Nicholas Lanigan

A Novel Metal-Containing Supramolecular Polymer

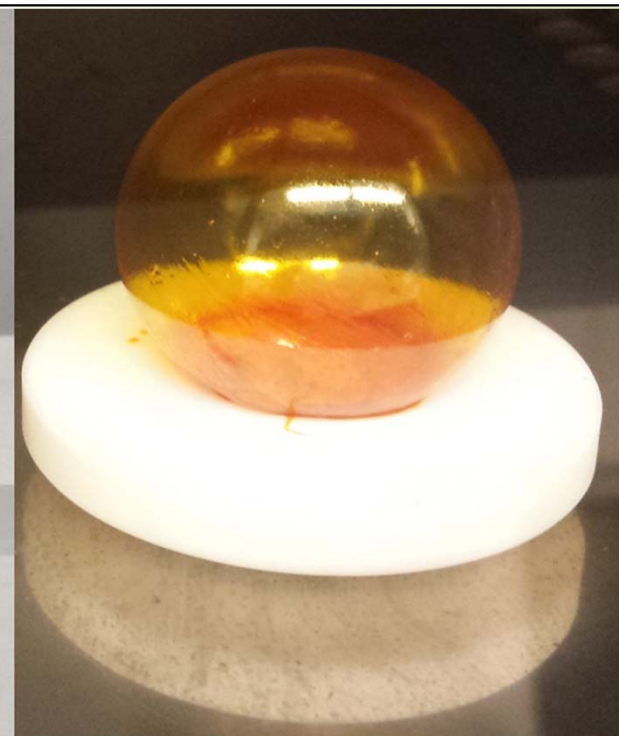
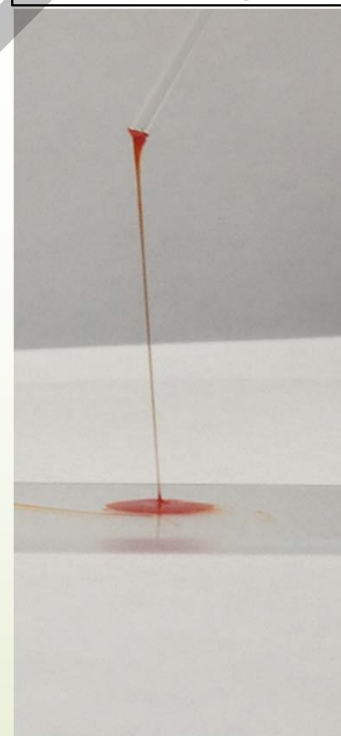
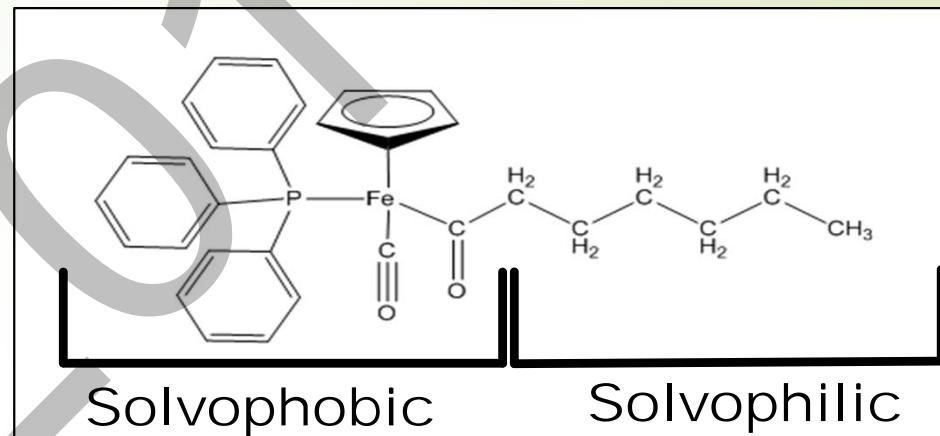


Nicholas Lanigan
Ph.D. Candidate

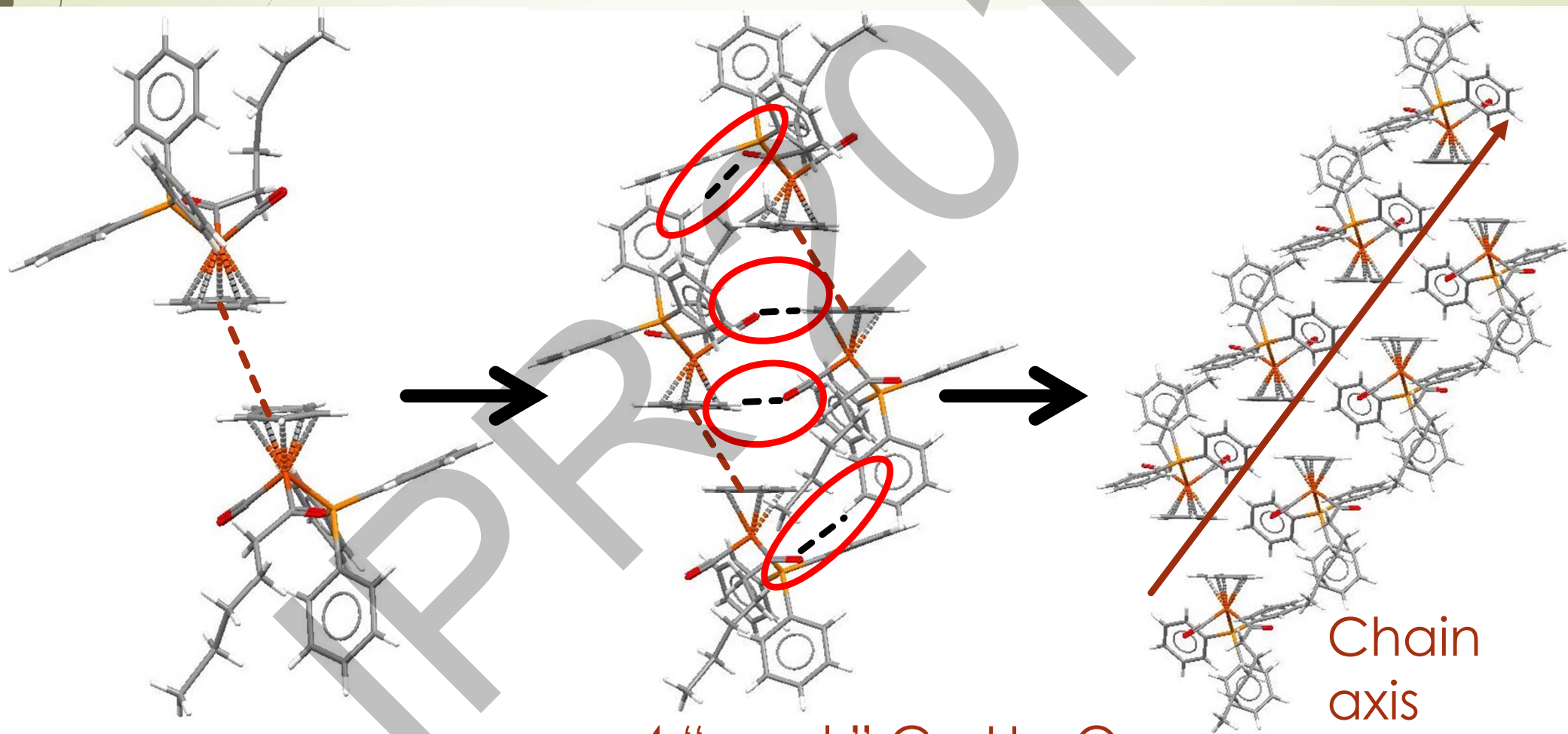
Supervisor: Xiaosong Wang

My Research: Organometallic Supramolecular Polymers

- Started as an investigation of a metal containing amphiphile: Carbonylcyclopentadienylheptanoyltriphenylphosphineiron (FpC_6)
- Instead of behaving like a small molecule, FpC_6 demonstrated polymeric behaviour.



Single Crystal Chain Structure of FpC₆

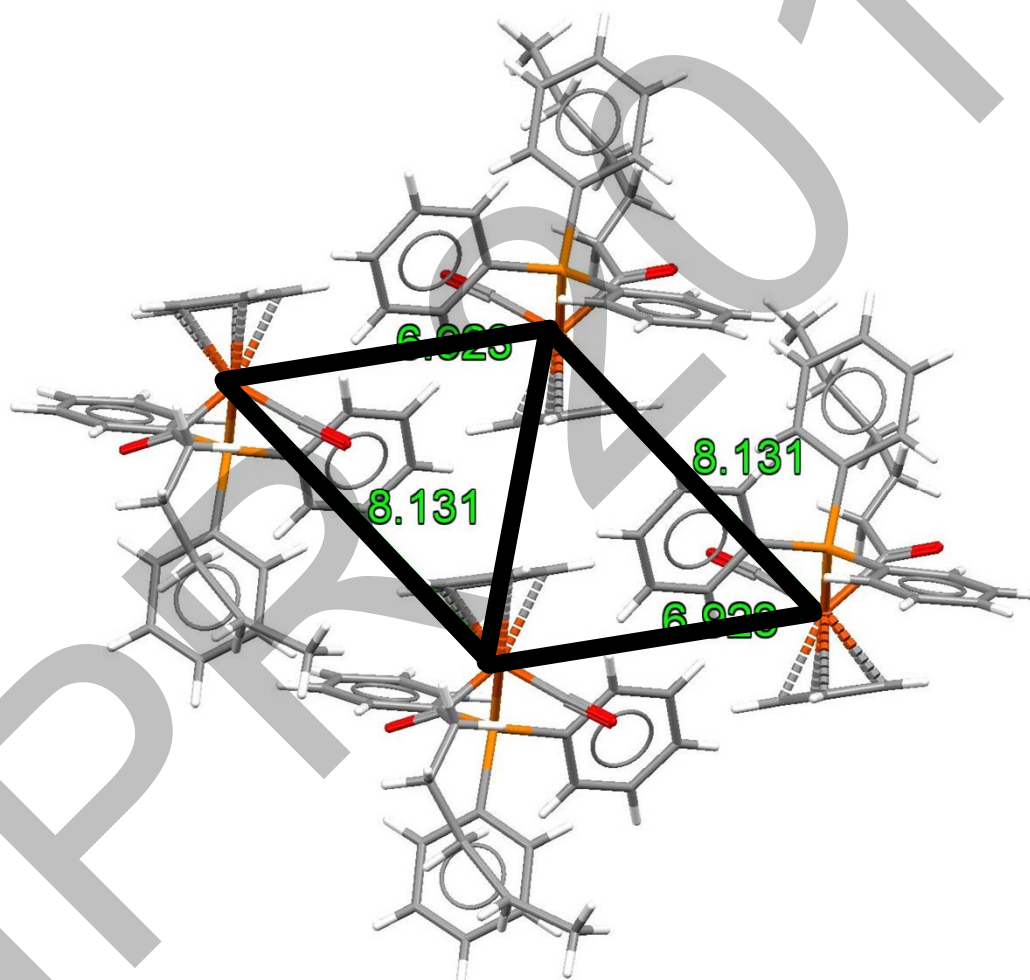


Parallel displaced π - π interaction: 3.94Å

4 "weak" C—H...O hydrogen bonds

Chain axis

PXRD Analysis of FpC₆



Organometallic Supramolecular "TRUSS" Polymer

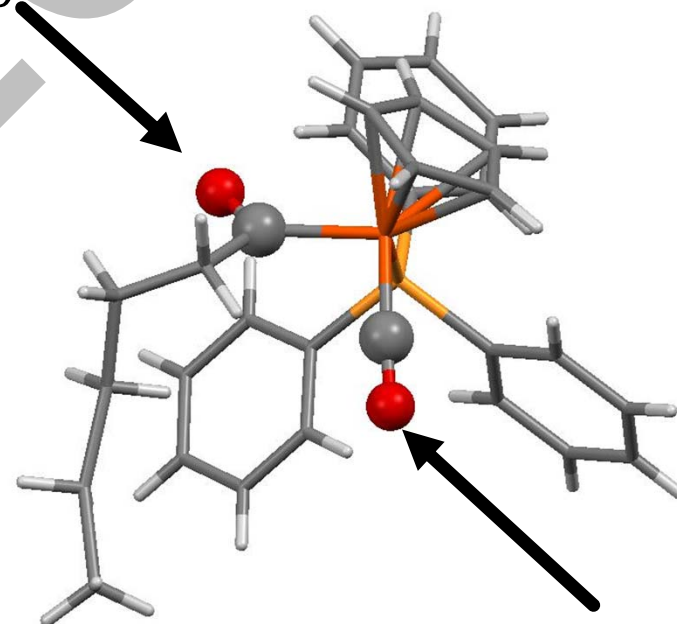
FTIR Analysis of FpC_6

Hydrogen Bonding

There is a gradually shift towards lower wavenumbers as the hydrogen bonding increases.

FTIR Carbonyl Peak Position		
Sample	Terminal $C\equiv O$ (cm^{-1})	Acyl $C=O$ (cm^{-1})
Solution (50 mg/mL BZN)	1911.5	1618.1
Amorphous (FTIR)	1909.6	1609.1
Crystalline (FTIR)	1900.8/ 1894.5	1605.1

Acyl $C=O$



Terminal $C\equiv O$

THANK YOU!

Polymer and Supramolecular Functional
Nanomaterials Group



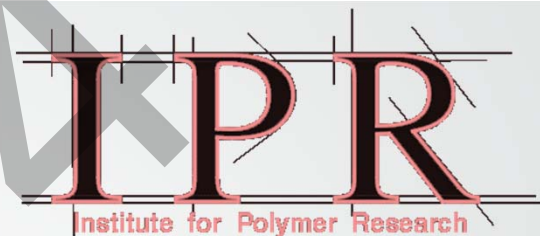
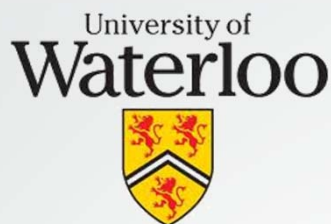
From Left: Kai Cao, Abdelrahman El-Temtamy, Nicholas Lanigan, Nimer Murshid, Jin Liu, Professor Wang.

Institute for Polymer Research

Celebrating 30 years of Official Institute Status

Symposium documents for

Solmaz Pirouz



Using Pyrene Fluorescence to Probe the Behaviour of Semicrystalline Polyolefins in Solution

Solmaz Pirouz and Jean Duhamel

Department of Chemistry

University of Waterloo

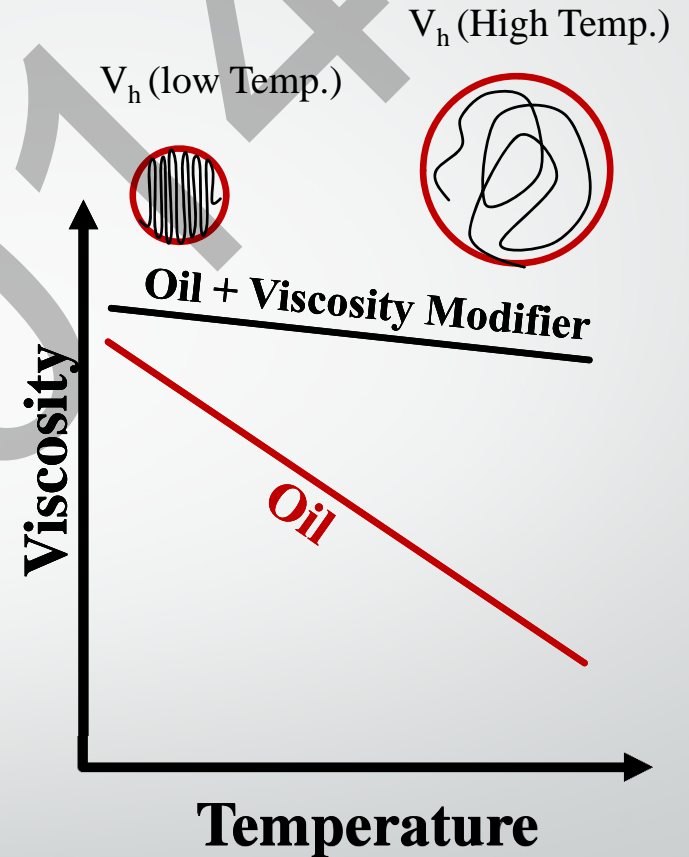
May 21st, 2014

Introduction

Engine oils are vital to all cars as they provide the lubrication needed between the moving parts of the engine.

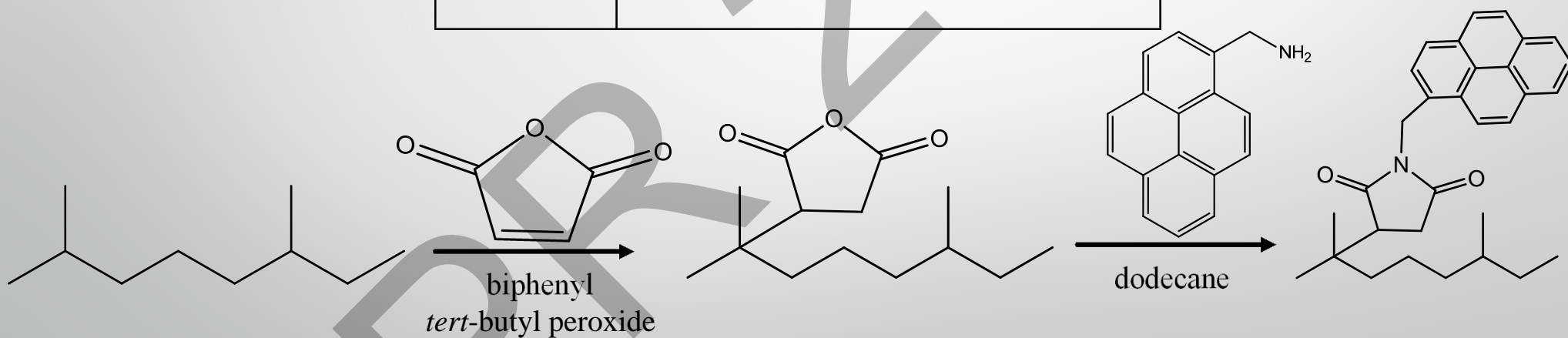
Problem: At high temperatures, liquids become thinner. On the other hand, at extremely low temperatures liquids become more viscous before they reach their freezing point.

Solution: This is where viscosity index improvers (VII) are introduced. VIIs are designed to reduce the change in a lubricant's viscosity when subjected to changes in temperature. Ethylene-propylene copolymers are commonly used as VIIs.

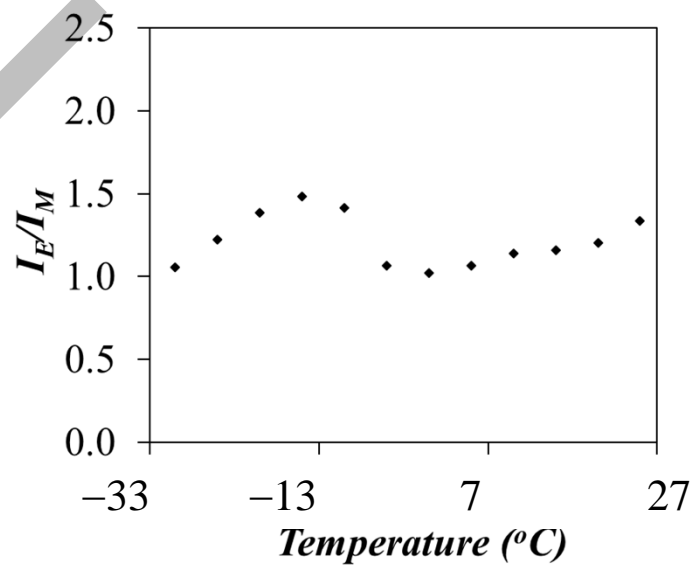
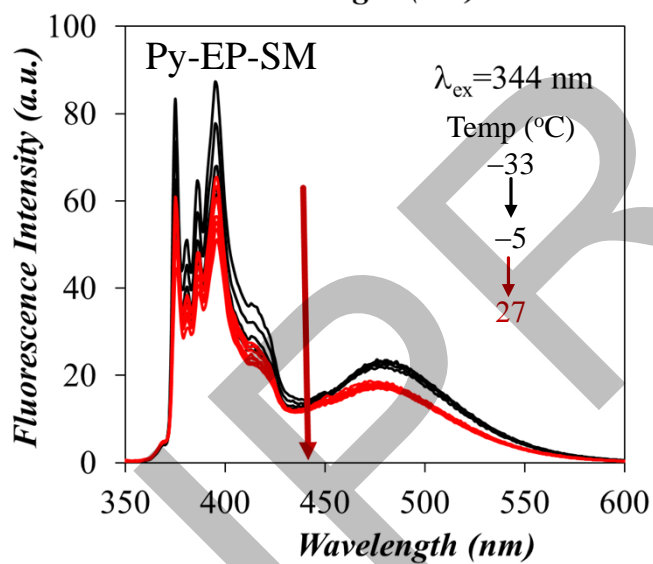
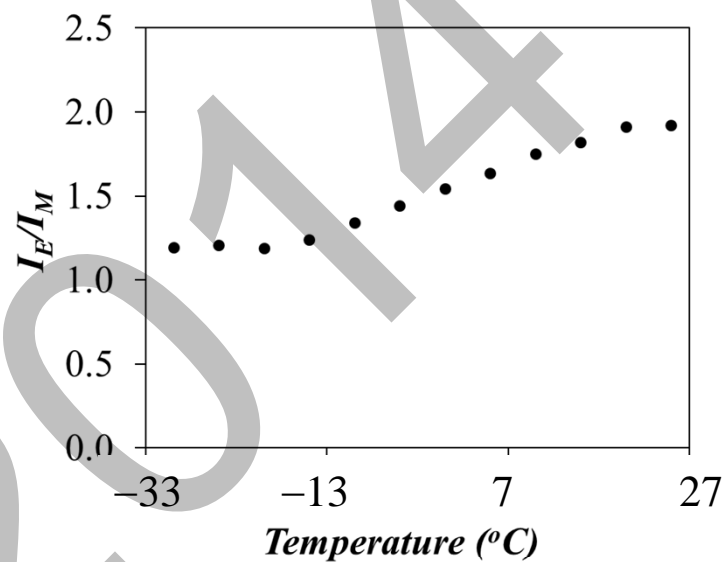
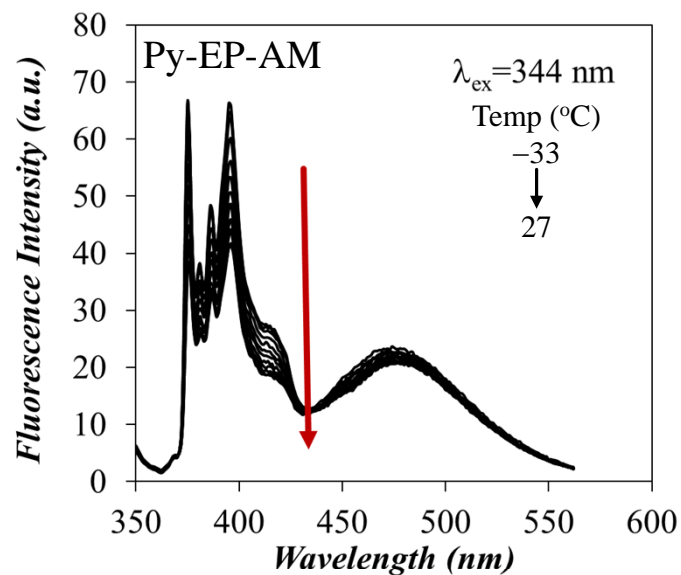


$$\eta = \eta_0 \left(1 + 2.5 \frac{V_h}{V} + 1.4 \left(\frac{V_h}{V} \right)^2 + \dots \right)$$

Sample	Type of EP-Copolymers
EP-AM	EP-Amorphous
EP-SM	EP-Semicrystalline



Steady-State Fluorescence Measurements



Acknowledgments

- Dr. Duhamel's Research Group
- Afton

THANK YOU !

QUESTIONS ?



Institute for Polymer Research

Celebrating 30 years of Official Institute Status

Symposium documents for

Marzieh Riahinezhad

Some Special Factors Influencing Copolymerization Kinetics of a Polyelectrolyte System

Marzieh Riahinezhad,
Neil McManus, and Alexander
Penlidis

May 21, 2014

Motivation & Goals

- ✓ Increasing demand for high performance & water-soluble polymers for Enhanced Oil Recovery (EOR) applications
- ✓ Case study: Acrylamide (AAm)/Acrylic acid (AAc)
- ✓ Need to have a clear understanding of AAm/AAc copolymerization kinetics to 'tailor' copolymer properties

Chain
microstructur
al properties

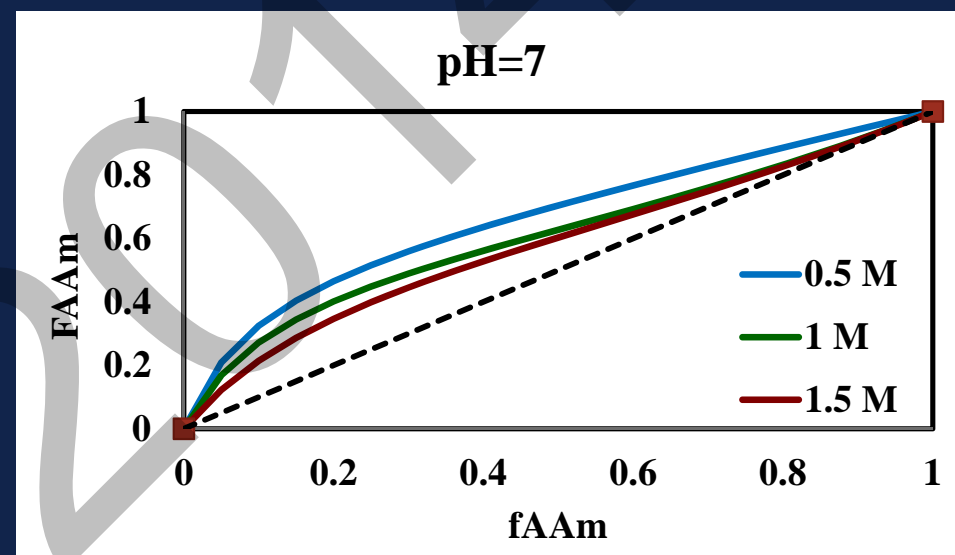
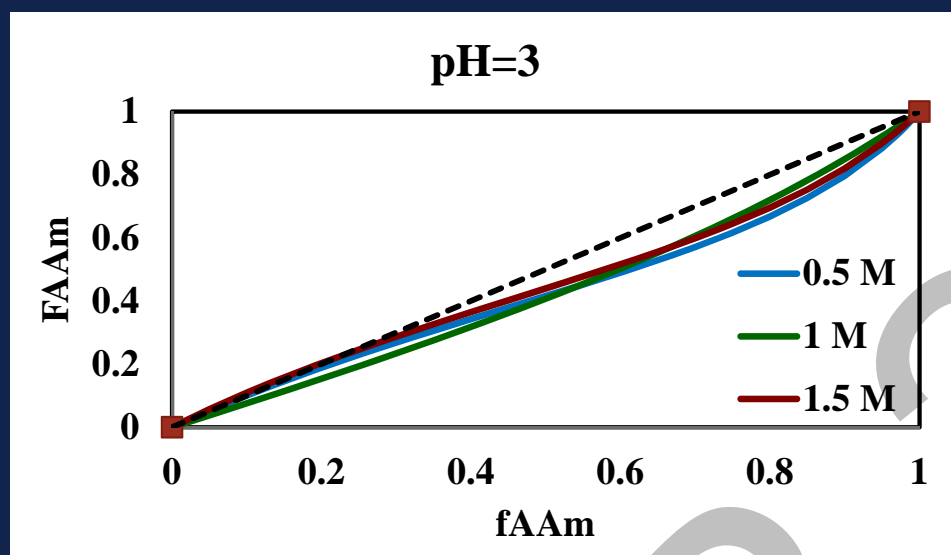
Bulk
macrostructur
al properties

Design of Experiments

Factorial/D-Optimal Design

Main Factors	Responses
Reaction pH	Molecular Weight
Ionic Strength	Monomer Conversion
Monomer Concentration	Copolymer Composition
Monomer Composition in Feed	Monomer Reactivity Ratios
	Monomer Sequence Length

AAm/AAc Copolymerization- pH Effect

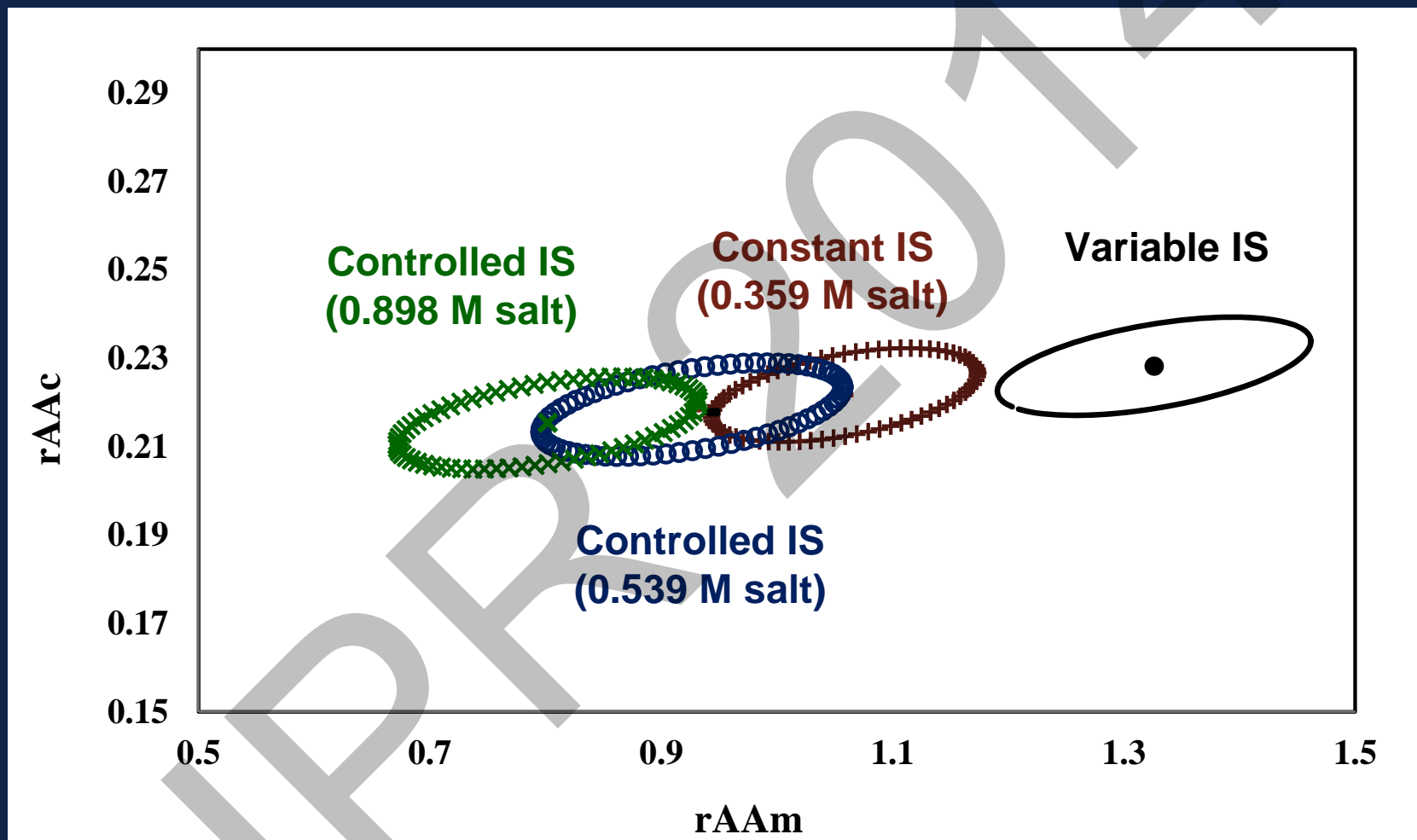


pH < 3 : AAc & partially protonated AAm

3 < pH < 6 : AAc, acrylate anion & AAm

pH > 6 : Acrylate anion & AAm

AAm/AAc Copolymerization- IS Effect





**Thank
You**

**Question
s?**

Experimental

Materials

Acrylamide, AAm and Acrylic acid, AAc
(Monomer)

Sodium hydroxide (pH-controller), ACVA
(Initiator)

Hydroquinone (Inhibitor), Sodium chloride (salt)

Estimation

Error-in-Variables Model (EVM) &
Direct Numerical Integration (DNI) approach

Characterization

Gravimetry for monomer conversion

Elemental analysis for copolymer composition

Inductively coupled plasma (ICP) analysis for
Na content

Polymerization

Temperature = 40 °C

Institute for Polymer Research

Celebrating 30 years of Official Institute Status

Symposium documents for

Ankita Saikia

Modelling the Vulcanization Reaction of Devulcanized Rubber

UNIVERSITY OF
WATERLOO

uwaterloo.ca

Ankita Saikia

Supervisor: Prof. Costas Tzoganakis

Background

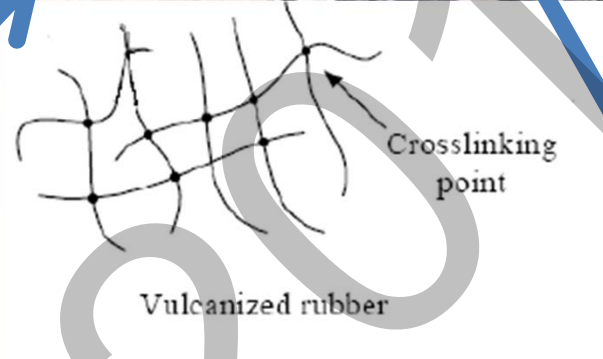
Virgin / Raw Rubber



Vulcanization/
Crosslinking

Vulcanized rubber

Is it same
or
different???



Pollution/
Health &
Fire Hazards

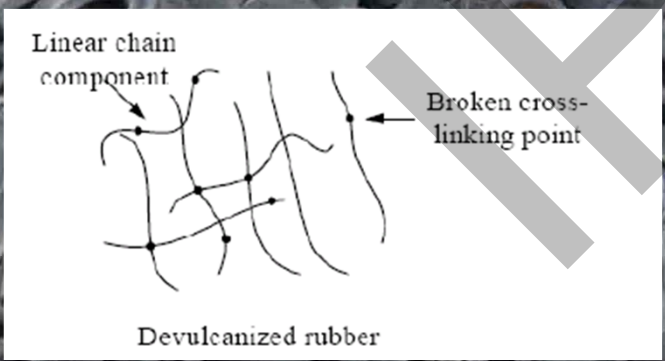
End life

Need to characterize the
vulcanization reaction!!!

Devulcanized Rubber

Devulcanization

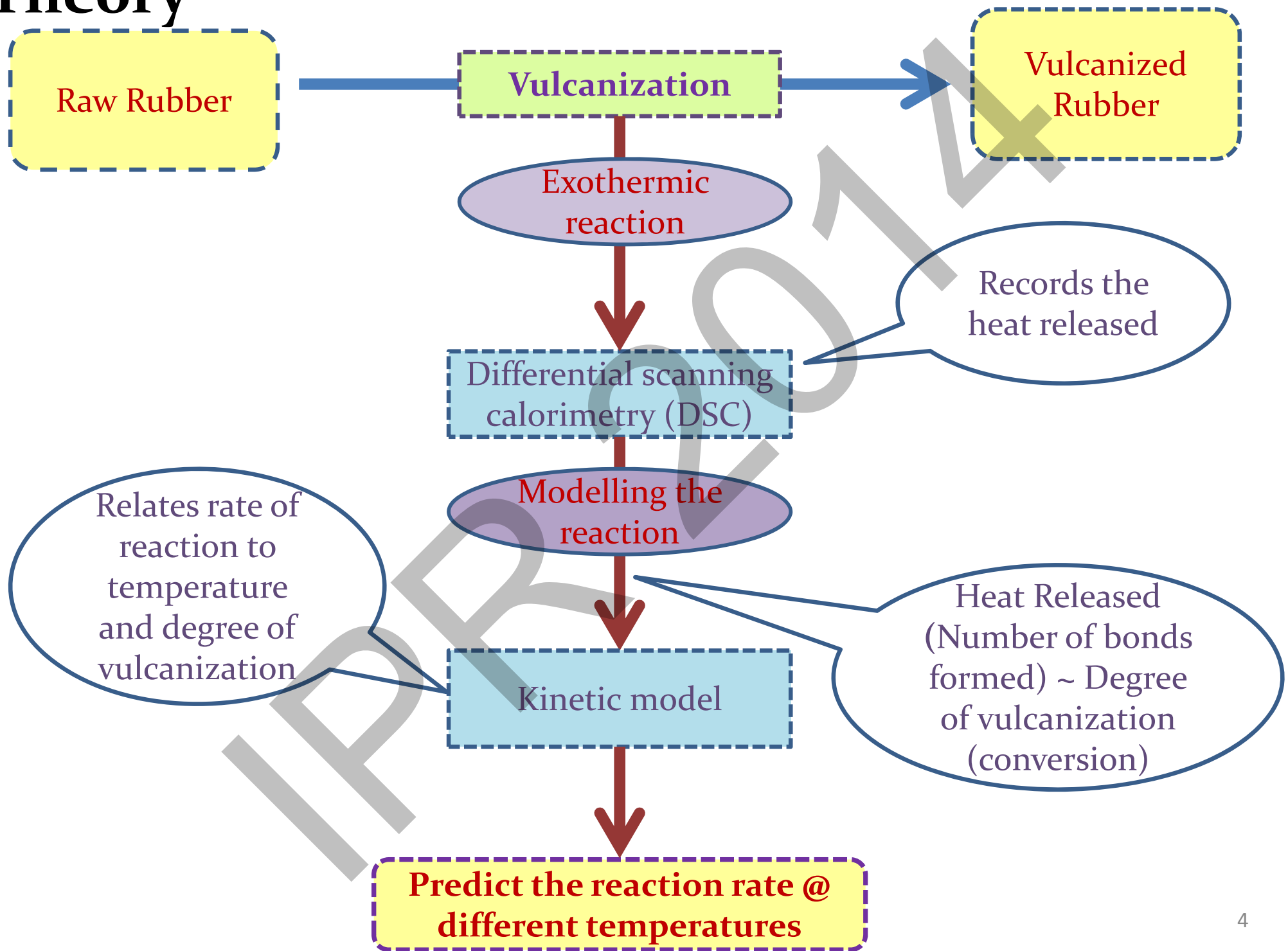
Scrap
tires/rubber



Objectives

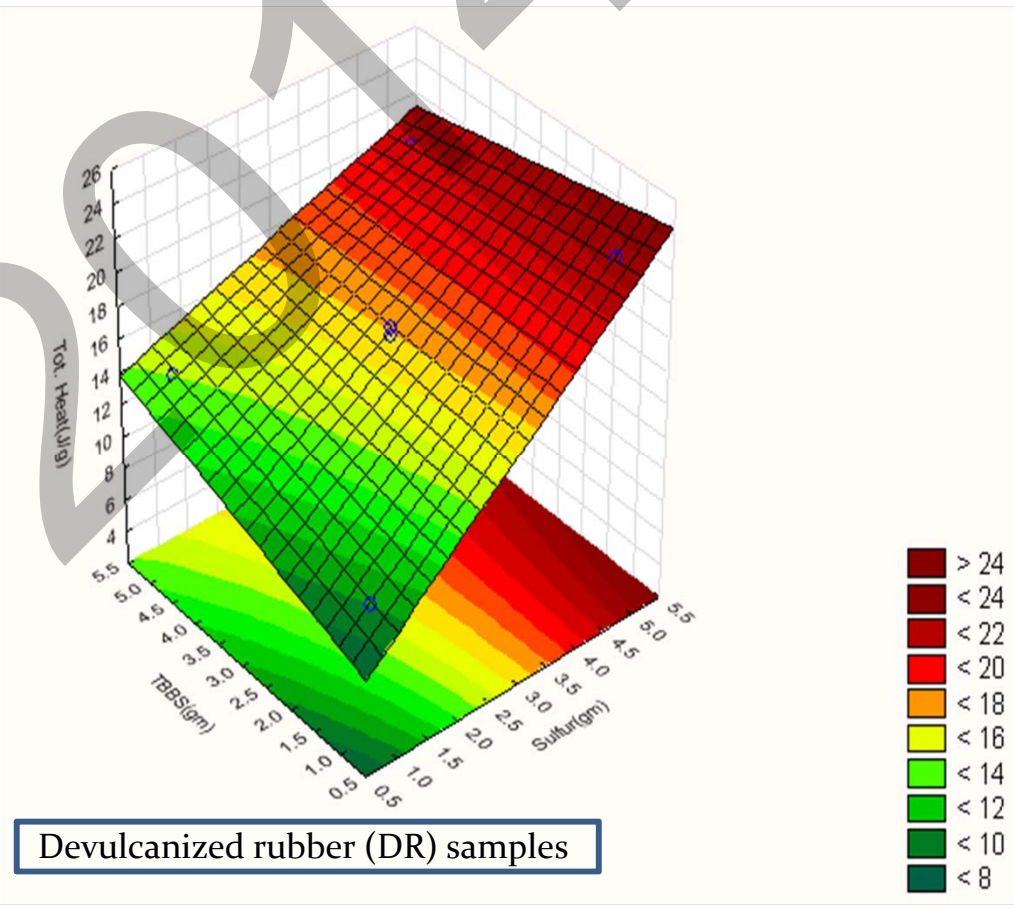
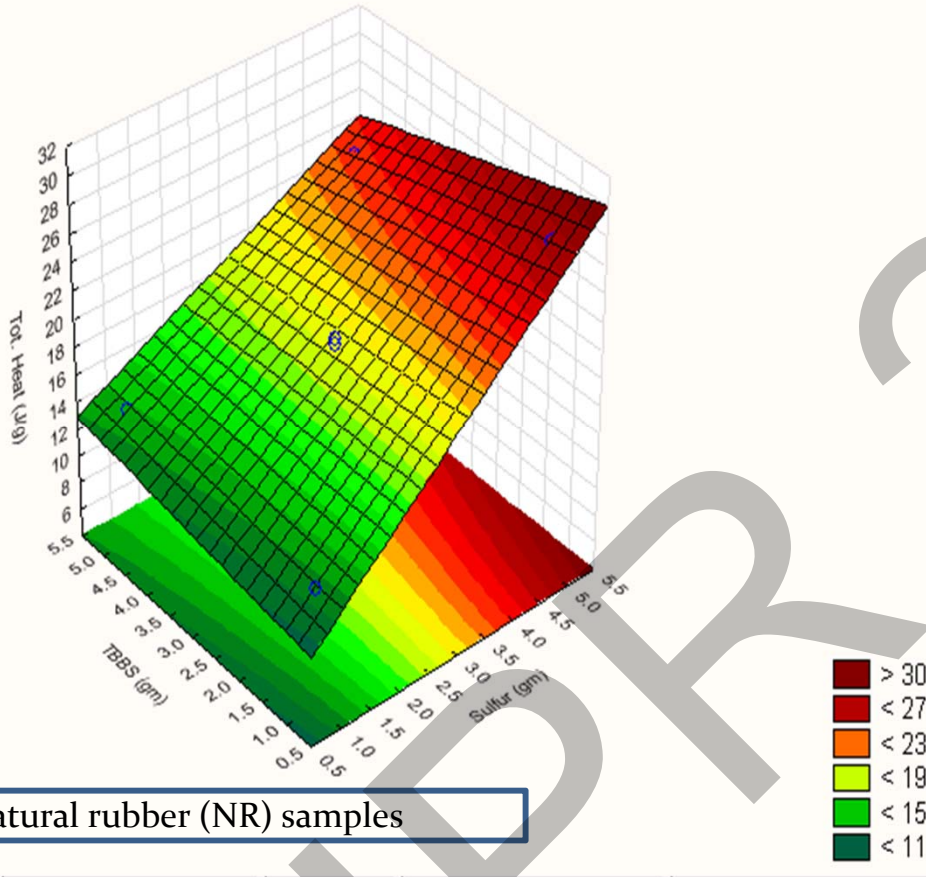
- To study the vulcanization reaction of devulcanized rubber by differential scanning calorimetry (DSC).
- To model the vulcanization behavior of devulcanized rubber.
- To compare the vulcanization behavior of virgin rubber and devulcanized rubber.

Theory

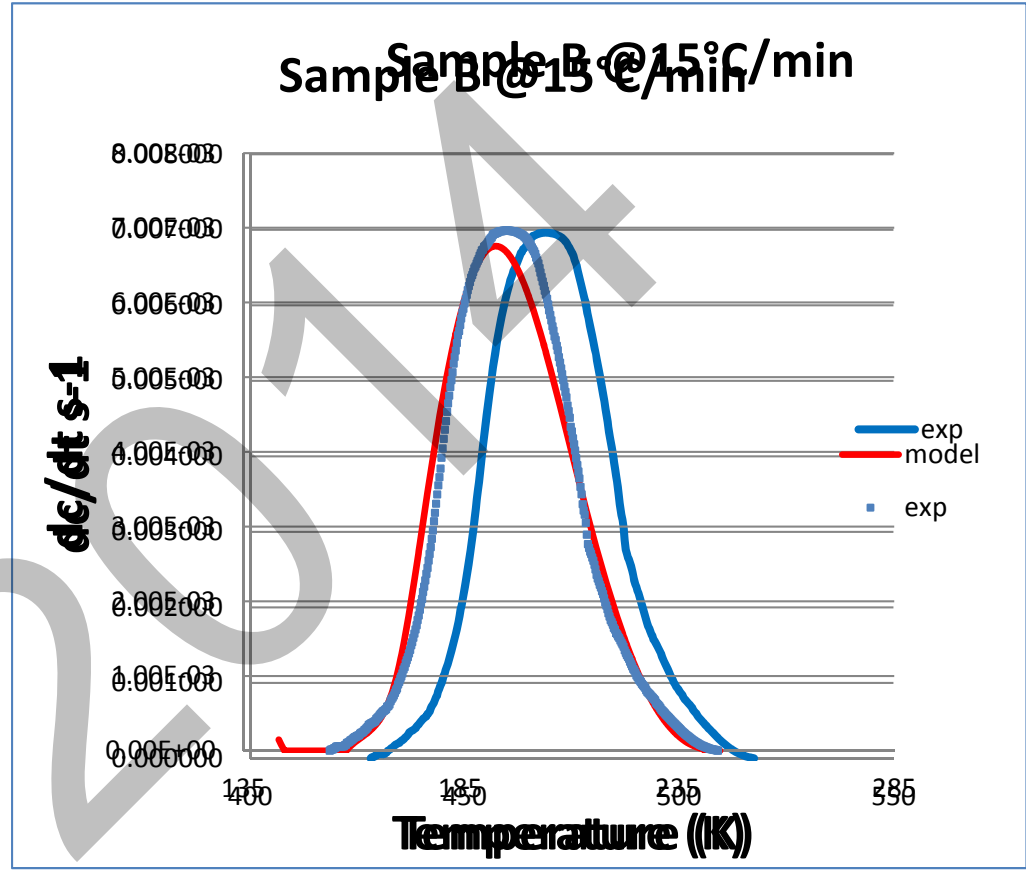
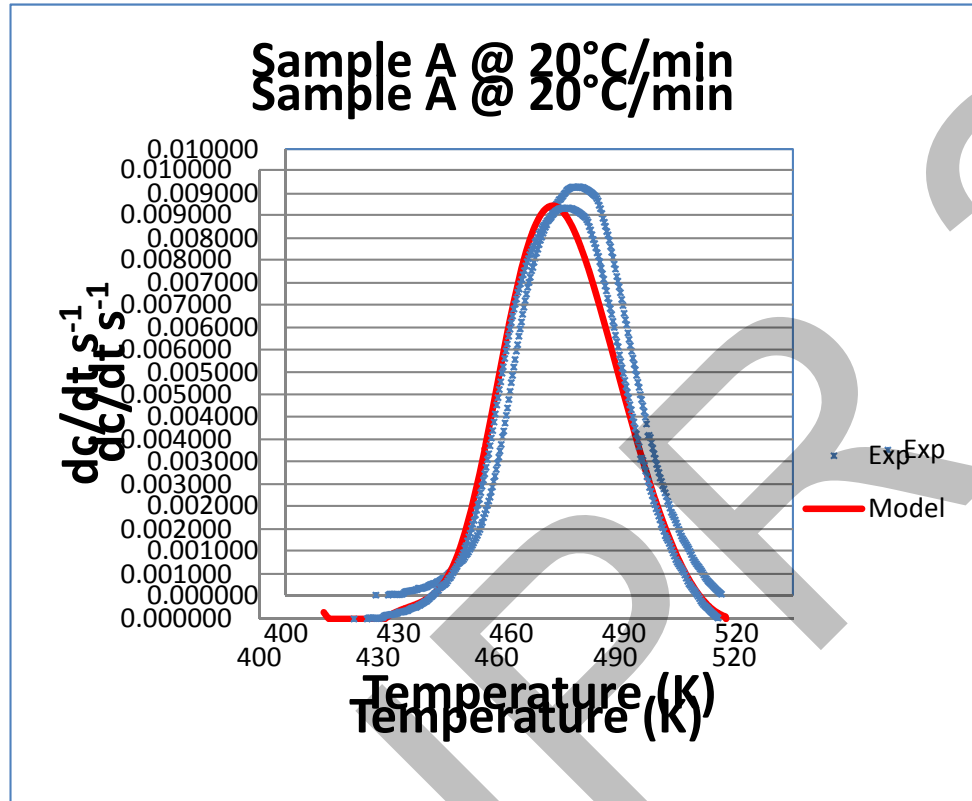


Results

- Effect of change in curative composition in total heat of reaction



➤ Fitted model and experimental data for natural rubber sample at different scan rates.



Summary

- The vulcanization enthalpy (heat of reaction) is seen to be linearly proportional to the initial sulfur content.
- The total heat of reaction follows the similar trend for both natural and devulcanized rubber .
- The fitted models are in good agreement with the experimental data , the constants obtained can be used to predict reaction rate and degree of vulcanization at different temperatures.

Thank you!!
Questions??

➤ Approaches to characterize a vulcanization reaction :

- Mechanistic model
- **Phenomenological model**

Kissinger Model

$$dc/dt = k(1-c)^n$$

dc/dt = rate of reaction
 k = rate constant
 c = degree of vulcanization
 n = order of reaction

Arrhenius Model $k(T) = a \exp(-E/RT)$

a = frequency factor
 E = activation energy
 T = Temperature
 R = Universal gas constant

Activation Energy

Kamal-Sourour Model

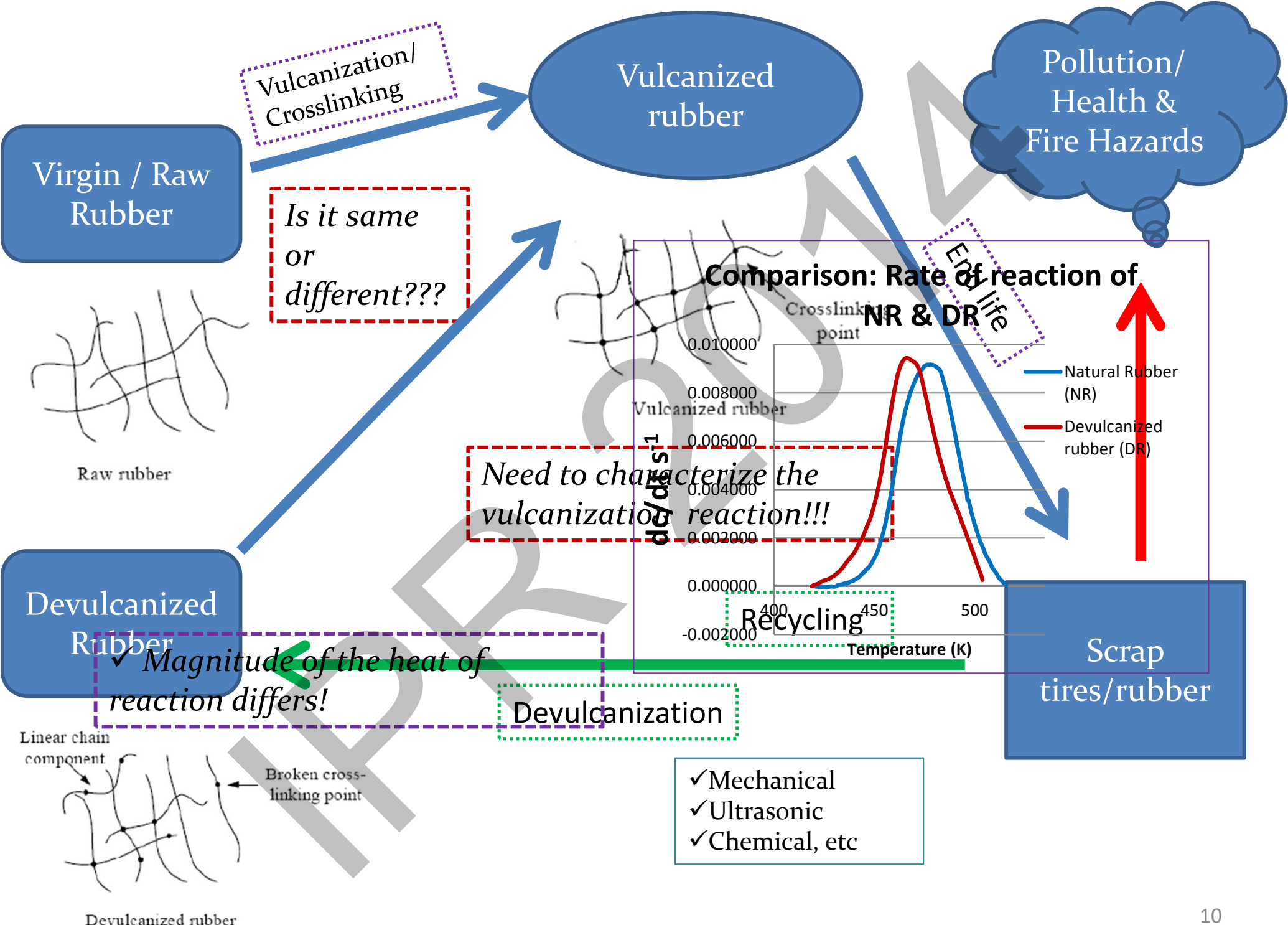
$$dc/dt = (k_1 + k_2 * c^m) * (1-c)^n$$

m and n are order of reaction.

6 parameters in the model (i.e. a_1, a_2, E_1, E_2, m and n) can be fit to experimental DSC data via least squares estimation algorithm.

References:

- Lopez, L. M.; Cosgrove, A. B.; Hernandez-Ortiz, J. P.; Osswald, T. A. Polym Eng Sci 2007, 47, 675–683.
- Musa R. Kamal, Polym Eng Sci 1974, 14, 231-239



Institute for Polymer Research

Celebrating 30 years of Official Institute Status

Symposium documents for

Bingqing Yang

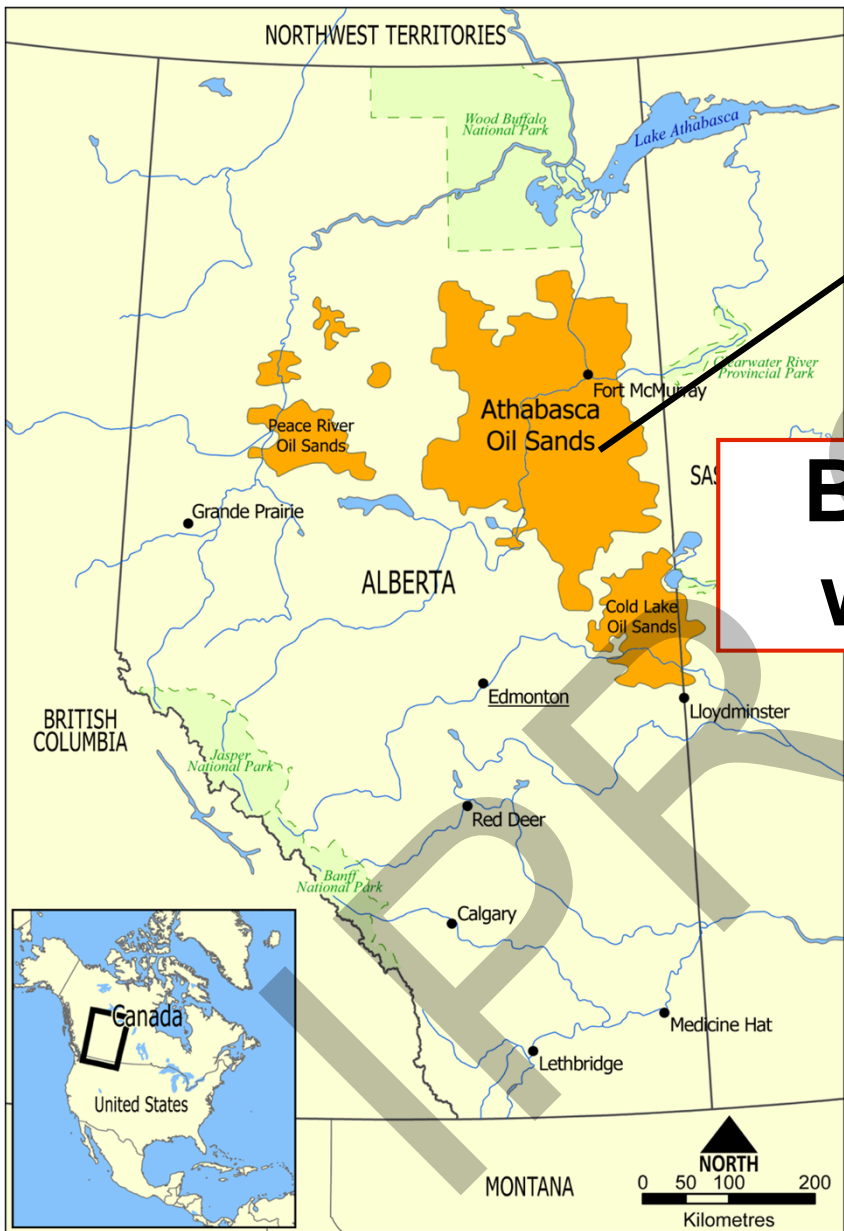


Preparation and Characterization of Temperature-Responsive Polymeric Surfactants

Bingqing (Alice) Yang
Supervisor: Dr. Jean Duhamel
Chemistry, University of Waterloo

May 21st, 2014

Background



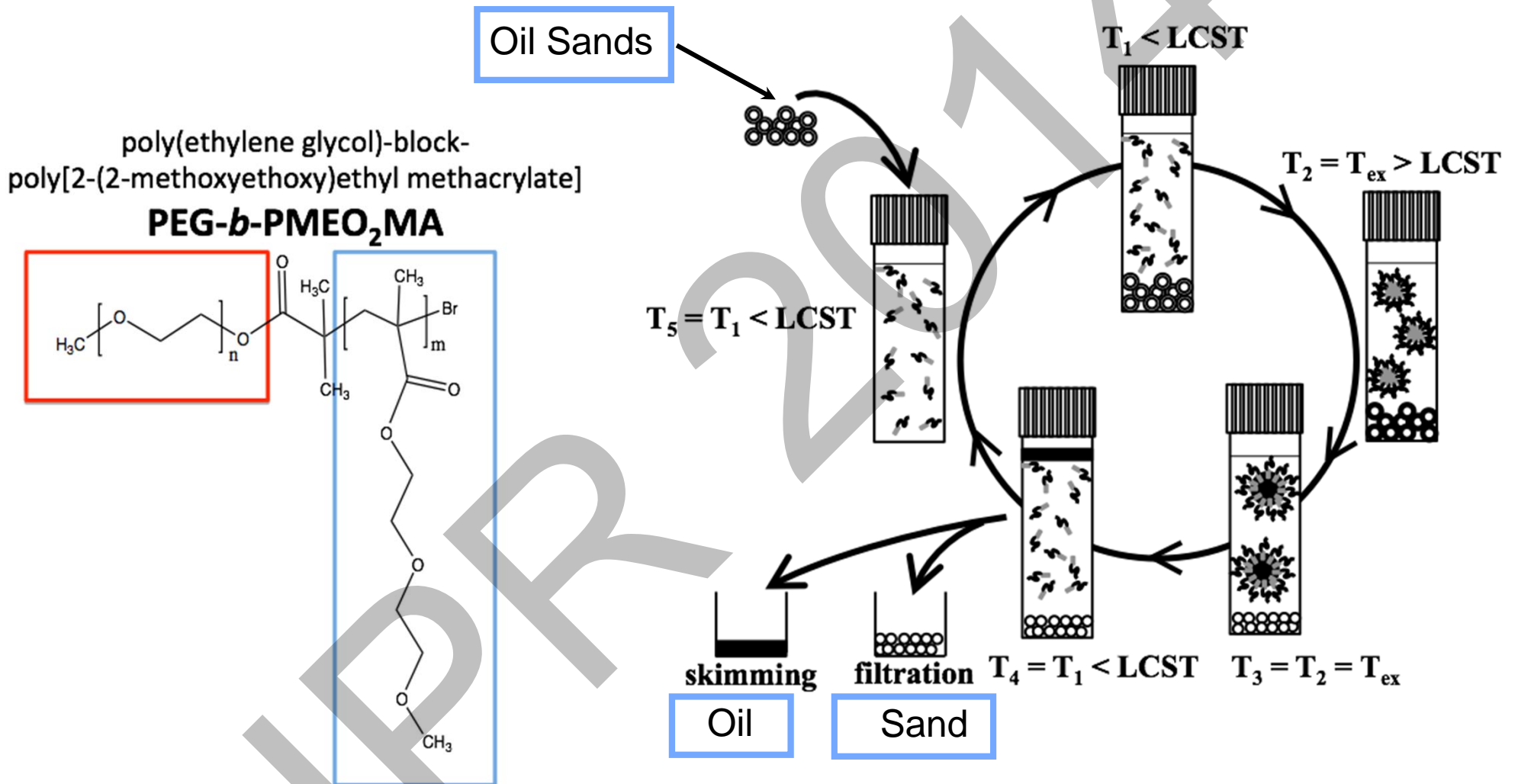
Better way?

oil sands

Problems of oil extraction:

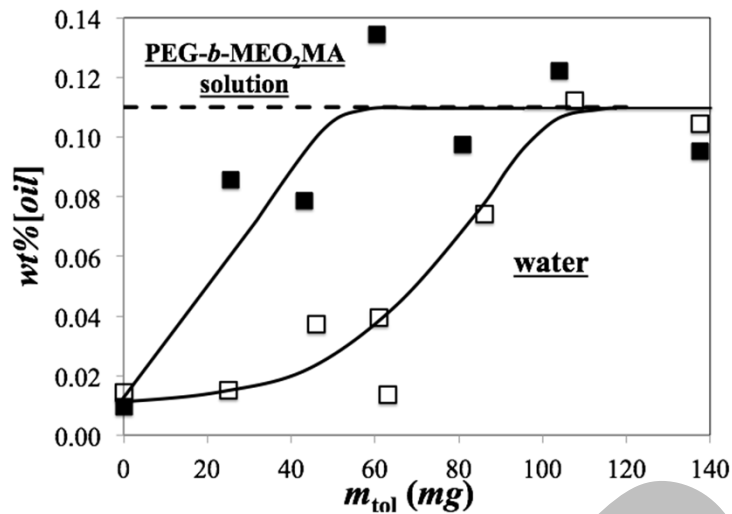
- (a) The heavy oil is usually solid at room temperature;
- (b) The oil and sand stick together.

Protocol Used for Oil Extraction

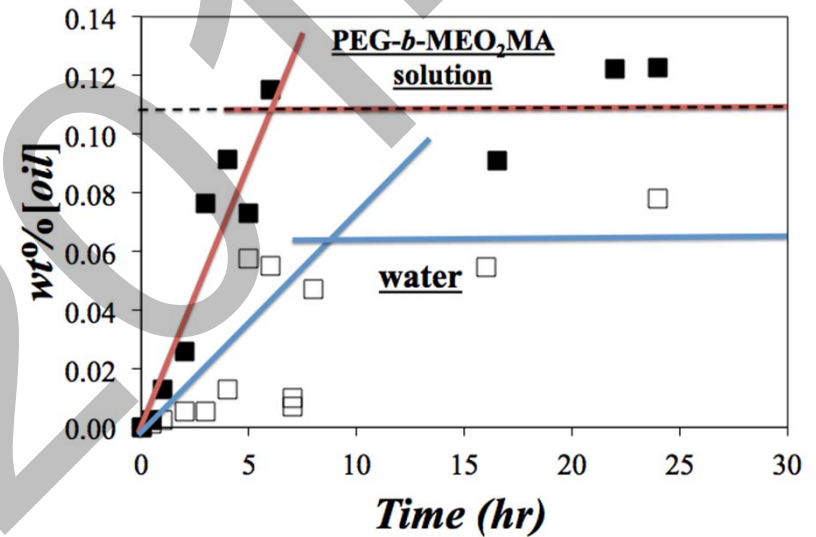


Oil Extraction Experiments

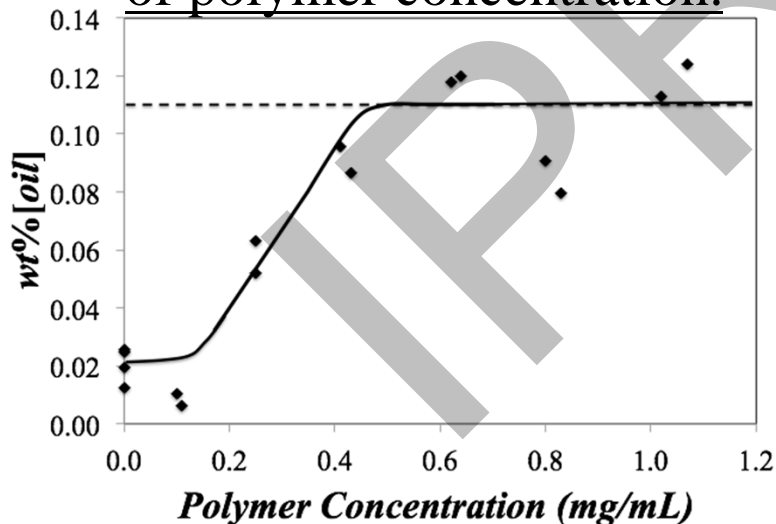
Extraction efficiency as a function of toluene amount.



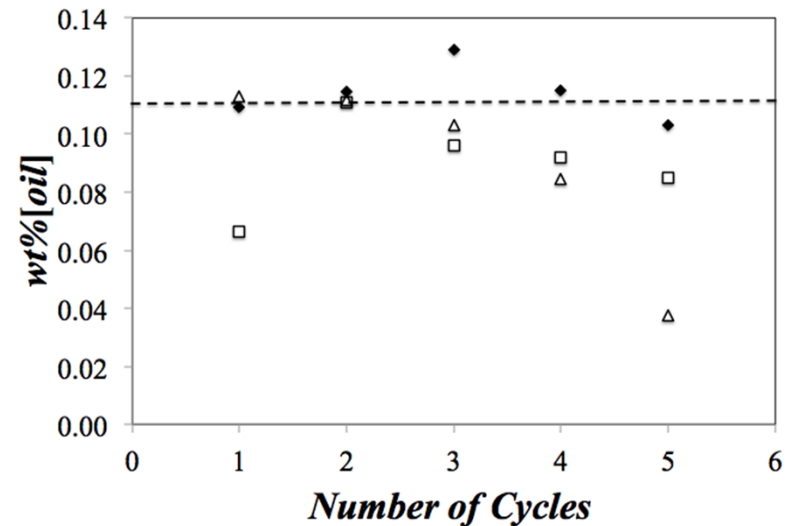
Extraction efficiency as a function of extraction duration.



Extraction efficiency as a function of polymer concentration.



Reusability of TRPS



Acknowledgements

- Prof. Jean Duhamel
- Prof. Xiaosong Wang and Prof. Mario Gauthier
- Lu Li, Junhui Xu, and Tom Gibson
- Duhamel and Gauthier Groups
- Imperial Oil and NSERC



Imperial Oil



NSERC
CRSNG

Institute for Polymer Research

Celebrating 30 years of Official Institute Status

Symposium documents for

Wei Yi

Probing Hydrophobical Collapse of Starch Nanoparticles by Pyrene Fluorescence and Transmission Electron Microscopy

Wei Yi

Supervisor: Prof. Jean Duhamel

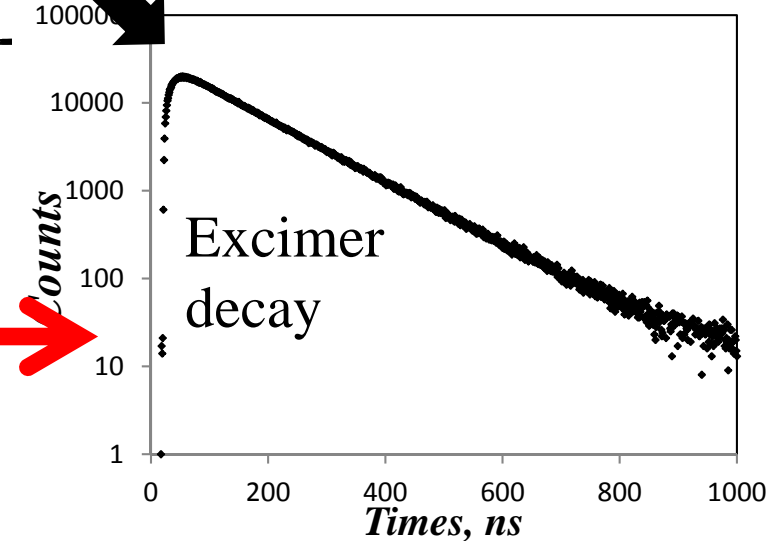
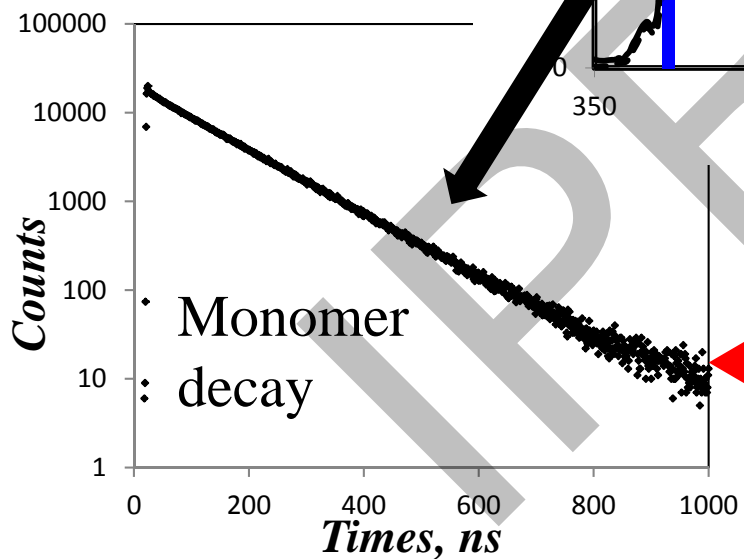
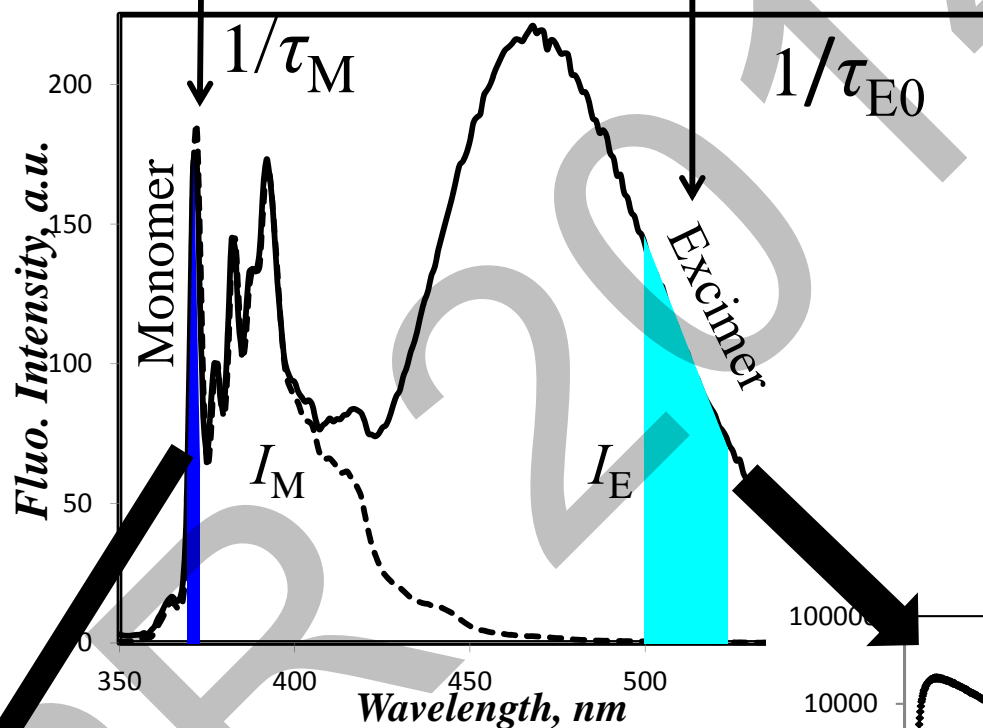
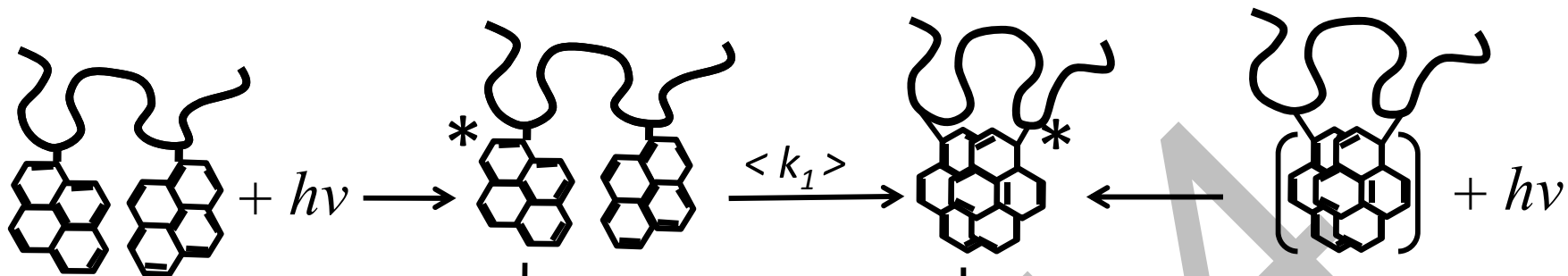
May, 21st 2014

UNIVERSITY OF
WATERLOO



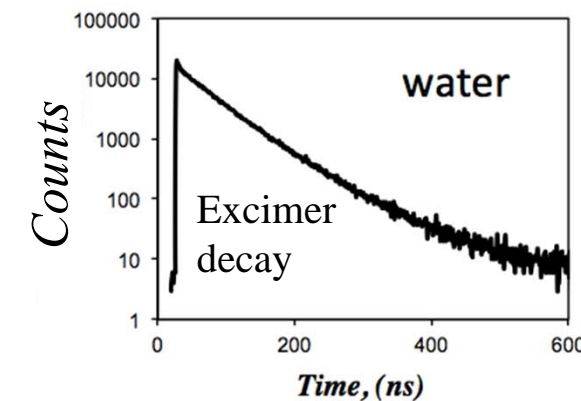
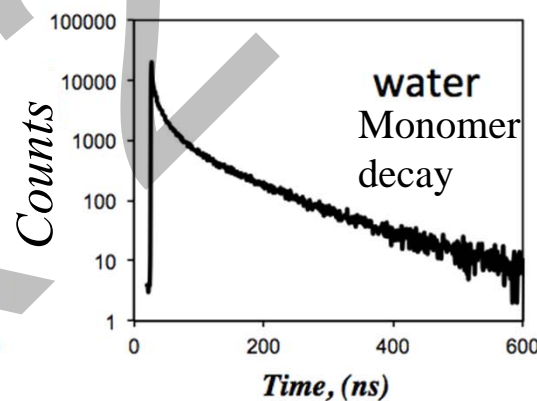
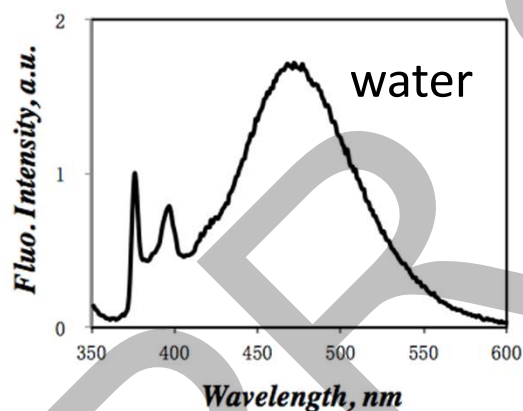
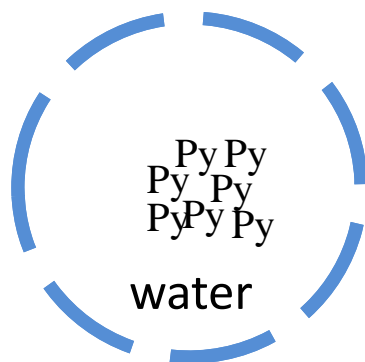
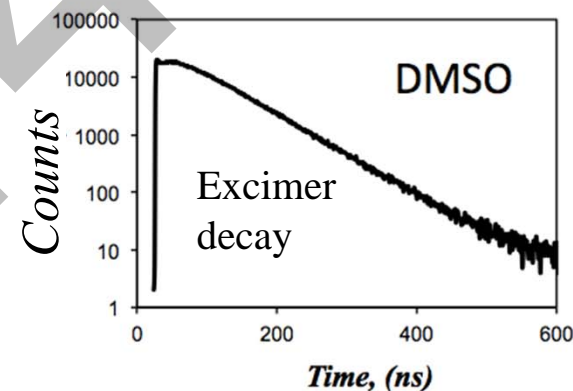
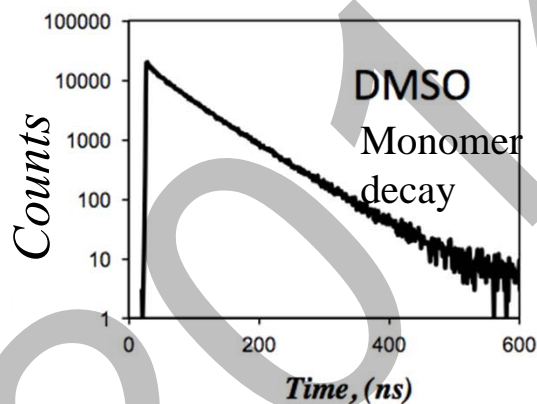
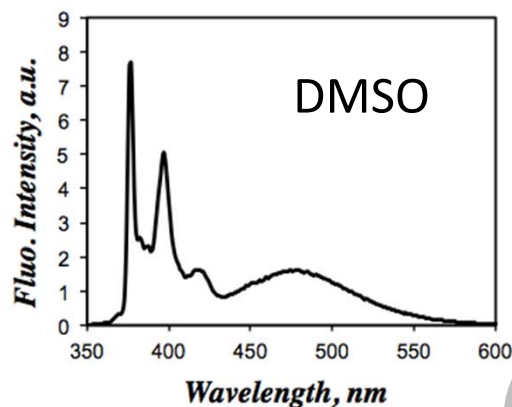
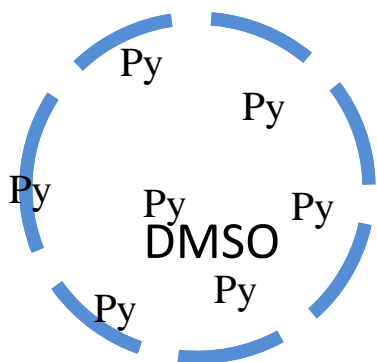
ECOSYNTHETIX®
SUSTAINABLE POLYMER FOR PLANET EARTH™

IPR
Institute for Polymer Research



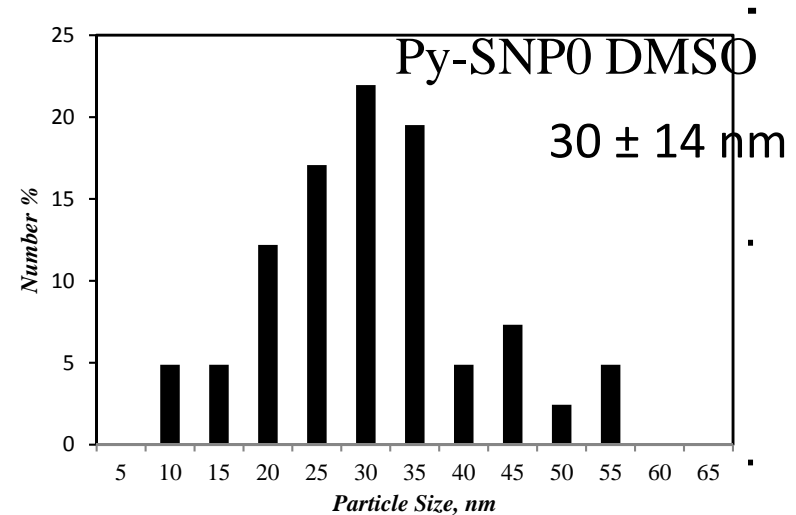
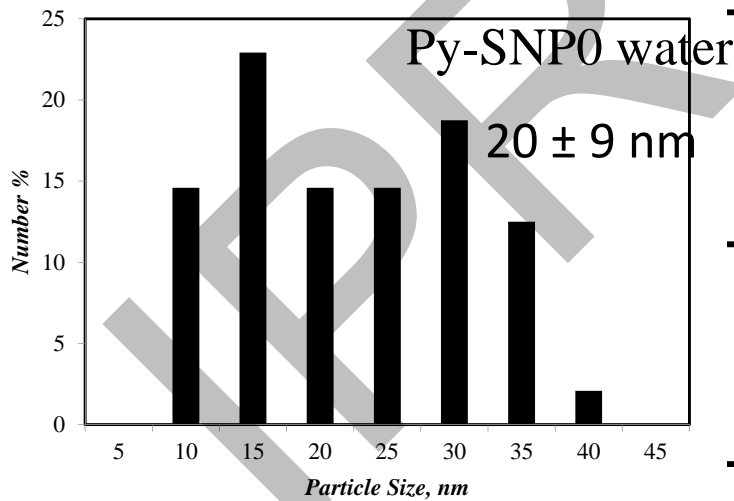
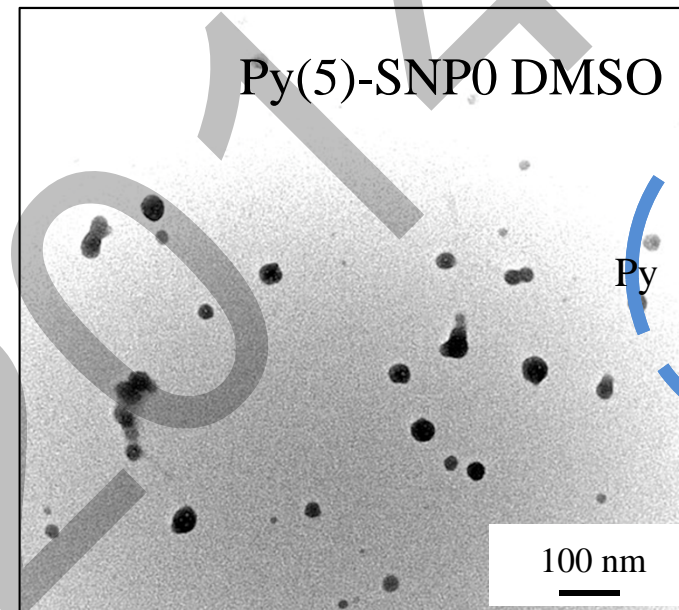
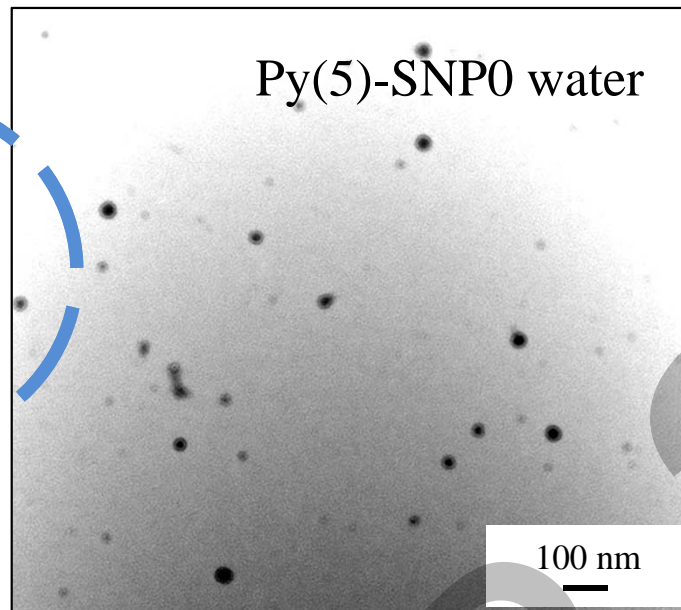
Coupled

Hydrophobic Effect on the Py-SNPs in Water



Solvent	η @25°C mPa.s	I_E/I_M	$\langle k \rangle$, μs^{-1}	f_{diff}	f_{free}	f_{agg}
DMSO	1.99	0.68	9.8	0.80	0.02	0.18
Water	0.89	5.65	52.1	0.05	0.00	0.95

Morphology of the Py-SNPs in Water



Acknowledgements

UNIVERSITY OF
WATERLOO

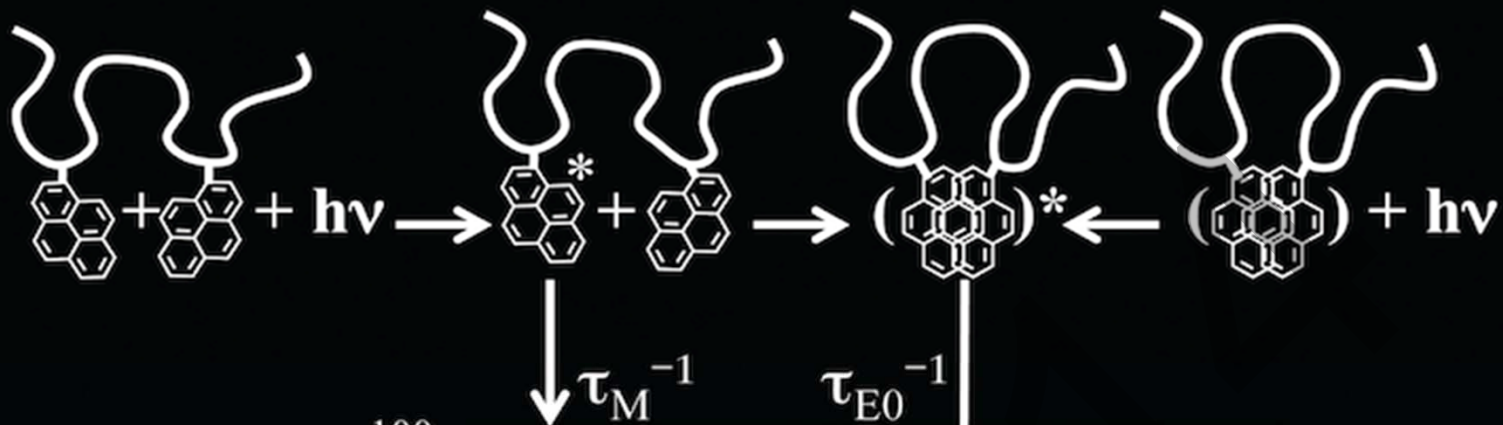


- Dr. Jean Duhamel
- Duhamel & Gauthier group
- ECO-WIN team

 **ECOSYNTHETIX**[®]
ADVANCED POLYMERS FROM PLANET EARTH[®]



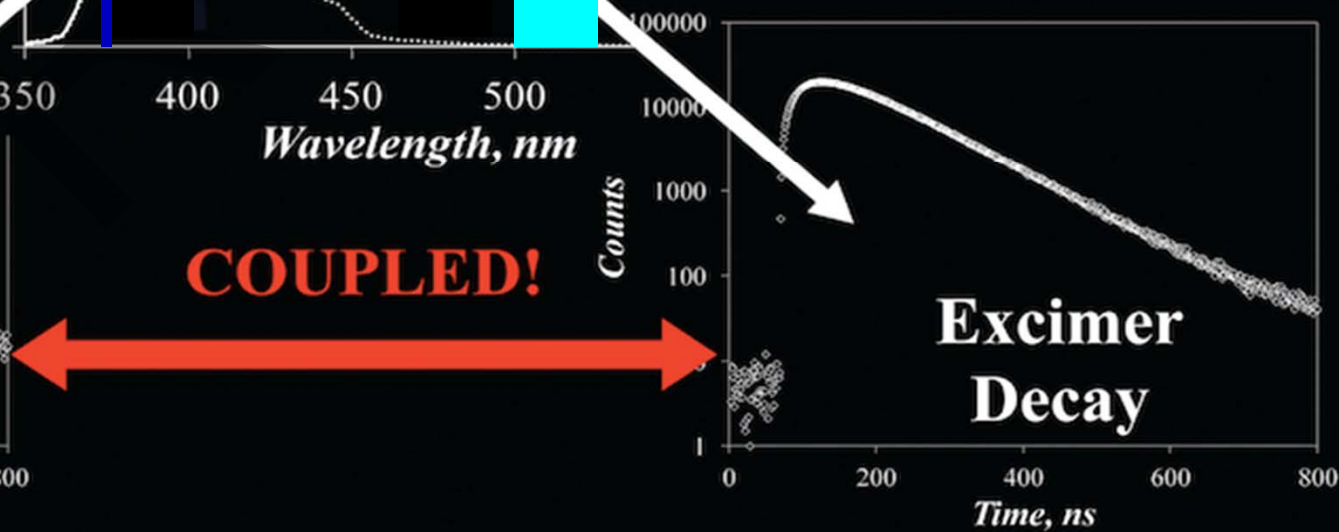
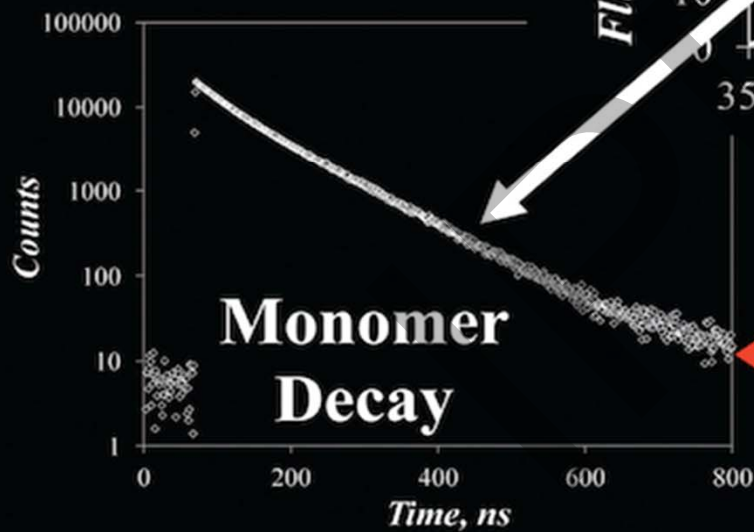
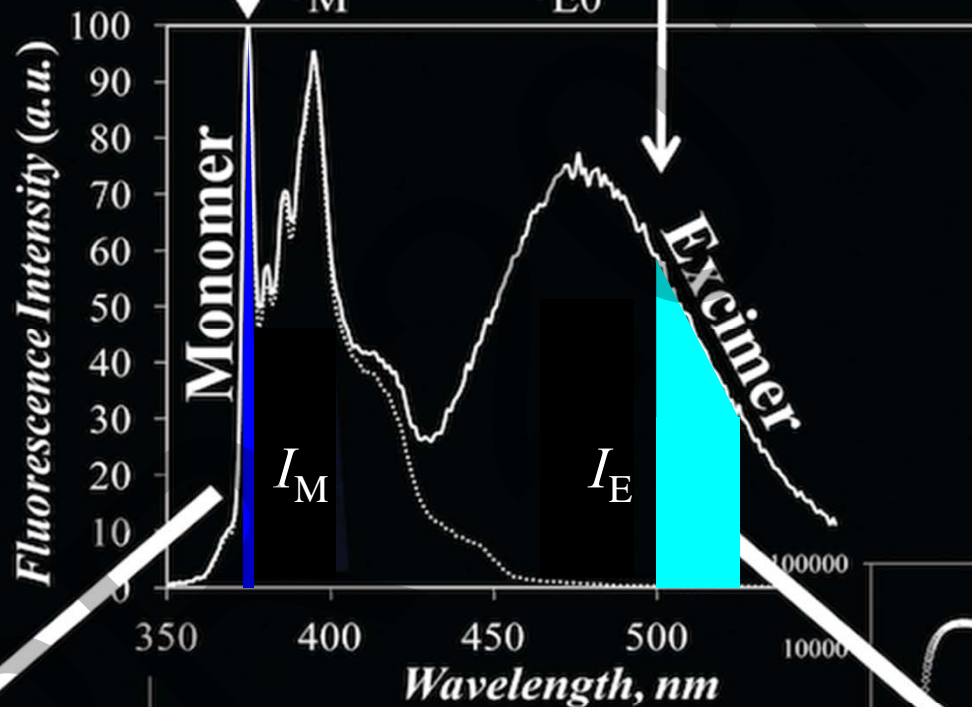
NSERC
CRSNG



$$I_E/I_M = Kk_1[\text{Py}]_{\text{loc}}$$

k_1 is the diffusion rate constant

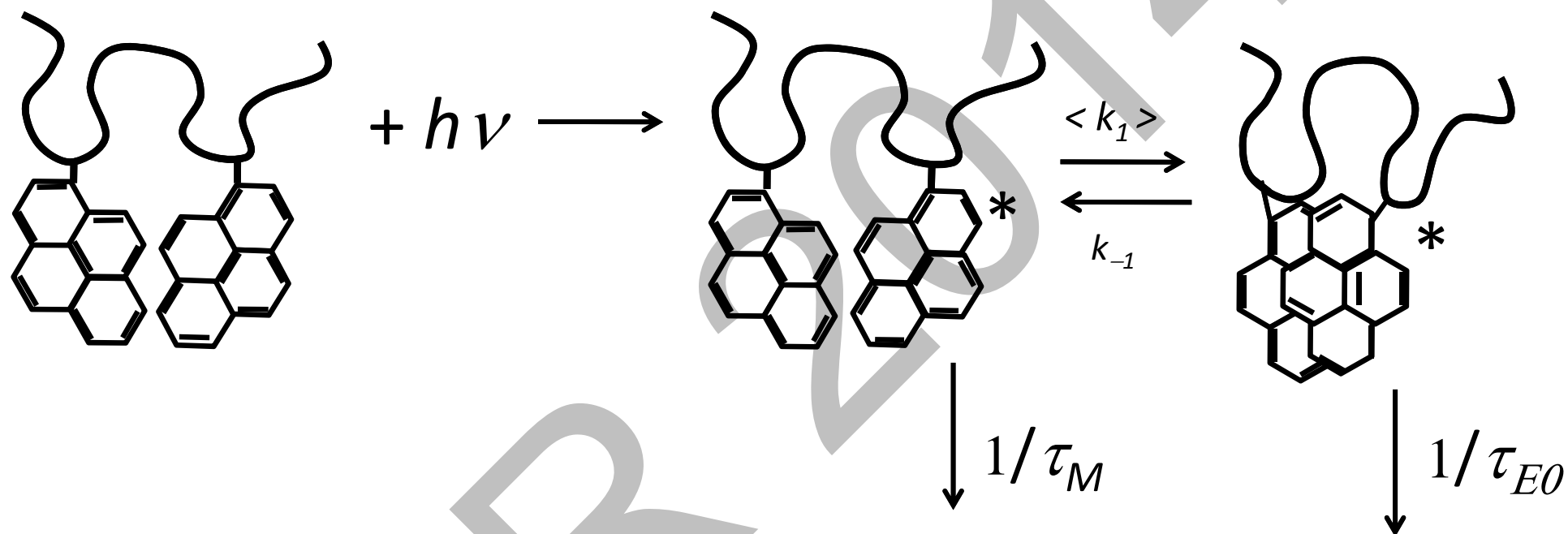
$[\text{Py}]_{\text{loc}}$ is the local pyrene concentration



COUPLED!

3. Analysis

Kinetics for pyrene excimer formation

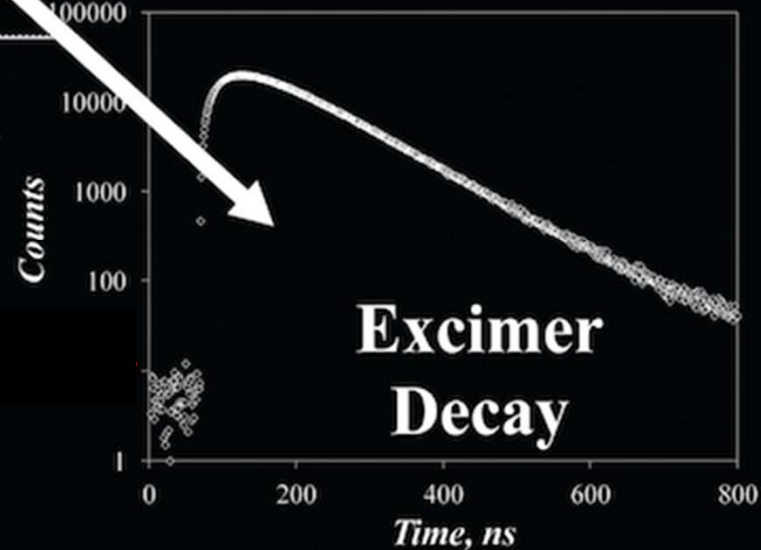
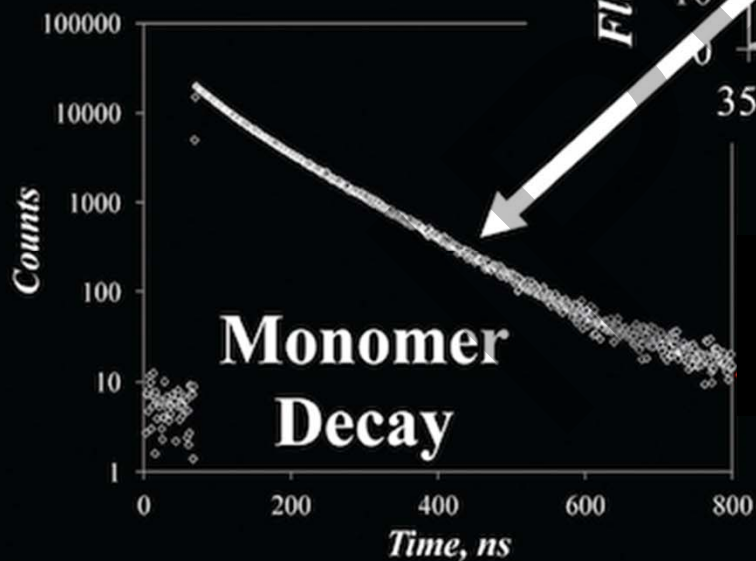
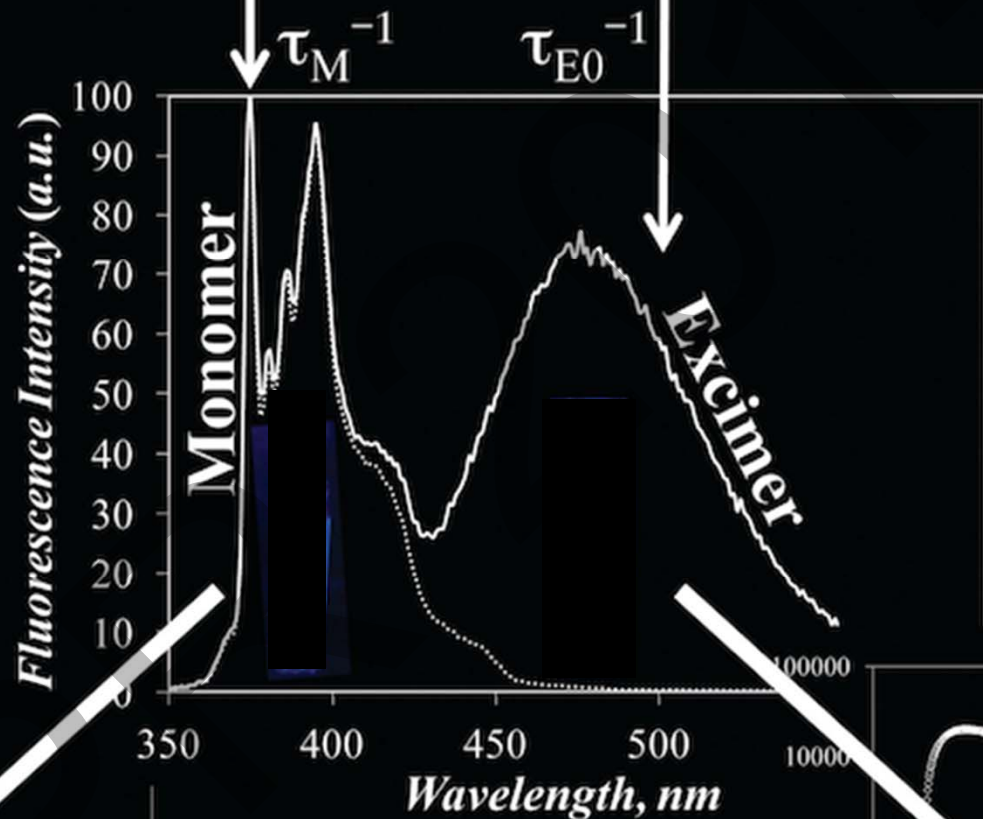
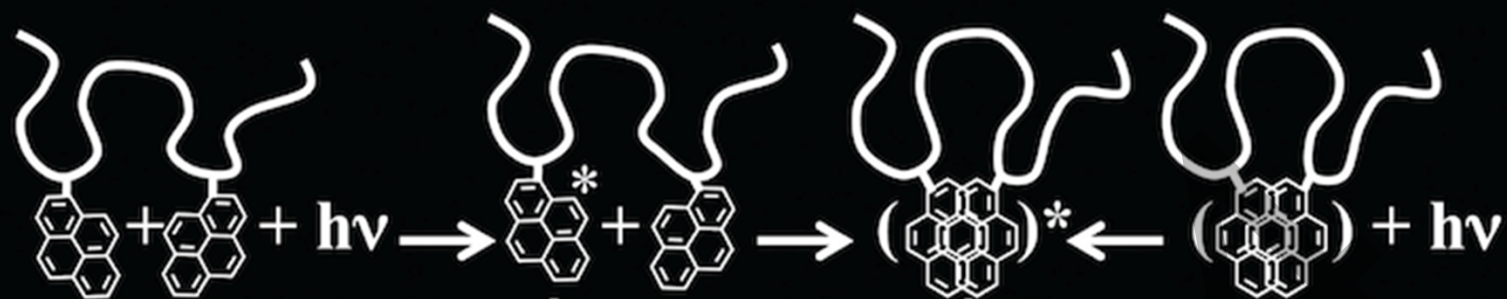


Monomer Emission

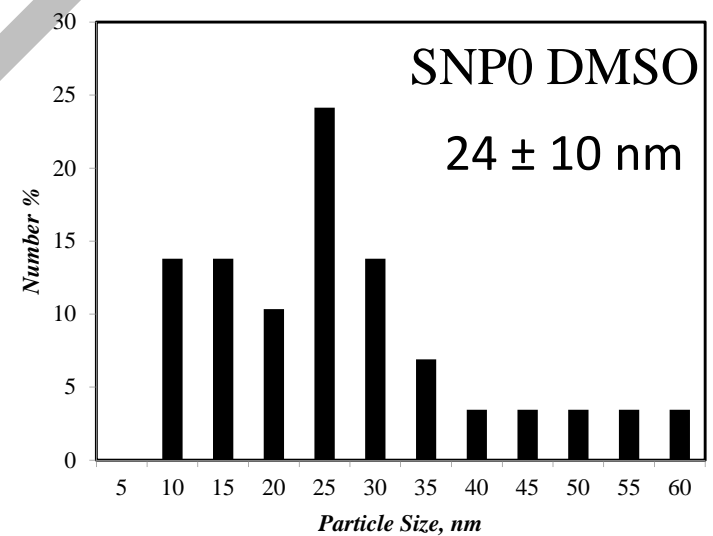
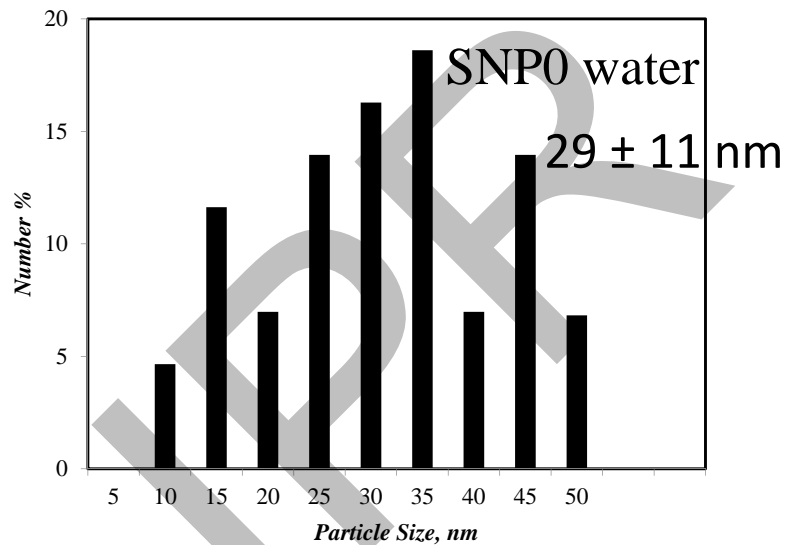
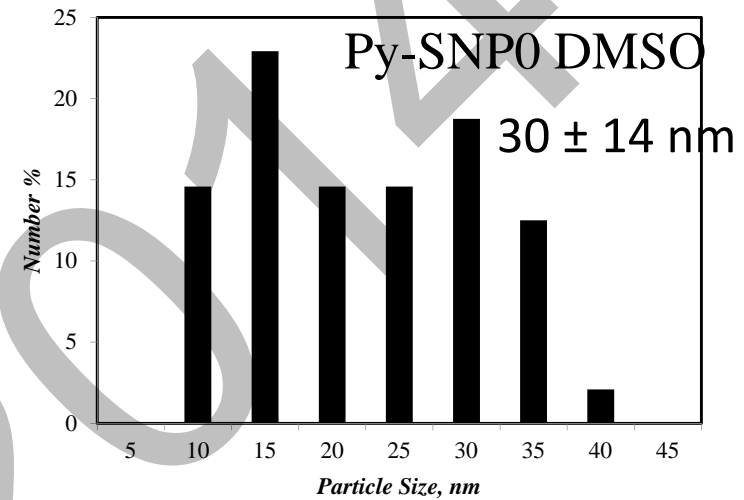
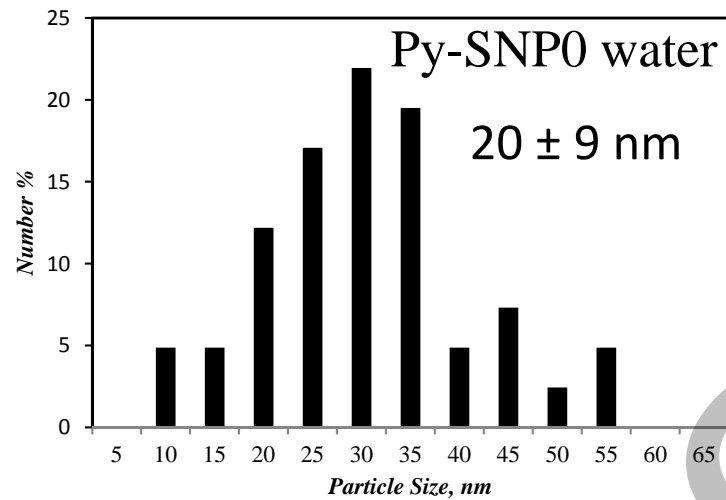
I_M : 372 - 378 nm

Excimer Emission

I_E : 500 - 530 nm



TEM Size Distribution of SNPs



Institute for Polymer Research

Celebrating 30 years of Official Institute Status

Thirty-Sixth Annual Symposium on Polymer Science/Engineering

Wednesday, May 21, 2014

Conrad Grebel University

University of Waterloo

Presentations (20-minute)

Yasaman Amintowli Chemical Engineering, Waterloo	Is It Possible to Increase Polypropylene Melt Strength via UV Radiation?
Kai Cao Chemistry, Waterloo	Migration insertion polymerization of $\text{CpFe}(\text{CO})_2(\text{CH}_2)_3\text{PPh}_2$ (FpP): A new route for the preparation of main-chain metal-containing polymer
Michael Fowler Chemistry, Waterloo	Temperature Response of Aqueous Solutions of Pyrene End-Labeled Poly(<i>N</i> -isopropylacrylamide)s Probed by Fluorescence
Niousha Kazemi Chemical Engineering, Waterloo	Reactivity Ratios in Terpolymerization Systems Do binary monomer reactivity ratios apply to terpolymerizations as well?
Mylène Le Borgne Chemistry, Waterloo	Solution-processable oligomeric semiconductors for organic solar cells
Lu Li Chemistry, Waterloo	Characterization of Structure and Dynamics of Starch Nanoparticles by Fluorescence
Jin Liu Chemistry, Waterloo	Synthesis and Migration Insertion Polymerization (MIP) of $\text{CpFe}(\text{CO})_2(\text{CH}_2)_6\text{PPh}_2$ (FpC6P)
Hamed Shahsavan Chemical Engineering, Waterloo	Thin Film Composite Nanofabrication and Characterization of Bioinspired Functionally Graded Adhesive Membranes Formed by Interfacial Polymerization
Bin Sun Chemical Engineering and Waterloo Institute for Nanotechnology (WIN), Waterloo	A record high electron mobility polymer semiconductor for organic thin-film transistors
Dihua Wu Chemical Engineering, Waterloo	Thin Film Composite Nanofiltration Membranes Formed by Interfacial Polymerization
Boya Zhang Chemical Engineering, Waterloo	Dairy flavor recovery by pervaporation using poly(ether block amide) membrane

Institute for Polymer Research

Celebrating 30 years of Official Institute Status

Symposium documents for

Yasaman Amintowlieh

Is it possible to increase polypropylene melt strength via UV radiation?

Y. Amintowlieh, C. Tzoganakis and A. Penlidis

IPR symposium (May 2014), Department of Chemical Engineering, University of Waterloo, Waterloo N2L 3G1 Canada

Polypropylene (PP) is a commodity plastic that can be used for various applications. Conventional methods for synthesizing PP result in low melt strength and low extensional viscosity in the polymer melt. In order to accommodate processing requirements in applications such as film blowing, blow molding, extrusion coating, thermoforming, foaming and fiber spinning, long chain branches should be introduced to the PP structure. The presence of long chain branches results in larger extensional viscosity and melt strength in PP^{1,2}.

For modification with UV radiation, photoinitiators such as benzophenone (BPH) have been used and UV energy is utilized to activate these photoinitiators^{3,4}. In this work, PP is modified in the solid state using BPH as photoinitiator. The operating conditions that maximize strain hardening in PP were identified. Processing conditions such as radiation time, UV lamp intensity and cooling rate, along with the concentration of the photoinitiator, were manipulated to yield maximum amount of long chain branching (LCB) in the PP structure. One issue that arises during modification of polymers by UV radiation is related to the depth of radiation⁵. It is known that penetration of UV light is limited and this can cause inhomogeneities in LCB (and crosslinking (CL)) of the samples^{6,7}. The effects of radiation duration and sample thickness on the amount of long chain branches were also investigated. Linear viscoelastic (LVE) properties, molecular weight (MW), and gel content were determined and compared for runs having different sample thicknesses, irradiated for different times.

Experimental Procedures and Characterization

PP homopolymer (Pro-fax PH 382M) from LyondellBasell with a melt flow rate (MFR) of 3.5 g/10 min was melt-mixed in a batch mixer at 190 °C (100 rpm) with benzophenone (Sigma Aldrich).

The samples were ground using a Wiley mill (model 1102, Arthur H. Thomas Co.). After grinding, PP-initiator blend granules were compression-molded into sheets at 190 °C under an applied force of 4,400 N for five minutes. The sheets were subsequently irradiated using a mercury UV lamp (Versa Cure) with total power of 1.8 kW.

Parallel plate rheometry (AR2000, TA instruments) and GPC measurements (Polymer CHAR, Spain) were used to determine linear viscoelastic properties (LVE) and molecular weight (MW) averages, respectively. ASTM D2765-11 was followed to measure sample gel content. The extensional flow properties of modified samples were measured using the Sentmanat extensional rheometer (SER) universal testing platform (Xpansion instruments).

A constant stress parallel plate rheometer was used to obtain storage modulus (G'), loss modulus (G''), complex modulus (G^*), loss tangent ($\tan \delta$), and complex viscosity (η^*) at different angular frequencies (ω). Having η^* vs. ω , the power-law shear thinning index (n), zero shear viscosity (η_0) and relaxation time (λ) of the polymer melt were acquired by fitting the Cross model (Equation 1) to the data⁸.

$$\eta^* = \frac{\eta_0}{1 + (\omega\lambda)^n} \quad \text{Equation 1}$$

It has been observed that long chain branched PP has higher η_0 , λ and lower n than the linear parent PP. On the other hand, smaller η_0 , longer Newtonian plateau (smaller λ) and larger shear power-law index compared to the parent PP can be evidenced in degraded linear PP.

Rheological polydispersity indices were determined using Equation 2 and 3⁸.

$$PI = \frac{10^5}{G_c(\text{Pa})} \quad \text{Equation 2}$$

$$ER = C_1 G'_{\text{at } G''=500 \text{ Pa}} \quad \text{Equation 3}$$

G_c in Equation 2 is the crossover modulus. In Equation 3, C_1 is the slope of the $\log(G')$ versus $\log(G'')$ curve. It should be noted that ER is only sensitive to the distribution of high MW chains. Runs with larger ER values indicate a broader distribution of the higher molecular weight chains. Increasing values of PI indicate broadening of the molecular weight distribution (MWD) in general.

Results and Discussion

In order to identify the processing conditions that maximize the LCB level in PP, the process operating conditions (photoinitiator concentration, duration of radiation, UV lamp intensity, cooling air pressure, and combinations thereof) were manipulated within the range summarized in Table 1.

Table 1: Selected factors and ranges to find processing conditions for LCB

Factor	Process variable (units)	Ranges
A	Photoinitiator concentration (wt %)	0.1-0.5 (with respect to polymer mixture)
B	Duration of radiation (s)	120-600
C	UV lamp intensity (%)	47-100 (with respect to total lamp intensity)
D	Cooling air pressure (%)	0-100 (with respect to total air flow pressure)

D-optimal design of experiments and statistical analysis were utilized to find the combinations of these variables (within the ranges mentioned in Table 1) that result in the greatest amount of LCB. Shear thinning index (n), zero shear viscosity (η_0), relaxation time (λ), and ER were calculated using η^* , G' and G'' vs. ω measurements (Equations 1 to

3). A criterion can be set for each of these responses (n , η_0 , λ and ER) to identify the processing window that results in long chain branching rather than degradation. Table 2 shows the chosen criteria to find the optimized processing conditions.

Contour plots corresponding to these criteria (Table 2) are shown in Figure 1; the optimal processing window, which satisfies these limits for the response variables (Table 2) is the yellow area. Figure 1 shows that samples with a high concentration of BPH (above 0.2 wt-%) which are radiated for times larger than 4 minutes at low lamp intensity at temperatures below 60 °C yield larger amounts of LCB.

Table 2: Criteria chosen for each response variable to find optimized processing conditions

Response	Criteria
n	<0.57
η_0 (Pa.s)	$>90,000$
λ (s)	>0.67 s
ER	>2.0

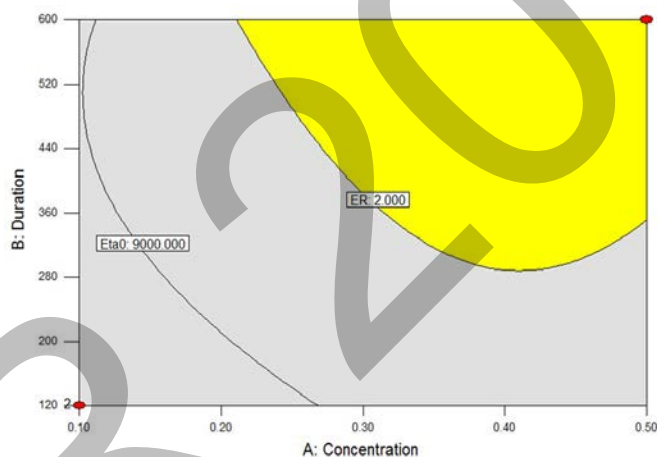


Figure 1: Conditions that yield high degree of LCB

Two runs in the processing range indicated in Figure 1 were chosen along with the parent PP for extensional rheometry measurements. The processing conditions for these two runs are cited in Table 3.

Table 3: Experimental conditions of the runs chosen within the optimized region

Run ID	Photoinitiator concentration (wt%)	Duration of radiation (s)	UV lamp intensity (%)
PP	-	-	-
1	0.5	600	47
2	0.3	360	74

Figure 2 shows the uniaxial tensile stress growth coefficient (η^+_{E}) of the parent PP and runs 1, 2 at four different Hencky strain rates (0.01, 0.1, 1 and 10 s^{-1}). The dashed lines in Figure 2 represent three times the shear stress growth coefficient (i.e., $3\eta^+_0(t)$). The parent PP shows a slight increase in uniaxial tensile stress growth, which might be due to

the presence of high MW linear chains and the broad MWD of the parent PP. η_E^+ clearly increased at all strain rates for runs 1 and 2 (compared to the parent PP). This provides clear and convincing evidence of a larger melt strength in runs 1 and 2, which have been modified under the conditions of Figure 1.

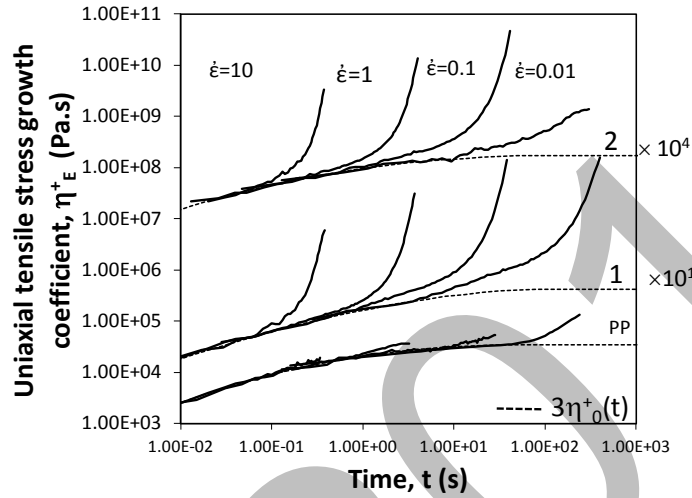


Figure 2: Uniaxial tensile stress growth coefficient (η_E^+) at Hencky strain rates of 0.01, 0.1, 1 and 10 s^{-1}

The next goal of this work was to study the effects of UV penetration depth along with UV radiation duration on the amount of LCB in the modified samples. For this purpose, solid discs (PP mixed with 0.5 wt-% BPH) with different thicknesses were radiated for different lengths of time at the same processing window of Figure 1 (47 % lamp intensity). Three-level factorial design experiments were conducted (Table 4). In Table 4, run 10 is PP after melt mixing with BPH and run 11 is the parent PP.

Table 4: Design of experiments for 3-level factorial design

Run ID	BPH (wt-%)	Thickness-A (mm)	Time-B (min)
1	0.5	1	5
2	0.5	1	10
3	0.5	1	15
4	0.5	2	5
5	0.5	2	10
6	0.5	2	15
7	0.5	3	5
8	0.5	3	10
9	0.5	3	15
10	0.5	1	0
11	0	1	0

Values for η_0 , λ , n and polydispersity indices (PI and ER) of the runs are summarized in Table 5. It can be seen that all radiated runs (1 to 9) have larger η_0 , λ , PI and ER, and lower n values compared to run 10, which is PP after melt mixing with BPH. Comparison between runs 1, 2 and 3 shows that longer exposure time to UV results in larger η_0 , λ , PI and lower n values (Table 5). This trend is also observed for the 2 mm (runs

4, 5 and 6) and 3 mm (runs 7, 8, and 9) samples. On the other hand, an increase in the thickness of the samples limits UV light penetration and subsequently results in lower η_0 , λ and higher n at the same exposure times (compare runs 1, 4 and 7, or 2, 5 and 8, or 3, 6 and 9). This is because all these LVE constants are indicators of an average property within the sample. Therefore, due to the limited UV penetration in the samples, formation of LCB or CL is not uniform in thicker samples.

In order to investigate the presence of gel (due to crosslinking) in each run, results from extraction experiments are also summarized in Table 5. Increases in radiation time cause larger percentage of CL (gel) in the samples with the same thickness. Moreover, a decrease in thickness increases the percentage of gel in the runs. An increase in gel content upon increasing radiation time is more significant at low thicknesses. This is the same trend observed in rheological properties earlier.

Table 5: Viscoelastic properties, molecular weight and gel content of the runs

Run ID	η_0 (kPa.s)	λ (s)	n	PI	ER	Gel (%)	\bar{M}_n (kg/mol)	\bar{M}_w (kg/mol)	\bar{M}_z (kg/mol)	PDI
1	6.6	1.5	0.50	4.22	1.46	-0	69.2	320.2	908.9	4.6
2	16.7	12.3	0.47	4.78	1.95	2.2	43.1	259.1	904.2	6.0
3	39.9	71.1	0.48	7.46	3.27	10.6	36.5	377.1	1,331.8	10.3
4	6.7	0.96	0.51	3.56	1.23	0.2	71.8	329.6	650.2	4.6
5	9.4	2.53	0.48	3.72	1.42	0.8	53.0	214.5	502.9	4.0
6	17.4	10.9	0.47	4.30	2.12	1.8	67.5	357.3	919.3	5.3
7	6.1	0.46	0.55	3.08	1.03	-0	77.7	310.9	676.7	4.0
8	7.0	0.82	0.52	3.26	1.28	0.6	76.3	330.4	582.4	4.3
9	10.0	2.37	0.49	3.52	1.39	1.6	66.8	277.9	700.8	4.2
10	5.3	0.30	0.60	3.43	0.82	-0	75.0	317.9	591.2	4.2
11	9.3	0.79	0.57	3.63	1.27	-0	78.4	361.4	714.8	4.6

These results have recently been extended to include the effect of acrylic co-agent on PP modification, and these more recent results will be discussed during the IPR poster session (in a related poster).

References

1. A. Gotsis, B. Zeevenhoven and A. Hogt, *Polym. Eng. & Science* **44**, 973-982 (2004).
2. D. Graebing, *Macromolecules*, **35**, 4602-4610 (2002).
3. N. Kukaleva; K. Stoll and M. Santi, U.S. Patent No. 2011,0136,931. (9 June, 2011).
4. Y. Amintowlieh, C. Tzoganakis, S. G. Hatzikiriakos and A. Penlidis, *Polymer Degrad. Stab.* (2014).
5. P. Zamotaev, E. Shibirin and Z. Nogellova, *Polymer Degrad. Stab.* **47**, 93-107 (1995)
6. Y. L. Chen and B. Rånby, *J. Polym. Sci. Part A: Polym. Chem.* **27**, 4077-4086 (1989).
7. Y. Amintowlieh, C. Tzoganakis, and A. Penlidis, *J. Appl. Polym. Sci.*, under review (2014).
8. R. Shroff and H. Mavridis, *J. Appl. Polym. Sci.* **57**, 1605-1626 (1995).

Is It Possible to Increase Polypropylene Melt Strength via UV Radiation?

Yasaman Amintowlieh, Costas Tzoganakis, and Alexander Penlidis

Institute for Polymer Research, Department of Chemical Engineering,
University of Waterloo, Waterloo, Ontario, N2L 3G1, Canada

Overview

Why?

- Why is melt strength important?
- Why UV radiation?

How?

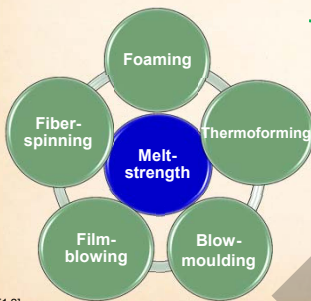
- How to increase PP melt strength?
- How to optimize the procedure?

What?

- What are the limitations?
- What are the solutions?

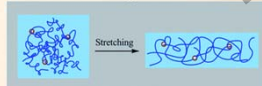
Why is melt strength important for PP?

❖ Melt strength: polymer resistance to extensional deformation



How to increase PP melt strength?

❖ Entanglements



❖ Chain interactions

Long chain branching (LCB)

Why UV radiation?



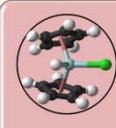
Peroxides

- Toxic
- Controlling the process



e-beam and gamma

- Cost
- Availability
- Safety



Synthesis

- Requires new plants



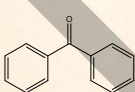
UV radiation

- Safe
- Available
- Easy to control
- Affordable

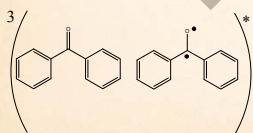
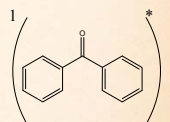
Why UV?

How UV irradiation can be used for PP modification (mechanism)

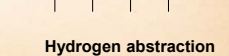
Photoinitiator



UV irradiation



+ PP chain

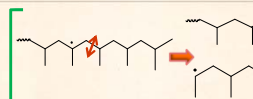


Hydrogen abstraction

How UV irradiation can be used for PP modification (mechanism)

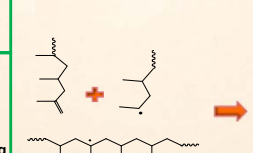
❖ β -scission

Disproportionation Degradation



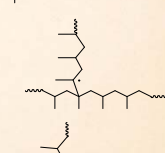
❖ Chain combination

Long chain branching

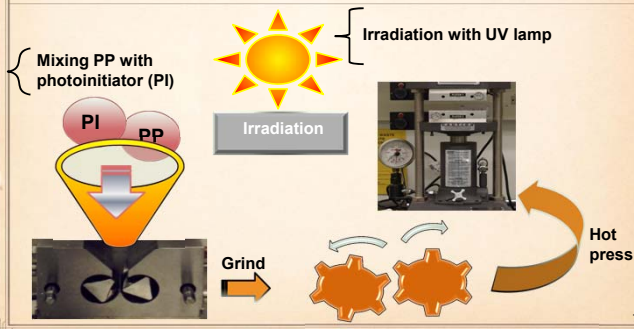


❖ Linear polymer

❖ Short chains & narrow molecular weight distribution



How to modify PP via UV irradiation (process steps)



7

What are the processing factors/variables?

❖ Processing variables and ranges

Factor	Process variable (units)	Range
A	Photoinitiator (PI) concentration (wt %)	0.1-0.5
B	Duration of radiation (s)	120-600
C	UV lamp intensity (%)	47-100
D	Cooling air pressure (%)	0-100
E	Type of photoinitiator (N/A)	BPH and DEBPH

❖ Design of experiments

• D-optimal; Design Expert was used; 32 experimental runs

❖ Responses

• Viscoelastic properties (η_0 , λ and n)

• Rheological polydispersity indices (PI and ER)

[8]

8

Extensional viscosity

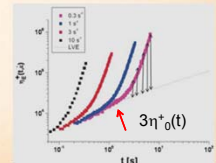
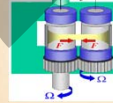
❖ The viscosity of a polymer melt under extensional stress

❖ Evaluation of extensional (elongational) viscosity

Extensional rheometers: Sentmanat extensional rheometer

Long chain branched PP shows

strain hardening

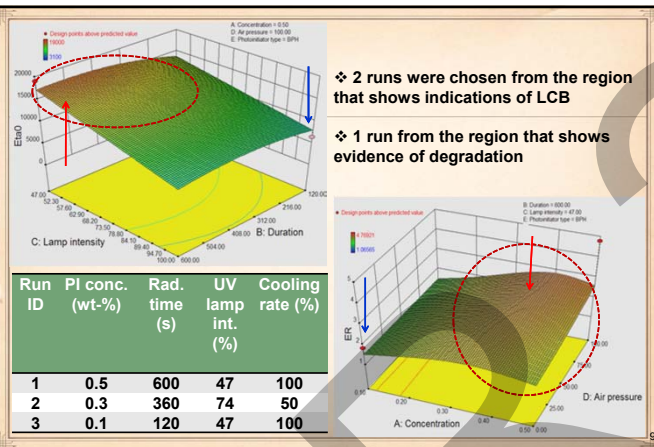


[9,10]

10

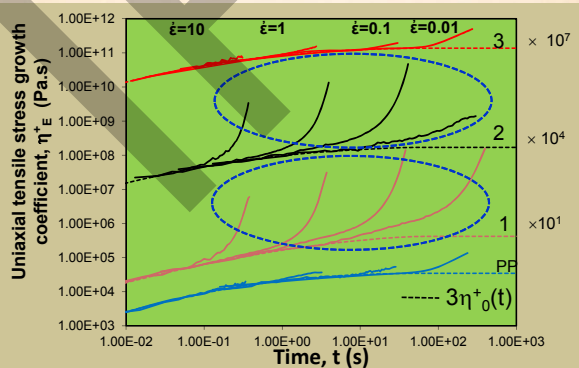
❖ 2 runs were chosen from the region that shows indications of LCB

❖ 1 run from the region that shows evidence of degradation



9

Clear increase in the η_E^+ of runs 1 and 2

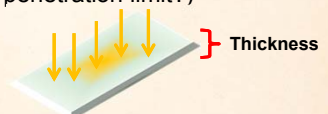


11

Possible limitations?

• Radiation depth (UV penetration limit?)

• Radiation time



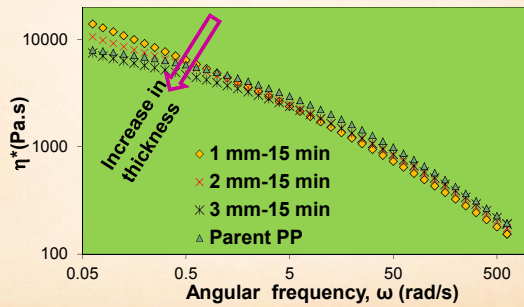
Study the effect of radiation time and depth

Variable (units)	Range
Sample thickness (mm)	1-3
Duration of radiation (min)	5-15
BPH Concentration (wt-%)	0.5
UV lamp intensity (%)	47
Cooling air pressure (%) / Temperature	100 / (<50 °C)

[11]

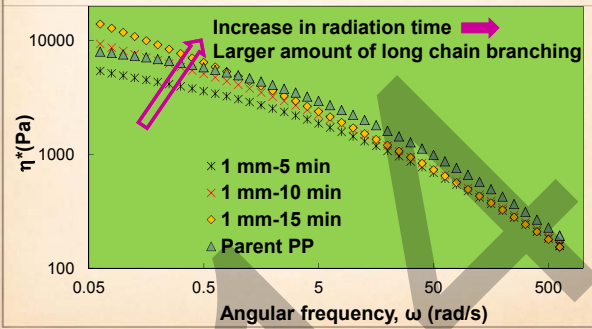
12

The effect of thickness on complex viscosity



13

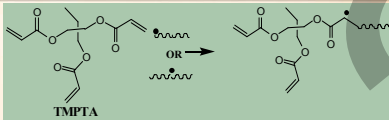
The effect of radiation time on complex viscosity



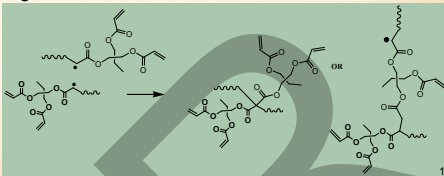
14

Further reduction of radiation duration: Co-agent

- What are co-agents?
- What is the mechanism?
- What are the challenges?



Gel Content



15

Study of the effect of co-agent on long chain branching and gel content

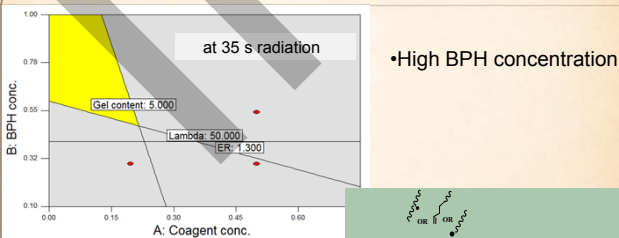
- **Objective**
Min gel; Max branching content
- **Central composite design of experiments**

Variable (units)	Range	Response	Specs
Co-agent conc. (wt-%)	0.25-0.75	n	<0.49
BPH conc. (wt-%)	0.1-0.5	η_0 (kPa.s)	>50
Radiation duration (s)	4-65	λ (s)	>50
UV lamp intensity (%)	47	ER	>1.3
Temperature (°C)	<50	Gel content (%)	<5

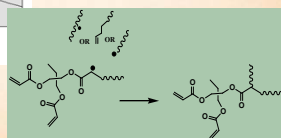
16

Example of operating map

Formation of LCB under these conditions is confirmed via GPC



•Low co-agent concentration



17

Concluding Remarks

- ❖ UV radiation is a safe, nontoxic method for PP modification
- ❖ UV radiation can be used to produce long chain branched PP (larger melt strength for packaging, thermoforming, blow-molding, extrusion coating and foaming applications)
- ❖ Variables such as photoinitiator type and concentration, lamp intensity, radiation time and temperature affect the process
- ❖ UV penetration depth and radiation time are possible limitations of the UV modification process
- ❖ Addition of co-agent decreases the radiation time needed for formation of long chain branching significantly
- ❖ US patent application for this work

18

Thank you for your attention



Back-up Slides

References

- Gotsis A, Zeevenhoven B, Hogt A. The effect of long chain branching on the processability of polypropylene in thermoforming. *Polymer Engineering & Science*. 2004; 44:973-982
- Figure copied from : <http://pubs.rsc.org/en/content/articlehtml/2013/sm/c2sm27233d>
- Graebing D. Synthesis of branched polypropylene by a reactive extrusion process. *Macromolecules*. 2002; 35:4602-4610
- Lugao A, Otaguro H, Parra D, Yoshiga A, Lima L, Artel B, Liberman S. Review on the production process and uses of controlled rheology polypropylene--Gamma radiation versus electron beam processing. *Radiat Phys Chem*. 2007; 76:1688-1690
- Rätzsch M, Arnold M, Borsig E, Bucka H, Reichelt N. Radical reactions on polypropylene in the solid state. *Progress in Polymer Science*. 2002; 27:1195-1282
- Parent JS, Bodsorth A, Sengupta SS, Kontopoulou M, Chaudhary BI, Poche D, Cousteaux S. Structure-rheology relationships of long-chain branched polypropylene: Comparative analysis of acrylic and allylic coagent chemistry. *Polymer*. 2009; 50:85-94
- He G, Tzoganakis C. A UV-initiated reactive extrusion process for production of controlled-rheology polypropylene. *Polymer Engineering and Science*. 2011; 51:151-157
- Amintowieh Y., Tzoganakis C., Hatzikiriakos S. and Penlidis A. Degradation and Stability 2014; 104:1-10.
- Figure copied from : <http://www.interempresas.net/Plastics/Articles/54066-Characterization-of-polyamide-used-for-foam-using-nonlinear-rheological-methods.html>
- Figure copied from : http://www.xpansioninstruments.com/products_principle.htm
- Amintowieh Y., Tzoganakis C., and Penlidis A. Accepted in *J Appl Polym. Sci.* (May 13, 2014)

How to characterize long chain branching (LCB) vs. degradation

Reference for comparisons: Linear PP with broad molecular weight distribution (MWD)

Rheological properties	Degradation	LCB	Comments
$\eta^* = \frac{\eta_0}{1 + (\omega\lambda)^n}$	$PI = \frac{10^5}{G_c(Pa)}$	$ER = C_1 G'_{at G^*=500 Pa}$	
G' at low frequencies	↓	↑	Higher G' → more elastic
G' - ω slope at low frequency	↓	↓	Indication of LCB
$\tan \delta - G^*$ (at low G^* ranges)	↑	↓	Deviations show the effect of molecular weight distribution
η' at low frequencies	↓	↑	
η_0	↓	↑	$\eta_0 \propto$ molecular weight
Shear thinning index (n)	↓	↓	Lower n → more shear thinning
Relaxation time (λ)	↓	↓	Shorter plateau region for LCB
Rheological polydispersity indices PI and ER	↓	↑	PI and ER → broader molecular weight distribution

G': Storage modulus G'': Loss modulus tanδ: Loss angle η': Complex viscosity
 PI: Rheological polydispersity index ER: Dispersity of high molecular weight tail of MWD

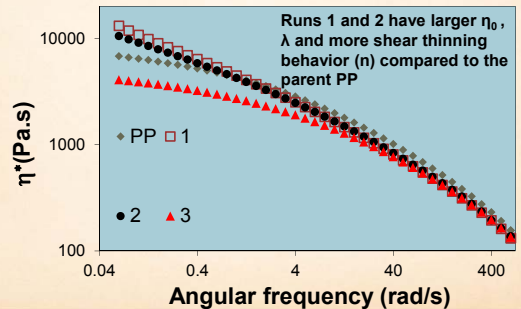
How to characterize long chain branching (LCB) vs. degradation

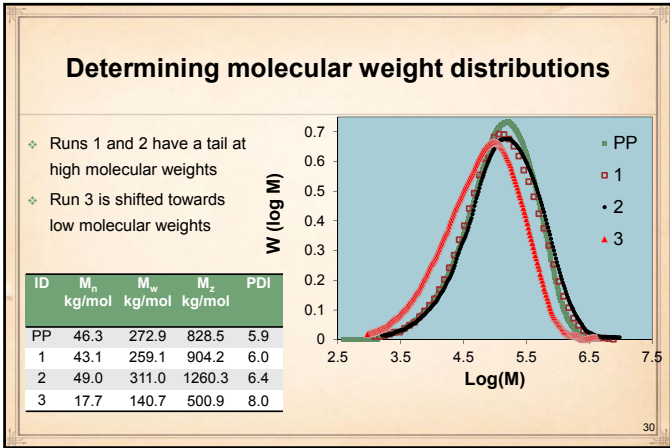
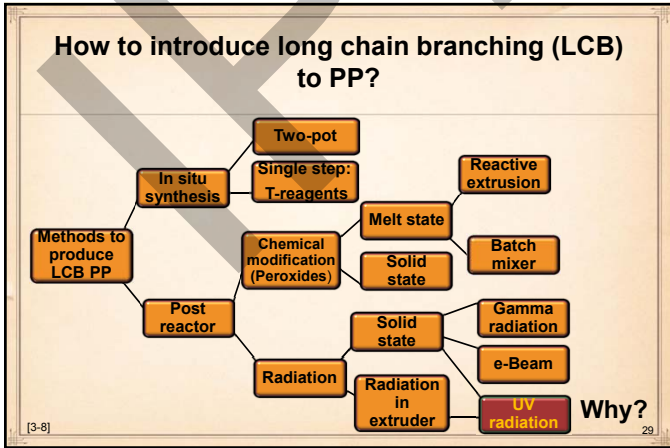
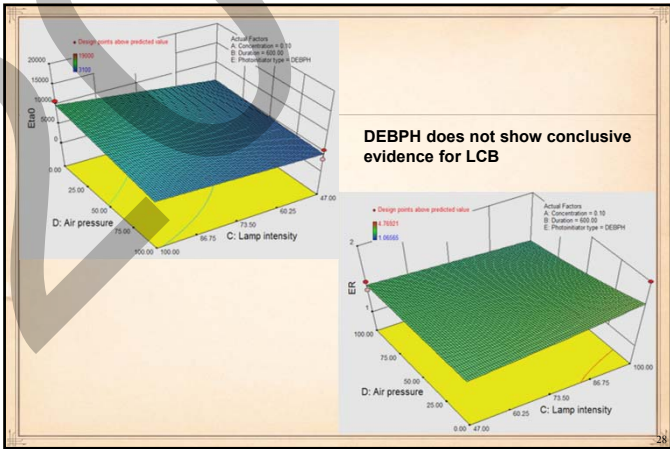
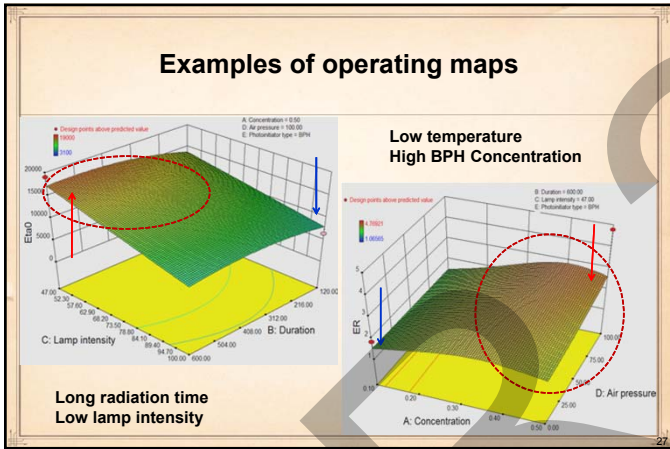
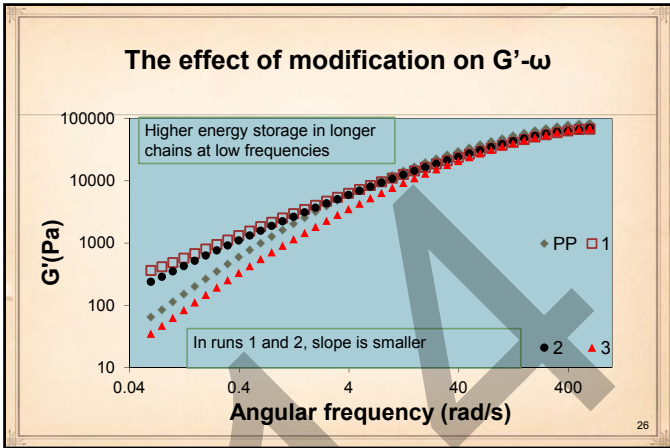
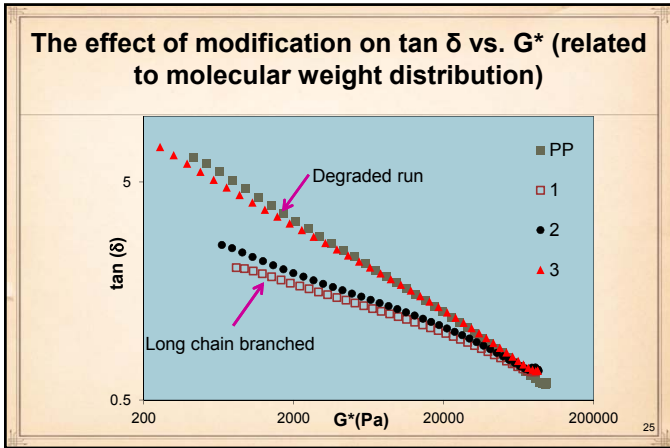
Reference for comparisons: Linear PP with broad molecular weight distribution (MWD)

Rheological properties	Degradation	LCB	Comments
$\eta^* = \frac{\eta_0}{1 + (\omega\lambda)^n}$	$PI = \frac{10^5}{G_c(Pa)}$	$ER = C_1 G'_{at G^*=500 Pa}$	
G' at low frequencies	↓	↑	Higher G' → more elastic
G' - ω slope at low frequency	↓	↓	Indication of LCB
η' at low frequencies	↓	↑	
η_0	↓	↑	$\eta_0 \propto$ molecular weight
Shear thinning index (n)	↓	↓	Lower n → more shear thinning
Relaxation time (λ)	↓	↓	Shorter plateau region for LCB
Rheological polydispersity indices PI and ER	↓	↑	PI and ER → broader molecular weight distribution

G': Storage modulus G'': Loss modulus tanδ: Loss angle η': Complex viscosity
 PI: Rheological polydispersity index ER: Dispersity of high molecular weight tail of MWD

The effect of modification on $\eta^* - \omega$

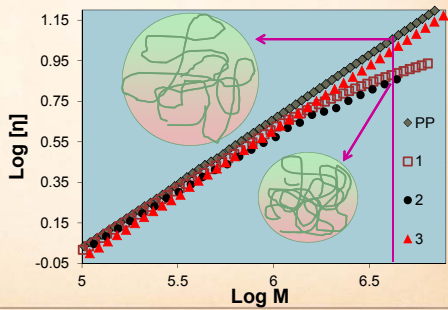




The effect of modification on intrinsic viscosity [η]

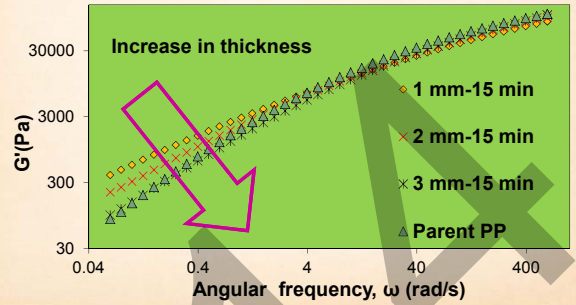
❖ Long chain branched PP has lower R_g compared to linear PP

$$[\eta] \propto \frac{R_g}{M}$$



31

The effect of thickness on storage modulus

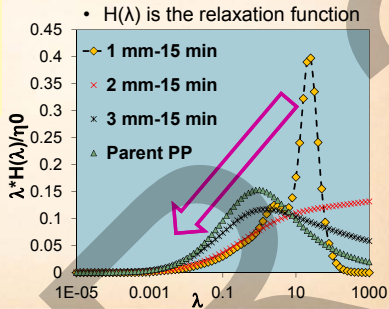


32

The effect of sample thickness on the relaxation spectrum

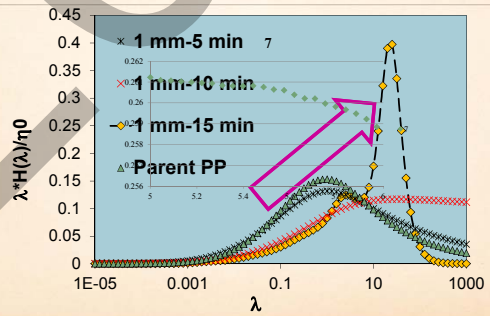
$$G'(\omega) = \int_{-\infty}^{+\infty} H(\lambda) \frac{(\omega\lambda)^2}{1 + (\omega\lambda)^2} d(\ln(\lambda))$$

$$G''(\omega) = \int_{-\infty}^{+\infty} H(\lambda) \frac{(\omega\lambda)}{1 + (\omega\lambda)^2} d(\ln(\lambda))$$



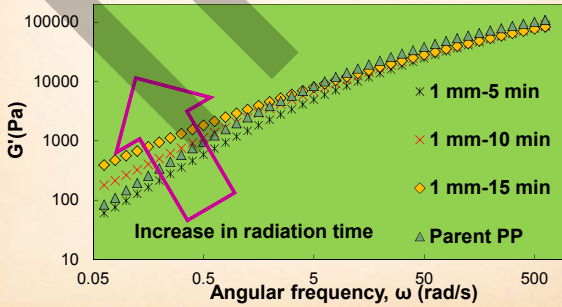
33

Relaxation spectrum



34

The effect of radiation time on storage modulus



35

Institute for Polymer Research

Celebrating 30 years of Official Institute Status

Symposium documents for

Kai Cao

Synthesis and Migration Insertion Polymerization (MIP) of $\text{CpFe}(\text{CO})_2(\text{CH}_2)_3\text{PPh}_2$ in Solution and in Bulk

K. Cao, X.S. Wang, IPR Symposium, University of Waterloo, ON, N2L 3G1, Canada

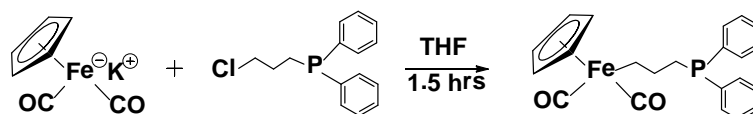
Introduction

The convergence of organometallic and polymer chemistry has led to the emergence of an interdisciplinary research field of metal-containing polymers (MCPs). Many MCPs exhibit interesting functions and self-assembly behavior, which render them very promising as building blocks for modern technologies. Taking advantage of the well-developed organometallic chemistry, synthesis of various metal-containing polymerizable compounds for processible macromolecules has therefore become a demanding, but challenging research topic.

Migration insertion reaction (MIR) is a well-studied organometallic reaction and has been explored for coordination polymerization of a number of organic monomers, including olefins, CO, CO_2 , for stereo-controlled organic polymers. Unlike previous reports which use metal complexes as catalysts, we have developed Migration Insertion Polymerization (MIP), in which metal complexes acting as monomers get involved into the construction of polymer backbones. As a result, a new class of main chain MCPs was produced. The polymers are also interested due to the presence of metal coordinated phosphorus, which may have properties complementary to previous reported phosphorus-containing polymers. It is well known that the reaction of alkyldicarbonylcyclopentadienyliron (FpR) with nucleophilic ligands, e.g. phosphine (PR_3), leads to air stable phosphine coordinated acyl complexes as a result of MIR. By combining both Fp and phosphine groups into one molecule via an alkyl spacer, bifunctional A-B type monomers of cyclopentadienyldicarbonyldiphenylphosphinopropyliron ($\text{CpFe}(\text{CO})_2(\text{CH}_2)_3\text{PPh}_2$), FpP, have been prepared. The solution reactions of FpP were systematically studied. The monomers undergo MIP leading to air stable poly(cyclopentadienylcarbonyldiphenylphosphinobutanoyliron), PFpP, with molecular weight up to 25700 g/mol.

Experiment

The monomer FpP was prepared from the salt-elimination reaction between 1-chloro-diphenylphosphinopropane and potassium cyclopentadienyldicarbonyliron (FpK) at room temperature, as shown in Scheme 1. Therefore, an A-B type bi-functional monomer which can undergo MIR was produced. The designed monomer's structure was confirmed by single crystal XRD, NMR and IR.



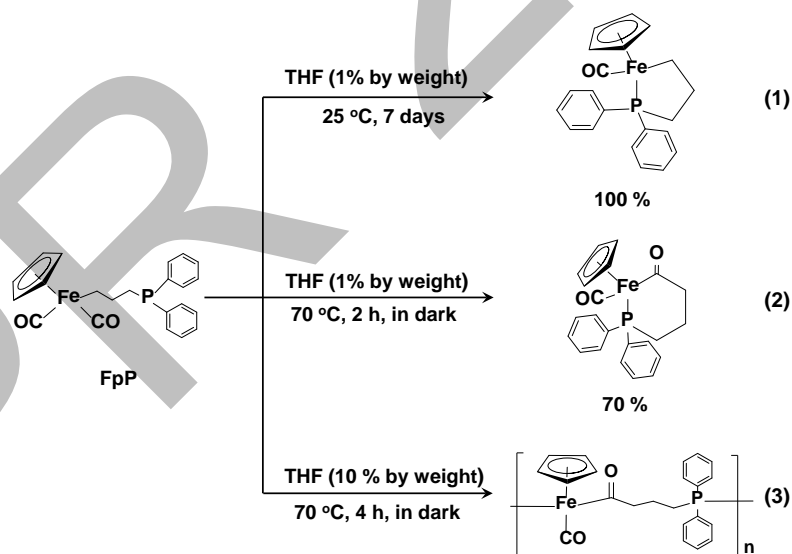
Scheme 1. Synthesis and migration insertion polymerization of FpP.

Solution reactions of FpP in THF was carried out at varied concentration and temperature. Solution polymerization of FpP with monomer concentration of 20 % was conducted in THF, leading to both THF soluble and insoluble PFpP. The THF soluble and insoluble PFpP was separated by centrifugation. The THF soluble PFpP was characterized by GPC, FT-IR, NMR while the THF insoluble PFpP was characterized by FT-IR, solid state NMR.

In order to suppress the possible cyclic reactions in solution and promote the inter-molecular reactions, bulk polymerization of FpP was attempted at 70 °C and 105 °C, respectively. In the case of polymerization in the presence of DMSO, 5% by weight DMSO was added to the monomer prior to the polymerization. The resulting polymer was characterized by GPC, NMR, FT-IR.

Results and Discussion

It was found that the FpP can undergo either intra-molecular or inter-molecular reactions depending on the reaction conditions, as shown in Scheme 2. When the solution with low FpP concentration (ca.1% by weight) was left at 25 °C, FpP was quantitatively converted to five membered rings (1) via CO release. On the other hand, when the same low concentration solution was heated at 70 °C in dark, intramolecular migration insertion reaction was promoted, leading to a high conversion of FpP (ca. 70%) to six membered cyclic Fp acyl derivatives (2). The two cyclic compounds are separated by chromatography.



Scheme 2. Solution reactions of FpP in THF

Solution polymerization of FpP in THF (20%) was conducted in THF, yielding both THF insoluble and soluble materials. Solid stated ^{31}P NMR, ^{13}C NMR and FT-IR indicate the THF insoluble materials arise from the migration insertion reaction. THF soluble PFpP was characterized by GPC and ^1H NMR, as shown in Figure 1, the GPC curve exhibits a molecular weight of 4200 g/mol with PDI of 1.24. In ^1H NMR, the chemical shifts at 4.3 ppm represent Cp rings in each Fp acyl repeat unit. The signal at

4.8 ppm represents Cp ring for the Fp end group of the polymer. Intensities of the chemical shifts for Cp at 4.3 and 4.8 ppm are compared for end group analysis, suggesting that the polymer has a DP of 11. Molecular weight estimated from the analysis is ca. 4400 g/mol, which is consistent with the GPC results.

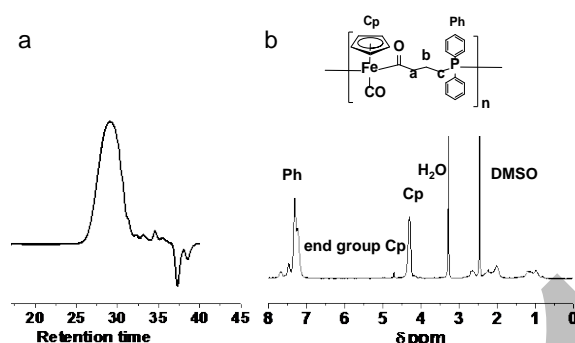


Figure 1. GPC curve for PFpP (a) and ^1H NMR of PFpP in $\text{DMSO-}d_6$ produced via solution polymerization of FpP in THF (b)

In order to suppress the intra-molecular cyclization reactions, MIP of FpP was performed in bulk. Temperature and DMSO effect on the polymerization was studied. The results are summarized in Table 1. PFpP with 7 was produced when the reaction temperature is $70\text{ }^\circ\text{C}$, which is attributed to the high $T_g=99\text{ }^\circ\text{C}$ of the polymer, as the polymer chain become vitrified during the polymerization. To address this issue, the polymerization was performed at $105\text{ }^\circ\text{C}$ in bulk. As a result, GPC analysis reveals that the resulting polymer has a number-average molecular weight (M_n) of 8200 g/mol with a PDI of 1.35.

It has been reported that DMSO can induce MIR via coordination to Fe, and a solvent-coordinated intermediate was revealed via ^1H NMR analysis in a previous report. We therefore performed MIP of FpP in the presence of a small amount of DMSO (ca. 5% by weight). When the polymerization was performed at $70\text{ }^\circ\text{C}$ (entry 3 in Table 1), the molecular weight for the resulting polymers remained low. However the molecular weight distribution was broad (PDI = 3.15) and the weight-average molecular weight (M_w) was 9400 g/mol, suggesting that a small amount of higher molecular weight polymer was produced. This result suggests that DMSO is exerting an influence on MIP, but this effect is limited due to the lower chain mobility at $70\text{ }^\circ\text{C}$. To overcome this limitation, polymerization in the presence of DMSO was performed at $105\text{ }^\circ\text{C}$. GPC analysis of the resulting polymer revealed that the polymer had a M_n of 25,700 g/mol with a PDI of 1.73

Table 1. Effect of temperature and DMSO on the polymerization of FpP in bulk^[a]

Entry	Temp. ($^\circ\text{C}$)	DMSO ^[b]	M_n (g/mol)	PDI
1	70	--	2800 ^[c]	--
2	105	--	8200 ^[d]	1.35
3	70	DMSO	3000 ^[d]	3.15
4	105	DMSO	25700 ^[d]	1.73

[a] Polymerization time was 20 hours. [b] DMSO (ca. 5% by weight) was added. [c] end group analysis. [d] GPC results: conventional calibration using PS standards for entries 2 and 3, as the samples did not scatter enough light to yield reliable light scattering data; triple detection used for entry 4.

In summary, a new type of bifunctional monomer FpP which can undergo MIP was synthesized. The intra-molecular and inter-molecular reactions of FpP in solution have been comprehensively studied. Temperature and DMSO effect on the bulk polymerization of FpP was investigated. High molecular weight polymer with M_n of 25,700 g/mol was prepared at 105 °C in the presence of DMSO.

Reference

- [1] Manners, I. *Synthetic Metal containing polymers*; WILEY-VCH Verlag GmbH & Co. LGA, 2004.
- [2] Whittell, G. R.; Hager, M. D.; Schubert, U. S.; Manners, I. *Nat. Mater.* 2011, 10, 176.
- [3] X. S. Wang, K. Cao, Y. B. Liu, B. Tsang, S. Liew, *J. Am. Chem. Soc.* 2013, 135, 3399-3402.
- [4] K. Cao, B. Tsang, Y. Liu, D. Chelladural, W. P. Power, X. Wang, *Organometallics* 2014, 33, 531-539.
- [5] K. Nicholas, S. Raghu, M. Rosenblum, *J. Organomet. Chem.* 1974, 78, 133-137.

INSTITUTE FOR POLYMER RESEARCH

Migration insertion polymerization of CpFe(CO)₂(CH₂)₃PPh₂ (FpP): A new route for the preparation of main-chain metal-containing polymer

Presenter: Kai Cao, PhD candidate

Supervisor: Dr Xiaosong Wang

Date: 21st, May, 2014



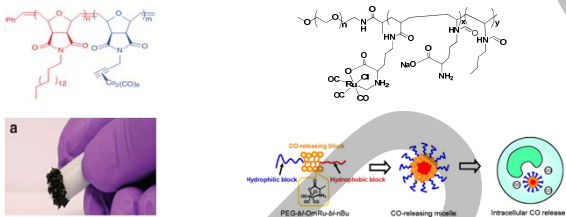
Outline

- Background
- Research objective
- Synthesis of monomer FpP
- Migration insertion polymerization of FpP in solution and bulk
- Synthesis alkylidiphosphine functionalized PFpP amphiphiles.
- Summary

Background

Metal-containing polymer

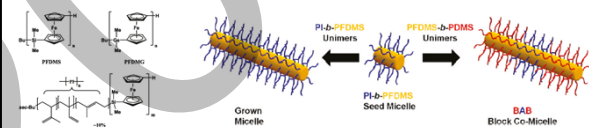
Electrical Optical Magnetic Catalytic Biological



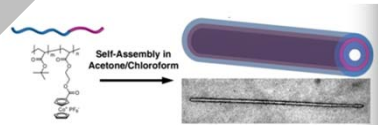
Zha, Y et al. *J Am Chem Soc* 2012, 134, 4493.

Hasegawa et al. *J Am Chem Soc* 2010, 132, 18273.

Background



orben Gädt et al. *Macromolecules* 2011 44 (10), 3777-3786

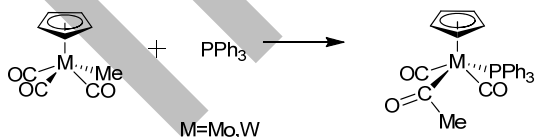


Lixia Ren et al. *J Am Chem Soc* 2010 132 (26), 8874-8875

It demanding to develop new synthetic techniques for the preparation of metal-containing polymers.

Migration insertion reactions

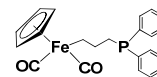
Example



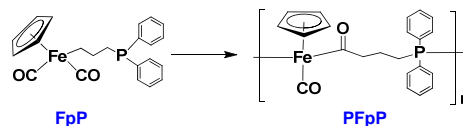
Adeyemi, O. G.; N. J. Coville. *Organometallics*. 2003, 22(11): 2284-2290.

Research objective

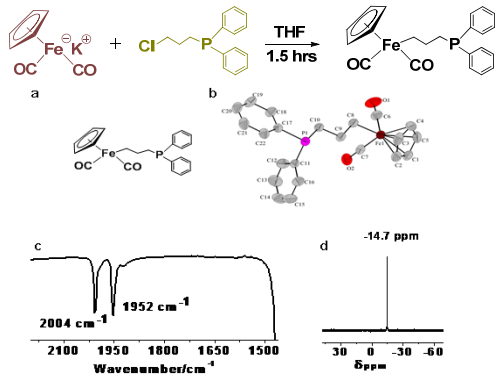
- Fp and phosphine groups connected by a alkyl spacer
- FpP act as a difunctional monomer



- MIR can be used to link organometallic units into a macromolecular chain structure

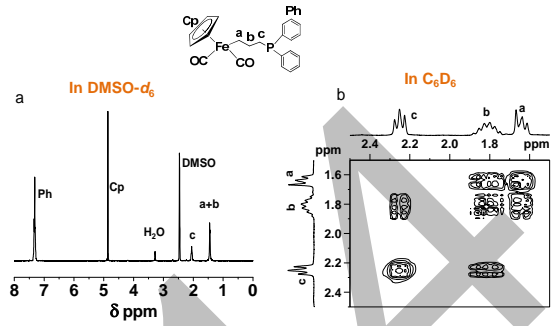


Crystal structure, FT-IR and ³¹P NMR of FpP



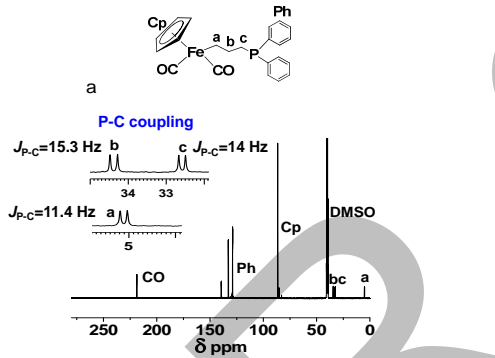
7

¹H NMR and ¹H-¹H COSY 2D NMR of FpP



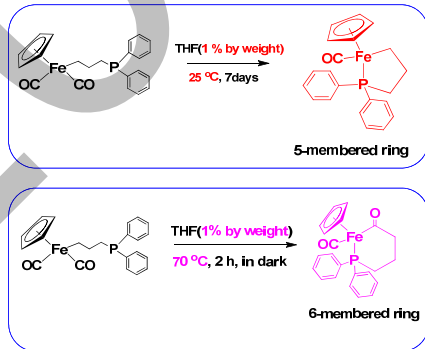
8

¹³C NMR of FpP



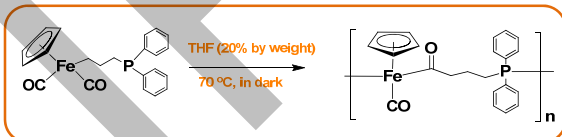
9

Cyclization reaction of FpP in dilute solution



10

Migration insertion polymerization of FpP in solution



Centrifugation

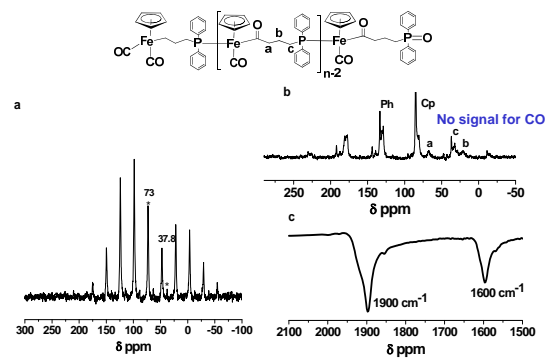
THF soluble
70 %

THF insoluble
30 %

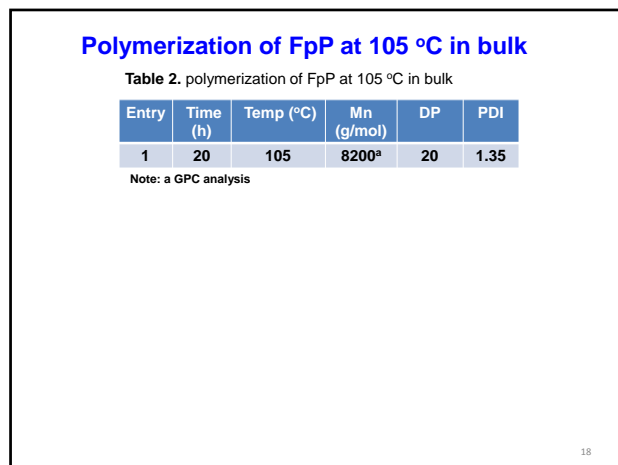
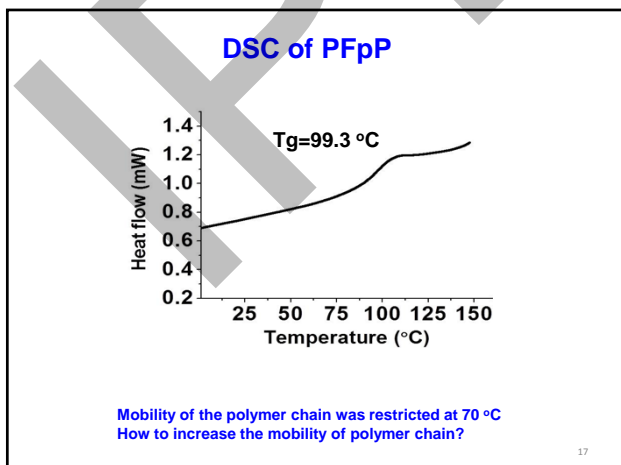
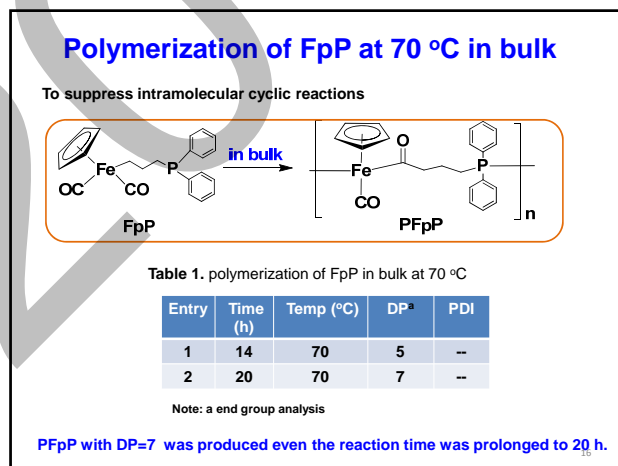
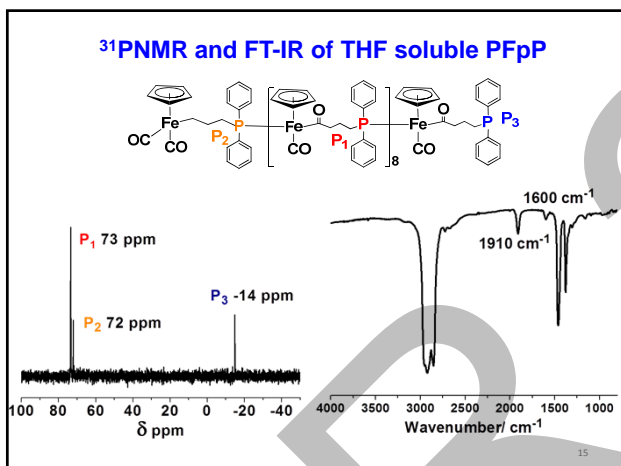
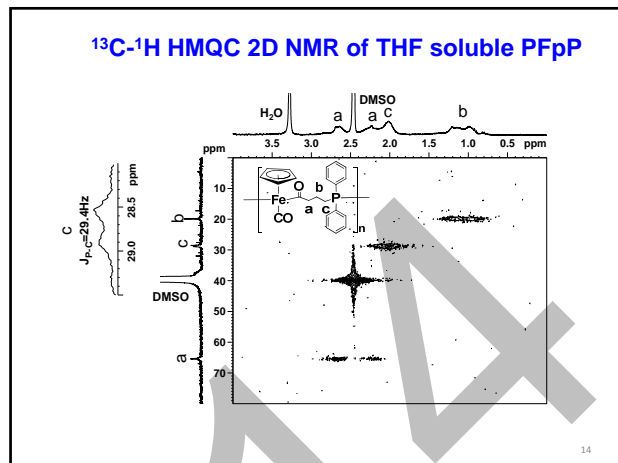
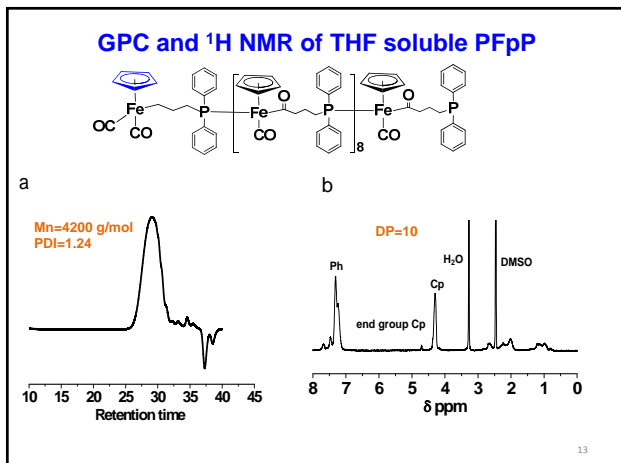
Precipitated in Hexane

11

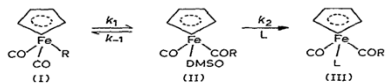
Solid state ³¹P NMR ¹³C NMR and FT-IR of THF insoluble PFpP



12



Polymerization of FpP in the presence of DMSO



DMSO can coordinated to the Fp group

Nicholas, K., Raghu, S., & Rosenblum, M. (1974). Intermediates in the intramolecular ligand transfer reactions of complexes. *Journal of Organometallic Chemistry*, 78(1), 133-137.

Table 3. polymerization of FpP at 70 °C at the presence of DMSO

Entry	Time (h)	Temp (°C)	Mn (g/mol)	DP	PDI
1	20	70	3000 ^a	7	3.15

Note: a GPC analysis

DMSO can promote the polymerization, but effect is very limited at 70 °C.

19

Polymerization of FpP at 105 °C in bulk in the presence of DMSO

Table 4. polymerization of FpP at 105 °C at the presence of DMSO

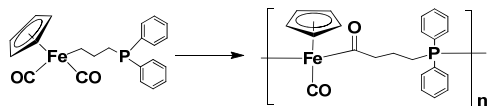
Entry	Time (h)	Temp (°C)	Mn (g/mol)	DP	PDI
2	20	105	25700 ^a	63	1.73

Note: a GPC analysis

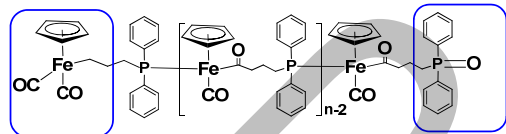
PFpP with high molecular weight was obtained at 105 °C in the presence of DMSO

20

Synthesis alkylidiphenylphosphine functionalized PFpP amphiphiles

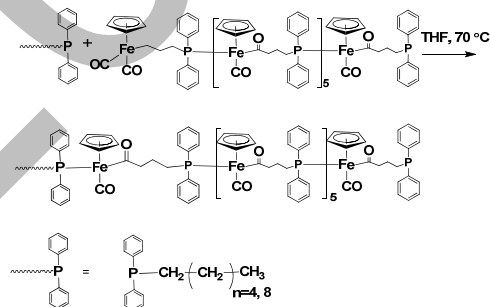


Two end group



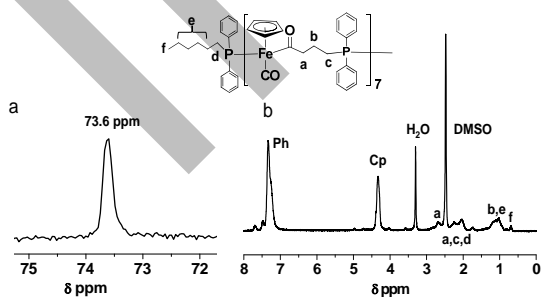
21

Scheme for the preparation of PFpP based amphiphiles



22

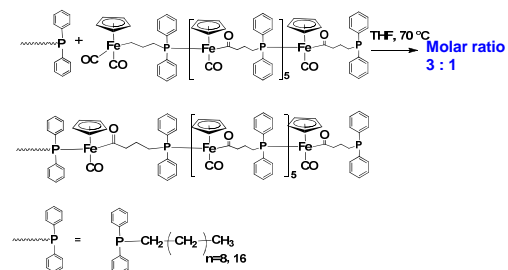
¹HNMR and ³¹PNMR of PPh₂-C6 functionalized PFpP



PPh₂-C6 functionalized PFpP was successfully synthesized

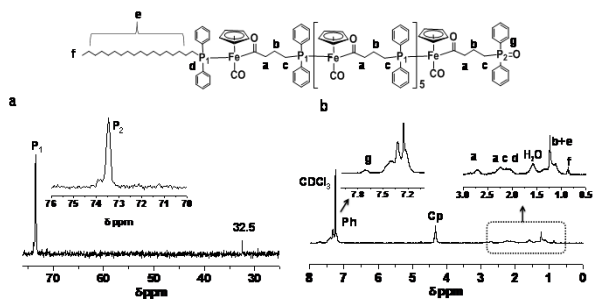
23

End group reaction of PFpP with PPh₂C10 and PPh₂C18



24

^{31}P NMR and ^1H NMR of $\text{PPh}_2\text{C18}$ functionalized PFpP



25

Summary

- FpP was prepared and characterized using single crystal XRD, FT-IR, ^1H NMR, ^{31}P NMR, ^{13}C NMR
- Migratory insertion polymerization of FpP in solution was attempted, which resulting both THF soluble and insoluble materials. The THF soluble part exhibits molecular weight of 4200 g/mol with PDI=1.24. The THF insoluble part was analyzed by solid state ^{13}C NMR and ^{31}P NMR.
- Polymerizations of FpP in bulk were performed. High molecular weight PFpP was produced at 105 °C in the presence of DMSO (5% by weight)
- Alkyldiphenylphosphine functionalized PFpP amphiphiles $\text{PPh}_2\text{C6}$ -PFpP, $\text{PPh}_2\text{C10}$ -PFpP and $\text{PPh}_2\text{C18}$ -PFpP were synthesized and characterized by ^1H NMR, ^{31}P NMR.

26

Acknowledgement

Supervisor:
Prof Xiaosong Wang

Committee member:
Prof Mario Gauthier
Prof Boxin Zhao
Prof Sonny Lee

Lab mate



University of
Waterloo



27

Thank you !

28

Institute for Polymer Research

Celebrating 30 years of Official Institute Status

Symposium documents for

Michael Fowler

Temperature Response of Aqueous Solutions of a Series of Pyrene End-Labeled Poly(*N*-isopropylacrylamide)s Probed by Fluorescence

M. Fowler, J. Duhamel, F. M. Winnik, X.-P. Qiu
IPR Symposium, University of Waterloo, ON N2L 3G1

Poly(*N*-isopropylacrylamide) (PNIPAM) has been the subject of considerable interest for over the past 50 years due to its ability to undergo a coil-to-globule transition (CGT) in aqueous solution when the temperature is increased above its lower critical solution temperature (T_c), typically reported as 32 °C. The CGT of PNIPAM has been used to mimic the CGT of proteins, to confer a temperature-dependent trigger to polymeric drug-delivery methods, and to allow a variety of self-assembly processes to take place above a set temperature. The nature of the end-groups present in telechelic PNIPAM has a significant effect on the value of T_c , where hydrophobic end-groups cause T_c to decrease with decreasing molecular weight while hydrophilic end groups result in the opposite trend. When hydrophobic groups (referred to herein as *lip*) are covalently attached to PNIPAM, as is the case for telechelic lip₂-PNIPAM, the resulting polymer chains form micellar aggregates in water due to intermolecular hydrophobic interactions, even at μM concentrations. A model has been proposed by F.M. Winnik et al.¹⁻⁴ to describe the behaviour of aqueous solutions of lip₂-PNIPAM as the temperature increases, the key points of which are presented hereafter.

Below 20 °C the lip₂-PNIPAM chains form stable micelles. The core is composed of the hydrophobes, the shell is composed of hydrated PNIPAM loops, and the middle region between the two consists of a mixture of water and dehydrated PNIPAM segments. As the temperature increases above 20 °C, the lip₂-PNIPAM solution enters the thermodynamic Regime I, where segments of the PNIPAM loops in the shell begin to dehydrate and collapse into the middle region, decreasing the size of the micelle. At T_c , the lip₂-PNIPAM solution enters Regime II where the micelles begin to associate with one another to form larger aggregates called mesoglobules. The apparent M_n of PNIPAM mesoglobules increases significantly as the temperature approaches the stable mesoglobule temperature of 34 °C (T_m), while the hydrophobic cores of the micelles within the mesoglobules begin to dissolve and disperse throughout the mesoglobule. At the same time, additional water is expelled from the mesoglobules. Above T_m , the lip₂-PNIPAM solution enters Regime III, where mesoglobules stabilize and do not grow any further. At this stage, the mesoglobules are either thermodynamically stable, or they are kinetically frozen and vitreous in nature. While the solutions of lip₂-PNIPAM show a M_n dependence for T_c , T_m is always found to equal 34 °C regardless of M_n .

The hydrophobic groups present in lip₂-PNIPAM, and the manner in which they interact, affect the polymer's solution behaviour and makes the determination of the association level and the time scale of interaction between these groups particularly interesting. This information may be obtained by monitoring the fluorescence of pyrene labels covalently attached onto the PNIPAM chains. Pyrene was chosen for these studies because it is not only a highly useful

fluorescent probe for studying hydrophobically modified polymers, but it is also strongly hydrophobic, resulting in minimal deviation from the typical behaviour observed with lip₂-PNIPAM in aqueous solution. Additionally, pyrene is able to form an excited dimer called an excimer, which is distinct in both spectrum and lifetime from the monomer. Excimer may be formed either from pyrenes that encounter one another via diffusion while the pyrene monomer is excited, or it may be formed instantaneously from pyrenes which are associated in the ground-state. The amount of excimer can be determined by measuring its intensity via steady-state fluorescence, while the rate of excimer formation and the amount of excimer formed via diffusion can be determined using time-resolved fluorescence.

This study applies the Model Free Analysis (MFA)⁵⁻⁸ to fit the fluorescence decays acquired with a series of Py₂-PNIPAM samples as a function of temperature. The parameters retrieved from the MFA of the decays enable the characterization of the behaviour of the Py₂-PNIPAM samples in aqueous solution as they pass through T_c and T_m . In turn, the trends obtained through this analysis are interpreted within the framework provided by the model proposed by F.M. Winnik et al.¹⁻⁴ to investigate the extent of its validity.

Results and Discussion:

T_c , was determined using turbidimetry and light scattering, and was found to increase with the number-average molecular weight (M_n) of the polymer. Light scattering was necessary since the fluorescence experiments were performed at low concentration, where turbidimetry was not sensitive enough to determine T_c .

The steady-state fluorescence spectra yielded the ratio of the fluorescence intensity of the excimer over that of the monomer, namely the $(I_E/I_M)^{SS}$ ratio, which was found to go through a maximum at T_c , as did the polydispersity index of the time-resolved monomer fluorescence decays. The average decay times of the monomer and excimer as well as the ratio a_{E-}/a_{E+} , which reflects the rise time in the excimer decays, all increased sharply at T_c . Combined, these trends indicate that mesoglobule formation either restricts the mobility of pyrene or reduces its local concentration.

These individual trends are useful, but can be error-prone as they are the result of unrestricted exponential fits of either the monomer or excimer decays alone. Global analysis of the time-resolved fluorescence decays of the pyrene monomer and excimer according to model-free analysis (MFA) is significantly more accurate, as any excimer formation by diffusion must be accounted for with identical lifetimes and pre-exponential factors in both the monomer and excimer decay. MFA allowed the calculation of the average rate constant of excimer formation $\langle k \rangle$ as well as the three fluorescence fractions f_{free} , f_{diff} , and f_{agg} describing the distribution of the pyrene labels in solution as pyrene labels which do not form excimer, form excimer by diffusion, and are aggregated, respectively. These values are shown in Figure 1.

$\langle k \rangle$ is high below T_c , and decreases significantly as the solution enters Regime II and forms mesoglobules. This behaviour is consistent with pyrene in the shell of the micelles forming excimer by diffusion via a fast process. When mesoglobules form, the chains in the shells are more hindered and $\langle k \rangle$ decreases.

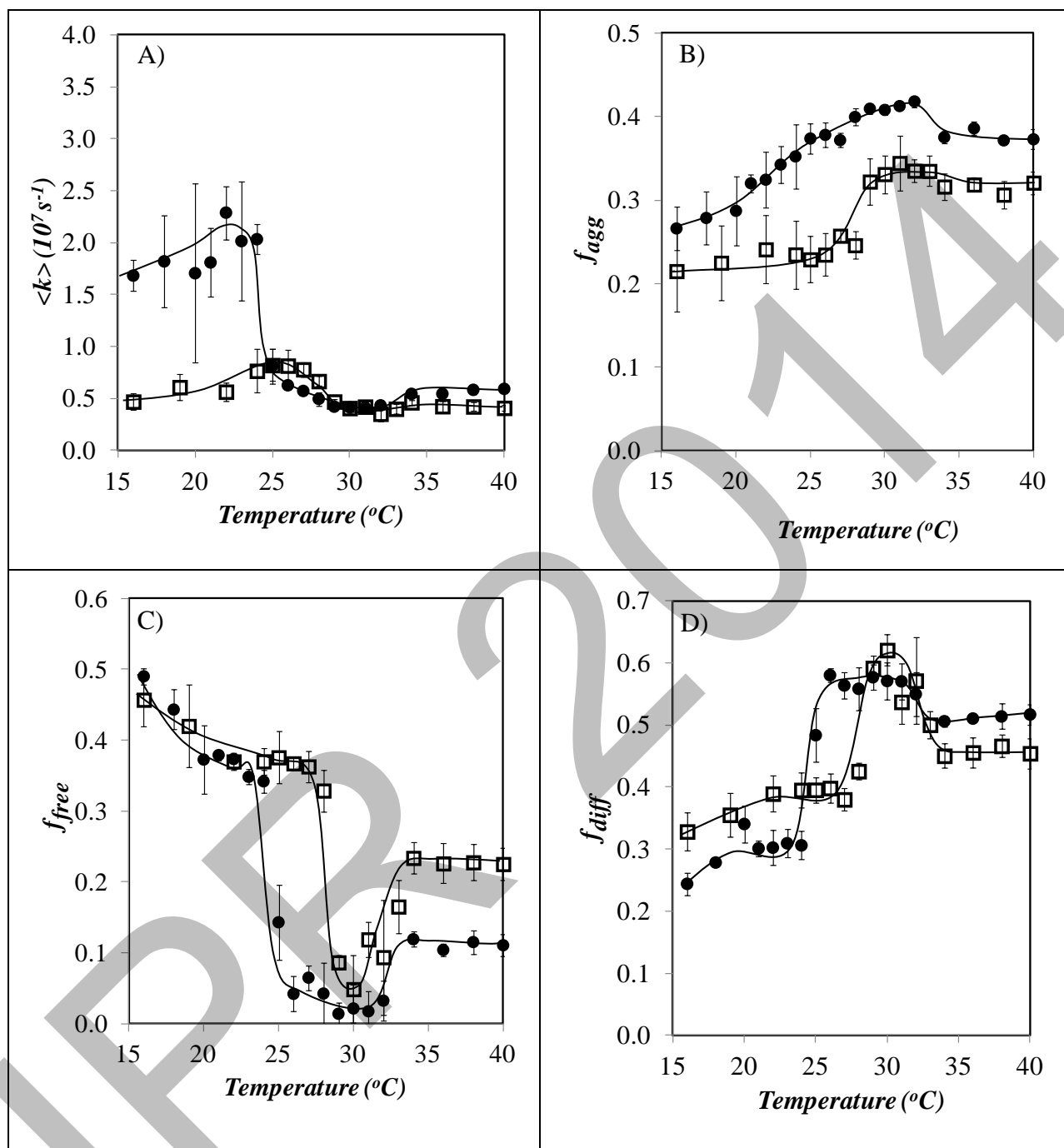


Figure 1: Light scattering and fluorescence results for aqueous solutions of the Pyrene-labelled PNIPAM samples. (●) and (■) are pyrene-labelled PNIPAM samples with a molecular weight of 14k and 25k, respectively.

f_{agg} increases steadily throughout Regime I, consistent with the micelles decreasing in size. T_c does not significantly affect f_{agg} since mesoglobule formation does not disrupt the

micellar cores. Increasing the temperature near T_m does cause f_{agg} to decrease though, as the hydrophobic cores disperse in this temperature region.

f_{free} and f_{diff} are essentially mirror images of one another. f_{free} decreases slightly in Regime I while f_{diff} increases, which is consistent with the micelles decreasing in size. f_{free} decreases sharply and f_{diff} increases sharply at T_c , indicating that the free pyrene is located in the shell. Mesoglobule formation causes the shells to overlap, thus in Regime II free pyrene is now able to encounter pyrenes from other micelles via diffusion and form excimer. Dissolution of the micelles within the mesoglobules at the end of Regime II causes an increase in f_{free} and a decrease in f_{diff} , as the local pyrene concentration is decreased. All parameters are constant above T_c . All of these results are consistent with the model proposed for telechelic PNIPAM by F. M. Winnik et al.

Conclusions:

The use of fluorescence to probe the behaviour of aqueous solutions of pyrene end-labelled PNIPAMs has provided detailed information on the behaviour of the hydrophobes present in the samples. Turbidimetry and light scattering showed that the value of T_c depends on the hydrophobe content of the telechelic polymers. $(I_E/I_M)^{SS}$, the lifetime and PDI of the monomer, the lifetime of the excimer, and the a_{E-}/a_{E+} ratio all undergo significant changes at T_c . Application of the MFA equations to the time-resolved fluorescence decays allowed the calculation of the rate constant for excimer formation $\langle k \rangle$, as well as the fluorescence fractions f_{agg} , f_{free} , and f_{diff} . The values of $\langle k \rangle$, f_{free} , and f_{diff} showed changes at both T_c and T_m which are largely consistent with the model developed by Winnik et al. for lip₂-PNIPAM in aqueous solution. Specifically, the movement of the chain segments from the shell into the middle region in Regime I, the formation of mesoglobules in Regime II, and the stabilization of the mesoglobules in Regime III have all been confirmed via steady-state and time-resolved fluorescence measurements. While the mesoglobules in Regime III do not appear to be vitreous and therefore kinetically frozen, these results otherwise conform to the predictions made by F.M. Winnik et al. with regard to the behaviour of lip₂-PNIPAM in water.

References:

1. Kujawa, P., Tanaka, F., Winnik, F.M. Temperature-Dependent Properties of Telechelic Hydrophobically Modified Poly(N-isopropylacrylamides) in Water: Evidence from Light Scattering and Fluorescence Spectroscopy for the Formation of Stable Mesoglobules at Elevated Temperatures. *Macromolecules* **2006**, 39, 3048-3055.
2. Tanaka, F., Koga, T., Kojima, H., Winnik, F.M. Hydration and phase separation of temperature-sensitive water-soluble polymers. *Chin. J. Polym. Sci.* **2011**, 29, (1), 13-21.

3. Koga, T., Tanaka, F., Motokawa, R., Koizumi, S., Winnik F.M. Theoretical Modelling of Hierarchically Associated Structures in Hydrophobically Modified PNIPAM Aqueous Solutions on the Basis of a Neutron Scattering Study. *Macromol. Symp.* **2010**, 291-292, 177-185.
4. Tanaka, F., Koga, T., Kaneda, I., Winnik, F.M. Hydration, phase separation and nonlinear rheology of temperature-sensitive water-soluble polymers. *J. Phys.: Condens. Matter* **2011**, 23, 284105-284112.
5. Yip, J., Duhamel, J., Bahun, G.J., Adronov, A. A Study of the Dynamics of the Branch Ends of a Series of Pyrene-Labeled Dendrimers Based on Pyrene Excimer Formation. *J. Phys. Chem. B* **2010**, 114, 10254-10265.
6. Siu, H., Duhamel, J. Comparison of the Association Level of a Pyrene-Labeled Associative Polymer Obtained from an Analysis Based on Two Different Models. *J. Phys. Chem. B* **2005**, 109, 1770-1780.
7. Chen, S., Duhamel, J., Bahun, G., Adronov, A. Quantifying the Presence of Unwanted Fluorescent Species in the Study of Pyrene-Labeled Macromolecules. *J. Phys. Chem. B* **2011**, 115, 9921-9929.
8. Keyes-Baig, C., Duhamel, J., Wettig, S. Characterization of the Behavior of a Pyrene Substituted Gemini Surfactant in Water by Fluorescence. *Langmuir* **2011**, 27, 3361-3371.

Temperature Response of Aqueous Solutions of Pyrene End-Labeled Poly(*N*-isopropylacrylamide)s Probed by Fluorescence

Michael Fowler
 Supervisor: Jean Duhamel
 Department of Chemistry
 University of Waterloo

Introduction

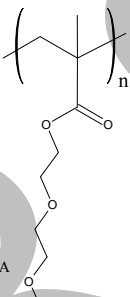
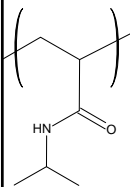
2

Temperature Responsive Polymers

Hydrophilic polymers that are water-soluble at low temperature, are water insoluble above their Lower Critical Solution Temperature (LCST)

Applications:

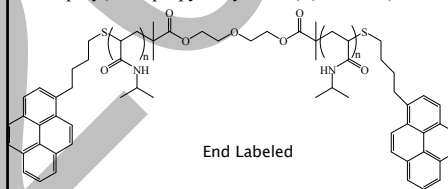
- Oil Recovery
- Thermo-responsive drug delivery
- Mimic for proteins' Coil-to Globule Transition



3

Hydrophobically Modified Water Soluble Polymers

- poly(*N*-isopropyl acrylamide) (PNIPAM)



Sample Mw:
14k
25k
45k

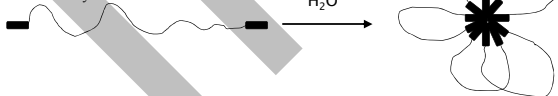
Why PNIPAM end-labeled with pyrene?

- Hydrophobic pyrenes associate in water
- Hydrophilic PNIPAM is water-soluble at low temperature, is water insoluble above its Lower Critical Solution Temperature (LCST) (~33 °C)

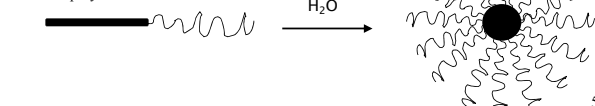
4

Micelle Formation:

Hydrophobically Modified Water Soluble Polymers

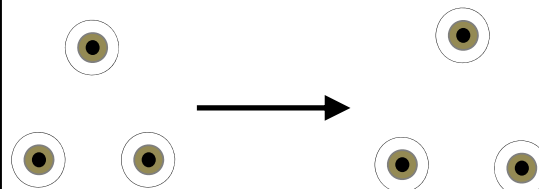


Block Copolymers



5

LCST:

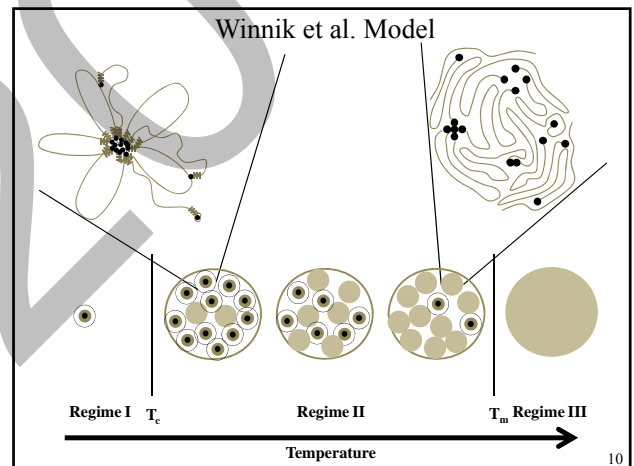
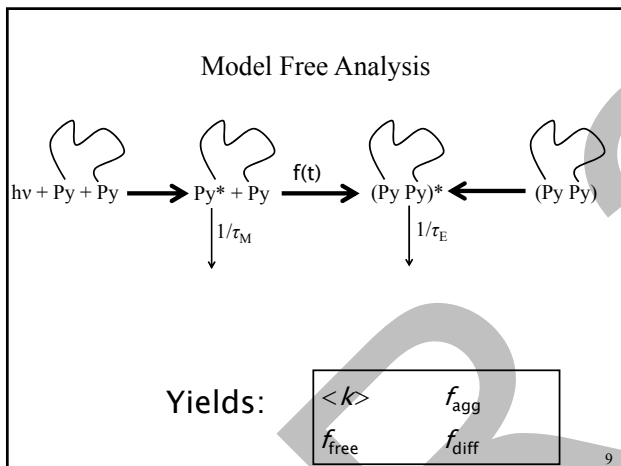
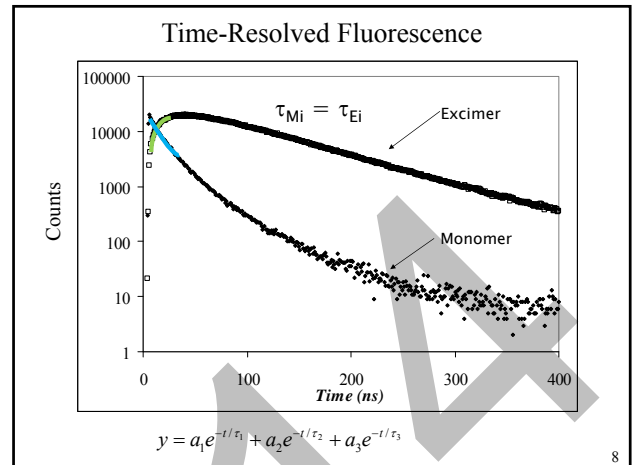
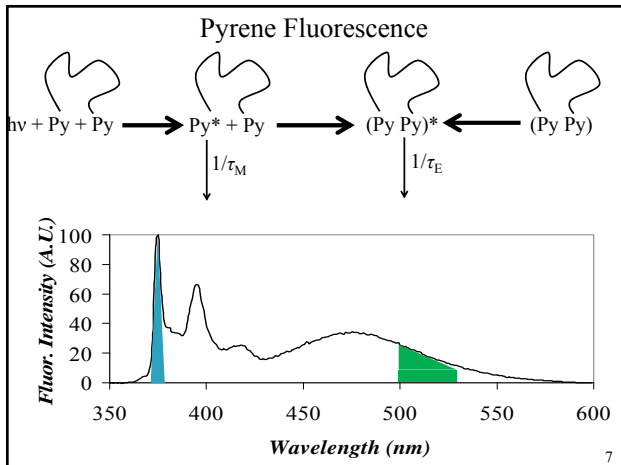


Cold Water
(Below LCST)

Warm Water
(Above LCST)

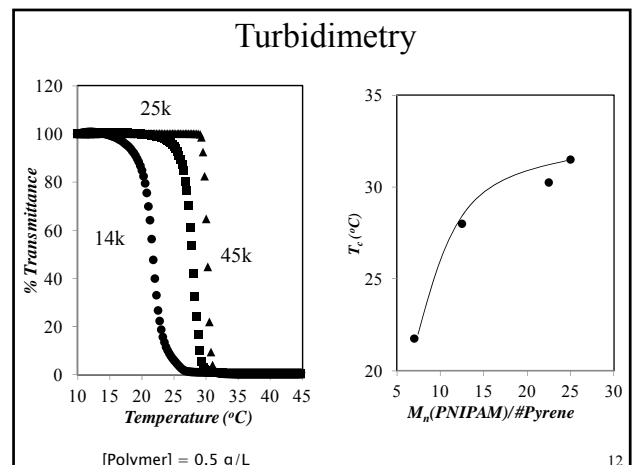
- More aggregation?
- Less diffusion?

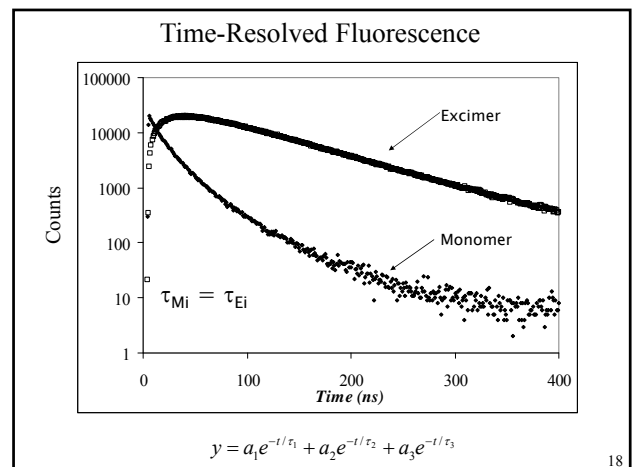
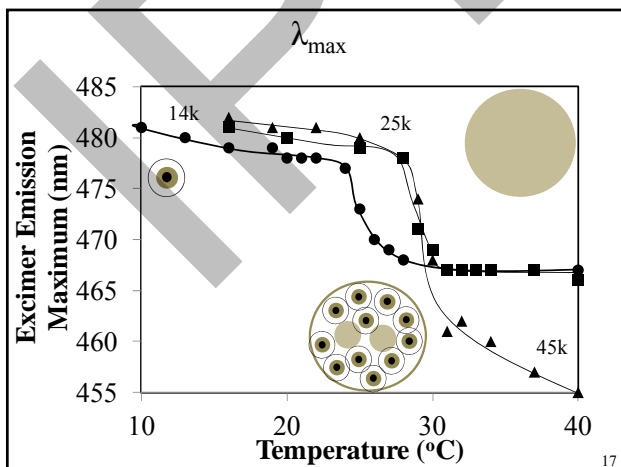
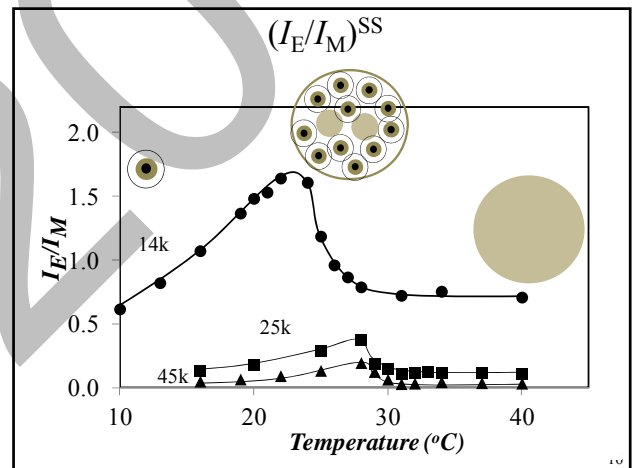
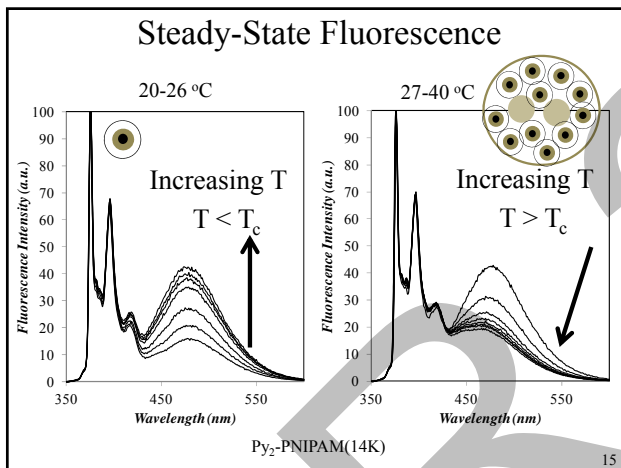
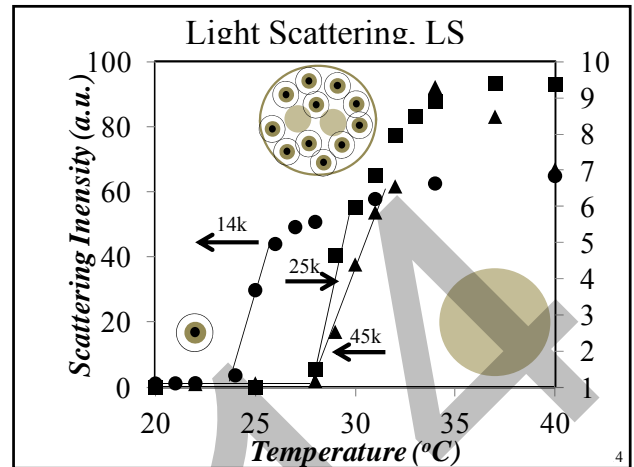
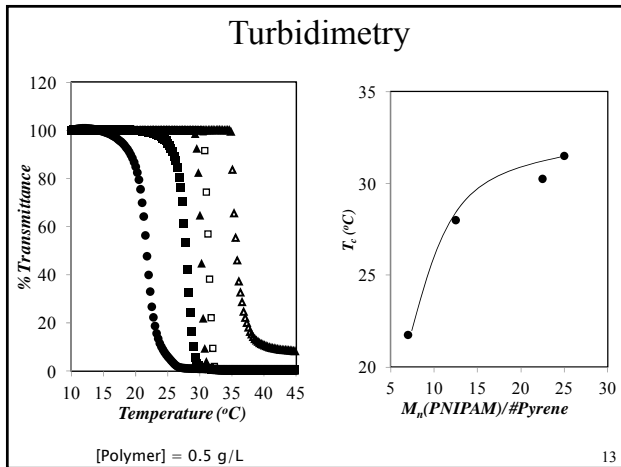
6

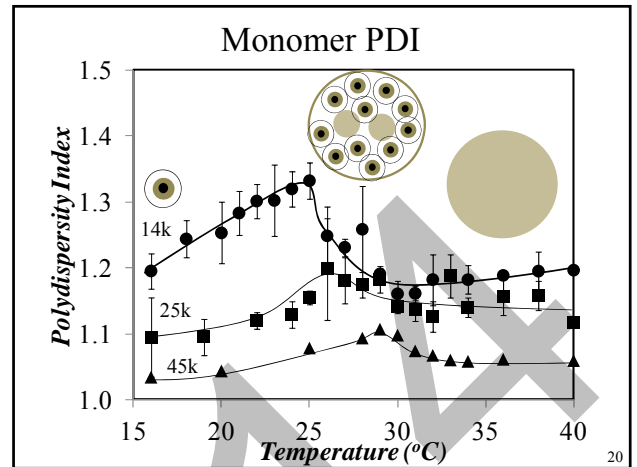
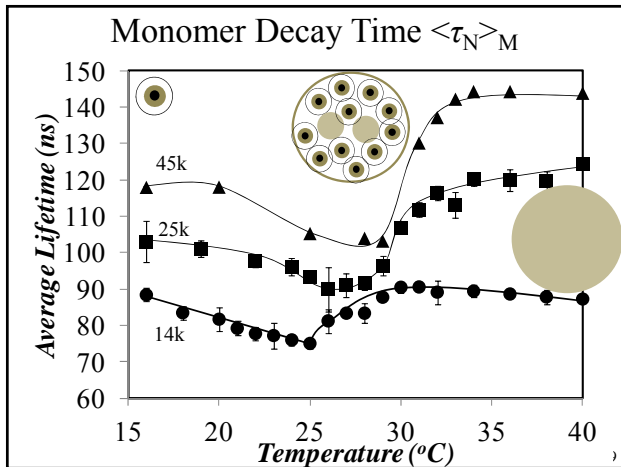


Results

11

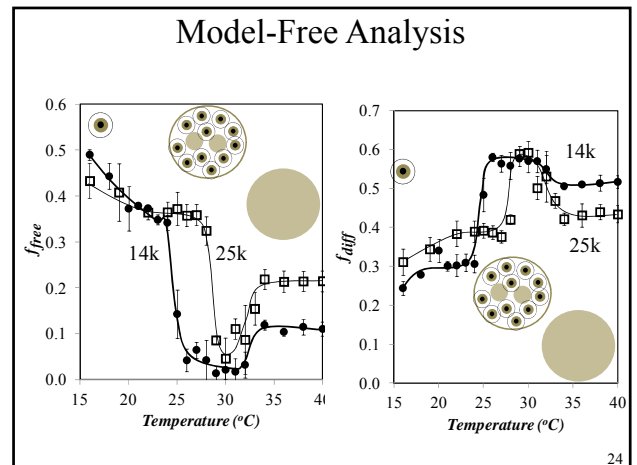
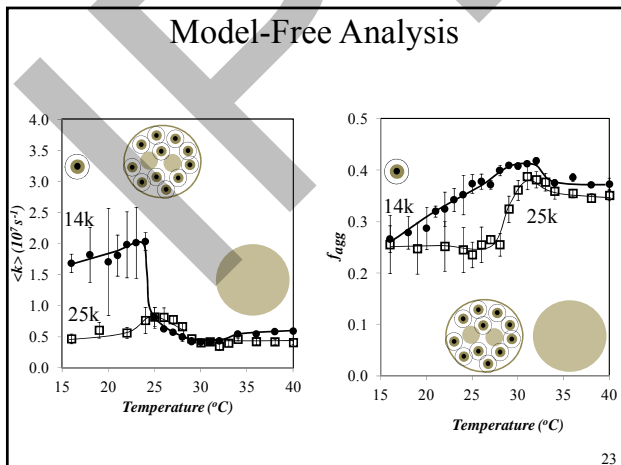
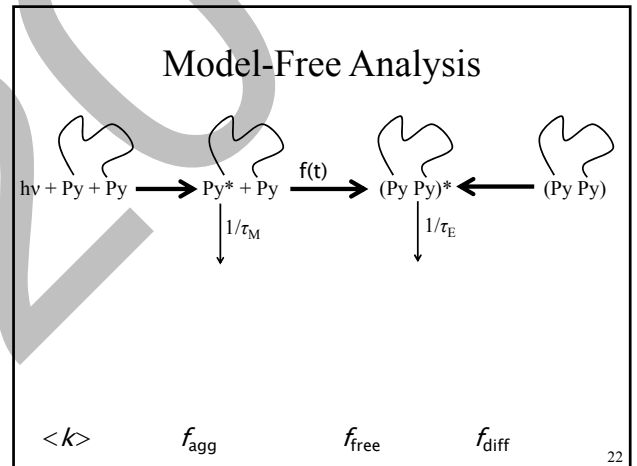


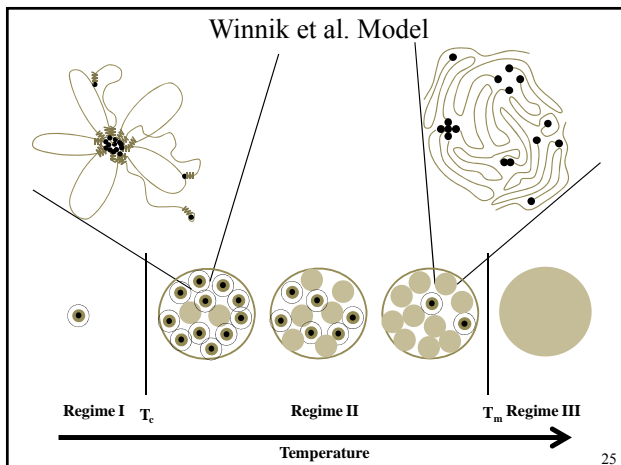




T_c Summary

Sample	T_c (°C) as determined by:							Average
	L.S.	$(I_E/I_M)^{SS}$	$\langle\tau_N\rangle_M$	PDI	$\langle\tau_N\rangle_E$	a_{E-}/a_{E+}	$\langle k \rangle$ (MFA)	
Py ₂ -PNIPAM(14K)	24	24	25	26	24	27	25	25.0 ± 1.2
Py ₂ -PNIPAM(25K)	28	29	28	30	28	30	29	28.9 ± 0.9
Py ₂ -PNIPAM(45K)	28	29	29	31	29	31	N/A	29.5 ± 1.2





Conclusions

- The T_c of Py_2 -PNIPAM increases with molecular weight, and can be determined using light scattering, steady-state and time-resolved fluorescence.
- MFA results show that $\langle k \rangle$ and the molar fractions of pyrene species show changes at T_c and T_m that are consistent with the model proposed by F.M. Winnik et al., however the mesoglobules are not vitreous above T_m .

26

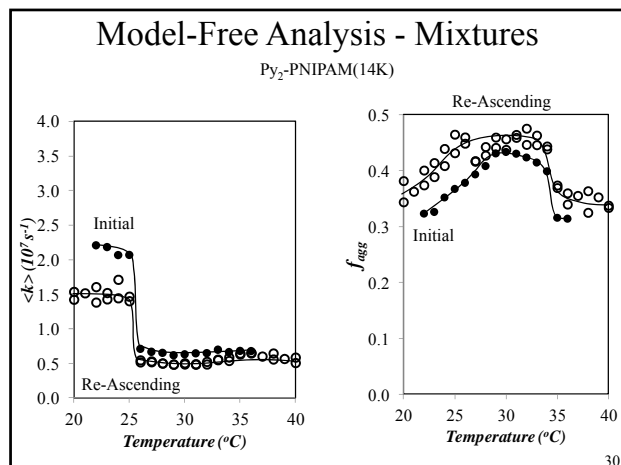
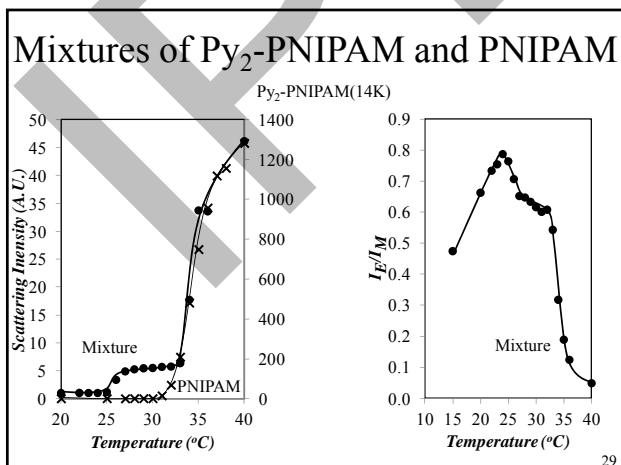
Acknowledgements

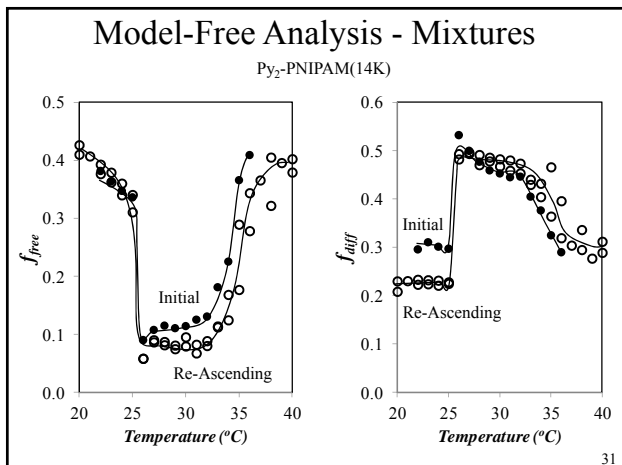
- Dr. J. Duhamel
- Françoise Winnik, Xing Ping Qiu
- Colleagues from the Duhamel and Gauthier labs, both current and former
- *Add NSERC logo*

27

Questions?

28





IPRR 2014

Institute for Polymer Research

Celebrating 30 years of Official Institute Status

Symposium documents for

Niousha Kazemi

Do binary monomer reactivity ratios apply to terpolymerizations as well?

Niousha Kazemi, Thomas A. Duever, and Alexander Penlidis

Terpolymerization systems (as representative of multicomponent polymerization systems that are largely unstudied) are undoubtedly of great importance in both academia and industry. There is always a need for understanding the underlying kinetics of such complex reaction systems and obtaining highly accurate values of rate parameters that govern these reactions and in turn determine the polymer composition and other physico-chemical properties.

Reactivity ratios in terpolymerization polymerization systems are critical parameters for describing characteristics of the systems, such as chain microstructure. Despite the importance of these terpolymerization reactivity ratios, not a lot of research has been conducted to estimate and study these parameters in terpolymerization modeling. This is mainly related to the fact that, based on an analogy between copolymerization and terpolymerization mechanisms, reactivity ratios obtained for binary pairs from copolymerization experiments have commonly (albeit misleadingly) been used in models dealing with terpolymerizations.

From even a quick screening of the literature regarding binary reactivity ratios, it can be realized that there are many ambiguities and inconsistencies around these reactivity ratios, even for the same copolymerization system. The inaccuracies in these reactivity ratios can simply propagate into the terpolymerization composition model, thus becoming a serious source of error in parameter estimation and prediction variance. Using binary reactivity ratios in terpolymerization studies also treats the ternary system as separate and unrelated to the binary pairs. In other words, interactions between the three monomers are effectively ignored. Therefore, the past approach is an unjustified simplification that could have been acceptable at a time when computation power was very limited, but not nowadays.

What is the correct approach for estimating reactivity ratios? The problem of reactivity ratio estimation, among several other nonlinear parameter estimation problems, where all variables (both dependent and independent) contain error, is encountered frequently in science and engineering, including process engineering studies, medical applications, polymerization reactors, thermodynamic models, and so on. For such cases, results from basic nonlinear regression, where only dependent variables contain considerable amounts of error, would yield imprecise and biased parameter estimates. A relatively recent approach is the error-in-variables-model (EVM) that is probably the most complete approach for situations where the dependent and independent variables do not need to be distinguished. This feature makes EVM the perfect method for estimating reactivity ratios in multicomponent polymerizations.

Examining the literature shows that for terpolymerization studies very little work has been done for the estimation of reactivity ratios directly from terpolymerization experimental data sets. In addition,

designing terpolymerization experiments for such a purpose (i.e., optimal selection of the location of the data points along the experimental operating region) has not been studied at all. Our intention is to evaluate how significantly the quality of reactivity ratio estimates can be improved if terpolymerization data are used directly. To do so, we wanted first to successfully estimate reactivity ratios from existing ternary experimental data in the literature; and subsequently, to compare these ternary-based reactivity ratios with binary ones that were reported in the literature. This approach has been applied for several ternary systems such as acrylonitrile/styrene/methyl methacrylate, ethylene/vinyl acetate/ methyl acrylate, indene/methyl methacrylate/acrylonitrile, acrylonitrile/styrene/maleic anhydride, etc. The observations from these analyses point to the following very important remarks:

- ✓ Our methodology does not use approximate binary reactivity ratios when ternary data are directly available.
- ✓ The methodology is not restricted to any simplifying assumptions regarding the error structure.
- ✓ The approach can apply to any terpolymer data set at any conversion level.
- ✓ Ternary reactivity ratios differ from binary ones; differences ranging from slight to considerable have been observed, depending on the values of the reactivity ratios.
- ✓ The basic premise of our investigations is that use of binary reactivity ratios may reduce the reliability of terpolymerization model predictions.
- ✓ Overall, the methodology provides reliable reactivity ratios.

How important is it to avoid using binary reactivity ratios in terpolymerization kinetic studies?

Since the binary reactivity ratios from copolymerization systems (commonly used in place of ternary reactivity ratios) are not determined based on terpolymerization experimental data, they can only be considered as an approximation to the real ternary reactivity ratios. In addition, the database of binary reactivity ratios in the literature is very inconsistent, suffering over many years from the implementation of several incorrect reactivity ratio estimation techniques. Therefore, if such binary values are to be used in a ternary system study, the question becomes: which values should be used in the terpolymerization study, amongst several incorrect (and widely differing) reactivity ratios for the same copolymerization system?!

Along with these issues, we now outline three other important risks/problems in using binary reactivity ratios in terpolymerization kinetic studies.

(1) Prediction performance of the terpolymerization composition equation: One of the main reasons for determining terpolymerization reactivity ratios is to be able to use the terpolymerization composition equation to predict the terpolymer composition. In the case of using approximate binary

reactivity ratios, their inaccuracies propagate in the ternary composition model, and this results in serious deviations between predictions of terpolymerization composition and experimental data. There are several examples of this malpractice in the literature, which have led researchers to question the credibility of the terpolymerization composition model instead of suspecting the values of the parameters used in the model!

On the contrary, by estimating ternary reactivity ratios and accounting properly for the presence of the third monomer, the reactivity ratios reflect the real nature of the activities of all three monomer, which in turn improves the prediction performance of the ternary composition model as well. An example of this point is for the investigation of the terpolymerization system of acrylonitrile (AN, M_1), styrene (Sty, M_2), and maleic anhydride (MA, M_3). This system was investigated by Kressler et al. (1987), where the corresponding binary reactivity ratios were obtained from the literature. Figure 1a shows the triangular composition plot for the experimental terpolymerization data and the predicted ones using the binary reactivity ratios. In our work, we estimated the ternary reactivity ratios directly from the experimental data and then used those values to predict the terpolymerization compositions. Figure 1b shows the experimental terpolymer compositions along with our predicted terpolymer compositions.

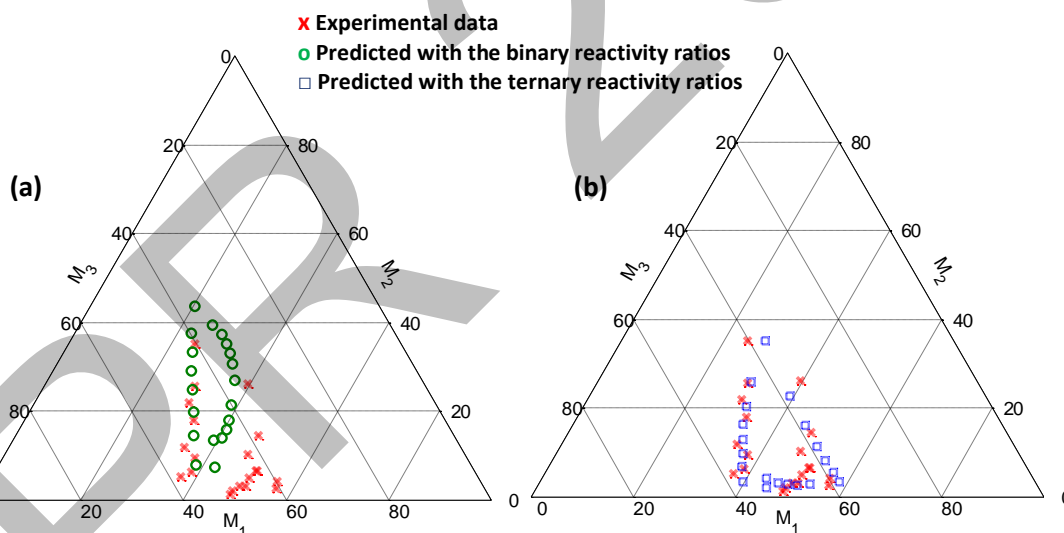


Figure 1. Experimental and predicted terpolymerization compositions for AN (M_1)/ Sty (M_2)/ MA (M_3) system

By comparing Figures 1a and 1b, it can be clearly seen that there is a large difference, and hence, unacceptable disagreement, between experimental data and calculated compositions based on binary reactivity ratios. To the contrary, the predicted composition values with the ternary reactivity ratios lie closely to the experimental points! Such results can be associated to, firstly, including the third monomer and the subsequent changes in the reaction medium in the estimation process compared to binary studies and, secondly, to the methodology that was used to obtain these estimated reactivity ratios. This influence

appears in the values of ternary and binary reactivity ratios, but more importantly it is noticeable through the change in the predicted composition values.

(2) Studying important characteristics of a terpolymerization system: Reactivity ratios in a ternary system not only describe the tendency of incorporation of monomers with respect to each other, but also they can be utilized to assess important characteristics of the ternary system. One of the important characteristics of a ternary system is whether the system has an azeotrope or not. Based on the definition of the azeotropic point, a polymer composition that remains constant throughout the polymerization and equal to the feed composition (thus resulting in a homogenous polymer product), it is of interest to identify such a composition with almost no compositional drift, at which there is a high probability of obtaining homogenous polymer product. The value of an azeotropic composition is calculated based on the values of the reactivity ratios of the system. Determining the ternary azeotropic composition seems to be controversial in the literature simply due to the fact that many terpolymerization systems exhibit the azeotropic behavior for certain compositions, however, using the binary reactivity ratios for the corresponding binary pairs does not result in an azeotropic point.

In our work, we looked at the problem of the azeotrope composition in ternary systems and found that, if the system has an azeotrope, using six “ternary” reactivity ratios can confirm that composition in all cases. Such observation is due to fact that the values of the reactivity ratios from binary pairs to a ternary system do change, and these values can subsequently affect the location (or even the existence) of the azeotropic point in a terpolymerization system. Thus, studying characteristics such as azeotropic compositions that are directly linked to the values of reactivity ratios highlights the importance of not using approximate binary reactivity ratios instead of accurate and direct ternary ones. More results on this will be shown at the time of the IPR conference.

(3) Experimental workload: An undeniable fact is that the success of the overall reactivity ratio estimation analysis (or any other parameter estimation analysis for that matter) strongly depends on the diligent work of the practitioner in gathering experimental data that are reliable and informative. Despite the unfortunate fact that this approach is usually translated in gathering experimental data from several different (randomly chosen) points, covering the whole range of experimentation, the correct approach is to implement design of experiments techniques and collect only necessary experimental data at optimal points. When it comes to estimating binary reactivity ratios for three pairs involved in a terpolymerization, the experimental work can be very extensive (assuming one does not want to dive into the questionable and inconsistent pool of reactivity ratios in the literature). It involves investigating three different binary systems and at least performing two experiments for each pair (at least six different experiments).

On the contrary, this extensive experimental workload can significantly be reduced by employing the correct approach for acquiring terpolymerization experimental data and using the data directly to estimate reactivity ratios. Figure 2 shows a triangular plot for a ternary system. Based on our optimal design of experiments, we can come up with a rule of thumb for the regions where the optimal experiments are located. These areas are located around the three peaks of the triangle (shaded areas in Figure 2), meaning that the three optimal experiments (three feeds) consider each monomer at a high concentration level, which makes physical sense! To obtain reliable reactivity ratios, one needs to perform only “three” experiments, which is 50% less experimental workload, compared to the procedure of finding the binary reactivity ratio pairs. Therefore our approach not only minimizes the workload, but also maximizes the reliability of the ternary reactivity ratios.

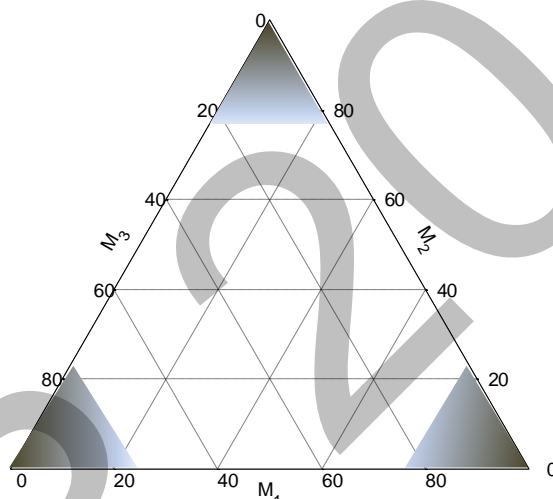


Figure 2. Terpolymerization composition triangle with optimal feed compositions as shaded areas

General Bibliography:

1. Kazemi, Niousha, Thomas A. Duever, and Alexander Penlidis. "Demystifying the estimation of reactivity ratios for terpolymerization systems." *AIChE Journal* (2014).
2. Kazemi, Niousha, Thomas A. Duever, and Alexander Penlidis. "A powerful estimation scheme with the error-in-variables-model for nonlinear cases: Reactivity ratio estimation examples." *Computers & Chemical Engineering* 48 (2013): 200-208.
3. Kazemi, Niousha, Thomas A. Duever, and Alexander Penlidis. "Design of Experiments for Reactivity Ratio Estimation in Multicomponent Polymerizations Using the Error-In-Variables Approach." *Macromolecular Theory and Simulations* 22.5 (2013): 261-272.
4. Kazemi, Niousha, Thomas A. Duever, and Alexander Penlidis. "Investigations on Azeotropy in Multicomponent Polymerizations." *Chemical Engineering & Technology* 33.11 (2010): 1841-1849.
5. Kressler J, Bieger W, Horvath B, Schmidt-Naake G. "Experimental investigation of ternary azeotropy in the copolymerization of acrylonitrile, styrene, and maleic anhydride". *Journal of Macromolecular Science, Part A*. (1987): 681–687.

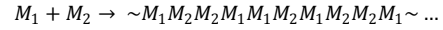
Reactivity Ratios in Terpolymerization Systems

Do binary monomer reactivity ratios apply to terpolymerizations as well?

Niousha Kazemi, Thomas A. Duever, and Alexander Penlidis
Institute for Polymer Research (IPR), Department of Chemical Engineering,
University of Waterloo, Waterloo, Canada

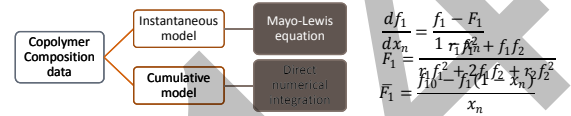
Modeling for Copolymerizations

In a typical binary copolymerization reaction...



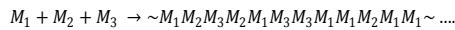
Reactivity ratios: tendency of incorporation of monomer 1 over monomer 2

$$r_1 = \frac{k_{11}}{k_{12}} \quad r_2 = \frac{k_{22}}{k_{21}}$$



Modeling for Terpolymerizations

In a typical terpolymerization reaction...



Reactivity ratios

$$r_{12} = \frac{k_{11}}{k_{12}} \quad r_{13} = \frac{k_{11}}{k_{13}} \quad r_{23} = \frac{k_{22}}{k_{23}}$$

$$r_{21} = \frac{k_{22}}{k_{21}} \quad r_{31} = \frac{k_{33}}{k_{31}} \quad r_{32} = \frac{k_{33}}{k_{32}}$$

Instantaneous terpolymerization composition equations
(Alfrey-Goldfinger (AG) model)

$$F_1 : F_2 : F_3 = f_1 \left\{ \frac{f_1}{r_{31}r_{21}} + \frac{f_2}{r_{21}r_{32}} + \frac{f_3}{r_{31}r_{23}} \right\} \left\{ f_1 + \frac{f_2}{r_{12}} + \frac{f_3}{r_{13}} \right\} :$$

$$f_2 \left\{ \frac{f_1}{r_{12}r_{31}} + \frac{f_2}{r_{12}r_{32}} + \frac{f_3}{r_{32}r_{13}} \right\} \left\{ f_2 + \frac{f_1}{r_{21}} + \frac{f_3}{r_{23}} \right\} :$$

$$f_3 \left\{ \frac{f_1}{r_{13}r_{21}} + \frac{f_2}{r_{23}r_{12}} + \frac{f_3}{r_{13}r_{23}} \right\} \left\{ f_3 + \frac{f_1}{r_{31}} + \frac{f_2}{r_{32}} \right\} :$$

Common Practice

Analogy between
copolymerization and
terpolymerization mechanisms

- Reactivity ratios obtained for binary pairs used in terpolymerizations
- Conflicting reactivity ratio values for copolymerization systems in the literature: a lasting issue!
- The presence of the third monomer is essentially ignored

- Inaccuracies** in binary reactivity ratios **propagate** through a more complex model
- Very little work** (and rather outdated) for ternary reactivity ratio estimation
- AG model problems:**
 - Using ratios as responses
 - Different combinations assign more weight to certain responses

Objectives

Determining **ternary reactivity ratios** directly from **terpolymerization experimental data**

The model	Parameter estimation	Design of experiments
<ul style="list-style-type: none"> Modifying the terpolymerization composition model Eliminate difficulties of working with AG model 	<ul style="list-style-type: none"> The Error-in-Variables-Model (EVM) technique Appropriate statistical approach for this problem 	<ul style="list-style-type: none"> Adequate information content Necessity of experimental design

Error-in-Variables-Model (EVM)

EVM consists of two statements:

Equating the vector of measurements (\underline{x}_i) to the vector of true values

$$\underline{x}_i = \underline{\xi}_i^* (1 + \epsilon_i)$$

The true values of the parameters (θ^*) and variables ($\underline{\xi}_i^*$)

are related via the model

$$g(\underline{\xi}_i^*, \theta^*) = 0$$

EVM objective function

$$\phi = \frac{1}{2} \sum_{i=1}^n r_i (\underline{x}_i - \underline{\xi}_i^*)' V^{-1} (\underline{x}_i - \underline{\xi}_i^*)$$

EVM is the perfect method for estimating reactivity ratios

Design of Experiments

- Minimize uncertainty in the estimated parameters
- Tidwell – Mortimer (1967) design criterion $f_{21} \cong \frac{r_1}{2+r_1}$ $f_{22} \cong \frac{2}{2+r_2}$
 - Min (|variance-covariance matrix|) or Max (|information matrix|)
 - Conflict with assumptions of Tidwell-Mortimer design criterion

- EVM design criterion**
$$\text{Max}_{\xi} \left[\sum_{i=1}^n Z_i (B_i V B_i)^{-1} Z_i \right]$$
 subject to $\begin{cases} g(\xi_i, \hat{\theta}) = 0 \\ L \leq \xi_i \leq U \end{cases}$

$$B_i = \left[\frac{\partial g(\xi_i, \hat{\theta})}{\partial \xi_i} \right] \quad Z_i = \left[\frac{\partial g(\xi_i, \hat{\theta})}{\partial \theta} \right]$$
 - Extends the idea from D-optimal design criterion
 - There is no attempt for designing ternary experiments!

The Recast Terpolymerization Composition Model

$$F_1 = \frac{f_1 \left(\frac{f_1}{r_{21}r_{31}} + \frac{f_2}{r_{21}r_{32}} + \frac{f_3}{r_{21}r_{33}} \right) \left(f_1 + \frac{f_2}{r_{12}} + \frac{f_3}{r_{13}} \right)}{f_1 \left(\frac{f_1}{r_{21}r_{31}} + \frac{f_2}{r_{21}r_{32}} + \frac{f_3}{r_{21}r_{33}} \right) \left(f_1 + \frac{f_2}{r_{12}} + \frac{f_3}{r_{13}} \right) + f_2 \left(\frac{f_2}{r_{12}r_{31}} + \frac{f_3}{r_{12}r_{32}} \right) \left(f_2 + \frac{f_1}{r_{21}} + \frac{f_3}{r_{23}} \right) + f_3 \left(\frac{f_3}{r_{13}r_{21}} + \frac{f_2}{r_{13}r_{22}} \right) \left(f_3 + \frac{f_1}{r_{31}} + \frac{f_2}{r_{32}} \right)}$$

$$F_2 = \frac{f_2 \left(\frac{f_1}{r_{12}r_{31}} + \frac{f_2}{r_{12}r_{32}} + \frac{f_3}{r_{12}r_{33}} \right) \left(f_2 + \frac{f_1}{r_{21}} + \frac{f_3}{r_{23}} \right)}{f_1 \left(\frac{f_1}{r_{21}r_{31}} + \frac{f_2}{r_{21}r_{32}} + \frac{f_3}{r_{21}r_{33}} \right) \left(f_1 + \frac{f_2}{r_{12}} + \frac{f_3}{r_{13}} \right) + f_2 \left(\frac{f_2}{r_{12}r_{31}} + \frac{f_3}{r_{12}r_{32}} \right) \left(f_2 + \frac{f_1}{r_{21}} + \frac{f_3}{r_{23}} \right) + f_3 \left(\frac{f_3}{r_{13}r_{21}} + \frac{f_2}{r_{13}r_{22}} \right) \left(f_3 + \frac{f_1}{r_{31}} + \frac{f_2}{r_{32}} \right)}$$

$$F_3 = \frac{f_3 \left(\frac{f_1}{r_{13}r_{21}} + \frac{f_2}{r_{13}r_{22}} + \frac{f_3}{r_{13}r_{23}} \right) \left(f_3 + \frac{f_1}{r_{31}} + \frac{f_2}{r_{32}} \right)}{f_1 \left(\frac{f_1}{r_{21}r_{31}} + \frac{f_2}{r_{21}r_{32}} + \frac{f_3}{r_{21}r_{33}} \right) \left(f_1 + \frac{f_2}{r_{12}} + \frac{f_3}{r_{13}} \right) + f_2 \left(\frac{f_2}{r_{12}r_{31}} + \frac{f_3}{r_{12}r_{32}} \right) \left(f_2 + \frac{f_1}{r_{21}} + \frac{f_3}{r_{23}} \right) + f_3 \left(\frac{f_3}{r_{13}r_{21}} + \frac{f_2}{r_{13}r_{22}} \right) \left(f_3 + \frac{f_1}{r_{31}} + \frac{f_2}{r_{32}} \right)}$$

- Symmetry in model (vs. the original AG model!)
- Using individual mole fractions instead of ratios
- Any two equations with two constraints

$$\begin{cases} F_1 + F_2 + F_3 = 1 \\ f_1 + f_2 + f_3 = 1 \end{cases}$$

Estimating Ternary Reactivity Ratios

Gather required initial information

&

Estimate reactivity ratios

⇓

Evaluate reliability of results

- Determine:
 - Find initial guesses for reactivity ratios
 - Variance-covariance matrix (V matrix)
- Use the EVM algorithm
 - Ternary experimental data at any conversion level
- Use global optimization technique

Estimating Ternary Reactivity Ratios

Gather required initial information

&

Estimate reactivity ratios

⇓

Evaluate reliability of results

- Evaluate precision of results:
 - Joint confidence regions (JCR) for reactivity ratio pairs

$$\begin{matrix} (r_{12}, r_{21}) \\ (r_{13}, r_{31}) \\ (r_{23}, r_{32}) \end{matrix}$$
 - Compare predicted versus experimental data
 - Validate reactivity ratio estimates
 - e.g., check the existence of an azeotropic feed composition

Results and Discussion Parameter Estimates

M_1 : DMAEM, M_2 : MMA, M_3 : DDMA

- Representative results
- Reactivity ratios are within reasonable joint confidence regions
- 'Acceptable' agreement between ternary and binary reactivity ratios

Data set from Soljic et al (2010)

Results and Discussion Composition Prediction

Terpolymerization of ethyl methacrylate (EMA, M_1) / n-phenylmaleimide (NPMI, M_2) / itaconic acid (EA, M_3)

	r_{12}	r_{21}	r_{13}	r_{31}	r_{23}	r_{32}
Binary reactivity ratios	0.375	0.104	2.331	0.801	0.103	1.156
Ternary reactivity ratios	0.326	0.433	3.477	0.212	0.078	1.828

- Experimental data (black dots)
- Binary predicted compositions (red dots)
- Ternary predicted compositions (green dots)

Data set from Naguib et al (2003)

13

Results and Discussion Azeotropic Composition

Terpolymerization of acrylonitrile (AN, M_1) / styrene (Sty, M_2) / 2,3-dibromopropyl acrylate (DBPA, M_3)

	r_{12}	r_{21}	r_{13}	r_{31}	r_{23}	r_{32}
Binary reactivity ratios	0.100	0.440	0.900	0.860	0.430	0.140
Ternary reactivity ratios	0.077	0.419	0.390	0.460	0.411	0.191

- Using binary reactivity ratios: **No Azeotrope.**
- An azeotropic point is found, but **ONLY** after using reactivity ratio estimates based directly on terpolymerization data .
- System studied in literature and shown to exhibit azeotrope!

Data set from Saric et al (1983)

14

Results and Discussion Optimal Experiments

Optimal design of experiments maximizes the information content of the experimental data

- ✓ Only 3 optimal experiments!
- ✓ Ideal terpolymerization system

$$r_{ij} = 1 \text{ for } i, j = 1, 2, 3$$

- ✓ General trend for the optimal feed compositions

Very useful rule of thumb

15

Results and Discussion Optimal Experiments

- **High information content:** 3 experiments
- **Low information content:** 7 experiments

Estimates from experiments with high information

Higher precision from a smaller data set

Data set from Soljic et al (2010)

16

Concluding Remarks

- Very generalized EVM parameter estimation methodology for determining ternary reactivity ratios
 - Based on **direct terpolymerization data**
 - **Consistent and reliable ternary reactivity ratios**
 - **No need to use binary reactivity ratios**
- Practical yet optimal design of experiments for terpolymerizations
 - **Only 3 optimal experiments**
 - **Optimal points are close to the corners of the ternary (triangle) composition plot**
- Should we use binary reactivity ratios for terpolymerization studies?
 - **No reason!**
 - **Inconsistent literature values!**
 - **Extensive (but unnecessary) experimentation for separate binary systems**
 - **No guarantee that binary reactivity ratios even apply...**

17

Institute for Polymer Research

Celebrating 30 years of Official Institute Status

Symposium documents for

Mylène Le Borgne

Solution-processable oligomer semiconductors for organic solar cells

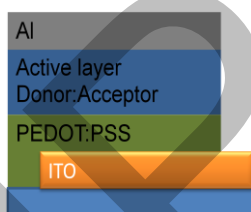
Mylène Le Borgne^{1,2,3}, Yuning Li¹, Bertrand Pavageau² and Guillaume Wantz³

¹University of Waterloo, ² Solvay (Bordeaux), ³Guillaume Wantz

Renewable Energy is a crucial challenge of this century. Converting the endless solar energy in electricity is one of the most promising solutions. In photovoltaic field, three devices generations are counted. The first one is inorganic solar cells based on multicrystalline Silicon or Germanium. This technology is the most popular as it is dominating the market. Its efficiency is around 22%. Their main drawback is the fabrication cost. The silicon needs to be heated at very high temperature that induces important energy consumption.^{1,2}

The Second generation is thin film solar cell. This category includes devices made of amorphous silicon, Cadmium telluride (CdTe), and copper indium gallium diselenide. Their efficiency is between 12-20%.²

The third generation is organic solar cells. It is the purpose of this research. Those devices allow flexibility and low cost fabrication compare to their counterparts. They can be deposited on any substrates, curved or planar. Thanks to this, the photovoltaic can cover much more surfaces. There are not at the commercialization stage yet but they will certainly revolutionize the photovoltaic field. Lots of techniques for large area have been developed like solution printing.³⁻⁵



Those devices are composed of organic donor / acceptor materials sandwiched between two electrodes. (Figure 1). This mixture is responsible of the solar energy conversion.

Figure 1

Much research focuses on the development of the π -conjugated donor materials. Those material structures have an impact on every step of the solar cells operating: light harvesting, charge separation, charge transport and charge collection. It is crucial to study and understand the structure effect on the properties to be able to design new materials.³⁻⁵

Experimental:

Donor materials can be polymers or small molecules. Polymers usually show better performance with efficiency around 8-10%, thanks to their great film forming and high hole transport. Nevertheless, during their synthesis, the structure is hard to control and induced important batch-to-batch variations that are inevitable.^{1,3}

For small molecules, the structure is well-defined. Relationship between structure and properties are possible. Besides, synthesis and purification are simpler. The efficiency is lower, around 8%.^{4,5} The film forming and the charge transport are more challenging. The compromise may be oligomers like dimers and trimers. The structure could be controlled and two-three motifs enough to get a nice film.

The required properties for a donor material is a large adsorption spectrum, a high hole mobility and appropriate energy levels. Diketopyrrolopyrrole (DPP) derivatives are well known for their interesting optical properties and favoured low band gap materials for organic solar cells. The energy levels can be tuned by changing the aryl surrounding the DPP.³⁻⁵ Also, another key parameter is the solubility as the deposition is solution process. It can be defined by alkyl chain on top of DPP. On top of that, purity is significant point too.⁶ An impurity can act as recombination centre which lowering the efficiency. Different synthetic pathways have been adopted to obtain products in high purity.

Cause of confidentiality, the structure will not be not completely shown.

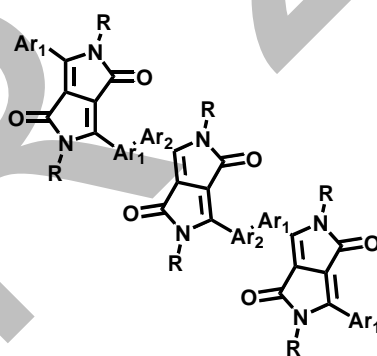
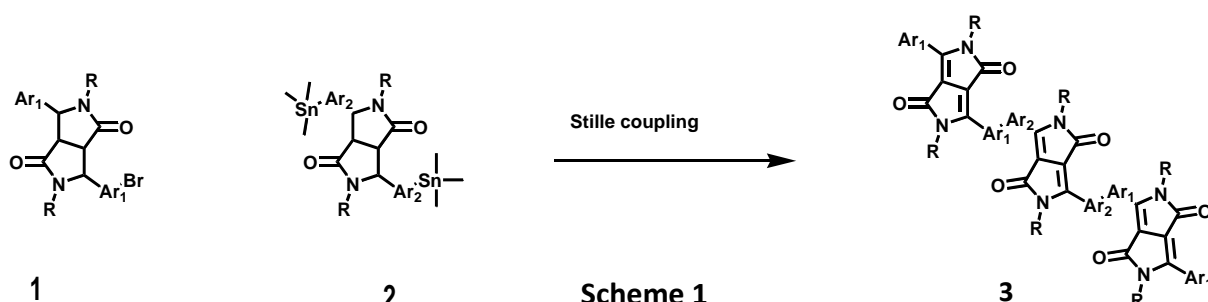
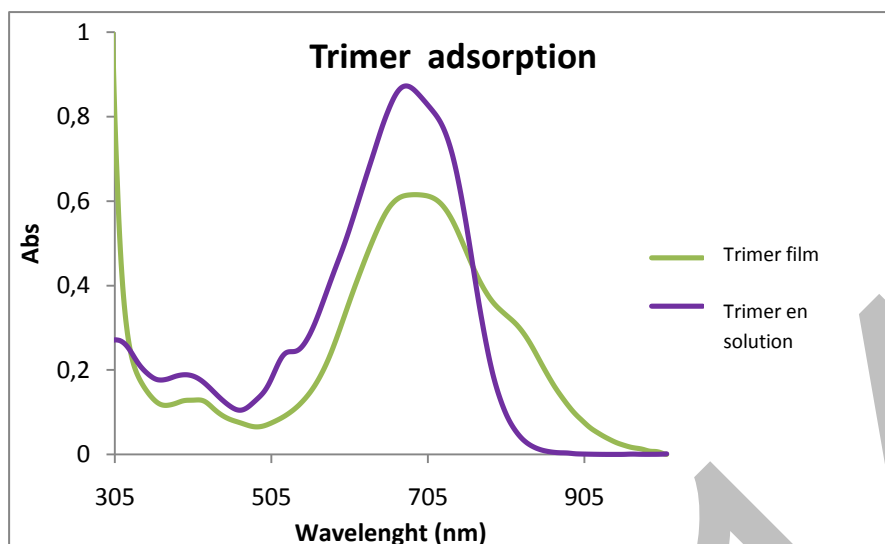


Figure 2

Results:

A first trimer was synthesized by Stille coupling. Two equivalent of mono bromo aryl DPP was coupling to one equivalent of ditrimethyltin DPP. (Scheme 1)

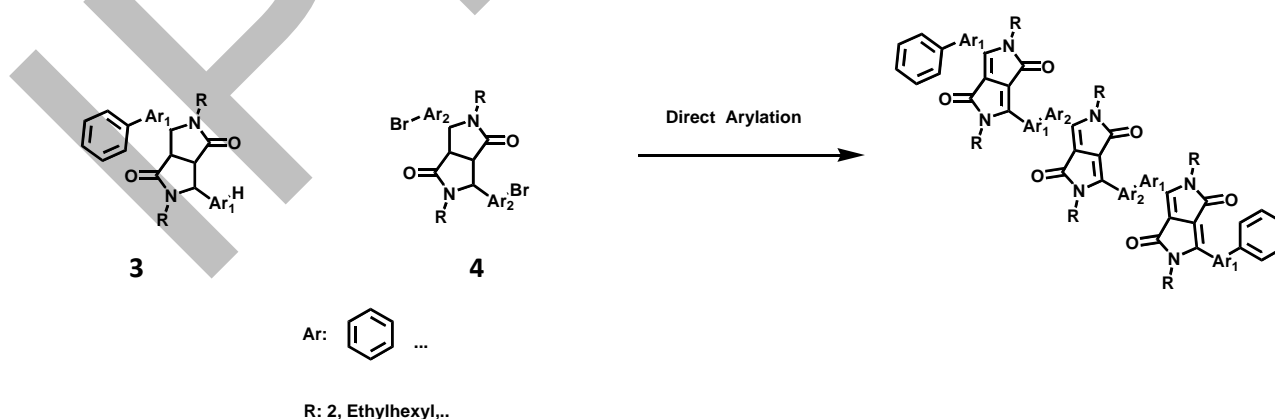




This molecule shows interesting absorption with an optical band gap of 1.33 eV. By cyclic voltammetry, HOMO level was calculated to be -5.51 eV. With both information, LUMO can be deduced and is -4.19 eV. The LUMO is too low, electron transfer between donor and acceptor may not be possible. Some devices have been made but their efficiency doesn't go over 0.3 % efficiency.

The second explanation of the low efficiency is the presence of impurities. During the reaction, co-products was obtained. Two dimers was formed by the molecule 1 - 2 coupling and the second by the 1-1 coupling. By silica gel column, only the product from the 1-2 coupling has been removed. 1-1 dimer has too similar polarity and solubility with the wanted trimer. After crystallisation in various solvents, the undesired compound is still remaining. On proton NMR spectrum, the peak of trimer and dimer overlap, so it is hard to distinguish the dimer. Only mass spectrum can identify the presence of both structure. This is not a quantitative measurement. The portion can't be determine by this technics.

Direct arylation (Scheme 2) is another synthesis pathways. In that case, only one dimer can formed: 3-4 dimer.



Scheme 2

This dimer has been removed on silica gel column. Only issue, trimer isomer can formed. By proton NMR, the trimer seems isolated. Further analysis need to be done to know if direct arylation provide isolated material.

Two synthesis pathways have been study to get an isolated oligomer. Direct arylation is an easiest and simplest way to produce the trimer.

Reference

¹ Omar. A. Abdulrazzaq, Viney Saini, Shawn Bourdo, Enkeleda Dervishi, and Alexandrus. Biris, *Particulate Science and Technology* , Vol 31, No. 5 2013, 427

² Robert W. Miles*, Guillaume Zoppi, and Ian Forbes, *Materialstoday*, Vol 10, 2007, 1120

³ D. Chandran and K.-S. Lee, *Macromol. Res.*, Vol 21, No. 3, 2013, 273

⁴ J.W. Lee et al., *Organic Electronics*, Vol 13, 2012, 3060

⁵ Jianhua Liu , Yanming Sun , Preecha Moonsin , Martijn Kuik , Christopher M. Proctor , Jason Lin , Ben B. Hsu , Vinich Promarak , Alan J. Heeger , and Thuc-Quyen Nguyen, *Advanced Materials*, Vol 25, No. 41, 2013, 5898

⁶ Wei Lin Leong, Gregory C. Welch, Loren G. Kaake, Christopher J. Takacs, Yanming Sun, Guillermo C. Bazan* and Alan J. Heeger, *Chemical Science*, Vol 3, No. 6, 2012, 2103

SOLUTION-PROCESSABLE OLIGOMERIC SEMICONDUCTORS FOR ORGANIC SOLAR CELLS

IPR Symposium

Mylène Le Borgne

Dr. Li Yuning, Dr. Guillaume Wantz and Bertrand Pavageau



OUTLINE

I) Introduction: Organic solar cells

II) Results and Discussion

- Synthesis and properties of oligomeric DPP

- Synthesis and properties of oligomeric DPP'

III) Summary

21/05/2014 IPR Symposium

2

I) INTRODUCTION: INORGANIC SOLAR CELLS COMPARE TO ORGANIC SOLAR CELLS

Inorganic



- Best PCE around 25%**
- Dominating the market
- Long life time
- Rigid and planar
- High production cost

Organic



- Best PCE around 10.6%*
- Large area process
- Low cost devices
- Flexible
- Short life-time
- Low efficiency

*You J. et al, Nature Communications, 2013, 4, 1446

**Zhao, J. et al, Solar Energy Materials & Solar Cells, 2001, 65, 429-435.

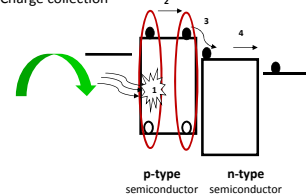
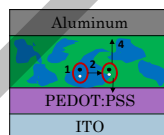
21/05/2014 IPR Symposium

3

I) INTRODUCTION: WORKING PRINCIPLE OF ORGANIC SOLAR CELLS

Photovoltaic processes

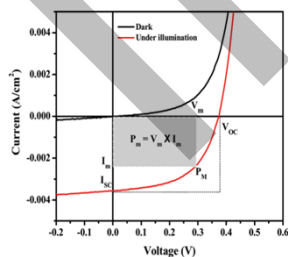
1. Photons absorption and exciton creation
2. Exciton diffusion
3. Charge separation
4. Charge collection



21/05/2014 IPR Symposium

4

I) INTRODUCTION: ORGANIC SOLAR CELLS CHARACTERIZATION



- Short circuit current density (I_{sc})

- Open circuit voltage (V_{oc})

- Fill Factor (FF)

$$FF = \frac{P_{max}}{I_{sc} V_{oc}}$$

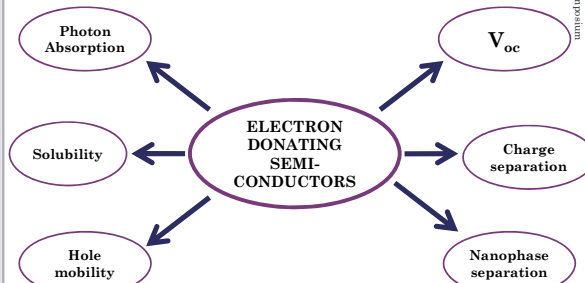
- Power conversion efficiency (PCE or η)

$$\eta = \frac{P_{max}}{P_{in}} = \frac{I_{sc} V_{oc} FF}{P_{in}}$$

21/05/2014 IPR Symposium

5

I) INTRODUCTION: ELECTRON DONATING SEMICONDUCTORS



21/05/2014 Symposium

6

I) INTRODUCTION: POLYMERS VERSU SMALL MOLECULES

Polymers

- Best PCE around 8.5%*
- Mechanically robust
- Good film quality
- Good hole transport
- **Larger batch-to-batch variations**
- **Difficult to purify**

Small molecules

- -Best PCE around 8%**
- Less synthetic steps
- Easy to purify
- Less batch-to-batch variations
- **Poor film quality**
- **Poor mechanical property**

*Cabanetos, C. et Al, *Journal of the American Chemical Society*, 2013, 135,12, 4656-4659

**Zhou J et Al, *Journal of the American Chemical Society*, 2013, 135, 23,8484-8487

21/06/2014 IPR Symposium

7

I) INTRODUCTION: OBJECTIVES

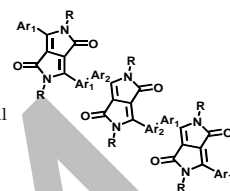
o Oligomers:

- Have defined structures
- Easier to synthesize than polymers
- Better film formation capability than small molecules
- Better mechanically property than small molecules

o Diketopyrrolopyrrole (DPP):

- Electron acceptor group
- Well known dyes
- Easy to synthesize
- Low cost
- PCE up to 5.5%*

*Jianhua Liu et Al, *Adv. Mater.* 2013, 25, 41, 5898-5903

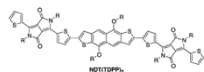


21/06/2014 IPR Symposium

8

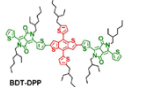
I) INTRODUCTION: DIKETOPIRROLOPYRROLE

- o Stephen Loser. *Et Al, J. Am. Chem. Soc.*, 2011, 133, 8142-8145



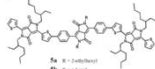
-System perfectly organized with PCBM
 -Interesting hole mobility:
 $\mu_h = 7.18 \cdot 10^{-3} \text{ cm}^2 \text{ V}^{-1} \text{ s}^{-1}$
 PCE = **4.06 %**

- o Jianhua Huang *et Al, ACS Appl. Mater. Interfaces*, 2013, 5, 2033-2039



Positive effect of 8-diiodooctane
 -PCE without additives: 3.59 %
 -PCE with 0.7% of additives: **5.29 %**

- o Jianhua Liu *et Al, Adv. Mater.* 2013, 25, 41, 5898-5903



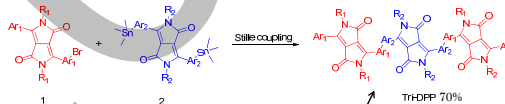
Compared to other DPP-containing molecules, V_{oc} (0.86 V) and FF (60%) have high value

PCE=5.5 %

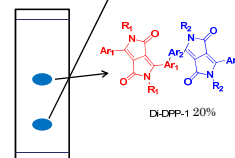
21/06/2014 IPR Symposium

9

II) RESULTS AND DISCUSSION: TRI-DPP: VIA STILLE COUPLING



On TLC or chromatography column, there were two blue spots: first one is Di-DPP-1 (20%) and the second one is 70% (Tri-DPP?)

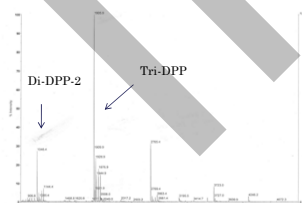


21/06/2014 IPR Symposium

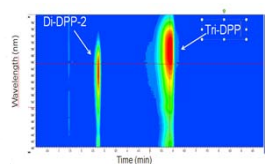
10

II) RESULTS AND DISCUSSION: TRI-DPP: PURITY ANALYSIS

Mass spectrum



Analytical HPLC



11

II) RESULTS AND DISCUSSION: IMPORTANCE OF PURITY

Role of trace impurities in the photovoltaic performance of solution processed small-molecule bulk heterojunction solar cells†

Wei Liu Leong, Gregory C. Welch, Loren G. Kaake, Christopher J. Takacs, Yanning Sun, Guillermo C. Bazan* and Alan J. Heeger*

Received 7th February 2012, Accepted 23rd March 2012
 DOI: 10.1039/c2cc30157g

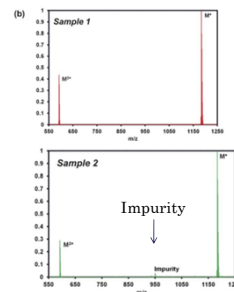
Trace of impurities can:

- act as a **recombination center**
- hole trap site

- Decrease the performances by **50%**

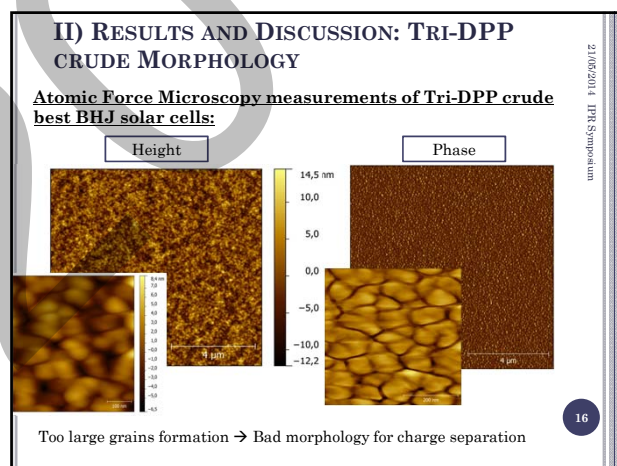
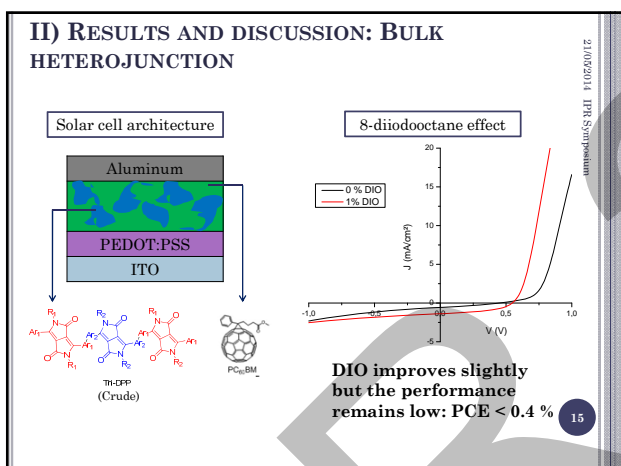
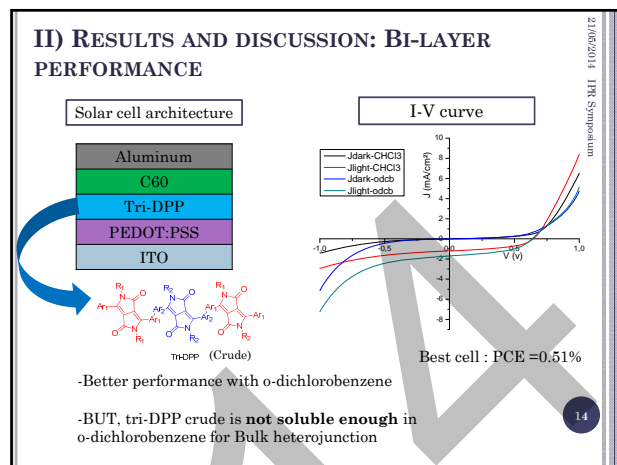
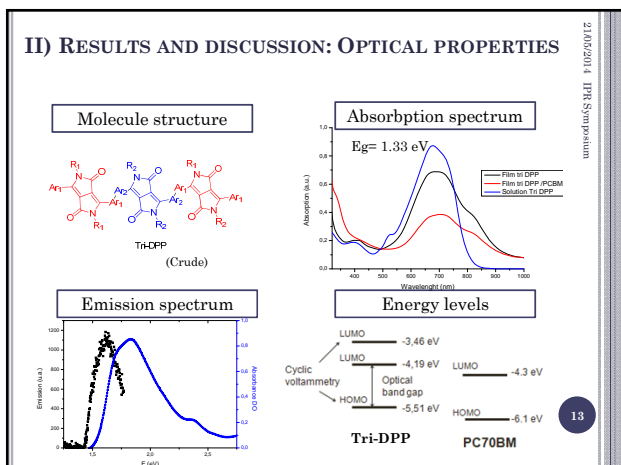


High purity is needed !!



21/06/2014 IPR Symposium

12



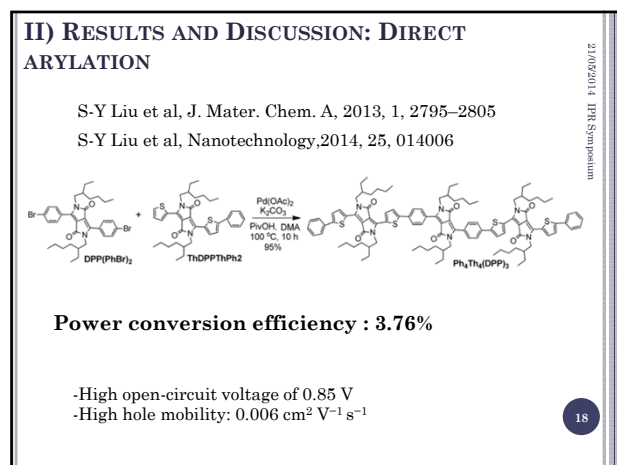
II) RESULTS AND DISCUSSION: SUMMARY ON TRI-DPP

21/02/2014 IPR Symposium

First tri-DPP reveals some challenges:

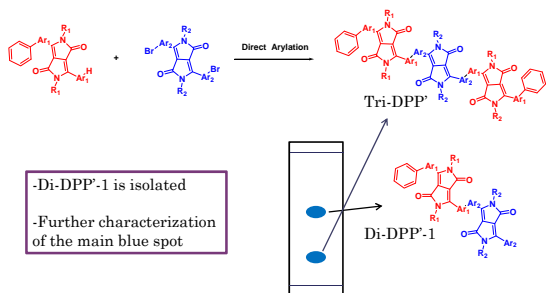
- Presence of by-product impurity
- LUMO level may be too low
- Bad morphology

17



II) RESULTS AND DISCUSSION: TRI-DPP' VIA DIRECT ARYLATION

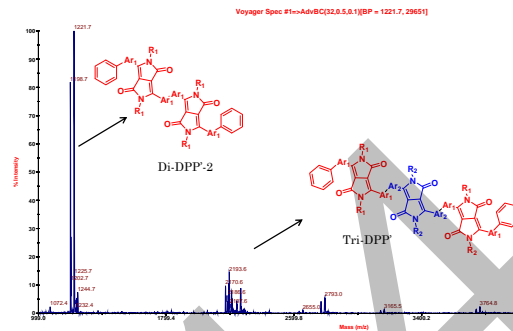
21/06/2014 IPR Symposium



19

II) RESULTS AND DISCUSSION: MASS SPECTRUM

21/06/2014 IPR Symposium



Di-DPP'-2 was mainly formed and only a poor quantity of Tri-DPP' was synthesized.

20

SUMMARY

21/06/2014 IPR Symposium

- o Stille coupling: Tri-DPP is the main product but can't be isolated
- o Direct arylation: Tri-DPP is not the main product
- o Future plan: The core DPP structure will be modified in order to modify the polarity of the tri-DPP and distinguished from the di-DPP

21

THANK YOU FOR YOUR ATTENTION

21/06/2014 IPR Symposium

22

Institute for Polymer Research

Celebrating 30 years of Official Institute Status

Symposium documents for

Lu Li

Characterization of the Internal Structure and Dynamics of Starch Nanoparticles by Fluorescence

L. Li, J. Duhamel, R. C. Amos, M. Gauthier
IPR Symposium, University of Waterloo, ON N2L 3G1, Canada

Introduction

Starch nanoparticles (SNPs) are a biobased material obtained by modifying native starch via reactive extrusion. In this process waxy corn starch, glycerol, and a crosslinking agent are fed into a twin-screw extruder at high temperature.¹ Crosslinks are generated on starch both intra- and intermolecularly, resulting in the formation of SNPs whose structure is depicted in Figure 1.

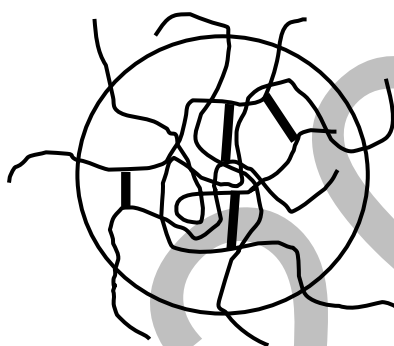


Figure 1. Proposed structure of SNPs. () Starch strands, () crosslinks

The primary application of SNPs has been as binder in the paper industry, where it replaces petroleum-based latex emulsions. These new binders have unique rheological and optical properties making them ideal for paper coating.² In this project, a series of SNPs prepared with increasing amounts of cross-linker were supplied by Ecosynthetix (Burlington, ON). These SNPs are referred to as X0, X0.5, X1, X2, X3, X4, and X5 where the number indicates their nominal crosslinking level.

This report aims to characterize the accessibility of the interior of these SNPs to the solvent. Information about the internal density and size of the SNPs was previously obtained by conducting intrinsic viscosity and dynamic light scattering experiments. These experiments showed that SNPs X2-5 had similar values of intrinsic viscosity and hydrodynamic diameter equal to 22 ± 2 mL/g and 14 ± 2 nm, respectively. SNPs X0, X0.5, and X1 were found to be less dense, with intrinsic viscosities of 57, 43, and 38 mL/g, and larger hydrodynamic diameters of 48, 29, and 23 nm, respectively. The accessibility of the interior of these particles to the solvent was probed by conducting fluorescence quenching measurements as a function of the crosslinking level. These experiments demonstrated that the interior of SNPs has the same accessibility to the solvent as amylopectin, the raw material used in extrusion to form the SNPs. However, hydrophobic modification of the SNPs generates hydrophobic pockets within the SNPs where apolar molecules are effectively shielded from the solvent.

Experimental

The SNPs were purified by dispersion (10% w/w) in DMSO and precipitation into methanol before use. The ^1H NMR spectrum of the purified SNPs showed the typical spectrum of starch and confirmed that the small organic molecules used in the extrusion process had been removed from the samples. The purified SNPs (0.33 g) were placed in 16 mL of Milli-Q water and the mixture was shaken at 250 rpm and 60 °C overnight to create a stable dispersion. The SNP dispersion was then spiked with 30 μL of a 1.48×10^{-4} M pyrene solution in DMSO. The resulting stock solution, with a 2.8×10^{-7} M pyrene concentration, was kept in the dark for one hour to allow the pyrene to diffuse into the SNPs. Half of the stock solution (8 mL) was mixed with 2 mL of a 0.14 M nitromethane aqueous solution to create Solution A, containing 1.6% w/w SNP, 2.2×10^{-7} M pyrene, and 32.7 mM nitromethane. The other half of the stock solution (8 mL) was mixed with Milli-Q water (2 mL) to create Solution B, containing 1.6% w/w SNP and 2.2×10^{-7} M pyrene. Solution B (2.2 mL) was placed in the fluorescence cuvette while Solution A was added to the cuvette in 30 μL increments until the overall nitromethane concentration reached 12 mM.

Amylopectin (Aldrich, 5% w/w) was dissolved in DMSO at 60 °C overnight. The sample was precipitated into methanol before use. Amylopectin solutions were prepared by the same procedures applied to the preparation of the SNP dispersions for the quenching experiments.

Sample X0.5 was hydrophobically modified with hexanoyl side-chains. The degree of substitution used was low (0.15) to ensure that the particles remained water-dispersible. The modified X0.5 SNP sample is referred to as MX0.5. Since MX0.5 was less compatible with water than the unmodified SNPs, the MX0.5 dispersion was prepared with a 0.1% w/w concentration instead of 1.6% w/w as used for the unmodified SNPs. To compare the results obtained with the 0.1% w/w MX0.5 dispersion with those obtained with the unmodified X0.5 SNP, a control fluorescence quenching experiment was conducted using the unmodified X0.5 SNP at the same concentration of 0.1% w/w.

Results

Information about the polarity of the interior of the unmodified SNPs and the modified SNP (mSNP) was obtained by steady-state fluorescence. Pyrene was selected as the chromophore since its emission spectrum is strongly affected by its local environment. As the polarity of the solvent increases, the intensity of the first peak (I_1 at 375 nm) increases with respect to that of the third peak (I_3 at 383 nm), so that the I_1/I_3 ratio increases. The pyrene emission spectra for pyrene in water, in a 1.6% w/w X0 dispersion, and a 0.1% w/w MX0.5 dispersion were normalized at 375 nm and are shown in Figure 2. I_3 increased slightly after the addition of SNPs, but more significantly in the presence of the MX0.5 SNPs. Regardless of the cross-linker content, all the unmodified SNPs showed a similar interior polarity with an I_1/I_3 ratio of 1.65 ± 0.06 , which is less than that of pyrene in water (1.80 ± 0.05). With an I_1/I_3 ratio of 1.35, the polarity of MX0.5 interior was much more hydrophobic, being close to that of methylene chloride.³ Note that 3 mM nitromethane was added to the solution to minimize interference with the measurements due to the fluorescence of pyrene not associated with MX0.5.

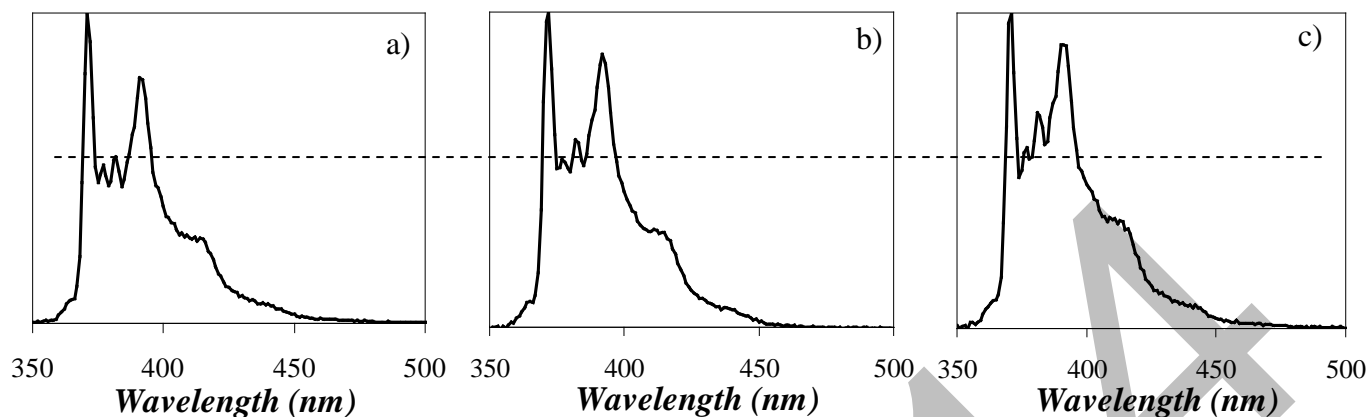


Figure 2 Fluorescence spectra for pyrene in a) water, b) 1.6% w/w X0 dispersion, c) 0.1% w/w MX0.5 dispersion with 3 mM nitromethane

The lifetime of pyrene inside the SNPs and the mSNP was measured by time-resolved fluorescence. In water, the dissolved molecular pyrene had a lifetime of 130 ns. Since the SNPs are less hydrophilic than water, apolar pyrene prefers to associate with the SNPs to reduce its exposure to water. Analysis of the fluorescence decays acquired with the pyrene aqueous solutions containing 1.6% w/w SNPs showed that 40% of the pyrene molecules in the aqueous solution interacted with the SNPs, and that the lifetime of pyrene increased from 130 ns in water to 200 ns in the presence of SNPs. The increase in the pyrene lifetime is due to reduced quenching by oxygen dissolved in water when pyrene associates with the SNPs. The level of protection from quenching by oxygen afforded by the SNPs was further enhanced by the hexanoyl substituents of MX0.5, which generated hydrophobic microdomains that provided a better shield for pyrene. The lifetime of pyrene inside the hydrophobic microdomains present in the MX0.5 dispersion was 300 ns. This long pyrene lifetime suggests that the hydrophobic domains are very viscous.⁴ However only 23% of the pyrene in aqueous solution associated with MX0.5, because the aqueous MX0.5 dispersion could only be prepared at a low (0.1% w/w) concentration before the mSNPs would begin to aggregate and ultimately precipitate out. A control experiment was also carried out with a 0.1% w/w unmodified X0.5. The fraction of pyrene interacting with the unmodified X0.5 SNPs was less than 8%. Consequently, hydrophobic modification increased the pyrene loading capacity 3-fold.

To study the influence of cross-links on the accessibility of the SNP interior to the solvent, fluorescence quenching experiments were conducted. Nitromethane was used as a neutral water-soluble quencher for pyrene. The effect that the addition of nitromethane had on the fluorescence decays of pyrene in water and pyrene in the X0.5 dispersion is shown in Figure 3. Pyrene was found to decay much faster when the SNPs were not present in the solution. In addition, at high quencher concentrations, the fluorescence decays of pyrene in the SNP dispersions showed increased curvature suggesting that different quenching processes occurred simultaneously. The decays were analyzed by fitting them with a sum of exponentials as shown in Equation 1.

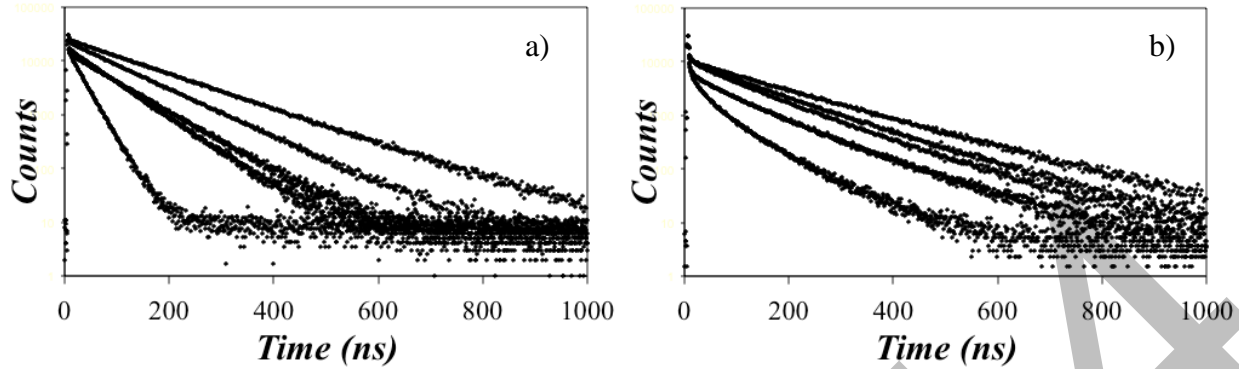


Figure 3. Pyrene quenched by nitromethane in a) water and b) 1.6% w/w X0.5 dispersion. [Nitromethane] = 0, 0.36 mM, 0.68 mM, 1.1 mM and 4.3 mM

$$I(t) = I_0 \times \left(f_w \exp(-t / \tau_{wQ}) + f_{SNPQ} \exp(-t / \tau_{SNPQ}) + f_{SNP} \exp(-t / \tau_{SNP}) + f_{bg} \times BG_{SNP}(t) \right) \quad (1)$$

Equation 1 assumes that pyrene can exist in solution in three different states. The pyrene located in water (Py_w) emits with a decay time τ_{wQ} . Pyrene can also interact with the SNPs. Upon binding to the SNPs, pyrene is either accessible to the solvent (Py_{SNPQ}) and emits with a decay time τ_{SNPQ} , or it is protected from the solvent (Py_{SNP}) and emits with a lifetime $\tau_{SNP} = 200$ ns. The molar fractions of the different pyrene species Py_w , Py_{SNPQ} , and Py_{SNP} are referred to as f_w , f_{SNPQ} , and f_{SNP} , respectively. Both τ_{wQ} and τ_{SNPQ} change with increasing quencher concentration, while τ_{SNP} does not as it represents the species Py_{SNP} that are protected from the solvent. Finally, the short-lived background fluorescence emitted by the SNPs was taken into account by introducing a term $f_{bg} \times BG_{SNP}(t)$ in Equation 1, which was determined separately. The proposed model allows the quantitative study of the behavior of pyrene in different solutions. Analysis of the fluorescence decays with Equation 1 yields the ratio $f_{SNP} / (f_{SNP} + f_{SNPQ})$ whose value is listed in Table 1 for the different starch samples.

Table 1. $f_{SNP} / (f_{SNP} + f_{SNPQ})$ obtained for the SNPs, mSNPs, and amylopectin.

Samples	X0	X0.5	X1	X2	X3	X4	X5	Amylopectin	MX0.5
$f_{SNP} / (f_{SNP} + f_{SNPQ})$	6.3%	2.7%	1.8%	16.1%	2.4%	2.1%	2.2%	24.8%	8.2%

A comparison of Stern-Volmer plots obtained for the quenching of pyrene by nitromethane in water and dispersions of SNPs, MX0.5, and amylopectin is shown in Figure 4. Pyrene dissolved in water is quenched effectively by nitromethane and the quenching rate constant k_q was calculated to be $7 \times 10^{-9} \text{ M}^{-1} \text{ s}^{-1}$. In the presence of SNPs, nitromethane must diffuse into the particles to quench pyrene, which is itself immobilized onto the SNPs. As a consequence, k_q decreases to $2 \times 10^{-9} \text{ M}^{-1} \text{ s}^{-1}$ for pyrene bound to the SNPs. However, quenching of pyrene by nitromethane does not seem to be greatly affected by the amount of cross-linker used to prepare the SNPs. In addition, repeating

these fluorescence quenching experiments with amylopectin yielded the same Stern-Volmer plot as the Snips, since as all data points obtained with the SNPs clustered around a similar master curve. These results imply that the cross-links do not slow down the diffusion of small quencher molecules such as nitromethane. By contrast, the hydrophobic domains of MX0.5 significantly decreased the accessibility of pyrene to nitromethane: The quenching rate constant, k_q for pyrene inside MX0.5 decreased to $0.42 \times 10^{-9} \text{ M}^{-1} \text{ s}^{-1}$.

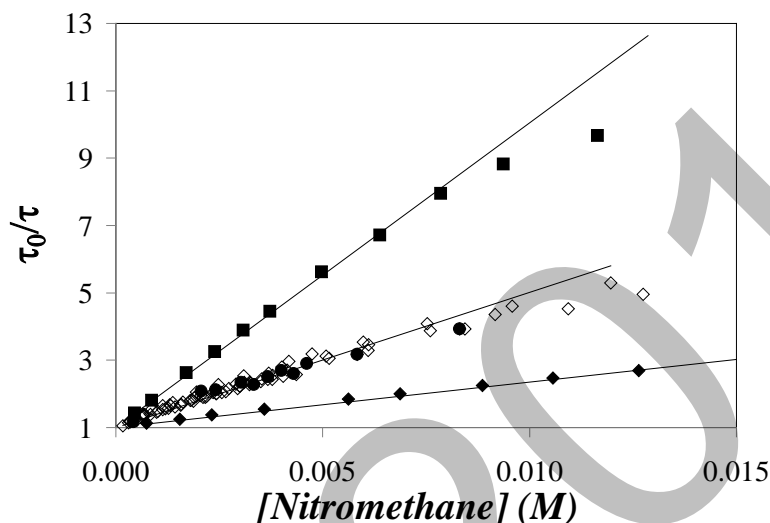


Figure 4. Stern-Volmer plots obtained for pyrene quenched by nitromethane in water (■), and in dispersions of SNPs (◇), amylopectin (●), and MX0.5 (◆)

References

1. Chakraborty, S.; Sahoo, B.; Teraoka, I.; Gross, R. Solution properties of starch nanoparticles in water and DMSP as studied by dynamic light scattering. *Carbohydr. Polym.*, **2005**, *60*, 475-481.
2. Lee, D. I.; Bloembergen, S.; Leeuwen, J. *Development of New Boibased Emulsion Binders*, Presented at PaperCon: Atlanta, 2010.
3. Dong, D. C.; Winnik, M. A. The *Py* Scale of Solvent Polarities. Solvent Effects on the Vibronic Fine Structure of Pyrene Fluorescence and Empirical Correlations with E_T and Y Values. *Photochem. Photobio.* **1982**, *35*, 17-21.
4. Claracq, J.; Santos, S.; Duhamel, J. Rigid Interior of Styrene-Maleic Anhydride Copolymer Aggregates Probed by Fluorescence Spectroscopy. *Langmuir*, **2002**, *18*, 3829-3835.

UNIVERSITY OF Waterloo

ECOSYNTHEIX®
SUSTAINABLE POLYMERS FOR PLANET EARTH™

Characterization of Structure and Dynamics of Starch Nanoparticles by Fluorescence

Name: Lu Li
Ryan Christopher Amos and Mario Gauthier
Supervisor: Prof. Jean Duhamel

IPR
Institute for Polymer Research

Introduction: Organization of the starch granule

High molecular weight and branched polymer – Amylopectin
alpha-1,4-glucan with 1,6-glycosidic linked branches containing 20-30 anhydroglucose units

Linear alpha-1,4-glucan – Amylose
(200 to 2000 anhydroglucose units)

ECOSYNTHEIX® 2

Starch nanoparticles

Native Starch Granules **Starch Nanoparticle Dispersion**

- Corn starch with glycerol as plasticiser and bifunctional crosslinker was fed to an extruder^{1,2}
- Patented reactive extrusion process

Glycerol

1. Steven Bloembergen, Edward VanEgdom, Robert Wikli, Ian J. McLennan, Do Ik Lee, Charles P. Klass, and John van Leeuwen, "Biolatex Binders for Paper and Paperboard Applications", *J. of Pulp and Paper Science*, 36, No 3-4, p. 151-161, 2011
2. Peter van Ballegooye, Phil Greenall, Steven Bloembergen and Ralph DeFong, "EcoSphere® biolatex® binders: Next generation solutions for today's paper coating industry", *World Pulp & Paper*, The International Review for the Pulp and Paper Industry, 2012, 100

ECOSYNTHEIX® 3

Predicted crosslink structure for SNPs

Illustration of one type of intermolecular crosslink structure with -R- representing an intermolecular crosslink (Note that other crosslinked structures exist)

Illustration of the hypothesis that a biobased latex nanoparticle can be thought of as one crosslinked macromolecular unit.

Steven Bloembergen, Ian J. McLennan, John van Leeuwen and Do Ik Lee, "Specialty Biobased Monomers and Emulsion Polymers Derived from Starch", 2010 PTS Advanced Coating Fundamentals Symposium, Munich, Germany, Oct. 11-13, 2010.

ECOSYNTHEIX® 4

Application of starch nanoparticles

Uncoated paper **Coated paper**

The pigmented coating layer reduces the penetration of ink into the paper sheet; the coating binder is the single most important additive that determines paper and print quality.

DS = 0.15

ECOSYNTHEIX® 5

SNPs samples received from Ecosynthetix

o SNPs made by different extrusion methods

Crosslink level increase →

	X0	X0.5	X1	X2	X3	X4	X5
D _v (nm)	47 ± 2	29 ± 1	23 ± 1	17 ± 0.5	15 ± 0.5	12 ± 0.5	12 ± 0.5
[η] (mL/g)	57	43	38	21	20	25	23

Results were obtained in DMSO

o Modified X0.5 (MX0.5) given by Ryan Amos (Mario Gauthier's group)

DS = 0.15

Crosslinker

Hydrophobic domains

ECOSYNTHEIX® 6

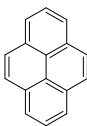
Characterization of interior polarity and dynamics of SNPs using fluorescence techniques

Why Use Pyrene?

Pyrene – an ideal chromophore

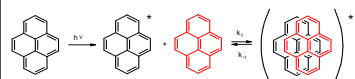
by far the most frequently used dye in fluorescently labeled polymers¹

- Large extinction coefficient
- Good quantum yield
- Long lifetime



Provides a suitable window to study the internal dynamics of macromolecules

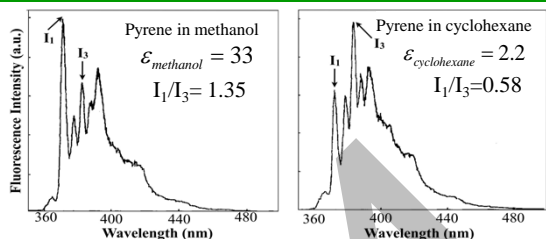
- Isolated excited monomer fluoresces around 375 nm and shifts to 480 nm when it associates with ground-state pyrene to form an excimer.



1. Winnik, F. W. *Chem. Rev.* **1993**, 93, 587-414.

ECOSYNTHEIX[®] 7

Determination of the interior polarity of SNPs by pyrene fluorescence



- Pyrene emission is affected by the solvent polarity.
- The ratio of I₁/I₃ equals 1.87 in polar water ($\epsilon_{\text{water}} = 80$).

K. Kalyanasundaram and J. K. Thomas, "Environmental Effects on Vibronic Band Intensities in Pyrene Monomer Fluorescence and Their Application in Studies of Micellar Systems", *J. Am. Chem. Soc.*, **1977**, 99, 2039-2044.

ECOSYNTHEIX[®] 8

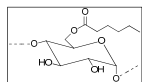
I₁/I₃ - The interior polarity of the SNPs

Sample	Concentration	I ₁ /I ₃	Solvent with similar polarity
Water	N/A	1.80 ± 0.05	Water
SNPs	1.6% w/w	1.65 ± 0.06	Formic acid, Glycerol, Acetone
Amylopectin	1.6% w/w	1.70	Formic acid
*Modified X0.5	0.1% w/w	1.35	Methylene Chloride

> All the SNP samples have a similar interior polarity (I₁/I₃ = 1.65 ± 0.06), less hydrophilic than water (I₁/I₃ = 1.80 ± 0.05).

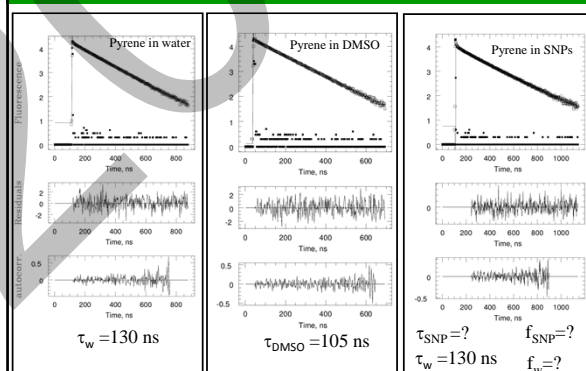
> The interior polarity of MX0.5 is much more hydrophobic; its polarity is close to that of methylene chloride.

*Modified MX0.5 was provided by Ryan Amos with a DS=0.15



ECOSYNTHEIX[®] 9

SNPs Lifetime analysis



ECOSYNTHEIX[®] 10

SNPs Lifetime analysis

Sample	Concentration	τ_w / f_w	$\tau_{\text{SNP}} / f_{\text{SNP}}$
Water	N/A	130 ns / 1.0	
SNPs	1.6% w/w	130 ns/0.63 ± 0.06	200 ns/0.37 ± 0.06
Amylopectin	1.6% w/w	130 ns/0.53	208 ns/0.47
X0.5	0.1% w/w	130 ns/0.92	192 ns/0.08
Modified X0.5	0.1% w/w	130 ns/0.77	302 ns/0.23

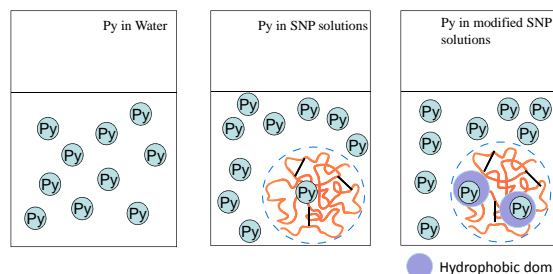
> For unmodified SNPs, τ_{SNP} is around 200 ns, and the fraction of the pyrene in SNPs is around 40% ([SNP] = 1.6% w/w).

> For modified X0.5s2, τ_{SNP} is 302 ns, and the fraction of the pyrene in SNPs is 23%. The interior of the hydrophobic domain is certainly very viscous.

*Modified X0.5s2 was provided by Ryan Amos with a DS=0.15

ECOSYNTHEIX[®] 11

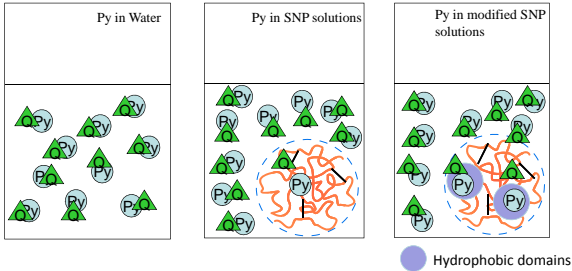
Fluorescence quenching experiments



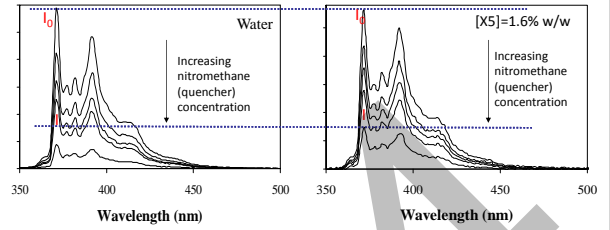
ECOSYNTHEIX[®] 12

Fluorescence quenching experiments

- ❖ Can the crosslinks affect the diffusion of the small molecules?
- ❖ What are the effects of hydrophobic domains?



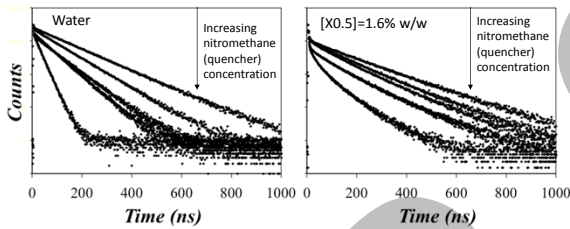
Fluorescence quenching and SNPs interior accessibility



➤ The SNPs can slow down quenching process for the pyrene inside.

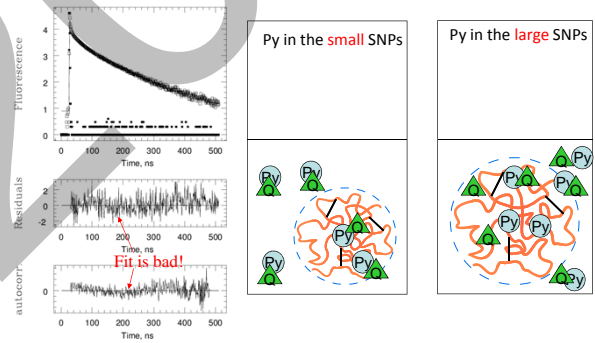
Fluorescence quenching and SNPs interior accessibility

$$I(t) = I_o \times (f_w \exp(-t/\tau_{wQ}) + f_{SNPQ} \exp(-t/\tau_{SNPQ}) + f_{bg} \times BG_{SNP}(t))$$



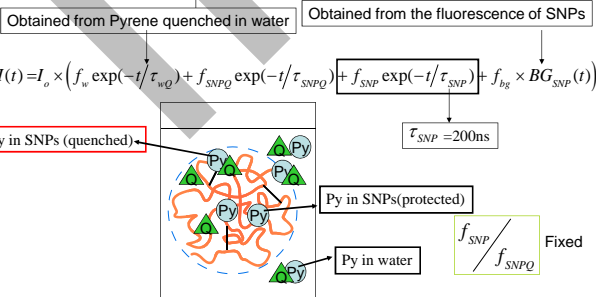
- The pyrene lifetime is reduced more strongly without SNPs.
- At higher quencher concentration, the pyrene fluorescence decay starts to curve for pyrene in SNP solutions.

Fluorescence quenching and SNPs interior accessibility

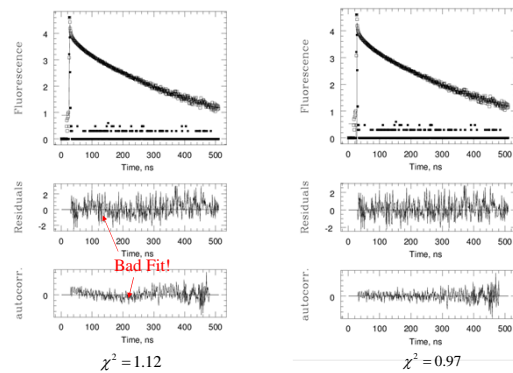


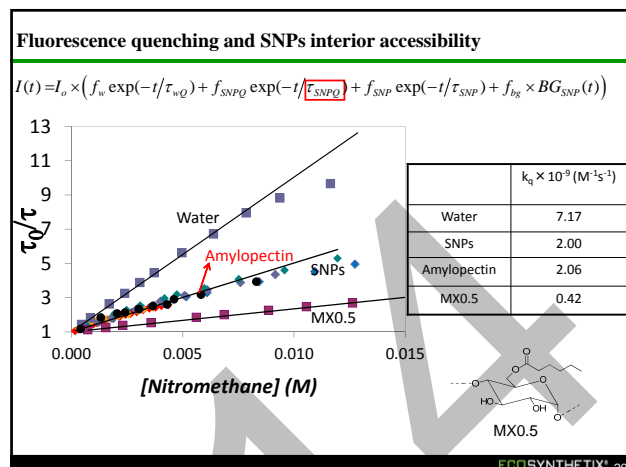
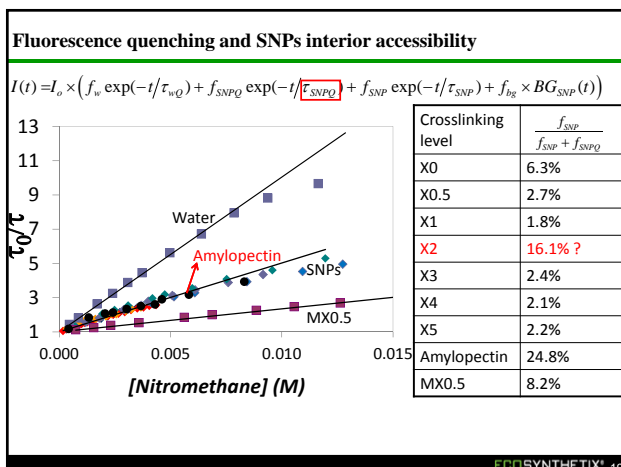
Fluorescence quenching analysis

$$I(t) = I_o \times (f_w \exp(-t/\tau_{wQ}) + f_{SNPQ} \exp(-t/\tau_{SNPQ}) + f_{bg} \times BG_{SNP}(t))$$



Fluorescence quenching and SNPs interior accessibility





Summary

- The pyrene I_1/I_3 ratio of SNP solutions is 1.65 ± 0.06 . The interior polarity is less than water (1.80 ± 0.05), but still relatively hydrophilic. The modified X0.5 solution has an I_1/I_3 ratio of 1.35, implying that the interior of the modified X0.5 particle is much more hydrophobic than the unmodified SNPs.
- For modified X0.5, τ_{SNP} is 302 ns. The interior of the hydrophobic domain is certainly very viscous. It gives a better protection for small molecules compared to unmodified SNPs.
- In the presence of SNPs, a fraction of the pyrene molecules added to the solution can not be reached by the quencher (nitromethane). It seems that more pyrene is protected at lower crosslinking levels.
- However, the crosslinks are not sufficient to slow down the diffusion of small molecules (nitromethane) into the SNPs.

ECOSYNTHE TIX® 21

Acknowledgements

Lab members:
 Duhamel Group Gauthier Group

Project colleagues:
 Wei Yi Ryan Amos
 Joanne Fernandez Duncan Li
 Magda Karski Alexander Ip
 Imran Khimji Howard Tsai
 Ziyi Sun

ECOSYNTHE TIX® 22

Institute for Polymer Research

Celebrating 30 years of Official Institute Status

Symposium documents for

Jin Liu

Synthesis and Migration Insertion Polymerization (MIP) of $\text{CpFe}(\text{CO})_2(\text{CH}_2)_6\text{PPh}_2$ (FpC6P)

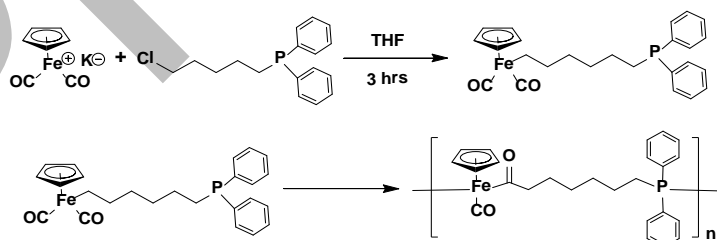
Jin Liu, Xiaosong Wang, IPR Symposium, University of Waterloo, ON N2L 3G1, Canada

Incorporation of metal centers into macromolecules has led to materials that combine the properties of metals, such as catalytic, magnetic, and electronic, with desirable mechanical and processing properties of polymeric frameworks. Comparing to side chain metal containing polymers (MCPs), the backbone for main chain MCPs involves metal elements constructed mainly from either metal-carbon or coordination bonds. Consequently, the polymers offer a range of unique properties derived from the metal complex backbone and has been explored as building blocks for novel materials and supramolecular chemistry. For example, light stimulated self-healing and shape memory materials have been developed from metal coordination main chain MCPs; metal-bridged conjugated systems offer unique optical or electronic properties; crystallization of polyferrocenylsilane (PFS) has been harnessed as a driving force for living self-assembly.

Among all techniques, living ring opening polymerization of strained ring-tilted metallocenophanes has been well developed, which allows precise design of polymetalocenophanes in terms of molecular weight, architecture and chemical composition. In contrast, other chemistry to prepare main chain MCPs is still rudimentary and not robust for designed synthesis. Migration insertion polymerization (MIP), as a new developed polymerization technology, was used to polymerize FpCnP ($n=3, 6$). FpCnP containing both Fp and phosphine group, acted as a difunctional monomer, can undergo MIP at an elevated temperature ($> 40\text{ }^\circ\text{C}$). The backbone of PFpCnP contains Fe metal, main-group P and C elements connected via both metal-carbon and metal coordination bonding. The polymer represents a new group of MCPs as well as phosphorus containing polymers.

Experimental

FpC6P was synthesized via the reaction of Fp anion with 6-chlorohexyldiphenylphosphine at room temperature and used as monomers for MIP in bulk (Scheme 1).



Scheme 1. Scheme for synthesis and MIP of PFC6P

FpC6P, like FpC3P, contains both Fp and phosphine groups, which is designed for MIP. During the polymerization by heating the monomer at 70°C , the original oil-like monomers with orange color gradually turned to reddish brown solids suggesting that polymers were formed. After 24 hours, the system was cooled to room temperature and THF was added to dissolve the solids. The resulting brown solution was slowly added to hexane to precipitate the polymers. Yellow powders as purified products were collected after removing solvents and drying under vacuum overnight.

Discussion

The purified polymers were analyzed by using NMR and IR. Both IR and ^{31}C NMR provides evidences that MIP occurred. IR analysis reveals two CO stretching absorption at 1909 and 1604 cm^{-1} , suggesting both terminal and inserted CO presented in the final products. In agreement with IR, ^{13}C NMR reveals two signals at 219 ppm and 278 ppm accounting for terminal CO and acyl group, respectively.

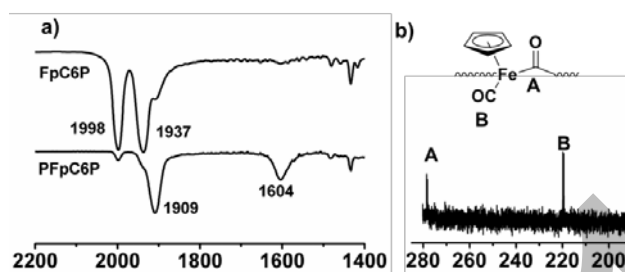


Figure 1. IR (a) and ^{13}C NMR(b) for PFpC6P

^{31}P NMR is illustrated in Figure 2b. As shown in the Figure, the appearance of the chemical shift at 74 ppm (P1) indicates phosphorus coordinated to Fe as a result of MIP. Signal at -14 ppm (P2) is attributed to phosphine end group. Additional peak at 35 ppm is due to the oxidation of phosphine, suggesting that the end group is partial oxidized as precipitation was conducted in air. As shown in ^1H NMR (Figure 2a), intensity for the signal at 4.58 ppm due to the Cp for FpC6P monomers decreased obviously. The remaining weak peaks can be attributed to unreacted Fp end group. Meanwhile, a new single accounting for main chain Cp appears at 4.4 ppm. This down field shift of the chemical resonance is well known as a result of migration insertion reaction. Integration ratio of these two peaks represents the degree of polymerization, which is 14. The molecular weight of PFpC6P was also determined by GPC with THF eluents, and polystyrene was used as standard. As illustrated in Figure 2c, the GPC curve exhibits a molecular weight of 4754 g/mol, which coincidentally match the NMR result.

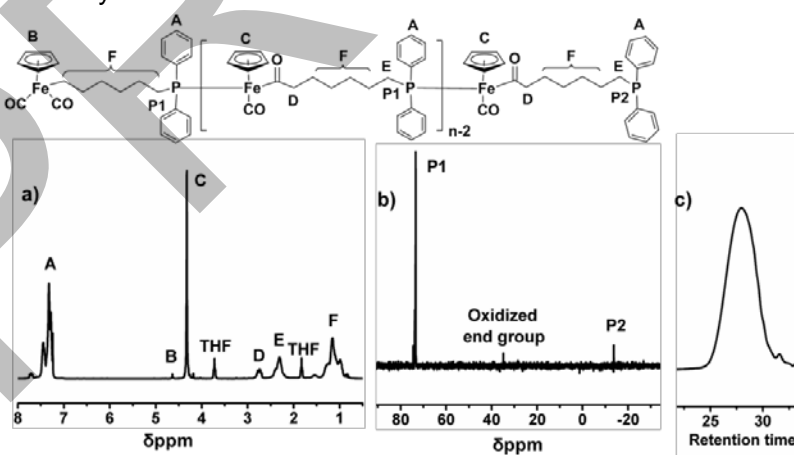


Figure 2. a) ^1H NMR, b) ^{31}P NMR for PFpC6P in CDCl_3 , c) GPC curve of PFpC6P

The polymer is soluble in most commonly used organic solvents, such as THF, DCM, toluene, DMF, but insoluble in hexane, methanol, and acetonitrile. In ethyl acetate, DMSO and acetone it is partial dissolved. In good solvents, the stability of the polymers was estimated by comparing the color of the solutions. No obvious color change is observed over 3 days for THF solution; while in other solvents, e.g. CHCl_3 , DCM, C_6H_6 , toluene, DMF, the color of the solution turned into dark

brown in one or two days, accompanying with the appearance of precipitates in most of these solvents except for DCM.

Cyclic voltammetry (CV) experiments of FpC6P were performed in DMF. As shown in Figure 3, the anodic and cathodic currents of the polymer are fully reversible with oxidation peak appeared at 0.726V and reduction peak at 0.578 V (relative to Ag/AgCl electrode). $[\text{CpFe}(\text{CO})(\text{PR}_3)\text{C}(\text{O})\text{CH}_2\text{SiMe}_2]_n$ -, prepared via MIR of phosphine with $[\text{CpFeCO}_2\text{CH}_2\text{SiMe}_2]_n$ -, also has Fp acyl repeat units, which is similar to FpC6P. Unlike with FpC6P, the phosphine ligands are not involved in the polymer backbone. CV experiment of this polymer shows irreversible oxidations at 0.59 V and 0.62 V (relative to Ag/AgCl). This comparison suggests that redox stability of organometallic polymers with similar metal coordination units could be varied depending on polymer chain configuration.

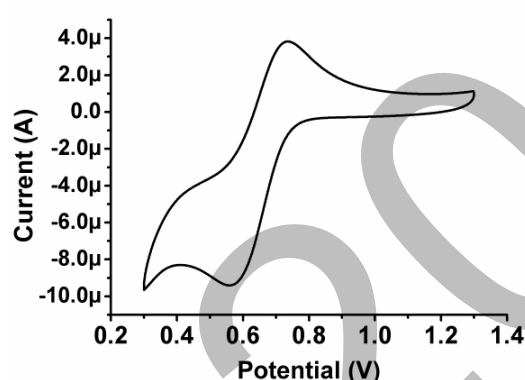


Figure 3. CV data of polymer in DMF

In summary, $\text{CpFe}(\text{CO})_2(\text{CH}_2)_6\text{PPh}_2$ (FpC6P) was synthesized and used for migration insert polymerization via bulk polymerization. The MCP, namely PFpC6P, was fully characterized. The polymer is soluble in most commonly used organic solvents and stable in THF. CV experiment demonstrated that the redox activity of Fe in PFpC6P is reversible.

Reference

1. Xiaosong Wang; Kai Cao; Yibo Liu; Brian Tsang; Liew, S., J Am Chem Soc 2013, 135 (9), 3399-3402.
2. Cao Kai; Tsang Brian; Liu Yibo; Chelladural Daniel; Power William P.; Xiaosong, W., Organometallics 2014, 33 (2), 531-539.
3. Kumar, M.; Metta-Magana, A. J.; Sharma, H. K.; Pannell, K. H., DALTON TRANSACTIONS 2010, 39 (30), 7125.
4. (a) Lidrissi, C.; Romerosa, A.; Saoud, M.; Serrano-Ruiz, M.; Gonsalvi, L.; Peruzzini, M., Angew. Chem.-Int. Edit. 2005, 44 (17), 2568-2572; (b) Yamamoto, Y.; Sawa, S.; Funada, Y.; Morimoto, T.; Falkenstrom, M.; Miyasaka, H.; Shishido, S.; Ozeki, T.; Koike, K.; Ishitani, O., J Am Chem Soc 2008, 130 (44), 14659-14674.

Synthesis and Migration Insertion Polymerization (MIP) of $\text{CpFe}(\text{CO})_2(\text{CH}_2)_6\text{PPh}_2$ (FpC6P)

Jin Liu,^{1,2} Kai Cao,¹ Braham Nayar,¹ Xiaohui Tian,² Xiaosong Wang¹

¹ Department of Chemistry, University of Waterloo

² School of Materials Science and Engineering, East China University of Science and Technology

May 21, 2014

Outline

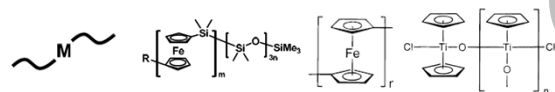
- Background
- Synthesis and Characterization of FpC6P
- Bulk Migration Insertion Polymerization of FpC6P
- Properties of PFpC6P
 - Solubility and Stability test
 - Chemical and Photodegradation of PFpC6P
 - Thermal Properties
 - Cyclic Voltammetry
- Summary

1

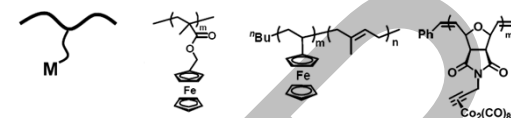
Background

Metal Containing Polymer (MCP):

Main-Chain Metallopolymers



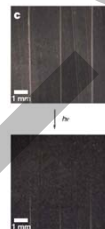
Side-Chain Metallopolymers



2

Application of MCP

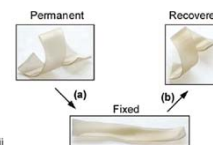
Optically healable supramolecular polymers



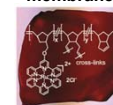
Rewritable phosphorescent paper



Shape memory materials



Anion exchange membranes



Solar cells

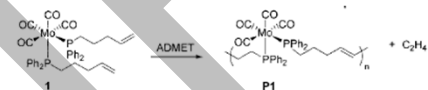
Nature **2011**, 472, 334. JACS. **2011**, 133, 12866.

Macromol. Rapid Commun. **2010**, 31, 671. JACS. **2012**, 134, 4493.

3

Methods of Synthesizing MCP

● Condensation

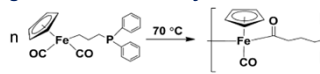


● Living Chain Polymerization

● Ring-Opening Polymerization



● Migration Insertion Polymerization

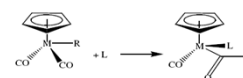


Macromolecules **2008**, 41, 5555. Angew. Chem. Int. Ed. **2007**, 46, 5060. JACS. **2013**, 135, 3399.

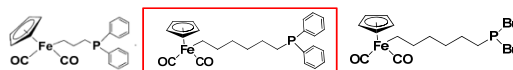
4

Migration Insertion Polymerization

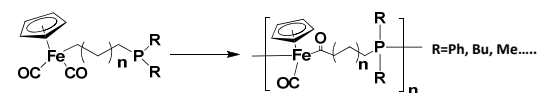
Migration Insertion Reaction:



Monomers:



Migration insertion polymerization:



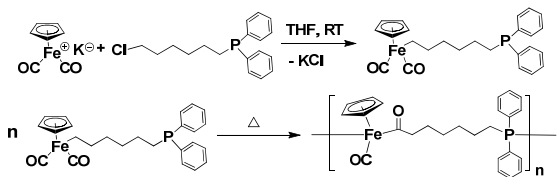
5

Scheme of Synthesis and MIP of FpC6P

Prospect for PFpC6P

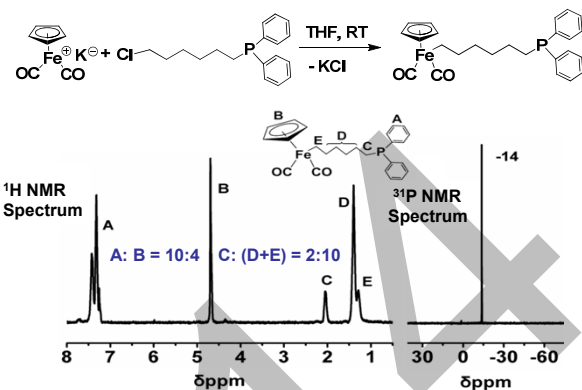
- Lower T_g than PFpC3P, as FpC6P has longer alkyl chain
- Avoid intramolecular cyclic reactions in polymerization process

Synthesis and Bulk Polymerization of FpC6P



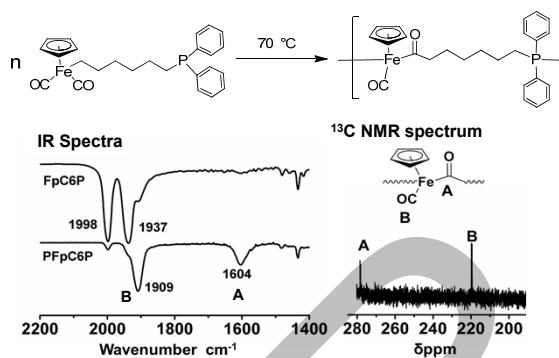
6

Synthesis and Characterization of FpC6P



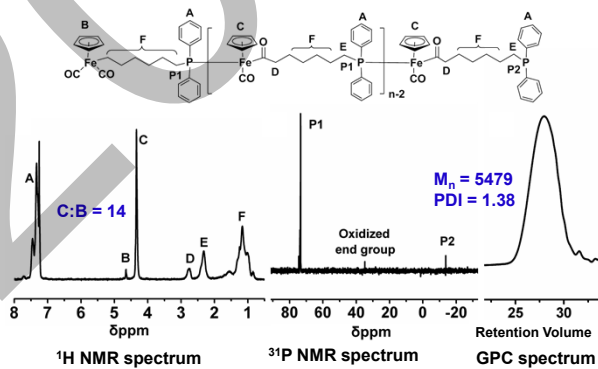
7

Bulk MIP of FpC6P



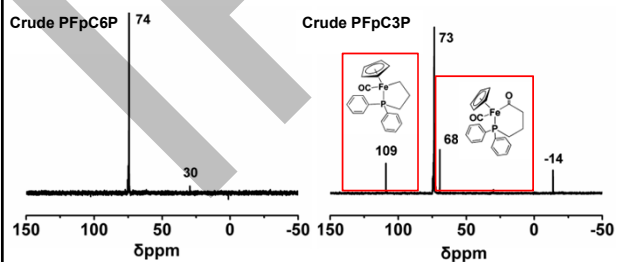
8

NMR and GPC Analysis of PFpC6P



9

^{31}P NMR Analysis of Crude PFpC6P

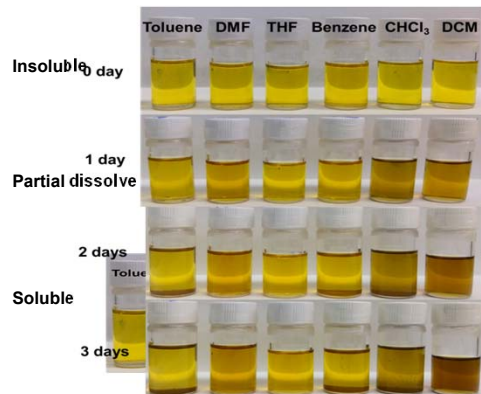


- For PFpC6P, Fp and phosphine separated by a longer spacer lead to unfavorable intramolecular cyclic reactions

Organometallics 2014, 33, 531.

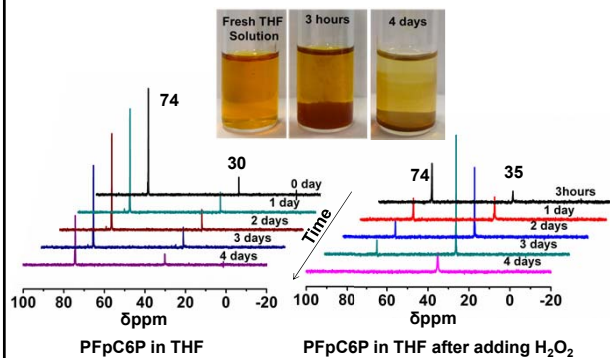
10

Solubility and stability of PFpC6P



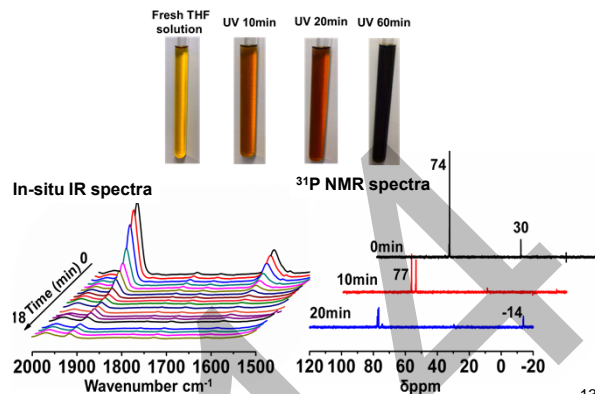
11

Chemical Degradation of PFpC6P in THF



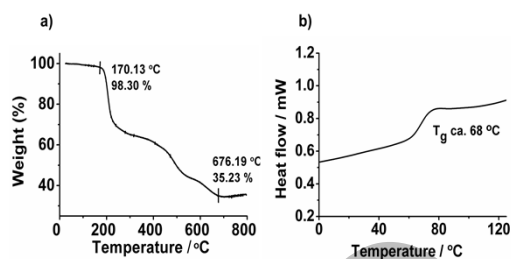
12

Photodegradation of PFpC6P in THF



13

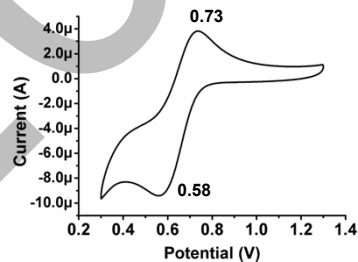
TGA and DSC of PFpC6P



- The polymer is thermal stable up to 170 °C, after 3 stages of weight loss, leaving ca. 35.2 % char yield at 676 °C
- PFpC6P has a T_g of 68 °C, which is much lower than the T_g of PFpC3P (99 °C)

14

CV of PFpC6P



- The polymer CV is fully reversible with oxidation peak appeared at 0.73V and reduction peak at 0.58 V (relative to Ag/AgCl electrode)

15

Summary

- Comparing with PFpC3P, MIP of FpC6P effectively suppressed intramolecular cyclic reactions.
- The polymer is soluble in most common used organic solvents and stable in THF for 3 days.
- Degradation of PFpC6P could be triggered by either H_2O_2 or UV.
- TGA and DSC analysis reveal the polymer is thermal stable up to 170 °C and has a T_g of ca. 68 °C.
- CV experiments demonstrated that the redox activity of Fe in PFpC6P is reversible.

16

Acknowledgement

Supervisor:
Prof. Xiaosong Wang
Prof. Xiaohui Tian
(ECUST, China)

Labmates:
Kai Cao
Nicholas Lanigan
Nimer Murshid
Abdelrahman El-Temtamy
Anand Lopez
Mohammad Aminur Rahman



17

**THANKS FOR
YOUR ATTENTION**

18

IPRR 2014

Institute for Polymer Research

Celebrating 30 years of Official Institute Status

Symposium documents for

Hamed Shahsavan

Fabrication and Characterization of Bioinspired Functionally Graded Adhesive Materials

H. Shahsavan and B. Zhao, IPR Symposium, University of Waterloo, ON N2L 3G1, Canada

Inspired by the amazing adhesive properties of the insects and lizards, a great deal of investigations has been conducted to manufacture synthetic and biomimetic adhesive commodities. Biological adhesive systems, either flat or structured surfaces, whether wet or dry, utilize long dissipative bonds and maximized real contact area to suppress the contribution of stored elastic energy in breakage of interfaces ¹. Accordingly, viscoelasticity of the soft, smooth and wet toe pads of tree frogs can be deemed as of the basic principles in manufacturing of traditional commercial Pressure-Sensitive Adhesives (PSAs) ². In addition, material independence, repeatability and flaw tolerance properties of hair-like structures found in lizards' toe pads introduced them as a unique prototype for new generation of Bioinspired Fibrillar Adhesives (BFAs) ³⁻⁵.

Besides biological adhesives, a plethora of natural substances and animals are benefitted from remarkable bulk resistance to cracking, deformation, and damage, thanking to the gradations of the physical and chemical properties on their exterior surfaces. For example, having the strongest elements located where the stress is the maximum, natural surfaces like bamboos, bones, and plant stems make the best use of gradient in their surface mechanical properties ⁶. Functionally Graded Materials (FGMs), the well-known group of materials in materials science, have been introduced and developed based on these principles. Although both FGMs and adhesive materials are well studied in the literature, there has been less attention to combination of them. In fact, graded adhesive structures have been the subject of studies in only a few published works ⁵. In our work, we aimed to use principles of FGMs for development of Functionally Graded Adhesive Materials that have more efficient properties comparing to their simple non-graded counterparts. For this, we have fabricated a hybrid adhesive structure consisting of an elastic film-terminated BFA coated with a viscoelastic layer of PSA.

The new hybrid structure demonstrated a remarkable increment of adhesive strength comparing to control samples. In addition, the common extensive bulk deformation of the PSA during the debonding process was drastically hampered. Having both remarkable adhesive strength and structural integrity during the debonding, Functionally Graded Adhesives can be great potentials to be used in industries requiring strong, adaptive, and durable adhesives. In addition, the systematic study on the synergetic effects between the adhesive mechanisms of the PSAs and BFAs provides additional fundamental insights to the current body of the literature. In this talk, we will present some of our latest progress in the development of bioinspired functionally graded adhesive materials as published in ³⁻⁵.

Experimental

Hexagonal arrays of PDMS micropillars with 50 μ m diameter, 150 μ m height and 115 μ m center-to-center spacing were fabricated through the soft-lithography technique. A 10% weight

mixture of PDMS resin and curing agent (Sylgard® 184, Dow Corning) was poured on a master-mold of micro-holes. The liquid PDMS was cured at 90°C for 1 hr and peeled off gently after curing. Then, the dipping method developed in reference ⁷ was used to fabricate elastic film-terminated micropillars. The fabricated micropillars in the previous step were placed up-side-down on a thin layer of PDMS which was spun on a glass slide. The thickness of the elastic film was varied from 8 to 24µm. The entire system was placed in the oven at 90°C for 1hr and peeled off the substrate. At last, a 1.5% weight mixture of PDMS was spun on the fabricated elastic film-terminated fibrillar structure and cured at 90°C for 1hr. The thickness of the top viscoelastic layer was varied from 18 to 50µm. Resultant samples were hybrid and graded structures consisting of a viscoelastic top-layer and an elastic film-terminated fibrillar interface (B-E12-VE50). Figure 1(a) shows the schematic view of the new hybrid structure and Figure 1(b) shows the SEM micrograph of the film-terminated fibrillar adhesive.

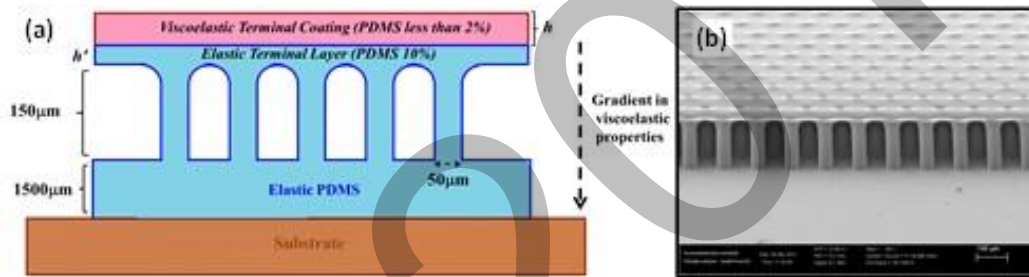


Figure 1: (A) The schematic view of the proposed Functionally Graded Adhesive structure, and (B) SEM micrograph of the film-terminated BFA ³⁻⁵.

The adhesive properties of the fabricated structures were determined through a series of indentation tests using a custom-made indentation apparatus. Fabricated samples were indented to different preloads by a 6 mm diameter hemispherical fused silica probe with loading and unloading velocity of 1 µm/s. Visual examination of the contact formation and separation processes were performed in real-time with a bottom-view camera. The load-displacement data were measured and recorded with a 0-10 g load cell. Indentation results of the new hybrid structure were compared to that of three control samples. The tested control samples were a flat viscoelastic PDMS layer on glass substrate (VE50), an elastic film-terminated fibrillar interface (B-E12), and an elastic PDMS film coated with a viscoelastic PDMS top layer (P-VE50).

Results and Discussion

Preliminary tests were performed on samples with different thickness of the elastic intermediate and the viscoelastic top layers to determine the optimum adhesive structure. It was revealed that the most efficient adhesive in terms of both adhesion strength and structural integrity is the one with the thinnest intermediate elastic and the thickest top viscoelastic layers ³⁻⁵. Accordingly, the remaining of the experiments were carried out on the optimum sample, i.e. B-E12-VE50.

Figure 2 (a) represents typical load vs displacement curves for four tested samples. Except sample B-E12, bonding process of other samples starts with a pronounced snap-in force due to the intermolecular surface forces. The vertical displacement continues up to the point that a certain preload is reached. The unloading process is linear for a remarkable range between the preload and pull-off points. The debonding for the elastic sample B-E12 is rapid and has several small zigzag steps, suggesting the presence of crack trapping mechanism during the separation. The debonding process of the viscoelastic samples is gradual and smooth but undergoes a slope change between the pull-off point and the separation. This slope change is indicative of the bulk deformation processes such as fibrillation, cavitation and other instabilities. The slope change is the most pronounced for the viscous film on PDMS (P-VE50), becomes less for the viscous film on glass (VE50), and is the least pronounced for the new hybrid structure (B-E12-VE50). This observation suggests that the new hybrid structure experiences less bulk deformation while having much greater pull-off force³⁻⁵. In fact, the new type of adhesive is stronger and has better structural integrity comparing to other control samples.

Figure 2 (b) shows the variation of the pull-off force vs preload. Apparently, the preload dependence of the new hybrid adhesive is significantly greater than other control samples. Preload dependence of this structure can be attributed to its graded nature. Functionally graded materials have been shown to have variation of the mechanical properties along the depth of their surface⁶. For instance, modulus of elasticity of the power law graded materials are known to vary with distance from the surface.

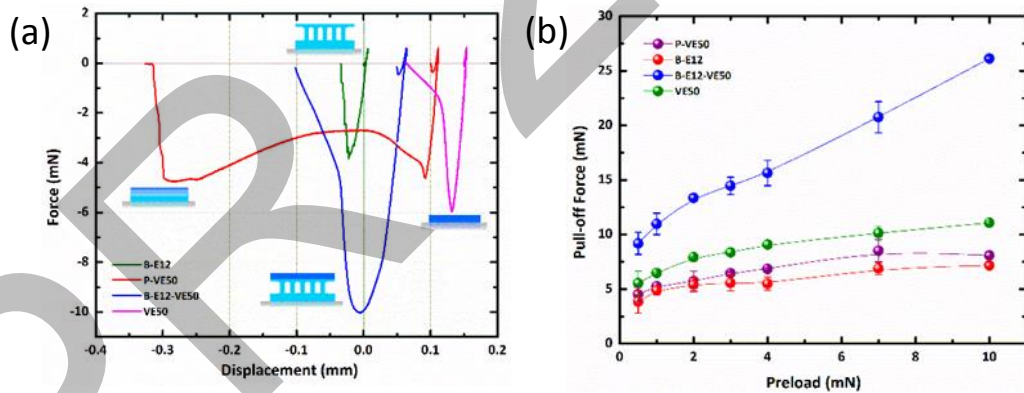


Figure 2: (a) Typical load vs displacement curves for the tested samples under preload of 0.5mN, and (b) variation of the pull-off force against preload⁵.

Figure 3 shows the evolution of contact and separation processes during a full cycle of indentation. First column is locus of the contact at preload point, the second column shows the contact at pull-off point, the third column shows an arbitrary point after the pull-off point, and the last column demonstrates the deformation left after a full indentation cycle. Apparently, the contact area at preload is always the greatest for sample B-E12-VE50, while the sample B-E12 has the smallest contact area. The contact area for samples VE50 and P-VE50 are roughly comparable to that of sample B-E12-VE50 under the preload of 0.5 mN. However, difference between them starts to grow for higher preloads. Similar trends were observed for displacements

δ at the preload point. Displacement at the preload is the largest for the sample B-E12-VE50 ($\approx 14 \mu\text{m}$ for preload 0.5 mN). Samples VE50 and P-VE50 have almost equal displacement at preload values ($\approx 10 \mu\text{m}$ for preload 0.5 mN), and the sample B-E12 under the same preload has considerably smaller value than that of other samples ($\approx 6.8 \mu\text{m}$). All these data suggests that the compliance of the new hybrid sample is the highest ⁵.

It is worth noting that, both bottom-view images and indentation data confirmed premature emergence of bending and buckling of the micropillars for sample B-E12-VE50. That is, the bending deformation for the micropillars, in control sample B-E12, usually takes place at preloads of $\sim 25\text{mN}$. However, for the new hybrid structure, we observed that the micropillars start to bend at the vicinity of 4mN preload. Hence, extraordinary compliance and preload dependence of the new hybrid structure can be attributed to facilitated bending and buckling of the base micropillars.

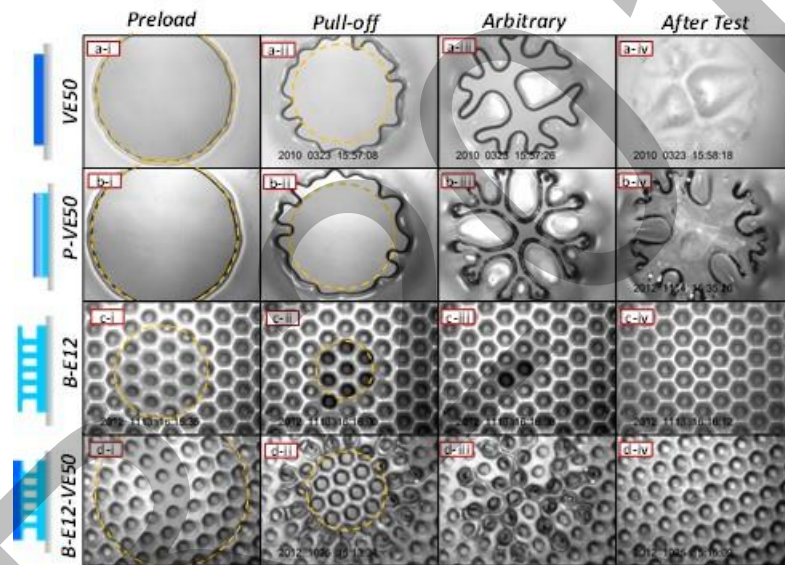


Figure 3: Bottom-view images of the contact for samples (a) VE50, (b) P-VE50, (c) B-E12 and (d) B-E12-VE50 ⁵.

We call this phenomenon shear-induced enhancement of compliance. The observed results advocates that there can be a set of extra shear forces acting on the top of the micropillars facilitating their bending and buckling. It is known that reversible buckling of the micropillars in film-terminated BFAs lead to enhancement of adhesion ⁸. In our new hybrid structure, the Poissonian deformation of the top viscoelastic layer, whether fully diffused in the underneath layer or not, likely induces stretching and consequently shear force on the elastic intermediate layer. Thus, the bending of the micropillars is strongly rendered in this sample comparing to the one without top viscoelastic layer. The possible mechanism of compliance enhancement is illustrated in Figure 4.

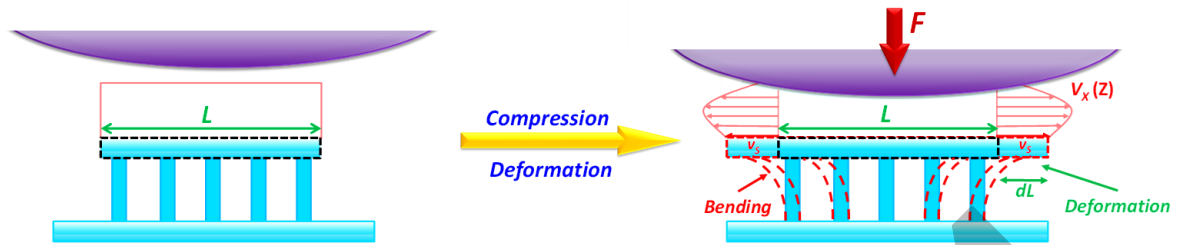


Figure 4: Interplay of the top viscoelastic layer and base micropillars during the compression⁵.

The new proposed adhesive structure benefits from adhesive mechanisms of both BFAs and PSAs. BFAs, theoretically, can increase adhesive strength and toughness of a flat control by enhancing the compliance and crack trapping. On the other hand, PSAs are capable of developing strong adhesive forces upon dissipation of the stored elastic energy through bulk deformation. In the hybrid structure, these mechanisms are coupled and create a strong yet durable adhesion. In summary, the biomimetic fibrillar interface functions as a spring foundation storing the elastic energy during the bonding. The stored energy in the pillars can be retrieved during the separation which facilitates the crack propagation at the interface instead of cohesive failure. The intermediate elastic layer facilitates integration of the viscous layer on top of the biomimetic fibrillar foundation and transfer the shear stress from the top to the base micropillars. The viscoelastic top layer dissipates a large amount of energy during the separation because of the bulk deformation and instabilities, which induced a shear stress at the interface and enhanced the bending and buckling of the fibril.

References

- (1) Persson, B. N. J. *J. Adhes. Sci. Technol.* **2007**, *21*, 1145–1173.
- (2) Gorb, S. N.; Sinha, M.; Peressadko, A.; Daltorio, K. a; Quinn, R. D. *Bioinspir. Biomim.* **2007**, *2*, S117–25.
- (3) Shahsavan, H.; Zhao, B. *Soft Matter* **2012**, *8*, 8281–8284.
- (4) Shahsavan, H.; Zhao, B. In *33rd Annual Meeting of Adhesion Society*; Daytona Beach, FL, USA, 2013.
- (5) Shahsavan, H.; Zhao, B. *Macromolecules* **2014**, *47*, 353–364.
- (6) Suresh, S. *Science (80-.)*. **2001**, *292*, 2447–2451.
- (7) Glassmaker, N. J.; Jagota, A.; Hui, C.-Y.; Noderer, W. L.; Chaudhury, M. K. *Proc. Natl. Acad. Sci. U. S. A.* **2007**, *104*, 10786–10791.
- (8) Noderer, W. L.; Shen, L.; Vajpayee, S.; Glassmaker, N. J.; Jagota, A.; Hui, C.-Y. *Proc. R. Soc. A* **2007**, *463*, 2631–2654.

UNIVERSITY OF Waterloo
 nanoTechnology

Fabrication and Characterization of Bioinspired Functionally Graded Adhesive Materials

Hamed Shahsavan and Boxin Zhao
 Department of Chemical Engineering
 Waterloo Institute for Nanotechnology
 University of Waterloo
 Ontario, Canada

2014 IPR Annual Meeting,
 May 2014

2

Common Traditional Glues and Adhesives

Inherent roughness of any surfaces → Full wetting and maximization of contact area

Contact:

- Inherent cracks in solid-solid contacts
- Soft and liquid-like polymers best candidates
- Conformation to surface asperities

Strong Adhesion

← **Cohesive failure and contamination**

Separation:

- Crack propagation is hindered
- Fibrillation, fingering, and cavitation instabilities
- Possibility of cohesive failure and contamination

Energy dissipation and bulk deformation during separation

Less Structural Integrity

Biological Adhesives Are Strong And Durable

3

Biological Adhesive Systems

❖ **Wet and fibrillar:**

- ✓ Maximized contact area
- ✓ Enhanced interfacial toughness
- ✓ Viscous dissipation in separation
- ✓ Capillary forces

❖ **Dry and fibrillar:**

- ✓ Maximized contact area
- ✓ Enhanced interfacial toughness
- ✓ Frictional adhesion
- ✓ Van Der Waals forces

Terminal Fibril Density

Fibrillar Dry Adhesive / Fibrillar Wet Adhesive

Body Mass

S.N. Gorb et al, *Bioinsp. Biomim.*, (2007)

4

Tokay Gecko Adhesive Pads

Gecko foot	Lamella	Setae	Branch	Spatula
Lengths	2mm			
Diameter				

Properties:

- 1- Strong attachment/easy detachment with low forces (1mm/s rubbing on a vertical wall)
- 2- Anti self-adhesion
- 3- Dry and self cleaning (superhydrophobic and repeatable)
- 4- Material independent (Van der Waals forces)
- 5- Anisotropic and smart

Hansen and Autumn, *PNAS*, 2005
 Autumn 2006

5

Biomimetic Fibrillar Adhesives (BFA)

Mechanisms:

- 1) Flaw tolerance (graded elasticity)
- 2) Interfacial toughness (surface splitting)
- 3) Crack trapping (crack propagation instabilities)
- 4) Enhancement of compliance (deformation of the fibrils)

Design parameters:

- 1) Surface coverage
- 2) Tip shape
- 3) Hierarchy
- 4) Aspect ratio (height and diameter)

Hierarchical BFA (Murphy et al, *ACS Applied Materials and Interfaces*, 2009)

Mushroom-terminated BFA (Cheung and Sitti, *Langmuir*, 2009)

Film-terminated BFA (Glassmaker et al, *PNAS*, 2007)

Simple micro-pillars

(a) (b) (c)

Shahsavan et al, *Langmuir*, 2011
 Shahsavan et al, *MAME*, 2012

6

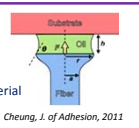
Motivation

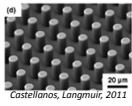
Adhesive strength vs **Cohesive strength**

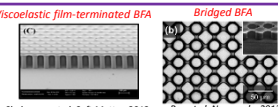
Can we combine them?

7

Current Literature

- Liquid-filled BFA**
 - ✓ Increment of pull-off and adhesion energy
 - ✓ Viscous loss and capillary force together
 - ✓ Hindering cohesive failure of the viscoelastic material
 - ✓ Non-durable and wet!

Cheung, J. of Adhesion, 2011 *Patil et al, Langmuir, 2012*
- Viscoelastic as the structural adhesive material**
 - ✓ Increment of pull-off force and adhesion energy
 - ✓ Surface adaptation and viscous loss
 - ✓ Durability might be issue due to buckling or plastic deformation


Castellanos, Langmuir, 2011
- Viscoelastic terminal layer**
 - ✓ Increment of pull-off force and adhesion energy
 - ✓ Surface adaptation and viscous loss
 - ✓ Better durability comparing to PSA counterpart

Shahsavani et al, Soft Matter, 2012 *Bae et al, Nanoscale, 2013*

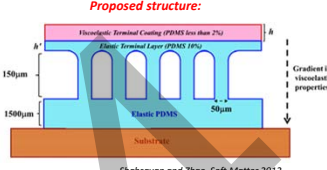
8

Functionally Graded Materials (FGM)

- ✓ Materials with gradient of mechanical properties (hard to soft)
- ✓ The greatest stress located on the stiffest part
- ✓ Resistance to surface damage and crack under harsh conditions



Proposed structure:



Shahsavani and Zhao, Soft Matter 2012 and Macromolecules, 2014

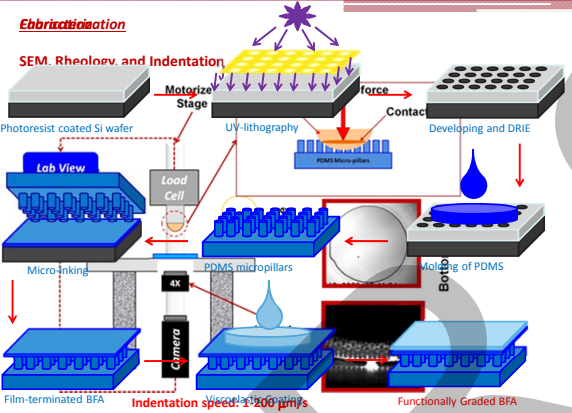
Most possible phenomena:

- Crack trapping and viscous dissipation at the terminal layer
- Separation instabilities in shape of bulk deformation
- Enhancement of compliant
- Enhancement of durability and structural integrity

9

Fabrication

SEM, Rheology and Indentation

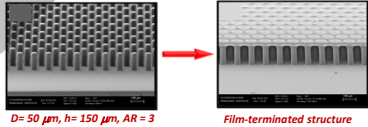


Photoresist coated Si wafer → Motorized Stage → UV-lithography → Contact → Developing and DRIE → PDMS Micro pillars → Molting of PDMS → Micro-inking → Camera → Indentation → Lab View → Load Cell → Film-terminated BFA / Functionally Graded BFA

Indenter speed: 1200 μm/s
Holding time: 30 s
Pillars geometry: Height: 150 μm, Diameter: 50 μm, Spacing: 115 μm

10

Results



$D = 50 \mu\text{m}, h = 150 \mu\text{m}, AR = 3$

Pressure Sensitive Adhesives

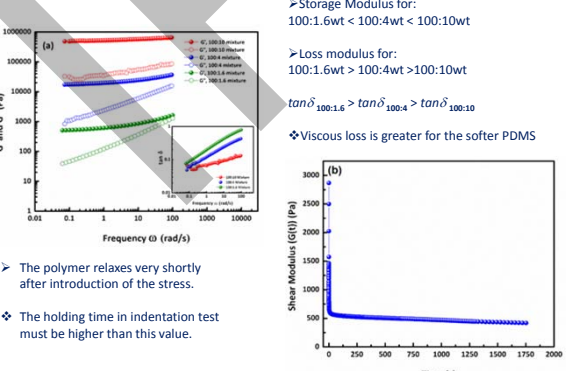
- Viscoelastic Layer
- Glass
- Non-graded (VE50)
- Viscoelastic Layer
- Elastic Layer
- Glass
- Chemically graded (P-VE50)

Gecko-Inspired Adhesive

- Elastic Layer
- Elastic Basement
- Glass
- Geometrically graded (B-E12)

11

Rheological Studies



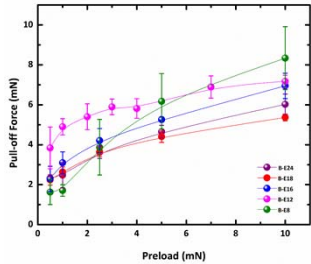
➢ Storage Modulus for:
 $100:1.6\text{wt} < 100:4\text{wt} < 100:10\text{wt}$
 ➢ Loss modulus for:
 $100:1.6\text{wt} > 100:4\text{wt} > 100:10\text{wt}$
 $\tan \delta_{100:1.6} > \tan \delta_{100:4} > \tan \delta_{100:10}$
 ❖ Viscous loss is greater for the softer PDMS

➢ The polymer relaxes very shortly after introduction of the stress.
 ❖ The holding time in indentation test must be higher than this value.

12

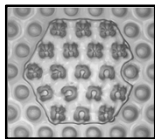
Optimization of Design

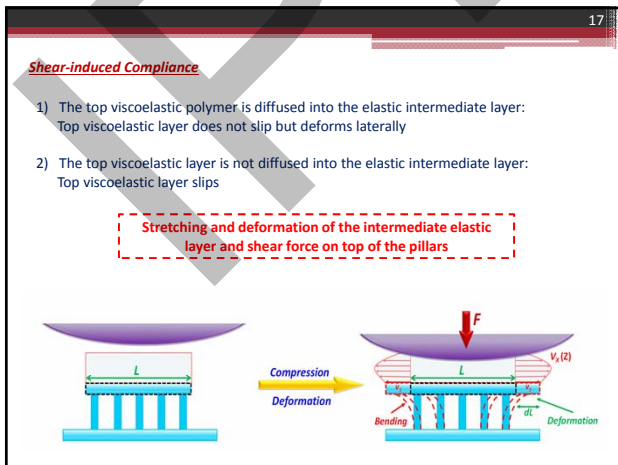
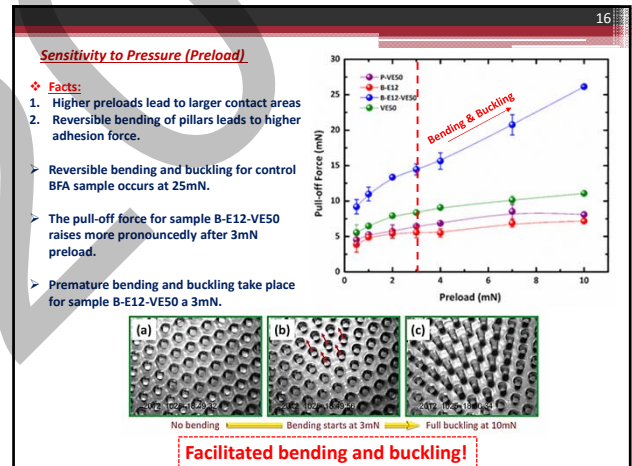
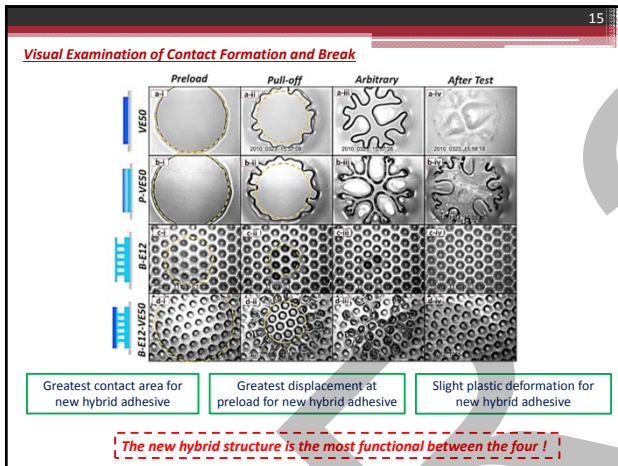
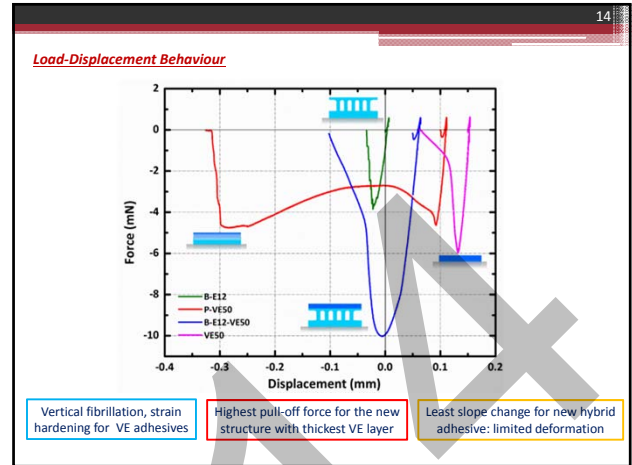
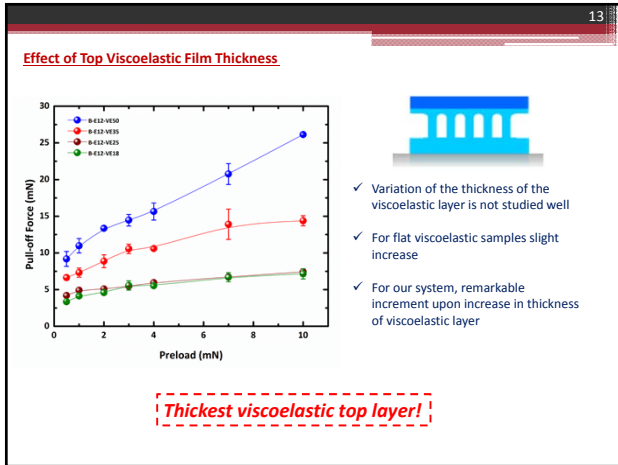
Effect of Intermediate Elastic Film Thickness



- ✓ Theoretically: energy release rate $\sim t^3$
- ✓ Decrease in thickness increases the adhesion force
- ✓ Very thin layers show separation instabilities on top of the fibrils

Thinnest elastic top layer as the base!





18

Conclusions

New hybrid structure benefits from:

- ✓ Higher pull-off force
- ✓ Higher adhesion energy
- ✓ Less bulk deformation
- ✓ Higher compliance and pressure sensitivity

19

Acknowledgment

Thanks to my supervisor:
Professor Boxin Zhao

Thanks to all my lab mates

Thanks to Professor Costas Tzoganakis and Dr. Shui Han Zhu for help in the rheological characterizations

This work was supported by the Natural Sciences and Engineering Research Council of Canada (NSERC) and Ontario Centre of Excellences (OCE).

20

Thank you for attention !

Soft Matter

Questions ?

Shahsavan and Zhao, *Soft Matter*, 2012, 8, 8281-8284

21

Applications

- Climbing robots
- Dust free aerospace adhesives
- Ultra-strong reversible dry adhesives
- Transfer printing
- Micro-manipulation
- Switchable wetting
- Switchable friction
- Biomedical adhesives

22

Adhesive Energy Contributions

$$U_{hys} = U_1 + U_2 = \int_0^{d_{max}} Fd\delta + \int_{d_{max}}^d Fd\delta = \oint Fd\delta$$

$$W_{adh} = \frac{U_{hys}}{\Delta A} = \frac{\int_0^{d_{max}} Fd\delta}{A_{max} - A_0} + \frac{\int_{d_{max}}^d Fd\delta}{A_d - A_{max}} = \oint Fd\delta / A_{max}$$

Required Energy for \rightarrow Sample \downarrow	Phase 1	Phase 2
	42%	58%
	12%	88%
	74%	26%
	46%	54%

Phase 1: Storage of strain energy in loading and energy put into system for initiation of crack.

Phase 2: The energy required for crack propagation, and other separation instabilities.

Cohesive strength:

Adhesion strength:

23

Theoretical Considerations

1) Crack growth patterns:

- controlled by competition between two factors:
 - Interfacial crack propagation: Energy release rate G_c
 - Propensity of the bulk for deformation: Young's Modulus E

1. Lower $G_c/E \rightarrow$ Interfacial crack propagation

2. Higher $G_c/E \rightarrow$ Bulk deformation ($E \rightarrow E'$)

Crosby et al, *J. Appl. Phys.*, 2000

24

Theoretical considerations

2) Energy release rate for viscoelastic systems is more complex:

$$G_c = G_0(1 + \varphi(a_T v))$$

Proportionality of damping factor to shift factor $\varphi(a_T v) \approx \tan \delta$

Gent and Kinloch, *J. Polym. Sci., Polym. Phys.*, 1971

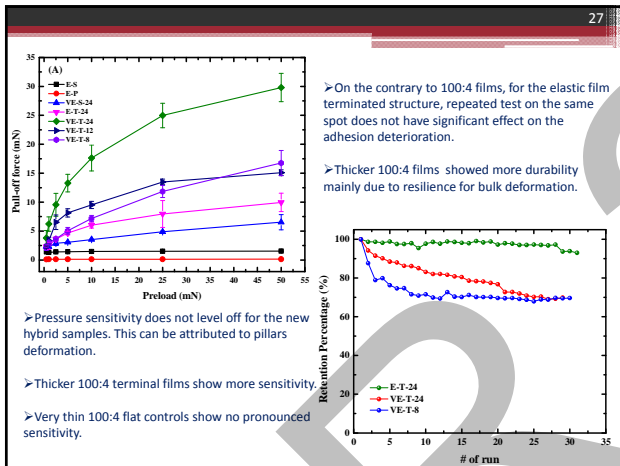
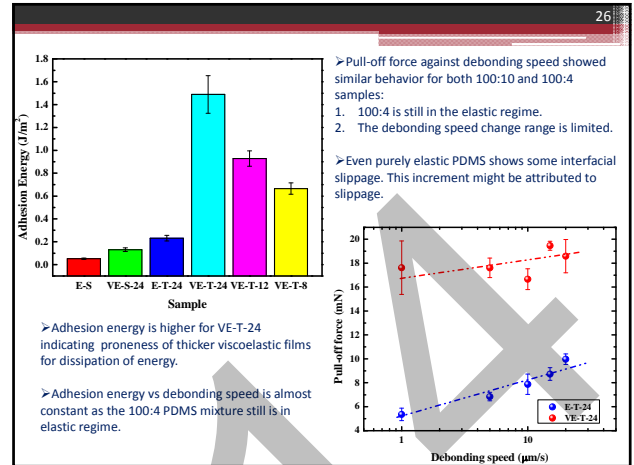
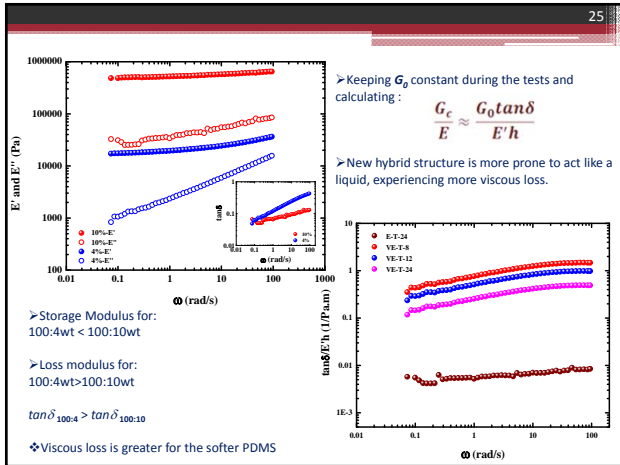
3) Confinement ratio (a/h) also affects the pattern of crack propagation in linearly elastic or viscoelastic thin films

Higher a/h , more pronounced shear undulation

Determining ratio: $\frac{G_c}{E} \approx \frac{G_0 \tan \delta}{E' h}$

Nase et al. PRL, 2008

Properties of the terminal thin film appears to be most influential



Institute for Polymer Research

Celebrating 30 years of Official Institute Status

Symposium documents for

Bin Sun

A record high electron mobility polymer semiconductor for organic thin-film transistors

Bin Sun,^{1,3} Wei Hong,^{1,3} Zhuangqing Yan,^{1,3} Hany Aziz*,^{2,3} Yuning Li^{1,3,*}

¹ Department of Chemical Engineering, ² Department of Electrical and Computer Engineering, and ³ Waterloo Institute for Nanotechnology (WIN), University of Waterloo, 200 University Ave West, ON N2L 3G1, Canada

Polymer based organic thin film transistors (OTFTs) can be used in radio-frequency identification (RFID) tags, flexible displays, medical sensors, memory devices, etc.; but their low charge carrier mobility has limited many applications.

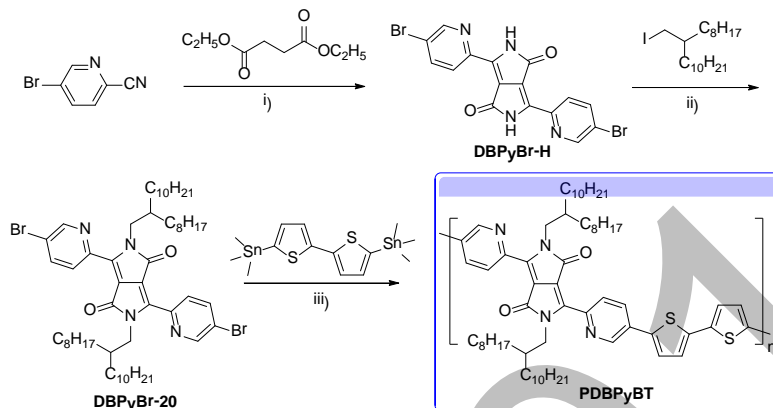
Recently, several classes of π -conjugated polymers having electron donor (D) and acceptor (A) units showed highly efficient charge transport performance with mobility higher than $1 \text{ cm}^2\text{V}^{-1}\text{s}^{-1}$ in OTFTs. Particularly, Diketopyrrolopyrrole (DPP)-based polymers are the best performing polymer semiconductors for OTFTs to date.^{1, 2} All the high mobility DPP polymers reported are based on highly coplanar five-membered ring-flanked DPP building blocks. The first reported phenyl-substituted DPP block (DBP) has been much less investigated for the OTFT application. This is mainly due to the fact that DBP has a large torsion angle of $\sim 20\text{-}40^\circ$ between the six-membered phenyl ring and the DPP core.³ Thus the DBP-based polymers showed very low mobility values.⁴

In this study, we use the sterically less demanding 2-pyridinyl units to flank the DPP core to achieve a high coplanarity (with a dihedral angle of 0°) of the resulting DBPy building block, which was substantiated by computer simulations. Pyridine is an electron deficient moiety, which would make DBPy a strong electron acceptor. Thus polymers based on DBPy are expected to exhibit efficient electron transport characteristics in OTFTs. We report here the first DBPy based polymer that showed record high electron mobility of up to $6.3 \text{ cm}^2\text{V}^{-1}\text{s}^{-1}$.

Experimental

A copolymer of DBPy and bithiophene (BT), PDBPyBT, was prepared according to the route shown in Scheme 1. The number (M_n) average molecular weights of PDBPyBT is 26,300, with a polydispersity index (PDI) of 3.56, determined using a high-temperature gel-

permeation chromatography (GPC) with 1,2,4-trichlorobenzene as the eluent at a column temperature of 140 °C.



Scheme 1. The synthetic route to PDBPyBT: i) $\text{tert-C}_4\text{H}_9\text{OK}/2\text{-methyl-2-butanol}/100\text{ }^\circ\text{C}$; ii) $\text{K}_2\text{CO}_3/\text{DMF}/70\text{ }^\circ\text{C}$; iii) $\text{Pd}_2(\text{dba})_3/\text{P}(o\text{-tolyl})_3/\text{chlorobenzene}/130\text{ }^\circ\text{C}$. Copyright 2014 WILEY-VCH Verlag GmbH & Co. [§]

The polymer was evaluated in bottom-gate, bottom-contact (BGBC) OTFT devices and top-gate, bottom-contact (TGBC) OTFT devices. Reflective XRD diagrams of polymer thin films spin coated on SiO_2/Si substrates were performed on a Bruker D8 Advance powder diffractometer using standard Bragg-Brentano geometry with $\text{Cu K}\alpha 1$ radiation ($\lambda = 1.5406\text{ \AA}$). Transmission XRD measurements were carried out on a stack of polymer thin films ⁵ using Bruker Smart Apex2 CCD with $\text{Mo K}\alpha$ radiation ($\lambda = 0.71073\text{ \AA}$). Atomic force microscopic (AFM) images were obtained on polymer thin films ($\sim 30\text{-}40\text{ nm}$) spin coated on SiO_2/Si substrates with a Dimension 3100 Scanning Probe Microscope.

Results

We used the cyclic voltammetry (CV) to determine the frontier energy levels of PDBPyBT. The HOMO and LUMO levels were calculated to be -5.69 eV and -4.33 eV , respectively. The very low LUMO level is beneficial for electron transport in OTFTs. ⁶

To investigate the polymer chain packing, X-ray diffractometry (XRD) measurements in a reflective mode were performed on polymer thin films on SiO_2/Si wafer substrates. For the as-spun polymer thin film, an intense primary diffraction peak at $2\theta = 4.36^\circ$ was observed,

which corresponds to a d-spacing of 2.03 nm. When the thin film was thermally annealed, the primary peak intensity increased dramatically, resulting from the improved crystallinity. To determine the in-plane chain packing, we conducted transmission XRD measurements on stacked polymer thin films. As shown in Fig. 1b, a prominent peak at $2\theta = 11.34^\circ$ was observed, which corresponds to a π - π distance of 3.60 Å. This short π - π distance would be beneficial for charge hopping along the in-plane π -stacking direction.

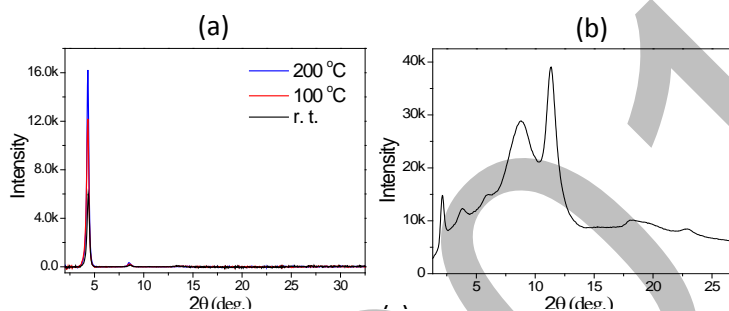


Fig. 1 (a) XRD spectrums of spin coated PBDPyBT thin films on bare SiO_2/Si substrates annealed at different temperatures measured in a reflection mode using $\text{Cu K}\alpha 1$ radiation. (b) XRD pattern of a stack of non-annealed PBDPyBT thin films in a transmission mode using $\text{Mo K}\alpha$ radiation. Copyright 2014 WILEY-VCH Verlag GmbH & Co. §

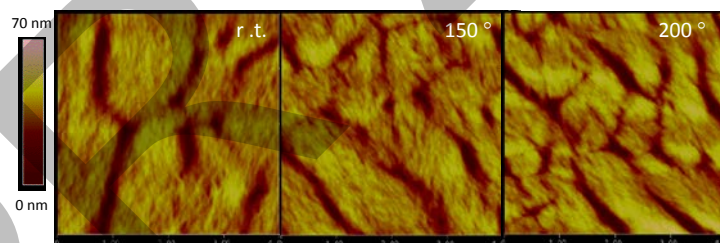


Fig. 2 AFM images ($2\mu\text{m} \times 2\mu\text{m}$ each) of PBDPyBT thin films on bare SiO_2/Si substrates annealed at different temperatures: the root-mean square (RMS) roughness is 8.2 nm, 8.3 nm, and 11.7 nm for the as-spun (r.t.), 150 °C-annealed, and 200 °C-annealed thin films, respectively. Copyright 2014 WILEY-VCH Verlag GmbH & Co. §

PBDPyBT was evaluated in bottom-gate, bottom-contact (BGBC) OTFT devices using heavily n-doped Si wafer substrates having a thermally grown SiO_2 layer (~ 200 nm), where the Si layer and the SiO_2 layer were used as the gate electrode and the dielectric, respectively. The polymer thin film was then annealed, followed by spin-coating with a PMMA

encapsulation layer (~500 nm). Devices annealed at 100 °C exhibited typical p-channel field effect behavior with hole mobility of up to $0.088 \text{ cm}^2\text{V}^{-1}\text{s}^{-1}$. The 200 °C-annealed devices showed increased mobility of up to $0.46 \text{ cm}^2\text{V}^{-1}\text{s}^{-1}$. It can be seen in the AFM image in Fig 2 that the polymer films are very rough surface. We found that the output and transfer curves of the devices are very noisy, which is probably due to the large grain boundaries in the polymer thin films and the poor contact of the polymer films to the DTS-modified SiO_2 dielectric layer.

To improve the interfacial contact between the dielectric and the PDBPyBT layer, we used a commercial fluorinated polymer, Cytop, as the dielectric in a top-gate, bottom-contact (TGBC) device configuration. Surprisingly, ambipolar charge transport performance was observed for all the TGBC devices. High average mobility values of $4.54 \text{ cm}^2\text{V}^{-1}\text{s}^{-1}$ for electrons and $2.20 \text{ cm}^2\text{V}^{-1}\text{s}^{-1}$ for holes were obtained for the 100 °C-annealed PDBPyBT devices. The best device showed electron and hole mobility values of $6.30 \text{ cm}^2\text{V}^{-1}\text{s}^{-1}$ and $2.78 \text{ cm}^2\text{V}^{-1}\text{s}^{-1}$, respectively. These are the highest mobility values reported for ambipolar polymer OTFTs so far. Especially, the electron mobility of $6.30 \text{ cm}^2\text{V}^{-1}\text{s}^{-1}$ is the record high value achieved for polymer semiconductor OTFTs to date. The high performance observed for PDBPyBT was believed due to the high backbone coplanarity, very high crystallinity, and a close π - π stacking distance of this polymer. The improved dielectric and polymer interface by adopting the TGBC device structure is also greatly contributable to the achievement of the record high electron mobility.

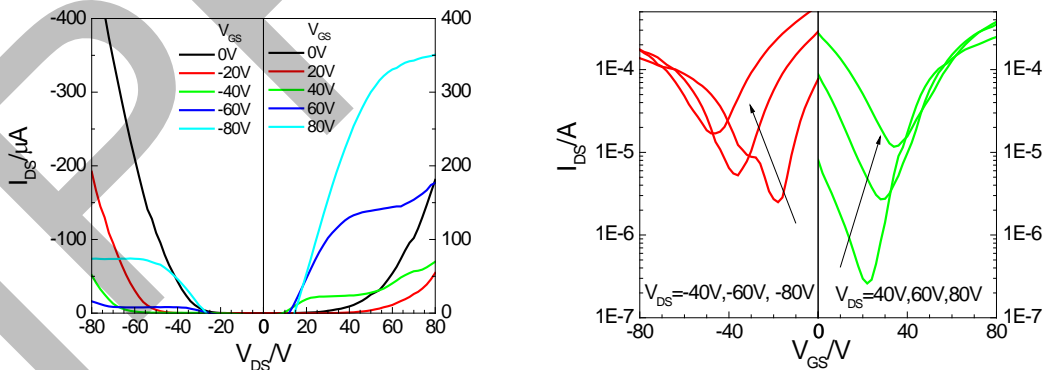


Fig. 3 Output (left) and transfer (right) curves of a typical top-gate, bottom-contact (TGBC) OTFT device with a PDBPyBT thin film annealed at 100 °C. Device dimensions: channel length $L = 30 \mu\text{m}$; channel width $W = 1 \text{ mm}$. Copyright 2014 WILEY-VCH Verlag GmbH & Co. [§]

In conclusion, pyridin-flanked DPP (DBPy) was used to construct a polymer semiconductor PDBPyBT with high backbone coplanarity structure and a very short π - π stacking distance of 0.36 nm. The strong electron withdrawing effect of DBPy facilitated the electron injection and transport of this polymer. Typical ambipolar charge transport performance was observed for PDBPyBT in top-gate bottom-contact OTFT devices. A record high electron mobility value of $6.30 \text{ cm}^2\text{V}^{-1}\text{s}^{-1}$ was achieved. Our results demonstrate that DBPy is a promising electron acceptor building block for high performance polymer semiconductors for printed electronics.

Acknowledgements

The authors thank the Natural Sciences and Engineering Research Council (NSERC) of Canada for financial support (Discovery Grants) and Jon Hollinger and Prof. Dwight Seferos of University of Toronto for the measurements of molecular weight.

§ This work is published in *Adv. Mater.* 2014, DOI: 10.1002/adma.201305981


References

1. Holliday, S., J. E. Donaghey, et al. *Chem. Mater.* **2014**, 26, 647
2. Li, Y.; Sonar, P.; Murphy, L.; Hong, W. *Energy Environ. Sci.* **2013**, 6, 1684
3. Kim, C.; Liu, J.; Lin, J.; Tamayo, A. B.; Walker, B.; Wu, G.; Nguyen, T. *Chem. Mater.* **2012**, 24, 1699
4. a) Wu, P.-T.; Kim, F. S.; Jenekhe, S. A. *Chem. Mater.* **2011**, 23, 4618. b) Kanimozhi, C.; Balraju, P.; Sharma, G. D.; Patil, S. *J. Phys. Chem. B* **2010**, 114, 3095. c) Chen, L.; Deng, D.; Nan, Y.; Shi, M.; Chan, P.; Chen, H. Z. *J. Phys. Chem. C* **2011**, 115, 11282
5. Pan H., Li Y., Wu Y., Liu P., Ong B. S., Zhu S., Xu G., *J. Am. Chem. Soc.* **2007**, 129, 4112.
6. Jones, B. A.; Facchetti, A.; Wasielewski, M. R.; Marks, T. J. *J. Am. Chem. Soc.* **2007**, 129, 15259. (b) Yan, H.; Chen, Z.; Zheng, Y.; Newman, C.; Quinn, J. R.; Dötz, F.; Kastler, M.; Facchetti, A. *Nature* **2009**, 457, 679

Waterloo IPR 36th ANNUAL SYMPOSIUM

A record high electron mobility polymer semiconductor for organic thin-film transistors

Bin Sun
 Department of Chemical Engineering, Institute of Polymer Research (IPR),
 and Waterloo Institute for Nanotechnology (WIN), University of Waterloo
 Supervisors: Profs Yuning Li & Hany Aziz
 May 21/2014



Waterloo

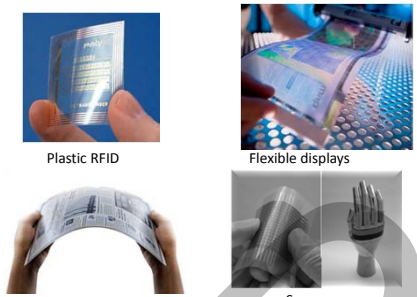
Outline

- Background
- PDBPyBT Polymer semiconductor design and synthesis
- OTFTs evaluation
- Conclusion

2

Waterloo

Electronics Based On Organic Thin-film Transistors(OTFTs)



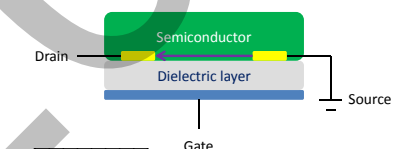
Plastic RFID Flexible displays
 Electronic Paper Sensors

Light weight
 Large area
 Flexibility
 Low cost


3

Waterloo

Organic Thin-Film Transistors



Drain — Semiconductor — Dielectric layer — Source
 Gate



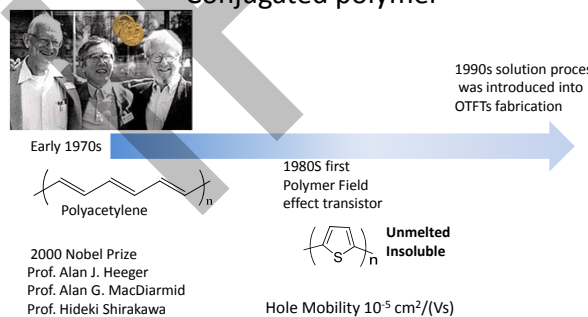
High mobility

Mobility 5~10 cm²/Vs for OLED

4

Waterloo

Conjugated polymer



1990s solution process was introduced into OTFTs fabrication

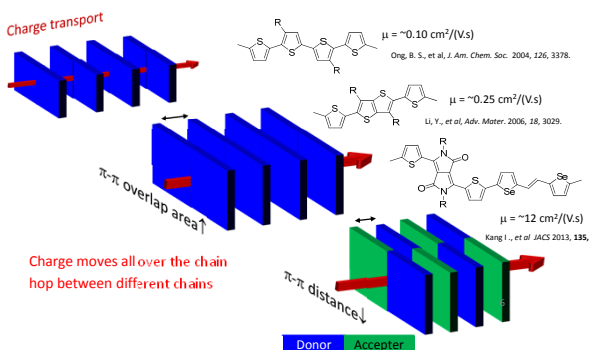
Early 1970s
 Polyacetylene
 2000 Nobel Prize
 Prof. Alan J. Heeger
 Prof. Alan G. MacDiarmid
 Prof. Hideki Shirakawa

1980S first Polymer Field effect transistor
 Unmelted Insoluble
 Hole Mobility 10⁻⁵ cm²/(Vs)

5

Waterloo

Donor-Acceptor Structure



Charge transport

Charge moves all over the chain hop between different chains

$\mu = \sim 0.10 \text{ cm}^2/(\text{V}\cdot\text{s})$
 Ong, B.S., et al, J. Am. Chem. Soc. 2004, 126, 3378.

$\mu = \sim 0.25 \text{ cm}^2/(\text{V}\cdot\text{s})$
 Li, Y., et al, Adv. Mater. 2006, 18, 3029.

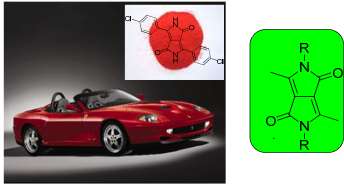
$\mu = \sim 12 \text{ cm}^2/(\text{V}\cdot\text{s})$
 Kang I., et al JACS 2013, 135, 1489

Donor Acceptor

6

Waterloo

Diketopyrrolopyrrole (DPP)



• An electron-accepting moiety

Pigment red 254 or 'Ferrari Red'
 •1974 first by Donald G. Farnum

7

Waterloo

Coplanarity of building block

Monomer	Angle
	~26-40°
	~0°
	<12°
	~0°

Chem. Mater. 2012, 24, 1699-1709.

Adv. Mater. 2013, 25, 1859-1880

Chem. Sci. 2012, 3, 181-185

Torsion angle

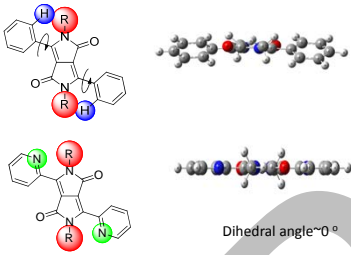
-4 E_{LUMO} , eV

E_{HOMO} , eV

8

Waterloo

2-Pyridine-DPP



Dihedral angle ~0°

<-4 E_{LUMO} , eV

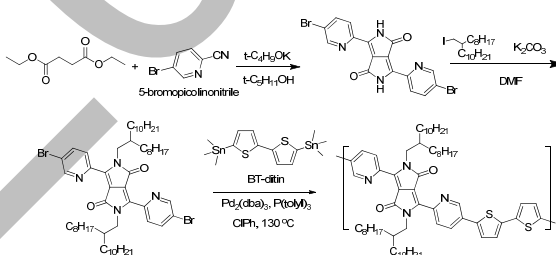
E_{HOMO} , eV

Five-membered ring (electron rich)
 Six-membered ring (electron deficient, lower LUMO, electron transport)

9

Waterloo

Synthesis of PDBPyBT

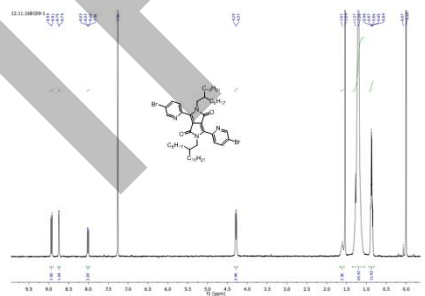


$M_n = 26,300$; PDI = 3.56

10

Waterloo

Proton NMR of monomer

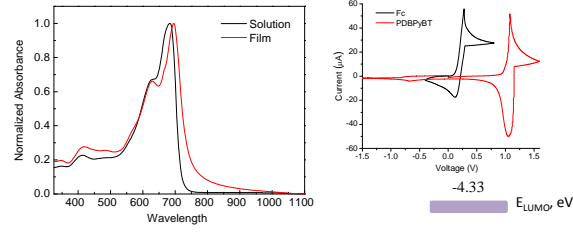


1H NMR (300 MHz, $CDCl_3$) δ 8.93 (d, $J = 8.5$ Hz, 2H), 8.74 (d, $J = 2.1$ Hz, 2H), 8.01 (dd, $J = 8.6, 2.3$ Hz, 2H), 4.28 (d, $J = 7.3$ Hz, 4H), 1.61 (m, 2H), 1.24 (m, 64H), 0.93-0.81 (m, 12H).

11

Waterloo

Energy Level of Polymer



UV-vis absorption spectra of PDBPyBT solution (chloroform) and as-cast thin film on quartz.

Maximum absorption wave length
 683nm in solution
 695nm in film

Cyclic voltammetry diagrams of PDBPyBT and the reference ferrocene (Fc)

-4.33 E_{LUMO} , eV

-5.69 E_{HOMO} , eV

12

Device Fabrication Process

Doped Si wafer with SiO₂

Spin-coating

Thermal evaporation

Photo lithography making substrate

13

BGBC OTFTs

T _{annl.} °C	SiO ₂ as dielectric layer			
	μ_{hr} cm ² V ⁻¹ s ⁻¹		I _{on} /I _{off}	
	$\mu_{h \max}$	$\mu_{h \text{ ave}}$		
100	0.088	0.072 (±0.014)	~10 ³	
150	0.25	0.23 (±0.022)	~10 ⁴	
200	0.46	0.39 (±0.046)	~10 ⁴	

SiO₂ modified with dodecyltrichlorosilane (DDTS)
Poly(methyl methacrylate) (PMMA)

14

Output and Transfer characteristics of BGBC OTFTs

Output characteristics (a), leakage current through gate (b), and transfer curves (c) of a bottom-gate, bottom-contact (BGBC) OTFT device using a PDBPyBT thin film annealed at 200 °C. Hole mobility: 0.46 cm²V⁻¹s⁻¹.

$$I_{DS} = \mu C_1 \frac{W}{2L} (V_{GS} - V_T)^2$$

C₁ = 17 nF/cm²
L = 30 μm, W = 1000 μm

15

AFM image

RMS = 8.2, 8.3 nm, 11.7 nm

AFM image of polymer film on Si/SiO₂ substrate annealed on hotplate in nitrogen Filled glove box for 10min

16

High performance in TGBC design

T _{annl.} °C	Cytop as dielectric			
	μ_{hr} cm ² V ⁻¹ s ⁻¹		μ_{hr} cm ² V ⁻¹ s ⁻¹	
	$\mu_{e \max}$	$\mu_{e \text{ ave}} \text{ (STD)}$	$\mu_{h \max}$	$\mu_{h \text{ ave}}$
100	6.30	4.54 (±1.27)	2.78	2.20 (±0.37)
150	3.91	3.50 (±0.40)	2.25	1.90 (±0.29)
200	3.32	2.30 (±0.62)	1.80	1.25 (±0.39)

$I_{DS} = \mu C_1 \frac{W}{2L} (V_{GS} - V_T)^2$
C₁ = 3.2 nF/cm²

Cytop

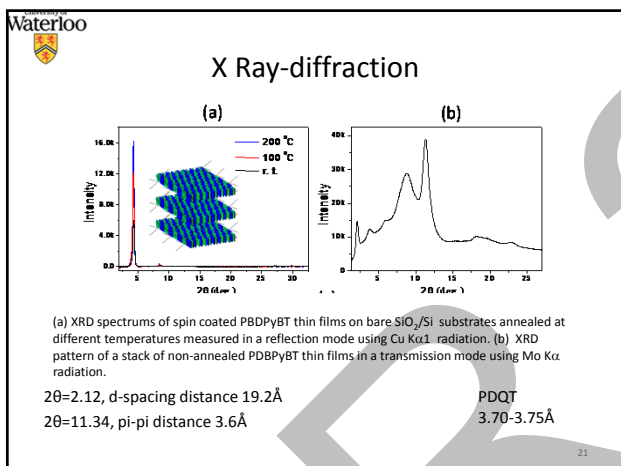
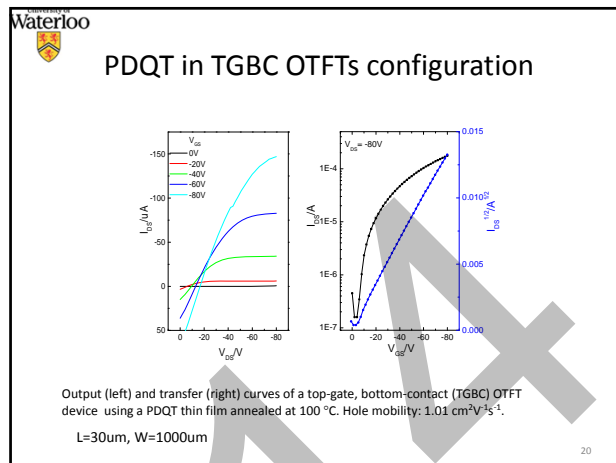
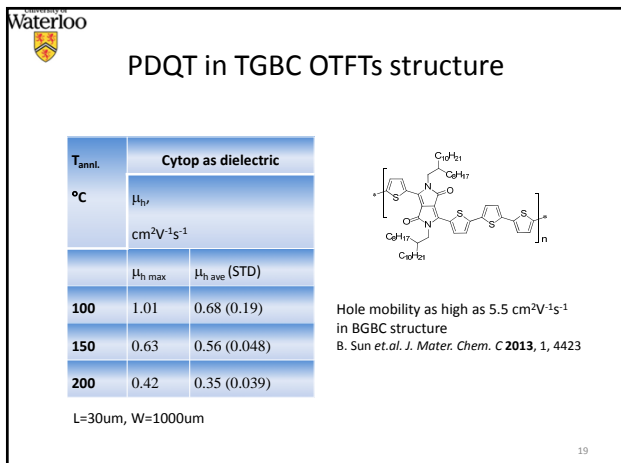
L = 30 μm, W = 1000 μm

17

Output and Transfer

- Annealed at 100 °C
- $\mu_e = 6.30 \text{ cm}^2\text{V}^{-1}\text{s}^{-1}$
- $\mu_h = 2.26 \text{ cm}^2\text{V}^{-1}\text{s}^{-1}$

18



- Waterloo
- ## Summary
- A donor-acceptor copolymer of PBDPyBT was synthesized, which showed high crystallinity and a very short π - π stacking distance of 0.36 nm.
 - High ambipolar charge transport performance with a record high electron mobility value of 6.30 $\text{cm}^2\text{V}^{-1}\text{s}^{-1}$ was achieved in OTFT devices at a mild annealing temperature of 100 °C.
 - Our results demonstrate that DBPy is a highly promising new building block for polymer semiconductors for OTFTs and other applications.
- 22

- Waterloo
- ## Acknowledgements
- Zhuangqing Yan for computer simulation
 - Dr. Wei Hong for UV-Vis and CV measurements
 - Jon Hollinger and Prof. Dwight Seferos of University of Toronto for the measurements of molecular weight
- The authors thank the Natural Sciences and Engineering Research Council (NSERC) of Canada for financial support (Discovery Grants)
- 
- B. Sun, W. Hong, Z. Yan, H. Aziz, Y. Li, *Adv. Mater.* **2014**, 26, 2636.
- 23

Waterloo

Thank you !

24

Institute for Polymer Research

Celebrating 30 years of Official Institute Status

Symposium documents for

Dihua Wu

Thin Film Composite Nanofiltration Membrane Formed by Interfacial Polymerization

Dihua Wu, IPR Symposium, University of Waterloo, ON N2L 3 G1, Canada

Nanofiltration (NF) is a pressure-driven membrane process between reverse osmosis (RO) and ultrafiltration (UF) in terms of membrane structure. It generally has a high flux, a high retention to multivalent ionic salts and organic molecules with molecular weights above 300 and a relatively low capital and operating costs. Since Cadotte and his co-workers^{1,2} fabricated high-flux, high-rejection reverse osmosis membranes by interfacial polymerization, thin film composite (TFC) membranes have become commonly used in industry. Preparation of TFC nanofiltration membranes based on interfacial polymerization is generally using two reactive monomers: a polyfunctional amine dissolved in water (i.e., aqueous reactant) and a polyfunctional acid chloride dissolved in a hydrocarbon solvent (i.e., organic reactant). The two solvents are in contact only at their interface, and this allows the reaction to take place at the interface. By employing this approach, an ultrathin polymeric layer (300 - 400 nm) can be formed and adhered to a microporous substrate, leading to a good combination of water permeability and selectivity.

Many efforts have been made to explore new monomers as reactants to improve membrane performance. Besides small molecular reactants with relatively low molecular weights, efforts have been made to investigate the behavior of polymeric amines for use as aqueous reactants. In our study, highly branched polyethylenimine (PEI) is chosen as the aqueous reactant. The high amine group density of PEI deriving from the macromolecular structure provides a large number of reactive sites,³ which favors the interfacial polymerization process. The lower reactivity of PEI⁴ due to the long polymer chain makes the reaction can be manipulated, so that the properties of the resultant membrane can be tailored. The organic reactant is trimesoyl chloride (TMC), the chemical reaction mechanism between PEI and TMC to form a polyamide layer is proposed in Figure 1.

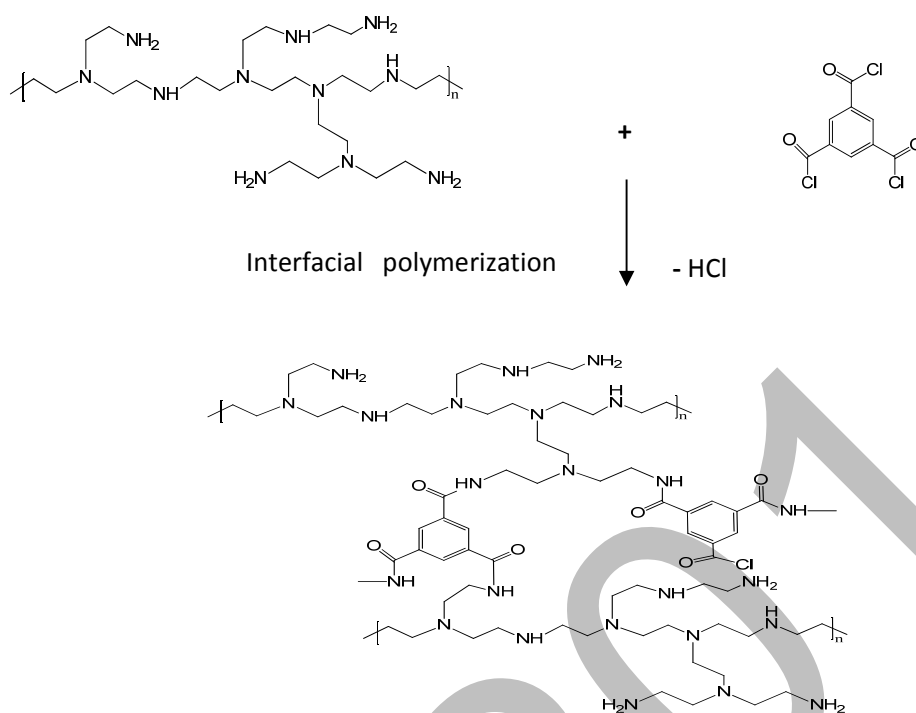


Fig. 1 Interfacial polymerization between PEI and TMC for polyamide formation

Experimental

The microporous flat-sheet polyethersulfone (PES) support membranes used for interfacial polymerization were presoaked in de-ionized water overnight. The aqueous phase reactant solution was prepared by dissolving PEI in de-ionized water. The organic phase reactant solution was composed of TMC in hexane. To begin with, the water wet substrate was dried in air. The aqueous solution of PEI was poured on top of the support membrane and allowed to contact with the PES layer. Then the excess aqueous solution was poured out and the membrane was drained. Then organic phase reactant solution was introduced to contact with the PEI-loaded PES substrate to induce interfacial polymerization. The excess organic solution was removed from the membrane surface. After this, the membrane was placed in an oven with forced air circulation at 95 °C for 20 min to ensure polymerization. Finally, the resulting membrane was washed and rinsed thoroughly with de-ionized water and stored in water for nanofiltration tests. Interfacial polymerization with a reversed sequence of reactant deposition was also carried out. That

is, the PES substrate membrane was first wetted with the organic phase reactant solution followed by contacting the aqueous phase reactant.

In order to improve the salt rejection of the membrane, the interfacial polymerization may be repeated to build up a layer-by-layer structure, i.e., membranes with multiple layers formed by interfacial polymerization, one layer at a time. For convenience of discussion, the membrane is considered to have one deposition layer after the deposition of the first reactant solution. After deposition of the second reactant phase, one interfacially polymerized layer was formed, and the membrane is considered to have two depositions of reactants (i.e., one polymerized layer). Then the membrane was allowed to contact with the first reactant solution again and the membrane is considered to have three reactant depositions (i.e., one polymerized layer and one deposition layer of the first reactant). These steps could be repeated to form membranes with multiple interfacially polymerized layers.

The membrane surface properties were characterized by attenuated total reflectance fourier transform infrared spectroscopy (ATR-FTIR), zeta potential analysis meter, field emission scanning electron microscopy (FE-SEM) and atomic force microscopy (AFM). The separation performance of the membrane was evaluated in terms of water flux and salt rejection. MgCl_2 , MgSO_4 , Na_2SO_4 and NaCl were used as four representative salts to characterize the separation performance of TFC membranes.

Results

Figure 2 shows the ATR-FTIR spectra of pristine PES substrate and two polyamide TFC membranes: PES-(PEI/TMC) and PES-(TMC/PEI). Compared to the ATR-FTIR spectrum of PES substrate, the presence of two new bands at 1645 cm^{-1} and 1545 cm^{-1} is observed for the thin film composite membranes comprising of a polyamide surface layer. The two bands at 1645 cm^{-1} and 1545 cm^{-1} are characteristic of amide-I (C=O stretching) band and amide-II (N-H) band of amide groups (-CONH-). Both thin film composite membranes PES-(PEI/TMC) and PES-(TMC/PEI) have characteristic peaks of polyamide. This confirms the occurrence of interfacial polymerization between PEI and TMC and the formation of amide linkage (-CONH-) in the active skin layer, regardless which reactant was deposited on the PES substrate first.

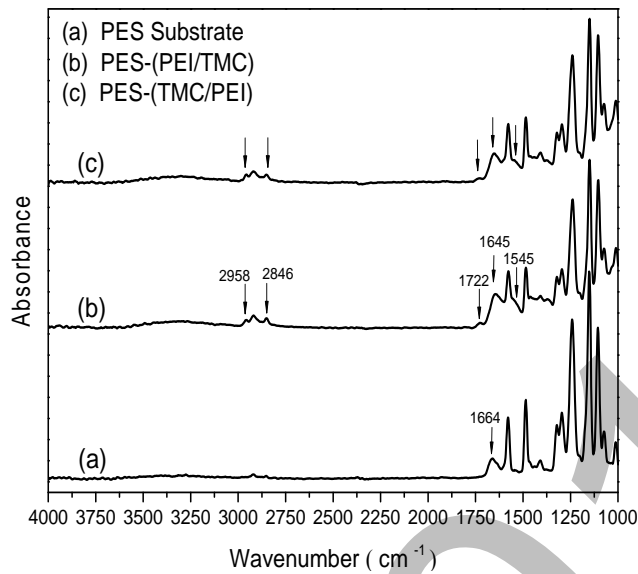


Fig. 2 ATR-FTIR spectra of (a) PES substrate, (b) composite membrane PES-(PEI/TMC) and (c) composite membrane PES-(TMC/PEI)

The separation performance of the multiple layers composite membranes fabricated by interfacial polymerization with reactant depositions in the sequence of PEI and TMC is shown in Figure 3 for the permeation flux (a) and salt rejection (b), respectively. For comparison, the separation performance of the PES substrate alone was also tested at a lower pressure of 0.2 MPa gauge.

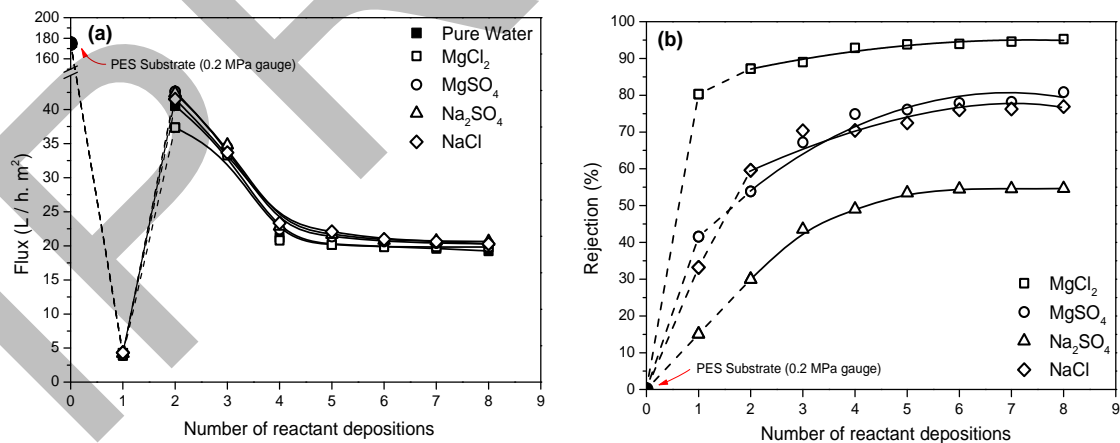


Fig. 3 Effect of number of reactant depositions on (a) permeation flux and (b) salt rejection for membranes prepared by interfacial polymerization in sequence of PEI-TMC. (Operating pressure: 0.8 MPa gauge, except for PES substrate which was tested at 0.2 MPa gauge; Salt concentration: 500 ppm)

As expected, the PES substrate has a high permeability, with a flux of 175 L/(m².h) at a transmembrane pressure of 0.2 MPa gauge. When coated with PEI (see membrane with “1” reactant depositions in Figure 3(a)), the permeation flux drops dramatically to about 4 L/(m².h) at a transmembrane pressure of 0.8 MPa gauge. It is interesting to note that the flux increases to about 40 L/(m².h) at 0.8 MPa gauge after the surface deposited PEI reacted with the TMC solution to form an interfacially polymerized polyamide layer (see membrane with “2” reactant depositions in Figure 3(a)). After a second cycle of interfacial polymerization, the membrane permeability is lowered by ~50%, as shown by the flux data (Fig. 3(a)) of membrane with “4” reactant depositions. The permeation flux begins to level off with a further increase in the number of sequential depositions of reactants PEI and TMC. The gradually increased salt rejection showed in Fig. 3(b) indicates that the increase in the number of reactant depositions has the potential to improve salt rejection.

References

1. Cadotte, J.E.; Cobian, K.E.; Forester, R.H.; Petersen, R.J., *NTIS Report* No. PB-253193, loc. cit., **1976**.
2. Cadotte, J.E.; Steuck M.J.; Petersen, R.J., *NTIS Report* No. PB- 288387, loc. cit., **1978**.
3. Tomalia, D. A., *Macromolecular symposia*, **1996**, 101, 243.
4. Sun, S. P.; Hatton, T. A.; Chung, T. S., *Environmental Science & Technology*, **2011**, 45, 4003.

Thin Film Composite Nanofiltration Membranes Formed by Interfacial Polymerization

PhD Candidate: Dihua Wu
 Supervisor: Professor Xianshe Feng
 IPR Symposium
 May 21, 2014

Department of Chemical Engineering
 University of Waterloo

1

Outline

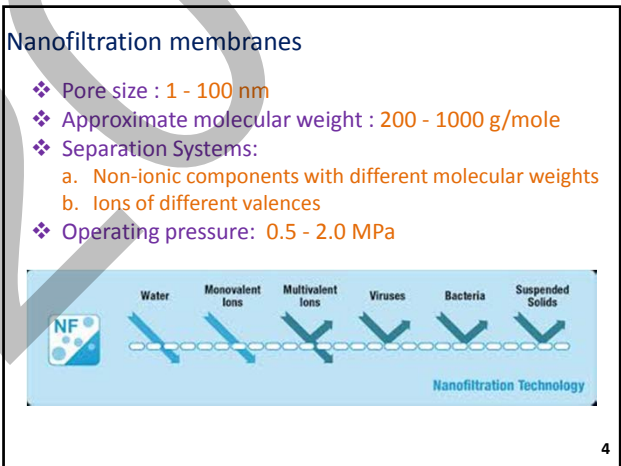
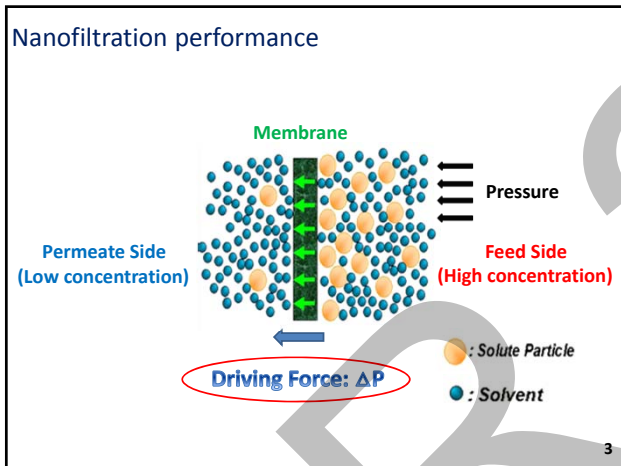
Introduction & Background

- What is nanofiltration (membrane) ?
- What is nanofiltration used for
- How to prepare nanofiltration membranes

Our Study

- What we did (Experiments) ?
- What we get (Results)

2



Applications of nanofiltration membranes

Wastewater treatment and reuse:

- ❖ Natural organic matters ✕
- ❖ Tastes, odours and colours ✕
- ❖ Herbicides ✕
- ❖ Disinfectants in drinking water ✕

Water softening:

- ❖ Hardness ↓ (Ca²⁺, Mg²⁺)

5

Applications of nanofiltration membranes

Product separation, concentration and recovery:

- ❖ Dairy Sector
 - Concentrate whey
 - Recycle clean solution
- ❖ Sugar Processing Sector
 - Concentrate dextrose syrup, thin sugar juice
 - Demineralization
- ❖ Edible Oil Processing Sector
 - Degumming

Food Industry

Chemical Industry

- ❖ Pharmaceutical and Biotechnical Sector
 - Recover valuable chemicals
 - Purify high value products

6

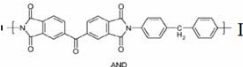
Applications of nanofiltration membranes



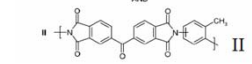
Organic Solvent Nanofiltration (OSN)
 ❖ Petroleum refinery for oil dewaxing



DuraMem® & PuraMem® Membrane Series



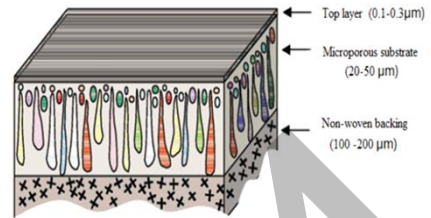
Membrane Separation in Organic Solvents



P84® polyimide: 20% I, 80% II

7

Thin film composite nanofiltration membranes



Top thin selective layer

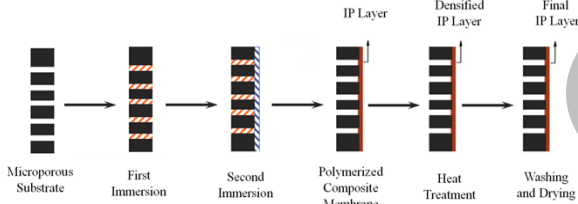
Microporous substrate

Can be tailored separately

- High flux
- High solute rejection
- Mechanical stability
- Thermal stability (0 - 45 °C)
- Wide pH tolerance (2 - 11)

8

Interfacial polymerization



Amine in aqueous phase

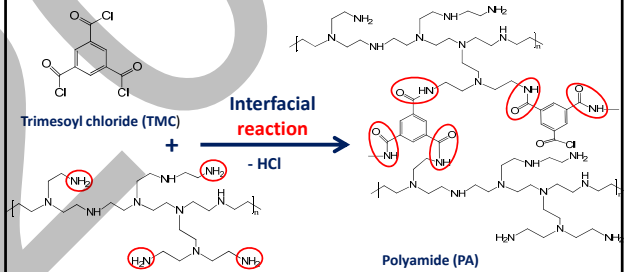
- m-Phenylenediamine (MPD) Nc1cccc(N)c1
- Piperazine (PIP) C1CCNCC1

Acyl chloride in organic phase

- Trimesoyl chloride (TMC) ClC(=O)c1cc(C(=O)Cl)cc1C(=O)Cl
- Isophthaloyl chloride (IPC) ClC(=O)c1cccc(C(=O)Cl)c1

9

Interfacial reaction between TMC and PEI

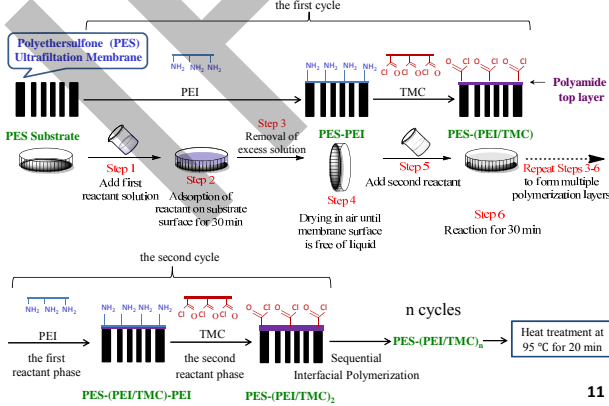


Polyethylenimine (PEI)
 $\bar{M}_n = 10,000$
 $\bar{M}_w = 25,000$

- Selection of PEI:**
- Macromolecular structure
 - high -NH₂ densities
 - lower reactivity than small molecular amines
- Formed thin film: loose → dense

10

Membrane preparation



11

Experimental work

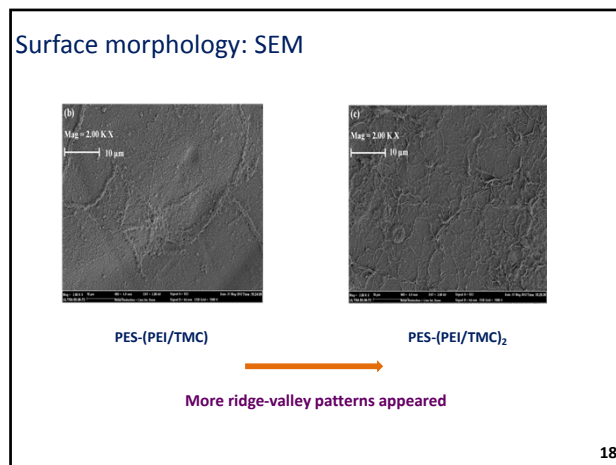
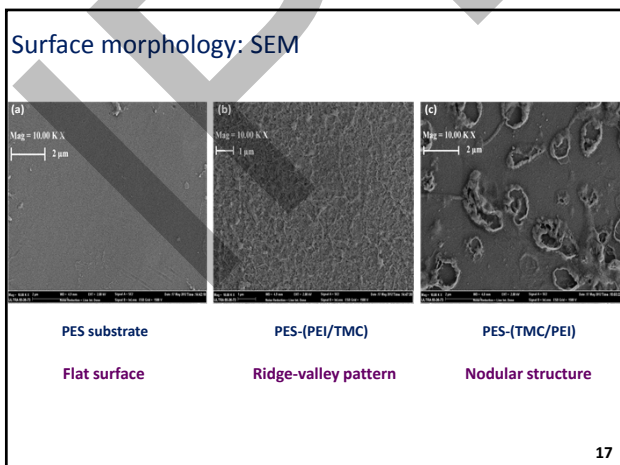
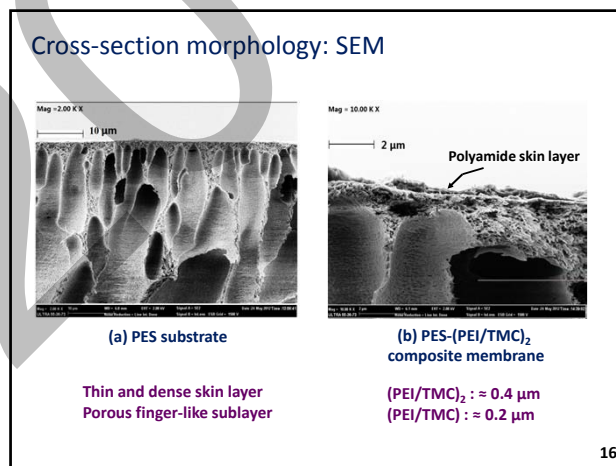
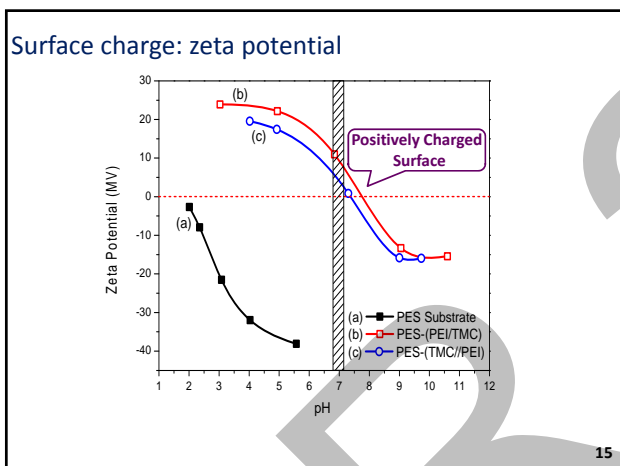
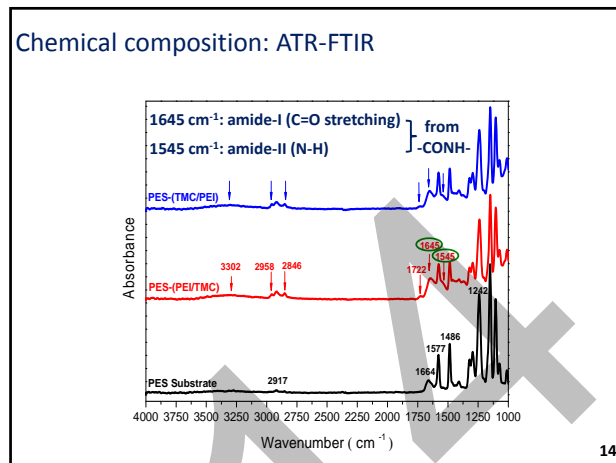
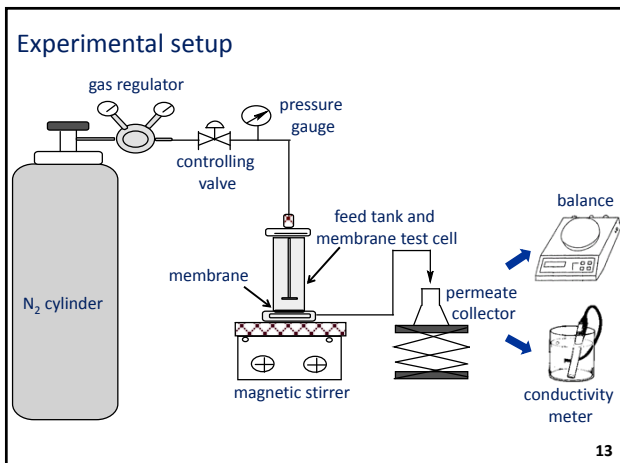
Characterization:

- Chemical composition: ATR-FTIR
- Surface charge: Zeta potential
- Surface morphology and topology: SEM & AFM

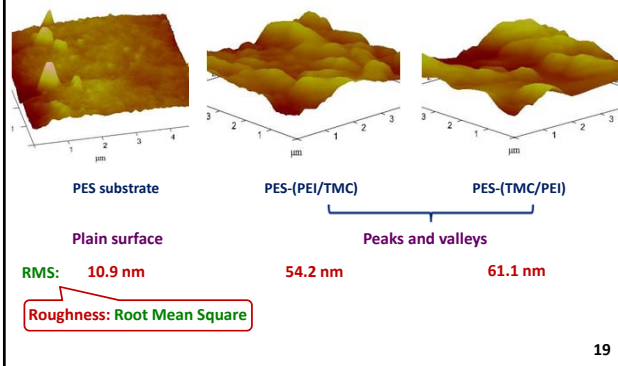
Separation properties:

- Permeation flux (J) $J = \frac{Q}{S \Delta t}$ [L/(m².h)]
 - Salt rejection (R) $R = (1 - \frac{C_p}{C_f}) \times 100 \%$
- Q: volume of permeate (L)
 S: membrane area (m²)
 Δt : time interval (h)
 C_p: solute concentration in the permeate (ppm)
 C_f: solute concentration in the feed (ppm)

12

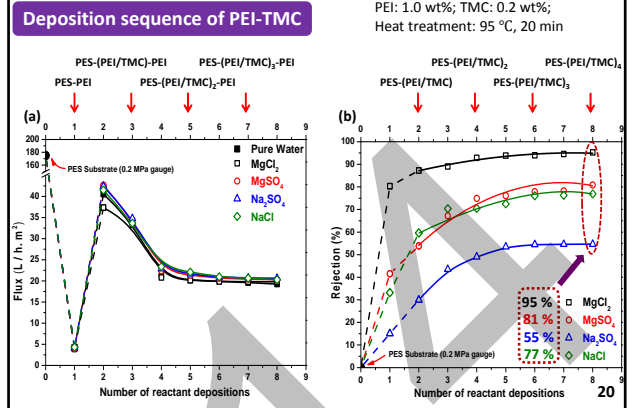


Surface topology: AFM



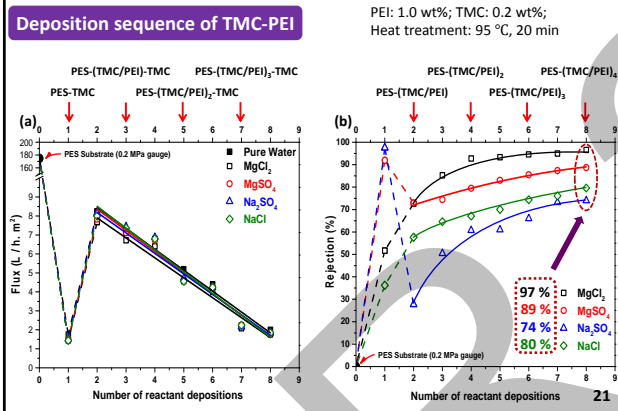
19

Separation performance: multiple layer membranes



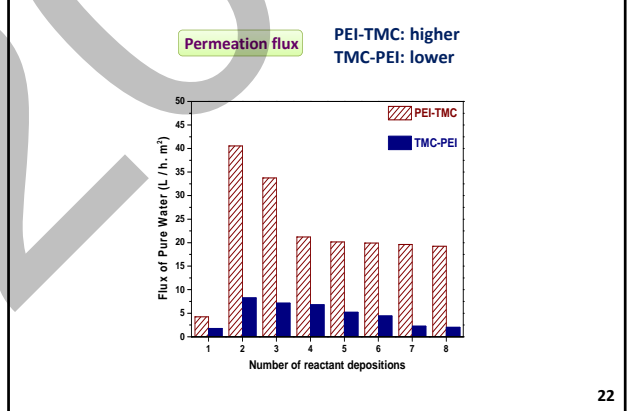
20

Separation performance: multiple layer membranes



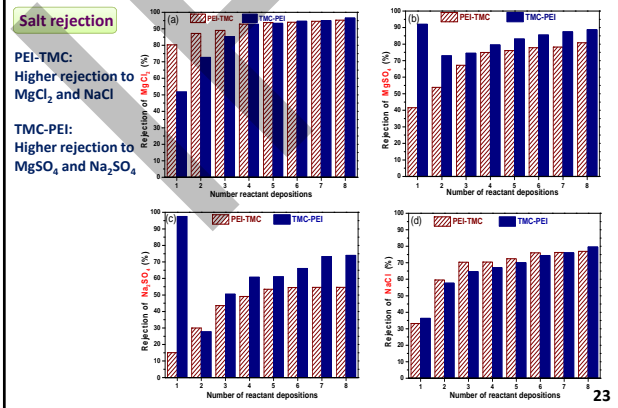
21

Comparison: two sequence of reactant depositions



22

Comparison: two sequence of reactant depositions



23

Conclusions

- Positively charged thin film composite nanofiltration membranes prepared by interfacial polymerization from PEI and TMC showed good performance for salt separation
- Membranes formed with the PEI-TMC deposition sequence showed an evenly distributed valley-ridge morphology, while membrane formed with the TMC-PEI deposition sequence showed irregularly distributed nodular structures
- Increasing the number of reactant depositions improved the salt rejection but decreased the permeation flux

24

Acknowledgement

- Financial support



- Prof. Xianshe Feng
- Members in Feng's group: Yifeng Huang, Boya Zhang, Shuixiu Lai, Xincheng Xu, Kai Wu

25

Thank you !

26

IPR 2014

Institute for Polymer Research

Celebrating 30 years of Official Institute Status

Symposium documents for

Boya Zhang

Recovery of dairy flavor compounds by pervaporation using poly(ether block amide)

Boya Zhang, Xianshe Feng, IPR Symposium, University of Waterloo, ON N2L 3G1, Canada

During dairy products processing, many flavor compounds are lost due to their high volatility. Even a small amount of loss of flavor compounds may significantly affect products' sensory quality. Since artificial flavors cannot satisfy consumers' interest anymore, it is necessary to recover these flavor compounds before commercial processing from raw dairy recourses and then add them back to the final products.

Traditional flavor fractionation processes are based on extraction, distillation, partial condensation, and gas stripping [1,2]. Pervaporation, as a novel separation technique, was introduced as an alternative to the current separation technologies. Its major advantages include: the moderate operating temperature used in pervaporation can reduce the energy consumption; the mild temperature can also protect product integrity from thermal degradation, especially for heat sensitive compounds. In a pervaporation process, a feed liquid mixture contacts one side of a dense membrane, while the preferential permeate diffuses through the membrane and evaporates on the other side by using a vacuum pump. The non-permeated components in the retentate are usually recycled into the feed stream for further recovery.

Polyether block amide (PEBA) 2533 is a copolymer comprising 80 wt.% poly(tetramethylene oxide) and 20 wt.% nylon 12. Its general formula is shown in Figure 1 [3], where PA and PE represent polyamide and polyether segments, respectively. PEBA 2533 has a good selectivity of flavor compounds due to the strong affinity between the polyether segments and the flavor compounds.

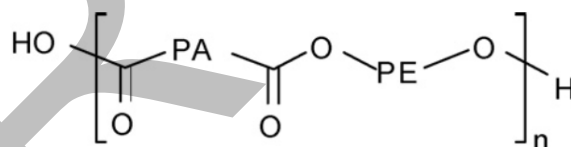


Figure 1 Structure of PEBA

The objective of this study is to investigate the pervaporation performance of PEBA 2533 membrane on separating flavor compounds from dairy model solutions. The effects of independent variables like feed concentration and operating temperature, on organic flux and enrichment factor were studied. The coupling effect was also investigated by comparing the pervaporation results obtained in binary and multicomponent systems.

1 Experimental

Eight flavor compounds, which represent six categories of dairy flavor compounds (esters, ketones, aldehydes, acids, sulfur compounds and aromatic compounds), were recovered by pervaporation. The flavor compounds included ethyl hexanoate (EH), ethyl butanoate (EB), 2-heptanone (2-Hep), diacetyl, methyl sulfone (MS), indole, nonanal and hexanoic acid (HA). For single flavor compound

pervaporation, each flavor compound was diluted by deionized water to make a dilute flavor–water binary feed solution. For multicomponent pervaporation, the feed solution was prepared by mixing the eight organics with deionized water.

Pervaporation experiments with binary and multicomponent feed solutions were carried out at various flavor concentrations and temperatures. Figure 2 shows the schematic diagram of the experimental set-up for pervaporation separation. The PEBA membrane was mounted into the permeation cell. The feed solution was continuously circulated through the membrane cell and back into the 1000 mL feed tank. Vacuum was applied on the permeate side to generate pressure difference, which providing the driving force. The permeate sample was condensed in a cold trap immersed in liquid nitrogen ($-196\text{ }^{\circ}\text{C}$), and analyzed by gas chromatography.

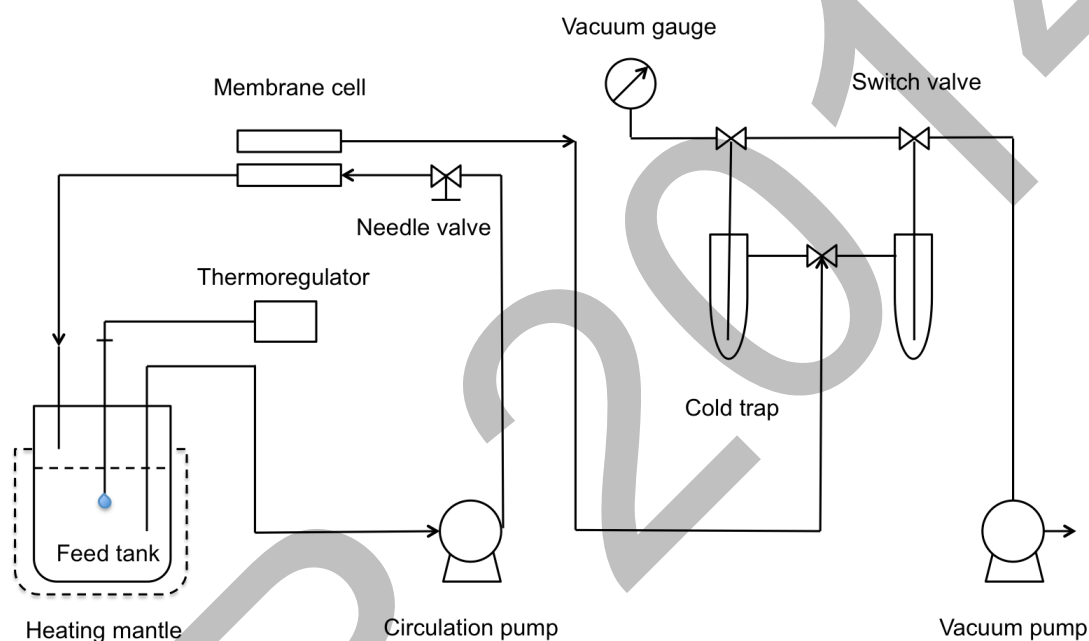


Figure 2 Schematic diagram of the pervaporation setup

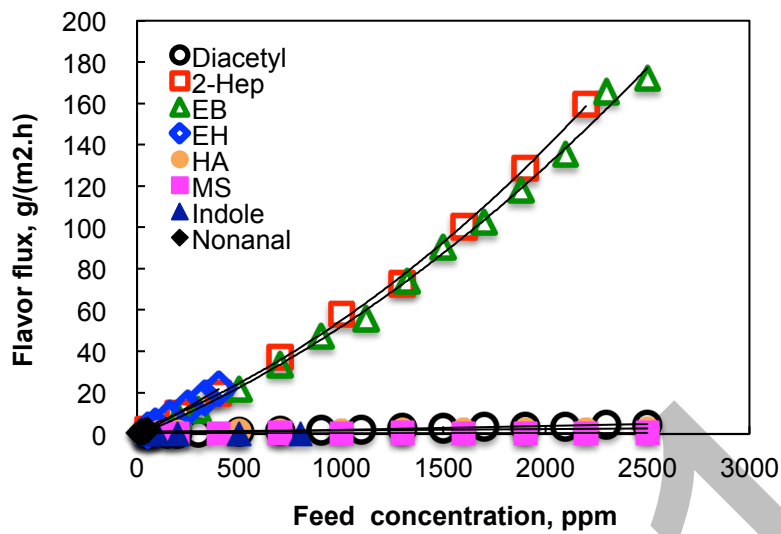
2 Results and discussion

2.1 Influence of feed concentration

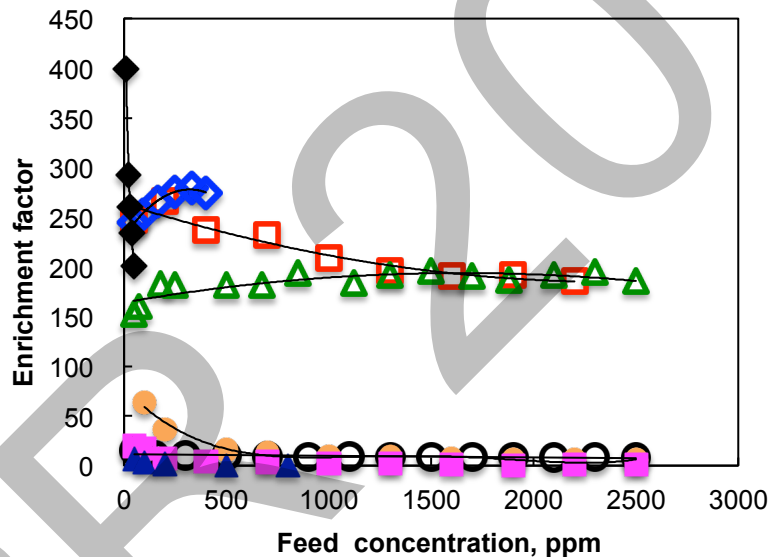
Pervaporation separation of flavor compounds from binary feed solutions with PEBA 2533 membrane was investigated at various feed concentrations and temperatures. Figures 3 (a) and (b) show the effect of the feed flavor concentration on the flavor permeation flux and enrichment factor, respectively.

All of the flavor compounds flux increases as the feed concentrations increase. That is because with the feed flavor concentration increasing, the partial pressure difference of the flavor compound between the two sides of the membrane increase, which leads to a higher driving force of the pervaporation process. The enrichment factors change little with the feed concentration, especially beyond 1000 ppm.

Moreover, the flux of the two esters (ethyl hexanoate and ethyl butanoate), one of the ketones (2-heptanone) and the aldehyde (nonanal) increase more significantly than other compounds when feed concentration increase; their enrichment factors are higher as well.



(a)



(b)

Figure 3 Effect of feed flavor concentration on (a) the flavor flux and (b) enrichment factor for binary flavor-water solutions using PEBA 2533 membrane.

2.2 Influence of operating temperature

Operating temperature has a significant influence on flavor compound flux. The flavor flux increases obviously as temperature increases. This is because an increase in temperature generally increases both the diffusivity of the permeant and the thermal motion of the membrane polymer chains, which facilitates the movement of permeant.

2.3 Pervaporation with multicomponent feed solutions

The multicomponent feed solutions were prepared by mixing eight flavors and water in different mass ratios. Figure 4 shows the comparison between the flavors

enrichment factors obtained from binary and multicomponent systems (the organics concentration: nonanal 15 ppm, indole 100 ppm, EH 100 ppm, other flavors 500 ppm; five operating temperatures were tested, the results shown are average value of the enrichment factors under the five temperatures). It clearly shows that the enrichment factors of most flavors are lower in multicomponent system than in binary system, which indicates coupling effects exist under such flavor concentrations. This happens probably due to the competition and interaction between the flavor compounds when they penetrating the membrane.

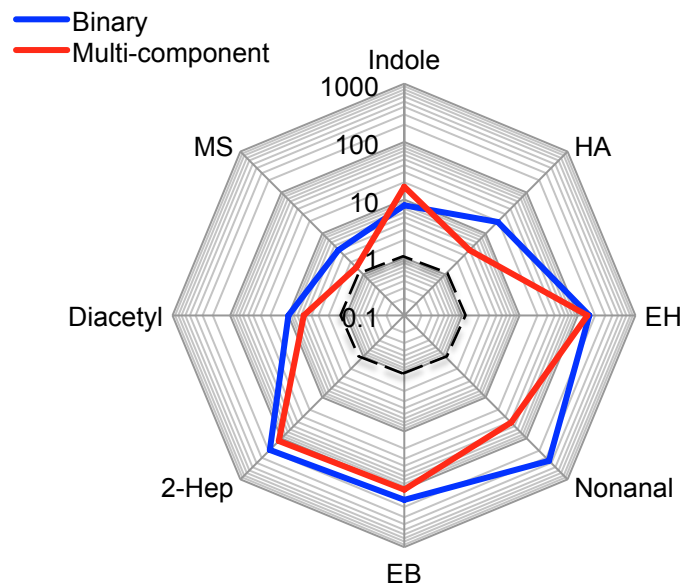


Figure 4. The flavors enrichment factors obtained from binary and multicomponent systems (the organics concentration: nonanal 15 ppm, indole 100 ppm, EH 100 ppm, other flavors 500ppm; the results shown are average value of the enrichment factors under the five temperatures).

Reference

- [1] H.E. Karlsson, G. Triigiirdh, *Aroma Recovery During Beverage Processing*, 34 (1998) 159–178.
- [2] A. Baudot, M. Marin, *Pervaporation of aroma compounds: Comparison of membrane performances with vapour-liquid equilibria and engineering aspects of process improvement*, *Food Bioprod. Process.* 75 (1997) 117–142.
- [3] M.K. Mandal, P.K. Bhattacharya, *Poly(ether-block-amide) membrane for pervaporative separation of pyridine present in low concentration in aqueous solution*, *J. Memb. Sci.* 286 (2006) 115–124.

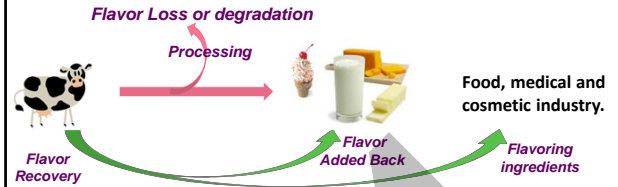
DAIRY FLAVOR RECOVERY BY PERVAPORATION USING POLY(ETHER BLOCK AMIDE) MEMBRANE

IPR symposium

Boya Zhang
Supervisor: Prof. Xianshe Feng
May 21, 2014



BACKGROUND



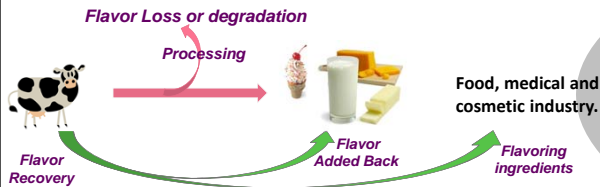
Traditional methods for recovering:

Distillation, partial condensation & gas stripping

Problems: product contamination and degradation, high energy consumption

IPR Presentation – BOYA ZHANG | 2

BACKGROUND



Pervaporation– an alternative recovery method

Why pervaporation?

High selectivity, low energy consumption, mild operating temperatures and no damage to heat-sensitive flavors

IPR Presentation – BOYA ZHANG | 3

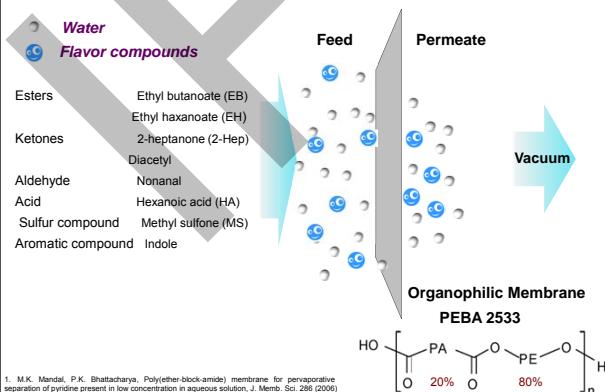
OBJECTIVE

To investigate pervaporation as a mean of recovering flavor compounds from dairy model solutions, using an organophilic membrane material: poly(ether block amide) (PEBA).

- To determine how the operating conditions affected the pervaporation of each flavor compound.
- To compare the pervaporation behavior of single flavor component and multiple flavor components, in order to determine whether there is any "coupling effect" between permeating species.

IPR Presentation – BOYA ZHANG | 4

Flavor pervaporation process



1. M.K. Mandal, P.K. Bhattacharya, Poly(ether-block-amide) membrane for pervaporative separation of pyridine present in low concentration in aqueous solution, J. Membr. Sci. 296 (2006) 115–124.

IPR Presentation – BOYA ZHANG | 5

Evaluation of pervaporation performance

Flux (J_i)

Permeate flow rate of component i per unit membrane area.

$$J_i = \frac{N_i}{A}$$

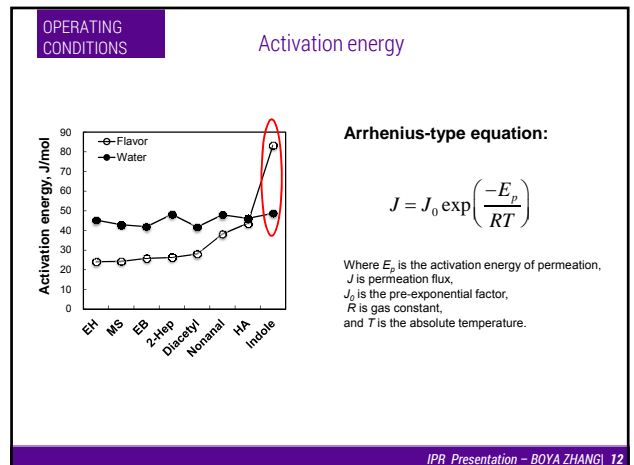
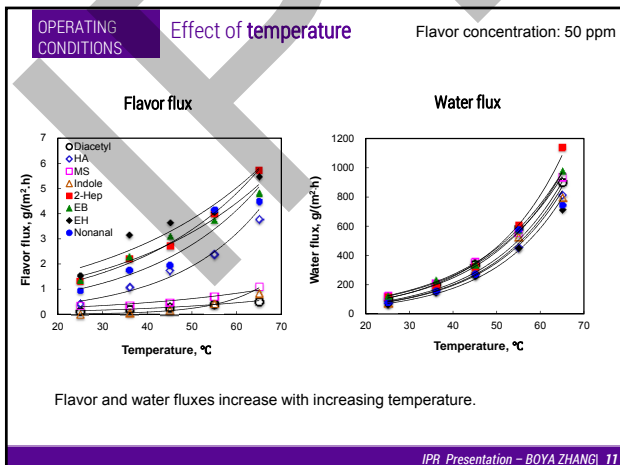
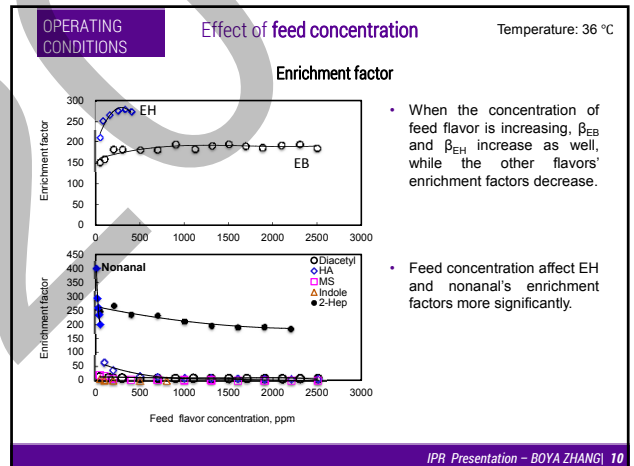
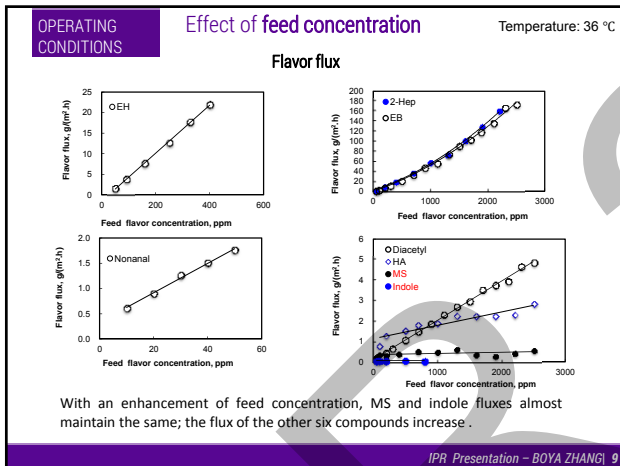
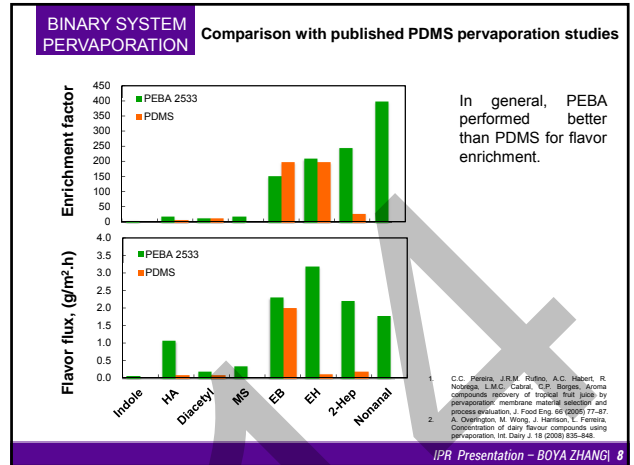
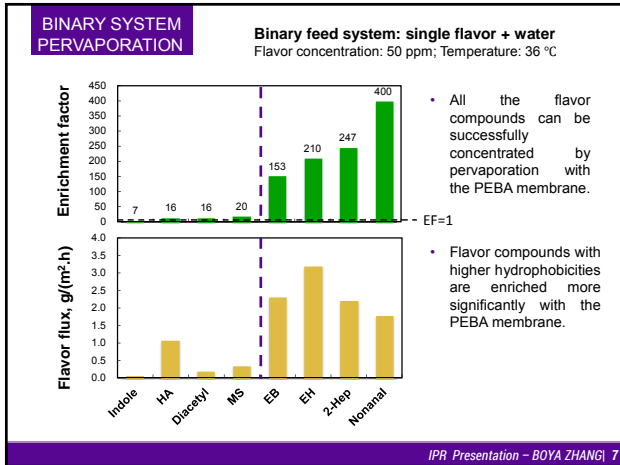
Enrichment factor (β_i)

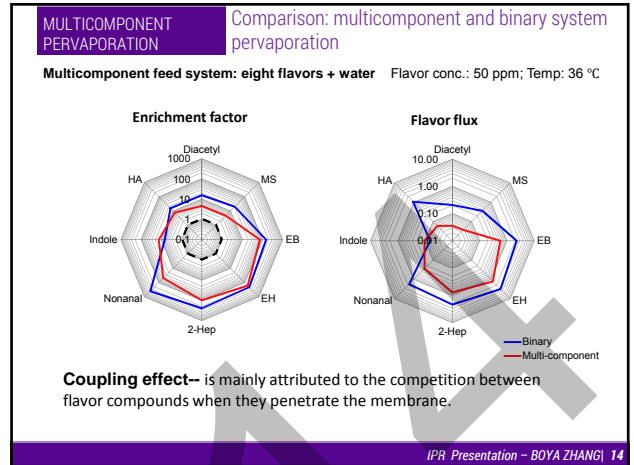
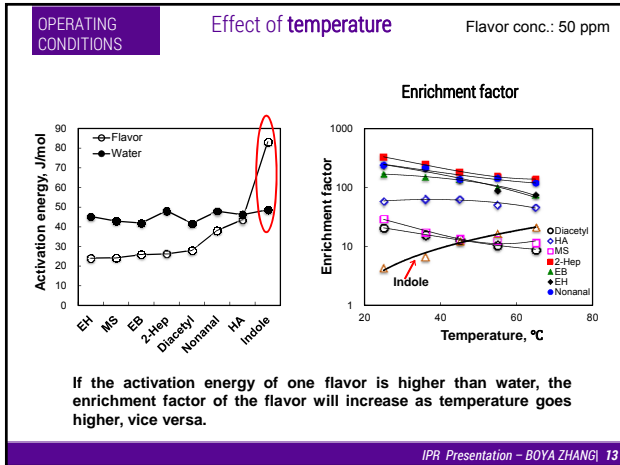
Ratio of component i 's concentrations in permeate and in feed.

$$\beta_i = \frac{C_{p_i}}{C_{f_i}}$$

Pervaporative enrichment process is effective only when $\beta_i > 1$.

IPR Presentation – BOYA ZHANG | 1





- CONCLUSIONS**
- PEBA 2533 has good pervaporation performance on concentrating dairy flavors, especially hydrophobic ones.
 - The increase in feed concentration has positive effects to the flavor fluxes; however, its impact on enrichment factor varies from compound to compound, depending on the nature of the flavor molecule.
 - Temperature affects the enrichment of dairy flavors as well. The temperature dependence of flavor and water fluxes obeys Arrhenius-type relationship. Flavors and water's activation energy determines the changing trend of enrichment factor.
 - In multicomponent pervaporation, the "coupling effect" between permeating species decreases the flavors enrichment.
- IPR Presentation – BOYA ZHANG | 15

- ACKNOWLEDGEMENT**
- Financial support
-
- Prof. Xianshe Feng
 - Members in Feng's group: Dihua, Yifeng, Shuixiu, Xincheng, Kai, Yijie, Guan.
- IPR Presentation – BOYA ZHANG | 16

Thank You!

IPR Presentation – BOYA ZHANG | 17

Institute for Polymer Research

Celebrating 30 years of Official Institute Status

Thirty-Sixth Annual Symposium on Polymer Science/Engineering

Wednesday, May 21, 2014

Conrad Grebel University

University of Waterloo

Posters

Yasaman Amintowli Chemical Engineering, Waterloo	Photoinitiator-induced Modification of Polypropylene: The Effect of Acrylic Co-agent
Remi Casier Chemistry, Waterloo	Using Visible Light to Probe Interparticle Diffusion in Latex Films
Shiva Farhangi Chemistry, Waterloo	Effect of Side Chain Length on the Internal Dynamics of Polymethacrylates in Solution
Michael Fowler Chemistry, Waterloo	Temperature Response of Aqueous Solutions of a Series of Pyrene End-Labeled Poly(<i>N</i> -isopropylacrylamide)s Probed by Fluorescence
Chang Guo Chemical Engineering and Waterloo Institute for Nanotechnology (WIN), Waterloo	Synthesis and Properties of Indigo based Donor–Acceptor Conjugated Polymers
Niusha Kazemi Chemical Engineering, Waterloo	Case Studies with Optimal Estimation of Reactivity Ratios in Terpolymerization Systems
Mylène Le Borgne Chemistry, Waterloo	Diketopyrrolopyrrole oligomer for solution process solar cells
Solmaz Pirouz Chemistry, Waterloo	A Novel Method to Determine the Chemical Composition of Polyisobutylene-Based Oil-Soluble Dispersants by Fluorescence
Marzieh Riahinezhad Chemical Engineering, Waterloo	Reactivity Ratios in Polyelectrolyte Copolymerization: Does Ionic Strength Play a Role?
Ankita Saikia Chemical Engineering, Waterloo	Modelling the Vulcanization Reaction of Devulcanized Rubber
K. M. E. Stewart Chemical Engineering, Waterloo	Doped Polyaniline for the Detection of Ethanol
Alice Yang Chemistry, Waterloo	Preparation and Characterization of Temperature-Responsive Polymeric Surfactants
Wei Yi Chemistry, Waterloo	Probing Hydrophobically Modified Starch Nanoparticles by Pyrene Fluorescence and Transmission Electron Microscopy

Institute for Polymer Research

Celebrating 30 years of Official Institute Status

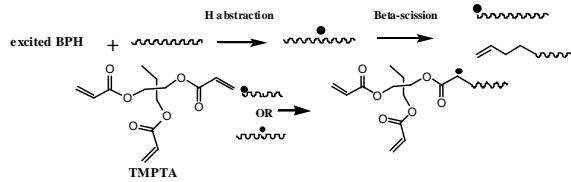
Symposium documents for

Yasaman Amintowlieh

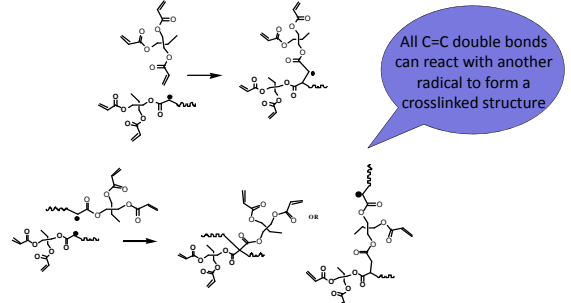
Introduction

- Melt strength (MS) of polypropylene (PP) has been modified utilizing benzophenone (BPH) as photoinitiator (PI) along with UV radiation
- Limitations of the process: long radiation time needed
- Trimethylpropane triacrylate (TMPTA) was used as co-agent to decrease radiation time
- Why TMPTA? Fast kinetics; Branching at low percentages
- Mechanism:

- A stable radical center is formed



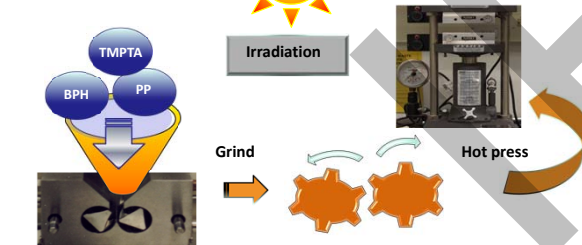
- Challenge: High gel content



Objective: Formation of long chain branching (LCB) rather than crosslinking using TMPTA along with photoinitiator in UV modification

Processing steps & Design of experiments

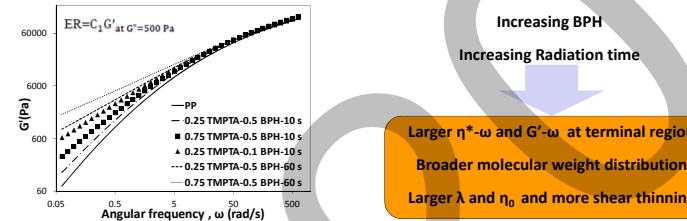
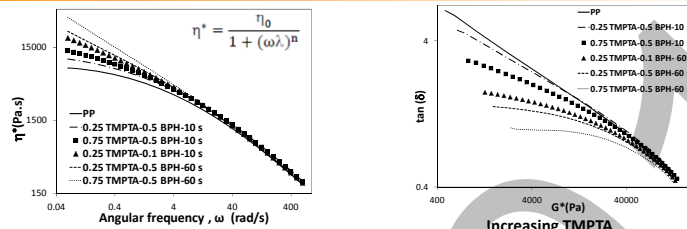
- Mixing photoinitiator (PI), PP and TMPTA
- Photoinitiator: Benzophenone (BPH)
- Radiation temperature <40 °C
- Radiation time changed



Process variable (units)	Range	2 ³ Factorial design	Response variables
Coagent (TMPTA) concentration (wt %)	0.25-0.75		
Photoinitiator (PI) concentration (wt %)	0.1-0.5		
Duration of radiation (s)	120-600		

Response variables: Viscoelastic properties, Gel content

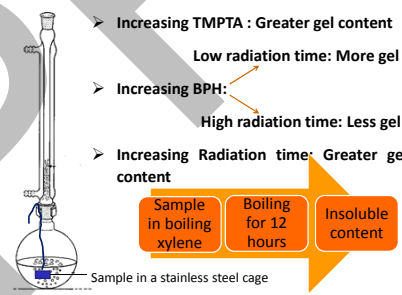
Rheological characterization: Viscoelastic properties



Run ID	Coagent (wt-%)	BPH (wt-%)	Time (min)	n	λ (s)	η ₀ (kPa)	ER
1	0.25	0.1	10	0.57	12.7	1.3	0.25
2	0.75	0.1	10	0.57	12.8	1.3	0.26
3	0.25	0.5	10	0.53	18.4	3.3	0.45
4	0.75	0.5	10	0.53	18.9	3.1	0.48
5	0.25	0.1	60	0.50	42.1	22.1	1.05
6	0.75	0.1	60	0.55	111.5	133.4	2.02
7	0.25	0.5	60	0.49	93.0	138.2	1.55
8	0.75	0.5	60	0.52	627.1	2,945.4	2.97
PP	0	0	0	0.61	8.8	0.6	0.13

Larger η*-ω and G'-ω at terminal region
 Broader molecular weight distribution
 Larger λ and η₀ and more shear thinning

Gel content



Increasing TMPTA: Greater gel content
 Increasing BPH: Low radiation time: More gel; High radiation time: Less gel
 Increasing Radiation time: Greater gel content

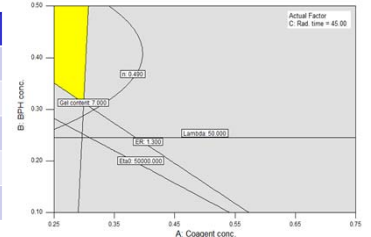
Run ID	Coagent-A (wt-%)	BPH-B (wt-%)	Time-C (min)	Gel Content (%)
1	0.25	0.1	10	1.2
2	0.75	0.1	10	6.2
3	0.25	0.5	10	5.9
4	0.75	0.5	10	13.3
5	0.25	0.1	60	7.5
6	0.75	0.1	60	36.1
7	0.25	0.5	60	5.6
8	0.75	0.5	60	26.4

Greater concentration of radicals increases the probability of combination between a stabilized radical center and another radical with no TMPTA in its backbone => less crosslinking

Optimized processing conditions

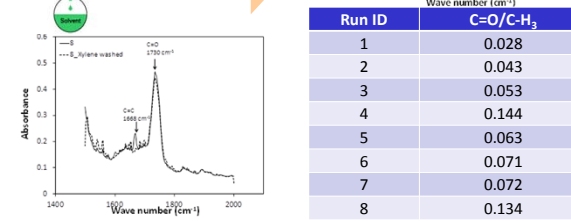
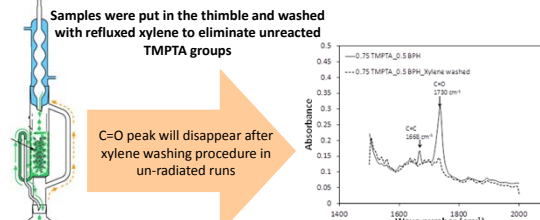
- The following criteria were used to find the processing window that results in the maximum long chain branching content with the lowest crosslinking

Response	Criteria
n	<0.49
η ₀ (Pa.s)	>50000
λ (s)	>50
ER	>1.3
Gel content (%)	<7



FTIR spectroscopy

- FTIR test was conducted on the runs after washing with xylene to verify TMPTA insertion in the PP chain



Concluding remarks and future steps

- Modification of PP via photoinitiation reaction was carried out in the presence of TMPTA as a coagent
- Increasing coagent content, or BPH content, or radiation time, will all lead to more shear thinning behavior and an increase in η₀, λ and ER due to formation of LCB
- It was confirmed via FTIR tests that increasing coagent content, or BPH content, or radiation time, leads to greater insertion of TMPTA monomer in PP chains, which results in formation of more long chain branches

Future steps

- Continuous modification process

Bibliography

- Parent JS, Bodsworth A, Sengupta SS, Kontopoulou M, Chaudhary BI, Poche D, Cousteaux S. Polymer 2009; 50: 85-94
- Shroff R, Mavridis H. J Appl Polym Sci. 1995; 57: 1605-1626
- Amintowlieh Y, Tzoganakis C, Hatzikiakos S. G. and Penlidis A. Polym Degrad and Stab. 2014; 104: 1-10.
- Socrates G. Infrared and Raman Characteristic Group Frequencies: Tables and Charts. Chichester; New York, Chichester; New York: Wiley, 2001

Institute for Polymer Research

Celebrating 30 years of Official Institute Status

Symposium documents for

Remi Casier

Remi Casier, Jean Duhamel, Mario Gauthier
Department of Chemistry

Institute for Polymer
Research (IPR)

Introduction

Films formed by aqueous latex dispersions have many applications, particularly in the paint industry. The conditions in which a uniform film is formed from latex particles strongly affect the rate at which the polymer chains in the particles interdiffuse. A film in which the latex particles are not allowed to fully coalesce can lead to poor mechanical strength and a performance below expected standards.^{1,2} The formation of latex films is generally divided into three main stages, as depicted in Figure 1.^{1,3,4}

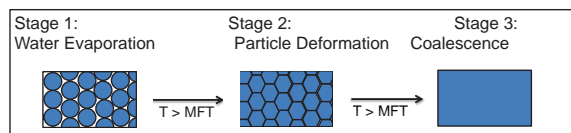


Figure 1: The formation of a homogeneous film from an aqueous latex dispersion.

In stage 1, the water is evaporated leaving behind a matrix of packed latex particles. Stage 2 involves the deformation of the latex particles as they fill in the voids in the matrix left from Stage 1. In Stage 3, interparticle polymer diffusion (IPD) generates the homogeneous film. In order for the latex particles to deform and coalesce, a certain minimum temperature is required, namely the minimum film formation temperature (MFT), which is generally close to or slightly above the glass transition temperature (T_g) of the polymer that constitutes the latex.

Fluorescence can be used to probe the diffusion of polymers in the latex as the films are being formed.^{1,2,5} In previous studies, two different fluorescently labeled latex polymers were required to probe the degree of IPD and the MFT of the latex film. Our proposal is to prepare a polymer randomly labeled with pyrene (Py) by emulsion polymerisation and use it to characterize the IPD and MFT of a latex film by probing pyrene excimer formation which avoids the use of a second fluorescently labeled latex.

Pyrene Fluorescence

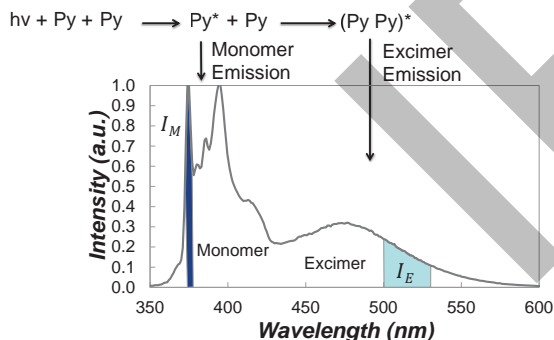


Figure 2: Reaction scheme for pyrene excimer formation (top) and resulting steady-state fluorescence spectrum (bottom).

Interparticle Polymer Diffusion

When pyrene is excited by a photon of light, it emits a blue colour. If an excited pyrene encounters a ground-state pyrene, it forms an excited dimer (excimer) which emits a turquoise colour, as described in Figure 2. The amount of excimer formed can be quantified with a steady-state (SS) fluorometer, by obtaining the ratio of the fluorescence intensity of the pyrene excimer (I_E) over that of the pyrene monomer (I_M), namely the I_E/I_M ratio.

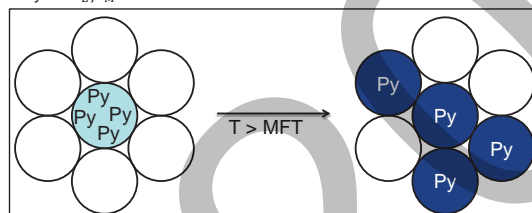


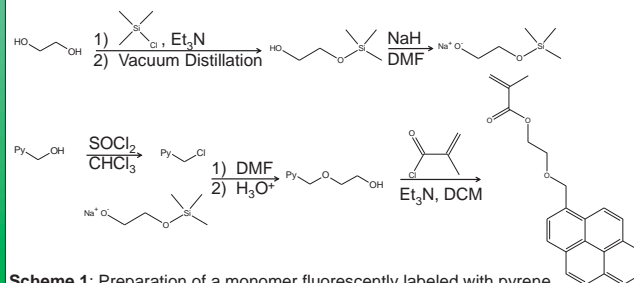
Figure 3: Interparticle diffusion of a pyrene labeled latex particle with neighbouring latex particles before (left) and after (right) annealing.

By preparing a polymer randomly labeled with pyrene by emulsion polymerization and incorporating it into a matrix of non-fluorescent latex particles, the I_E/I_M ratio can be used to determine the MFT and monitor the degree of IPD. The I_E/I_M ratio at annealing time t depends on the local concentration of pyrene (C_{py}) in the film. When the fluorescently labeled latex particles are first mixed into a matrix of native latex the $I_E/I_M(t=0)$ ratio is expected to be high, and the film should fluoresce with a turquoise colour. As the film is heated above its MFT and the pyrene-labeled polymer diffuses throughout the matrix, C_{py} should decrease and the $I_E/I_M(t > 0)$ ratio decreases.

In order to quantitatively describe IPD, the fraction of mixing at annealing time t ($f_m(t)$) can be calculated using the experimental $I_E/I_M(t)$ ratios via Equation 1, where $(I_E/I_M)_{t=\infty}$ is the I_E/I_M ratio after a long annealing time. Further by applying Fick's law to molecules diffusing out of a spherical particle, the polymer diffusion coefficient D can also be found.^{2,5}

$$f_m(t) = \frac{\left(\frac{I_E}{I_M}\right)_{(t)} - \left(\frac{I_E}{I_M}\right)_{(t=0)}}{\left(\frac{I_E}{I_M}\right)_{(t=\infty)} - \left(\frac{I_E}{I_M}\right)_{(t=0)}} \quad (1)$$

Pyrene Labeled Monomer



Scheme 1: Preparation of a monomer fluorescently labeled with pyrene.

Proof of Concept

To demonstrate that pyrene-labeled latex films can generate sufficient excimer fluorescence to monitor film formation, a *n*-butyl methacrylate copolymer randomly labeled with 4.7 mol% of pyrene from Scheme 1 (Py[4.7]-PBMA) was synthesized by free radical polymerization. The film prepared from this copolymer had a high I_E/I_M ratio. The film was then diluted down to 1 wt% using a non-fluorescent PBMA polymer to represent a time when the film has fully annealed. This resulted in a significant decrease in I_E/I_M as is demonstrated in Figure 4.

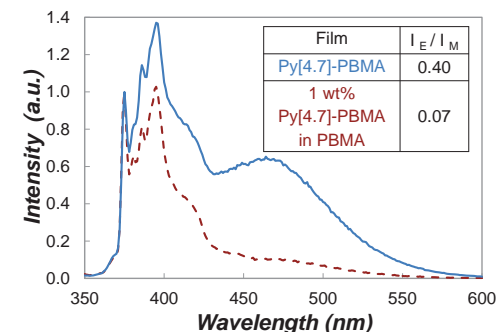


Figure 4: Steady-state fluorescence spectrum of films prepared with Py[4.7]-PBMA (—) and 1 wt% Py[4.7]-PBMA in PBMA (- -).

Emulsion Polymerization

A surfactant-free approach was used with a low solids content (1.5 % solids) using ammonium persulfate as the initiator. Polymerizations with *n*-butyl methacrylate at 90 °C for 2 hours produced well defined latex with a particle size of 150 nm.

Thus far, incorporation of the pyrene labeled monomer (Scheme 1) has met several challenges. The current obstacles faced are the low incorporation of pyrene, low molecular weight of the resulting polymers, and removal of pyrene that is not covalently attached to the polymer chains.

References

- Gauthier, C.; Guyot, A.; Perez, J.; Sindt, O. Film Formation and Mechanical Behavior of Polymer Latices. *Film Formation in Waterborne Coatings*, Chapter 10, 1996, 163-178. Washington, DC: American Chemical Society.
- Winnik, M.A. Latex Film Formation. *Current Opin. Colloid Interface Sci.* 1997, 2, 192-199.
- Eckersley, S.T.; Rudin, A. Film Formation of Acrylic Copolymer Latices: A Model of Stage II Film Formation. *Film Formation in Waterborne Coatings*, Chapter 1, 1996, 2-21. Washington, DC: American Chemical Society.
- Wang, Y.; Winnik, M. A. Polymer Diffusion across Interfaces in Latex Films. *J. Phys. Chem.* 1993, 97, 2507-2
- Zhao, C.; Wang, Y.; Hruska, Z.; Winnik, M.A. Molecular Aspects of Latex Film Formation: An Energy-Transfer Study. *Macromolecules* 1990, 23, 4082-4087

Acknowledgements

• Xiaozhou Chen



Institute for Polymer Research

Celebrating 30 years of Official Institute Status

Symposium documents for

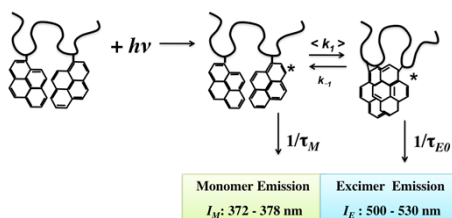
Shiva Farhangi

Introduction

The dynamics of polymer chains in solution are often invoked to rationalize the role of polymers in a number of phenomena such as the shear-thickening or thinning of solutions of viscosity modifiers or the folding of proteins in aqueous solution. Consequently, techniques capable of characterizing polymer chain dynamics in solution have attracted strong scientific interest. This study uses pyrene excimer formation to probe the internal dynamics of several pyrene-labeled poly(methacrylates).

Mechanism

The Kinetics for Pyrene excimer formation



$h\nu$ is the energy of one photon

k_1 is the excimer formation rate constant

k_{-1} is the excimer dissociation rate constant

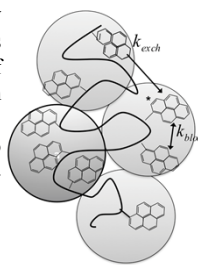
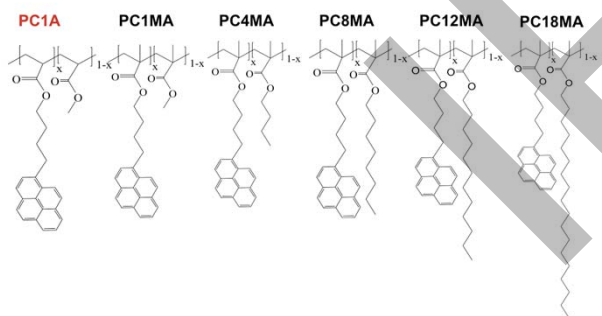
τ_M is the lifetime of the monomer

τ_{E0} is the lifetime of the excimer

Sample Preparation

Poly(methacrylates) randomly labeled with pyrene;

Radical copolymerization: 1-Pyrenebutyl methacrylate + Monomer



Molecular Weight and PDI

Py-PC1A			Py-PC1MA			Py-PC4MA		
Pyrene Content [mol %]	Mn [g/mol]	PDI [-]	Pyrene Content [mol %]	Mn [g/mol]	PDI [-]	Pyrene Content [mol %]	Mn [g/mol]	PDI [-]
0.3	265,000	1.38	0.3	134,000	1.70	0.3	174,000	1.93
2.6	236,000	1.40	1.3	130,000	1.42	1.1	272,000	1.99
2.6	313,000	1.40	2.7	200,000	1.33	2.2	296,000	1.44
3.0	173,000	1.42	4.0	135,000	1.60	3.0	197,000	1.39
5.0	138,000	2.08	5.3	206,000	1.70	3.6	264,000	1.68
6.2	145,000	1.38	5.6	170,000	1.55	5.3	275,000	1.97
6.7	870,000	2.40	7.3	176,000	1.80	7.2	416,000	1.76
Py-PC8MA			Py-PC12MA			Py-PC18MA		
Pyrene Content [mol %]	Mn [g/mol]	PDI [-]	Pyrene Content [mol %]	Mn [g/mol]	PDI [-]	Pyrene Content [mol %]	Mn [g/mol]	PDI [-]
0.4	244,000	1.87	0.5	530,000	1.72	0.7	563,000	1.54
1.8	305,000	1.88	1.4	265,000	1.70	1.4	810,000	1.52
2.7	312,000	1.75	3.5	244,000	2.43	4.5	480,000	1.44
4.3	146,000	2.04	5.6	507,000	1.70	5.9	663,000	1.42
5.1	371,000	1.83	6.0	174,000	2.17	6.8	705,000	1.41
6.1	234,000	1.88	7.7	662,000	2.10	6.7	719,000	1.49
7.3	271,000	2.07	10.2	265,000	1.68	14.2	770,000	1.45

Table-1: Molecular Weight and PDI of PC1A, PC1MA, PC4MA, PC8MA, PC12MA, and PC18MA obtained by GPC.

Results and Discussion

The steady-state fluorescence spectra and time-resolved fluorescence decays acquired for a series of Py-PC12MA samples with different pyrene content ranging from 1-10 mol% are shown in Figure 1.

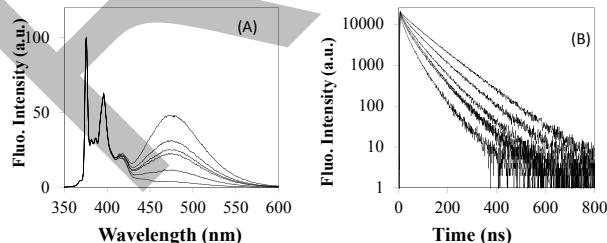


Fig. 1. Steady-state fluorescence spectra of Py-PC12MA in THF; Pyrene content decreased from top (10 mol%) to bottom (1 mol%). B) Time-resolved fluorescence decay of Py-PC12MA in THF. Pyrene content increased from bottom.

As the pyrene content of the polymer increases, more excimer is being formed as shown in the fluorescence spectra. The fluorescence decays of the pyrene monomer are shorter-lived reflecting enhanced excimer formation.

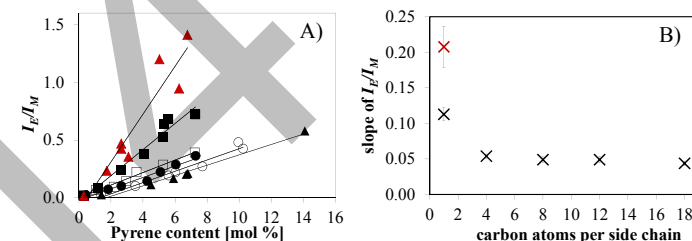


Fig. 2. A) I_E/I_M ratios for all polymers with increasing pyrene contents; \blacktriangle PC1MA, \blacksquare PC1MA, \square PC4MMA, \bullet PC8MMA, \circ PC12MMA, \blacktriangle PC18MMA. B) Slope of the I_E/I_M of PC1A, PC1MA, PC4MA, PC8MA, PC12MA, and PC18MA. The slope reaches a plateau as the side chain length increased from C4-C18.

I_E/I_M increases linearly with increasing pyrene content, but the slope decreases with increasing side-chain length due to slower internal dynamics of the main chain. Quantitative information about the changes in internal dynamics are obtained from the global analysis of the fluorescence decays according to the Fluorescence Blob Model (FBM).

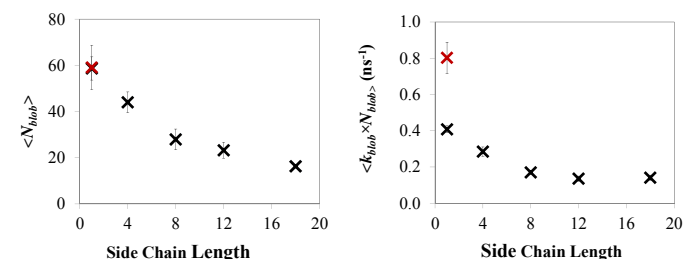


Fig. 3. $\langle N_{blob} \rangle$ values for pyrene labeled copolymers as a function of side-chain length. \times polymethacrylates, \star polyacrylate

Fig. 4. $\langle k_{blob} \rangle \times N_{blob}$ values for pyrene labeled copolymers as a function of side-chain lengths; \times polymethacrylates, \star polyacrylate

Conclusion

Pyrene labeled PC1A, PC1MA, PC4MA, PC8MA, PC12MA, and PC18MA were synthesized. The fluorescently labelled polymer samples were studied using steady-state and time-resolved fluorescence. Two important parameters, namely N_{blob} and $k_{blob} \times N_{blob}$, were determined with the FBM analysis. For each polymer series, both N_{blob} and $k_{blob} \times N_{blob}$ remained constant within experimental error with pyrene content, but their average value $\langle N_{blob} \rangle$ and $\langle k_{blob} \rangle \times N_{blob}$ decreased substantially with increasing side-chain length, demonstrating that an increase in bulkiness of the side-chain is associated with a pronounced decrease in chain mobility.

Acknowledgements

The authors thank NSERC for generous support.

Institute for Polymer Research

Celebrating 30 years of Official Institute Status

Symposium documents for

Michael Fowler

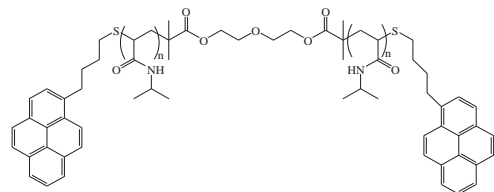
Michael A. Fowler,¹ Jean Duhamel,¹ Xing Ping Qiu,² Françoise Winnik²

¹Department of Chemistry, University of Waterloo, ON, CANADA N2L 3G1

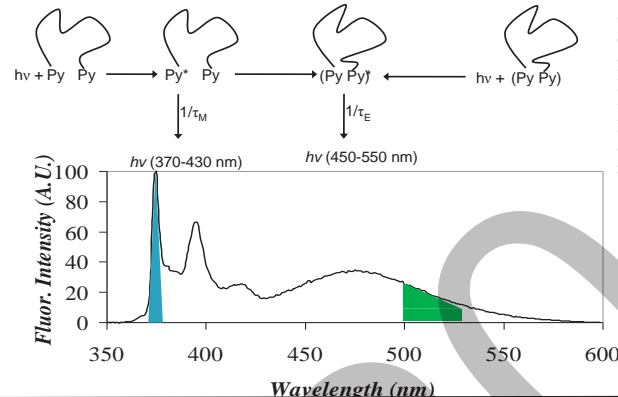
²Faculty of Pharmacy and Department of Chemistry, Université de Montréal, CP 6128 Succursale Centre Ville, Montréal QC H3C 3J7, Canada

Background

In this study, a series of poly(N-isopropylacrylamide) (PNIPAM) polymers end-labeled with pyrene were dissolved in aqueous solution and their fluorescence properties were determined as a function of temperature.



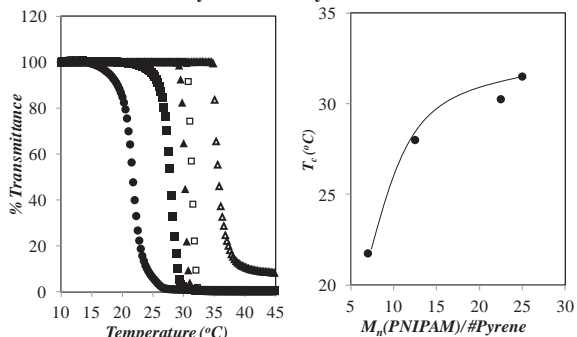
PNIPAM was chosen since it possesses a lower critical solution temperature (LCST) commonly reported as 32 °C. Pyrene was chosen since it is strongly hydrophobic, fluorescent and able to form an excited dimer called an excimer.



Winnik et al. Model:
The behaviour of hydrophobically end-labelled PNIPAM has been described using a model developed by F. M. Winnik et al., broken down into 3 thermodynamic regimes.

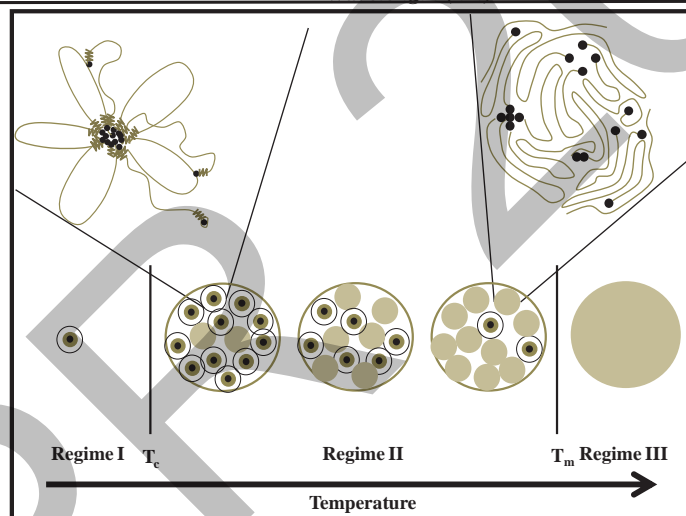
Regime I
• Temperatures below T_c .
• Chains form micelles with a shell of hydrated PNIPAM, a hydrophobic core composed of pyrene labels, and a middle region composed of dehydrated PNIPAM
• As T increases, PNIPAM in the shell dehydrates and the micelles decrease in size
Regime II
• Temperatures between T_c and T_m .
• At T_c , the PNIPAM micelles aggregate to form particles called mesoglobules.
• As T increases, PNIPAM further dehydrates as the mesoglobules grow in size.
• Eventually, the core-shell structures within the mesoglobules are disrupted and the hydrophobes disperse throughout a continuous phase of dehydrated PNIPAM.
Regime III
• Temperatures above T_m .
• The PNIPAM chains have finished dehydrating.
• The mesoglobules are stable in both size and composition

LCST Determination by Turbidimetry:

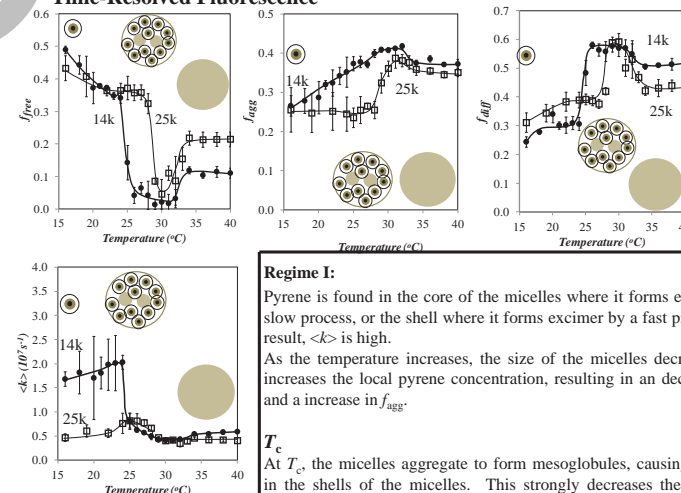


(●) Py₂-PNIPAM(14K), (■) Py₂-PNIPAM(25K), (▲) Py₂-PNIPAM(45K), (□) Py₁-PNIPAM(25K), (Δ) PNIPAM(22K). [Polymer] = 0.5 g/L

As the M_w increases, the pyrene content decreases and the LCST (T_c) increases.



Time-Resolved Fluorescence



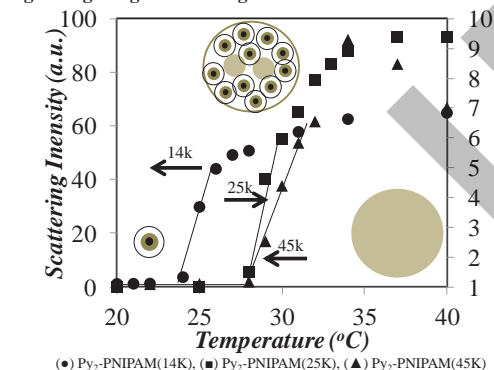
Regime I:
Pyrene is found in the core of the micelles where it forms excimer via a slow process, or the shell where it forms excimer by a fast process. As a result, $\langle k \rangle$ is high. As the temperature increases, the size of the micelles decreases. This increases the local pyrene concentration, resulting in a decrease in f_{free} and an increase in f_{agg} .

T_c
At T_c , the micelles aggregate to form mesoglobules, causing an overlap in the shells of the micelles. This strongly decreases the mobility of pyrenes in the shell and sharply increases the local pyrene concentration, hence the sharp drop in $\langle k \rangle$ and f_{free} , and the sharp increase in f_{diff} .

Regime II:
 $\langle k \rangle$ and the fluorescence fractions remain stable in Regime II until the temperature causes the micelles to disperse. This causes the local pyrene concentration to decrease, reducing f_{agg} and f_{diff} but increasing f_{free} .

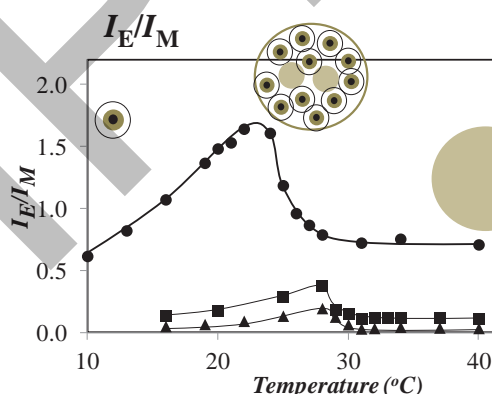
Regime III:
At T_m the solution enters Regime III, where the micelle behaviour stabilizes. This is reflected in the stable values for $\langle k \rangle$ and the fluorescence fractions.

Right-Angle Light Scattering:



(●) Py₂-PNIPAM(14K), (■) Py₂-PNIPAM(25K), (▲) Py₂-PNIPAM(45K)

Under the dilute conditions used for fluorescence, the light scattering intensity of the sample was far more sensitive than turbidimetry and was used to determine T_c .



Regime I:
The I_E/I_M ratio increases due to a decrease in the size of the micelles

Regime II:
 I_E/I_M decreases as the micelles aggregate to form mesoglobules, either decreasing the mobility or the concentration of pyrene

Regime III:
 I_E/I_M is stable since the micelles are stable

Conclusions:

Light scattering, steady-state and time-resolved fluorescence were used to determine the aggregation behaviour of pyrene-labelled polymers in aqueous solution as the temperature increased. The sample shows changes in behaviour that are consistent with what is predicted by the model proposed by F. M. Winnik et al.

Institute for Polymer Research

Celebrating 30 years of Official Institute Status

Symposium documents for

Chang Guo

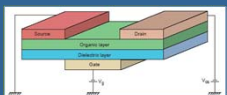
Synthesis and Properties of Indigo based Donor–Acceptor Conjugated Polymers

Chang Guo, Bin Sun, Jesse Quinn, Zhuangqing Yan
and Yuning Li*

Department of Chemical Engineering and Waterloo Institute for Nanotechnology
(WIN), University of Waterloo

Introduction

Organic thin-film transistors (OTFTs):



Transistors: work as electronic switches to control the electrical current between source / drain electrodes by applying an input voltage on "gate".

Transport holes or electrons, depending on the organic semiconductor.

Polymer semiconductors normally bearing donor-acceptor (D-A) structure synthesized by transition-metal catalyzed D-A units crossing-coupling reactions.

D-A Polymer:



Donor: π -electron rich moiety
Acceptor: π -electron deficient moiety

Easy to tune the bandgap of resultant conjugated polymer

Making the polymer chains tightly packed along the π - π stacking direction

Indigo (ID) Molecule:



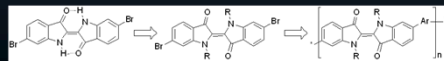
A natural dye indigo used as early as 1600 BCE.

A strong electron withdrawing unit, with a highly coplanar geometry.

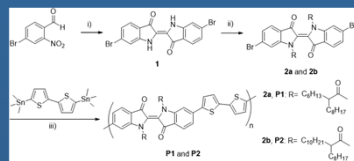
An isomer of isoindigo (IID), which shows good performance in OTFTs.

No report to make the molecule soluble for polymerization yet.

What if indigo molecule could be incorporated into polymers as an acceptor unit as below?



Polymer Synthesis



i) NaOH / acetone / rt.; ii) a) NaH / NMP / rt. b) RCOCl / rt.; iii) Pd₂(dba)₃ / P(o-tolyl)₃ / chlorobenzene / 90 °C.

Substitution: the nitrogen atoms of indigo molecule could be readily substituted with acyl groups by using the chemistry we used for diketopyrrolopyrrole (DPP) unit.

Long branched side chains: 2-hexyldecanoyl and 2-octyldecyldecyl provide the desirable solution processability to PIDBT (P1 and P2).

Purification of PIDBT: by Soxhlet extraction method, finally dissolved in 130 °C 1,1,2,2-tetrachloroethane (TCE), both polymers obtained as a bluish film.

Polymer Characterization

Molecule Weight:

	Mn(kDa)	PDI	Mw(kDa)
P1 (TCE)	13.5	3.50	47.4
P2 (CHL)	12.4	10.6	130.6

Characterized by Gel Permeation Chromatography (GPC), by using polystyrenes as standards and chlorobenzene as an eluent at column temperature of 40 °C.

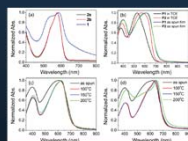
The molecular weight of P2 dissolved in TCE could not be measured because of its very poor solubility. However, we can reasonably assume that the molecular weight of P2 in the TCE fraction should be higher than that of P1. The results used for the following discussions were obtained using the fractions of P1 and P2 dissolved in TCE.

UV-vis Absorption:

The blue shift of ~10 nm for the λ_{max} for 2a and 2b with respect to compound 1 in TCE solution (a) is likely to be the result of the twisted indigo moiety caused by the acyl groups.

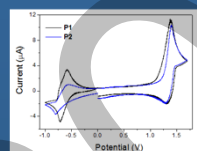
As-spun thin film (b): λ_{max} ~ 527 nm for P1 and ~ 572 nm for P2, blue shift is due to the higher molecular weight and thus the longer effective conjugation length of P2.

P1 thin film annealed at 100 °C (c): λ_{max} red shifted to 626 nm. P2 thin film annealed at 100 °C, 150 °C and 200 °C (d): λ_{max} red shifted progressively to 639, 643 and 651 nm. Thermal annealing increased the chain ordering and led to more extended π -conjugation of the polymer backbone.



Electrochemistry and energy levels of

PIDBT:



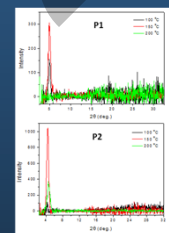
E_{HOMO} calculated from the oxidative onset potential: -5.69 eV for P1 and -5.78 eV for P2 (ferrocene as the standard).

Lower E_{HOMO} of P2 than that of isoindigo based polymers, due to the strong electron-withdrawing effect of indigo unit.

$E_{LUMO} = E_{HOMO} + E_{g}^{opt}$, the obtained values are closed to those calculated from the reductive onset potential.

	E_g	HOMO	LUMO (CV based)	LUMO (UV based)
P1	1.69eV	-5.69eV	-4.00eV	-4.00eV
P2	1.69eV	-5.78eV	-4.02eV	-4.10eV

XRD patterns of PIDBT film:

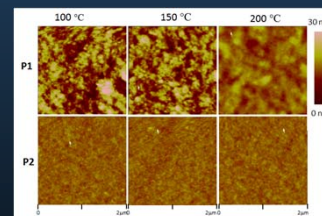


Thin film of both polymers showed much intensified peaks when annealed at 150 °C, manifesting improved crystallinity.

The corresponding d-spacing was calculated to be ~18.4 Å for P1 and 20.2 Å for P2, respectively.

Increasing the annealing temperature to 200 °C, the intensity of the primary peak decreased and the d-spacing further decreased, due to the loss of the side chains as corroborated by the thermal analysis data.

Thin film AFM images:



the 100 °C - and 150 °C -annealed P1 thin films contain large grains.

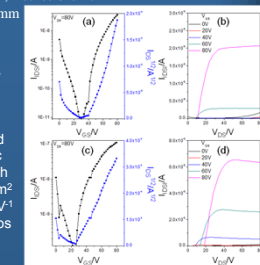
The 200 °C -annealed P1 thin film became more uniform, probably due to the removal of the side chains.

all of the P2 thin films are very smooth and the surface morphology was not much influenced by thermal annealing.

Characterization of OTFTs:

Gate	Gate dielectric	Channel length
Semiconducting	SiO ₂	L = 30 mm;
Source	Drain	W = 1000 mm

Transfer and output curves of OTFT devices with P1 (a and b) and P2 (c and d) thin films annealed at 150 °C for 20 min.



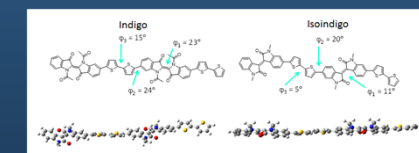
Devices with P1 or P2 thin films annealed at 100 °C showed no field effect performance.

Devices with thin films annealed at 150 °C showed characteristic electron transport behaviour with a mobility as high as $6.6 \times 10^{-4} \text{ cm}^2 \text{ V}^{-1} \text{ s}^{-1}$ for P1, and $1.1 \times 10^{-3} \text{ cm}^2 \text{ V}^{-1} \text{ s}^{-1}$ for P2. (current on-to-off ratios of $\sim 10^4$).

Further increasing the annealing temperature to 200 °C resulted in the absence of field effect performance for both polymers, due to the deteriorated molecular ordering caused by thermal decomposition of the side chains.

The observed mobility values are much lower in comparison to isoindigo counterpart.

Simulated geometry of ID and IID:



The dihedral angle between the two indol moieties (ϕ_1), as well as that between two thiophen units (ϕ_3) of ID based polymers are greater than those of IID based polymers, according to the simulated results.

The backbone twisting led to the poor main chain conjugation, then resulted in the relatively low mobility.

Conclusions

For the first time, the novel D–A polymers based on indigo as acceptor, were synthesized and applied as organic semiconductor in OTFTs.

The low-lying HOMO/LUMO levels and rather low band gap manifested the strong electron withdrawing capability of the indigo moiety.

P1 and P2 showed characteristic electron transport performance in OTFTs with electron mobilities of up to $6.6 \times 10^{-4} \text{ cm}^2 \text{ V}^{-1} \text{ s}^{-1}$ for P1 and $1.1 \times 10^{-3} \text{ cm}^2 \text{ V}^{-1} \text{ s}^{-1}$ for P2, respectively.

The lower than expected field effect performance of these polymers in comparison to their counterpart isoindigo polymers was considered to be due to the backbone twisting according to the simulation result, which is undesirable for extended delocalization of electrons.

This research was supported by the Natural Sciences and Engineering Research Council (NSERC) of Canada. The authors thank Dr Jianfu Ding at the National Research Council Canada (NRC) for the GPC measurements, and Angstrom Engineering Inc. for providing the thermal deposition system for the fabrication of the OTFT devices.

Institute for Polymer Research

Celebrating 30 years of Official Institute Status

Symposium documents for

Niousha Kazemi

Niousha Kazemi, Alison J Scott, Marzieh Riahinezhad, Thomas A Duever, and Alexander Penlidis
 Institute for Polymer Research (IPR), Department of Chemical Engineering, University of Waterloo

Introduction

- **Terpolymerization systems are of great importance** in both academia and industry, and there is always a need for understanding the underlying kinetics of such complex reaction systems.
- **Reactivity ratios** describe the tendency of incorporation of monomers with respect to each other.
- Based on an analogy between copolymerization and terpolymerization mechanisms, binary reactivity ratios have been **commonly, albeit misleadingly**, used in models dealing with terpolymerizations.
- **Our objectives:**
 - ✓ **Illustrate the correct approach for estimating ternary reactivity ratios directly based on terpolymerization data**

Experimental Case Study

Terpolymerization

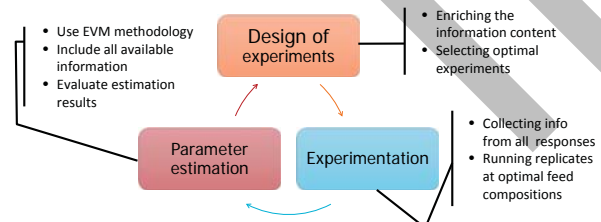
2-Acrylamido-2-methylpropane sulfonic acid (AMPS), Acrylamide (AAM), Acrylic acid (AAc)

- A water-soluble polymer with several applications in enhanced-oil-recovery, drug delivery, wastewater treatment, ...
- Reactivity ratios
 - *inform about kinetics of this system*
 - *improve the prediction performance of the model for further studies*
- A systematic study for determining reactivity ratios for this system:



EVM Framework

- A sequential process, within the Error-in-Variables-Model (EVM) context, that provides the most reliable reactivity ratio estimates

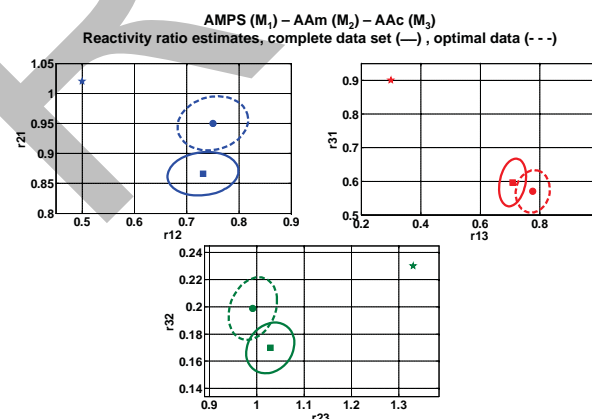
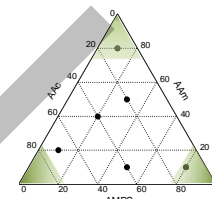


Literature Binary Reactivity Ratios

- AMPS/AAM copolymerization**
 - AAm is more reactive than AMPS
 - Reactivity ratios at pH=7 : $r_{AMPS}=0.5$, $r_{AAm}=1.02$
- AMPS/AAc copolymerization**
 - AAc is more reactive than AMPS.
 - Reactivity ratios at pH=7 : $r_{AMPS}=0.3$, $r_{AAc}=0.9$
- AAM/AAc copolymerization**
 - AAm is much more reactive than AAc.
 - Reactivity ratios at pH=7 : $r_{AAm}=1.33$, $r_{AAc}=0.23$

Ternary Reactivity Ratio Estimation

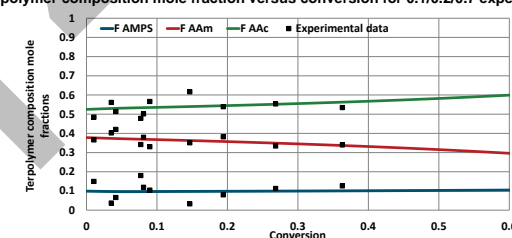
- Experiments were performed at 40°C, pH=7, [M]=1
- Samples were collected at low conversion levels as well as at medium-high conversion levels
- The experiment with **80% AAm** has the highest rate of polymerization and the experiment with **70% AAc** has the lowest rate of polymerization.



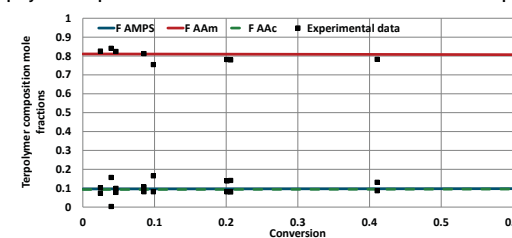
- Overall, the ternary reactivity ratio estimates **differ from binary values**.
- Reactivity ratio estimates from the complete data set and optimal data are in agreement, while the optimal reactivity ratios are estimated with only three experiments (**50% less experimentation!**)
- This system should have an **azeotrope at 0.155/0.840/0.005** feed composition.

Terpolymer Composition Predictions

Terpolymer composition mole fraction versus conversion for 0.1/0.2/0.7 experiments



Terpolymer composition mole fraction versus conversion for 0.1/0.8/0.1 experiments



- The optimal ternary reactivity ratios provide **very good predictions** for the experimental data.
- A **'pseudo-azeotropic' composition (0.1/0.8/0.1)** shows almost **no composition drift**.

Concluding Remarks

- The **correct approach for estimating ternary reactivity ratios** is illustrated for the AMPS/AAM/AAc terpolymerization system.
- Optimal ternary reactivity ratios are estimated based on **three experiments only!**
- Ternary reactivity ratios show **considerable differences compared to binary** reactivity ratios.
- The joint confidence regions and the prediction results confirm that the EVM framework provides **reliable and accurate** reactivity ratios for this terpolymerization system, and for terpolymerizations, in general.

Bibliography

- Kazemi, N., Duever, T. A., and Penlidis, A., *AIChE Journal* (2014), 60, 1752-1766.
- Kazemi, N., Duever, T. A., and Penlidis, *Computers & Chemical Engineering* (2013), 48, 200-208.
- Riahinezhad, M., Kazemi, N., McManus, N., & Penlidis, A., *Journal of Polymer Science Part A: Polymer Chemistry*, (2013), 51, 22, 4819-4827.
- Abdel-Aziz, A.-A. A., Farahat, M. S., Atta, A. M. and Abdel-Fattah, A. A., *Polymers for Advanced Technologies* (1998), 9, 282-289

Institute for Polymer Research

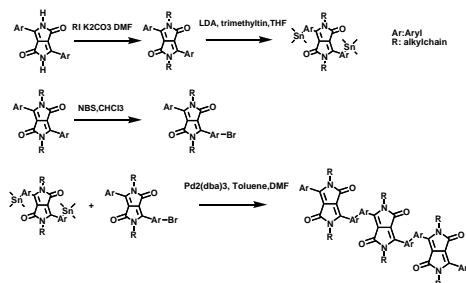
Celebrating 30 years of Official Institute Status

Symposium documents for

Mylène Le Borgne

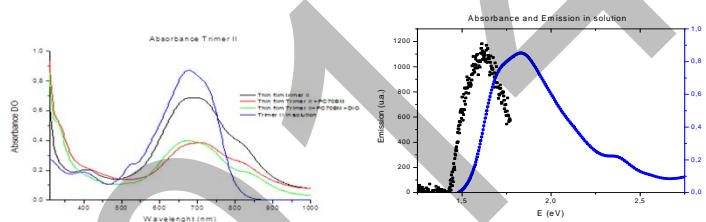
Introduction: Small molecule organic semiconductors are receiving much attention for the organic solar cell application. This is mainly due to their easy purification and structural manipulation compared to their polymer counterparts.^{1,2} Among them, the diketopyrrolopyrrole (DPP) family succeed to stand out thanks to their broad optical absorption, ability to lower the energy frontier and high charge carrier mobility.^{3,4}

Synthesis of DPP trimer :

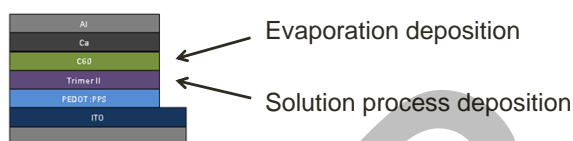


Stille coupling synthesis

Optical properties



Bilayer devices

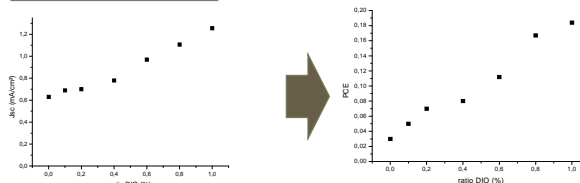


Solvent		J _{sc} (mA/cm ²)	V _{oc} (V)	FF	PCE (%)
Chloroform	average	1,23	0,60	0,40	0,30
	max	1,29	0,67	0,50	0,43
o-dichlorobenzene	average	1,69	0,59	0,43	0,43
	max	1,71	0,64	0,47	0,51

Bulk heterojunction devices: Addition of DIO



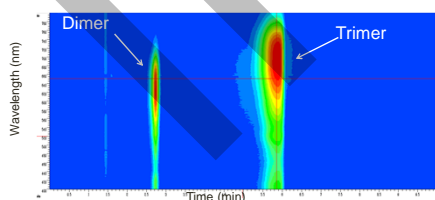
Solution spin coated:
Trimer:PC₇₀BM 1:1 dissolved in chloroform and various ratio DIO (1,8-diiodooctane)



Low efficiency can be explained by three reasons :

Impurities :

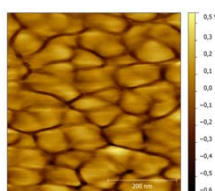
Separation by HPLC → UV-Visible 2D map



Some dimers remain as impurity

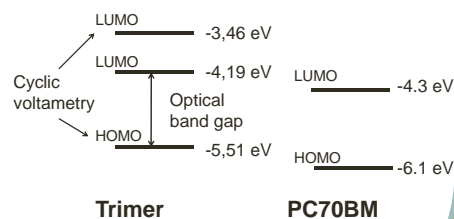
Bad Morphology

AFM images of trimer's active layer from best bulk heterojunction devices:



Large grains (100nm) formation → important recombinations

Energy levels:



Too low LUMO level → No electron transfer

Conclusion and perspectives: For now, bilayer structure gives the best performance with a PCE around 0.5%. In bulk heterojunction, the morphology may not allow good collection of charge carriers and good charge generation. By using additives like diiodooctane, the repartition between the two compounds can be controlled and brings better performance. The project will pursue on the addition of new additives.

Institute for Polymer Research

Celebrating 30 years of Official Institute Status

Symposium documents for

Solmaz Pirouz

A Novel Method to Determine the Chemical Composition of Polyisobutylene-Based Oil-Soluble Dispersants by Fluorescence

Solmaz Pirouz, Yulin Wang, Michael Chong, Jean Duhamel
Institute of Polymer Research (IPR), Department of Chemistry, University of Waterloo

INTRODUCTION

Succinimide dispersants are among the most important additives that are currently used in engine oils. They adsorb on the surface of carbon-rich particles generated during engine operation, stabilizing them in solution, and consequently reducing the emission of ultrafine particles (UFPs) and the formation of sludge. This research intends to characterize the chemical composition of a series of succinimide-based dispersants. The chemical composition of polyisobutylene succinic anhydride (PIBSA) and a series of polyisobutylene succinimide (PIBSI) dispersants were determined by more common characterization methods such as ^1H NMR, FTIR, UV-Vis, and a procedure based on GPC analysis. Steady-state and time-resolved fluorescence measurements were used as a new and unique method to determine the chemical composition of PIBSI dispersants.

PROBLEMS

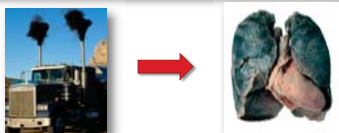


Figure 1. Lung failure caused by UFPs emission in to the air

UFPs are typically formed by the incomplete oxidation of fuel during ignition and can be released into the air. Since releasing UFPs from engines into the air can cause heart and lung failure, governmental regulations were issued to reduce their emission. This, in turn, results in higher concentrations of UFPs in the engine oil which leads to sludge formation. To prevent this phenomenon, dispersants were added to the engine oil.



Figure 2. Sludge formation caused by circulating the exhaust gas back into the oil

SOLUTION

UFPs which are smaller than 100 nm in diameter have polar groups on their surface which are generated by the oxidation of the oil during engine operation. In apolar oil, UFPs self-aggregate into large particles (LPs, $d_{LP} \sim 1 \mu\text{m}$) to minimize their surface exposure to the oil.

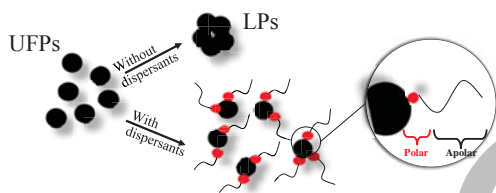
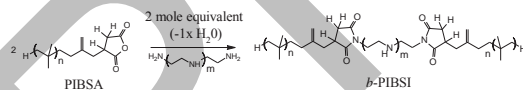


Figure 3. UFPs in the oil: (top) aggregated UFPs in the absence of dispersant, (bottom) stabilized UFPs in the presence of dispersant

LPs can cause sludge formation resulting in oil blockage and engine failure. Therefore, dispersants are added to the engine oil to minimize UFPs aggregation into LPs. Dispersants are typically composed of a polar head group and an oil-soluble apolar tail. The polar core of the dispersant is expected to be adsorbed onto the surface of the UFPs, whereas the apolar tail stabilizes the particle in the oil.

SYNTHESIS PROTOCOL



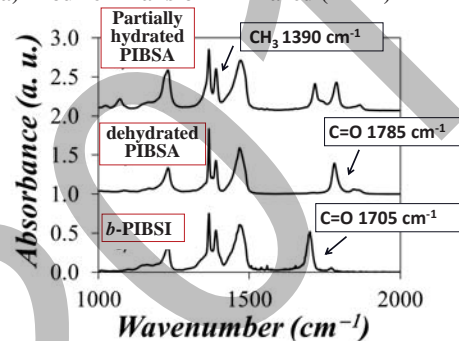
Scheme 1. Synthesis of succinimide dispersants

Diethylenetriamine (DETA)	$\text{H}_2\text{N}-(\text{CH}_2\text{CH}_2-\text{NH})_1-\text{CH}_2\text{CH}_2-\text{NH}_2$
Triethylenetetramine (TETA)	$\text{H}_2\text{N}-(\text{CH}_2\text{CH}_2-\text{NH})_2-\text{CH}_2\text{CH}_2-\text{NH}_2$
Tetraethylenepentamine (TEPA)	$\text{H}_2\text{N}-(\text{CH}_2\text{CH}_2-\text{NH})_3-\text{CH}_2\text{CH}_2-\text{NH}_2$
Pentaethylenhexamine (PEHA)	$\text{H}_2\text{N}-(\text{CH}_2\text{CH}_2-\text{NH})_4-\text{CH}_2\text{CH}_2-\text{NH}_2$
Hexamethylenediamine (HMDA)	$\text{H}_2\text{N}-(\text{CH}_2)_6-\text{NH}_2$

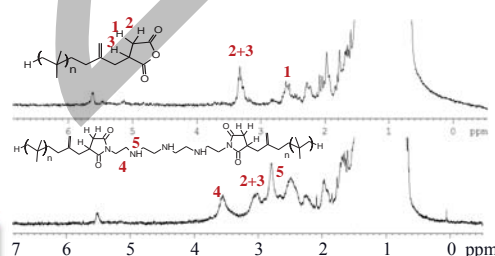
RESULTS

Determination of Chemical Composition

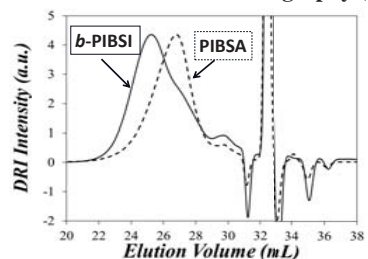
a) Fourier Transform Infrared (FTIR)



b) Nuclear Magnetic Resonance (^1H NMR)



c) Gel Permeation Chromatography (GPC)



d) UV-Visible Spectrophotometry (UV-Vis)

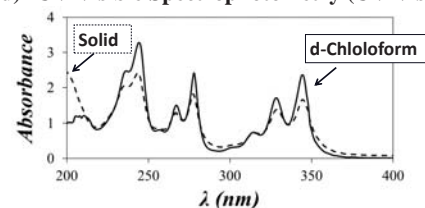
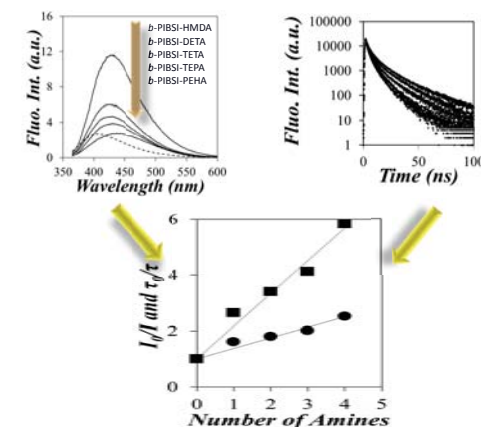


Table 1. Summary of PIBSA and PIBSI Chemical Compositions

Dispersants		^1H NMR	FT-IR (Peak Height)	GPC	UV-Vis
PIBSA	N_{SA} / N_{IB}	1:55±2	1:49±1	1:52	-
b-PIBSI	N_{SI} / N_{IB}	1:31±3	1:39±2	-	-
m-PIBSI- PyNH ₂	N_{SI} / N_{IB}	1:45	1:44	-	1:55

Pirouz, S.; Wang, Y.; Chong, M.; Duhamel, J. "Characterization of the Chemical Composition of Polyisobutylene-Based Oil-Soluble Dispersants by Fluorescence", *J. Phys. Chem. B* 2014, 118, 3899-1911

e) Fluorescence Measurements



SUMMARY

- The chemical composition of PIBSA and PIBSI dispersants were characterized quantitatively by using a novel characterization method
- This study confirmed the existence of H-bonds between the secondary amines of the polyamine spacer and the succinimide carbonyls of the b-PIBSI dispersants
- Stern-Volmer plots of the ratios I_0/I and τ_0/τ as a function of the number of secondary amines showed a linear behavior suggesting that fluorescence quenching measurements can provide a reliable measure of the secondary amine content of a given b-PIBSI dispersant.

ACKNOWLEDGMENTS

The authors thank Imperial Oil and NSERC for funding.

Institute for Polymer Research

Celebrating 30 years of Official Institute Status

Symposium documents for

Marzieh Riahinezhad

Reactivity Ratios in Polyelectrolyte Copolymerization: Does Ionic Strength Play a Role?

Marzieh Riahinezhad, Neil McManus, and Alexander Penlidis
Department of Chemical Engineering, University of Waterloo

Research Motivation

To investigate and clarify the largely unstudied effect of ionic strength on monomer reactivity ratios and copolymerization rates of acrylamide (AAm) and acrylic acid (AAc), in the form of sodium acrylate (NaAc), at a chosen pH.

Experimental

Acrylamide, AAm and Sodium acrylate, NaAc (Monomer)

Materials
Sodium hydroxide (pH-controller)
4,4'-azo-bis(4-cyano valeric acid), ACVA (Initiator)
Hydroquinone (Inhibitor), Sodium chloride (salt)

Estimation
Error-in-Variables Model (EVM) &
Direct Numerical Integration (DNI) approach for
estimating monomer reactivity ratios

Characterization
Gravimetry for monomer conversion
Elemental analysis for copolymer composition
Inductively coupled plasma (ICP) analysis for Na content

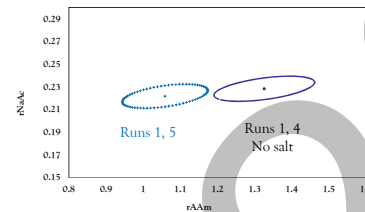
Polymerization
Total monomer concentration = 1 M
Temperature = 40 °C
Solution pH = 7±0.2
AAm monomer proportions in feed = 0.1, 0.46

Run #	f_{0AAm}	Ionic Strength (M)	Salt (M)
1	0.1	0.898	0
2	0.1	1.078	0.181
3	0.1	1.437	0.539
4	0.46	0.538	0
5	0.46	0.898	0.359
6	0.46	1.078	0.539
7	0.46	1.258	0.719
8	0.46	1.437	0.898

Ionic Strength & Reactivity Ratios

Copolymerization with Constant Ionic Strength at

$$f_{0AAm} = 0.46$$

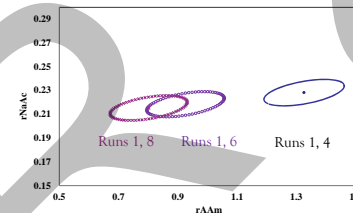


OBSERVATION
By keeping ionic strength constant:
 r_{NaAc} has remained almost the same,
 r_{AAm} has shifted to lower values.

REASONING
Without adding salt, the polyelectrolyte chains containing acrylate anions are more extended because of charge-charge repulsion between anionically charged groups along the chain.

Copolymerization with Controlled but Variable Ionic Strength at

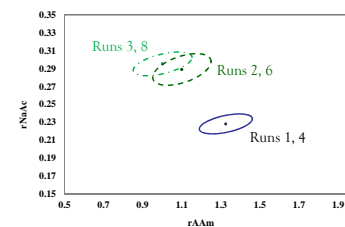
$$f_{0AAm} = 0.46$$



OBSERVATION
By increasing ionic strength:
 r_{NaAc} has slightly shifted to lower values,
 r_{AAm} has noticeably shifted to lower values.

REASONING
Having more salt means greater chance of diminishing the repulsive interactions between unshielded negative charges & yielding denser random coil structure.

Copolymerization with Constant Ionic Strength at $f_{0AAm} = 0.1$

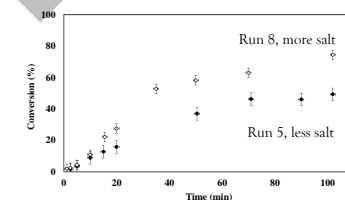


OBSERVATION
By increasing ionic strength:
 r_{NaAc} has shifted to higher values,
 r_{AAm} has shifted to lower values.

REASONING
Incorporating salt shields the negative charge interactions of acrylate anions, which results in higher reactivity for NaAc units.

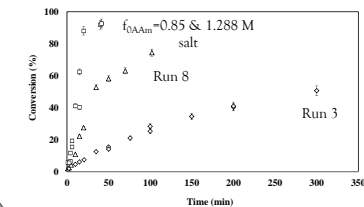
Ionic Strength & Polymerization Rate

Variable Ionic Strength



Higher salt level, faster copolymerization rate; due to the shielding effect of salt & less repulsion interactions between reacting species.

Constant Ionic Strength



Higher NaAc in the feed composition, slower overall copolymerization rate; due to the electrostatic repulsion between negatively charged reacting species.

Concluding Remarks

- ✓ Incorporating salt in the reaction solution, at various feed compositions, affects monomer reactivity ratios as well as the copolymerization rate, by decreasing the electrostatic repulsions between charged ions.
- ✓ Depending on the initial feed composition of the solution, the effect of ionic strength on reactivity ratios is different. By adding salt to the polymerization solution with initial feed composition of $f_{0AAm} = 0.46$, r_{NaAc} remains almost unchanged, whereas at $f_{0AAm} = 0.1$, the effect on r_{NaAc} is more obvious.

Institute for Polymer Research

Celebrating 30 years of Official Institute Status

Symposium documents for

Ankita Saikia

Ankita Saikia, Costas Tzoganakis
 Department Of Chemical Engineering, University of Waterloo
 Waterloo, Ontario, Canada

Background

- The increasing amount of scrap tire generation is accompanied by many environmental problems ;
- Scrap tires can be devulcanized and reused;
- The devulcanized rubber may have different characteristics than virgin rubber;

Objectives

- To study the vulcanization reaction of devulcanized rubber by differential scanning calorimetry (DSC) ;
- To model the curing behavior of devulcanized rubber ;
- To compare the curing behavior of virgin rubber and devulcanized rubber.

Experimental

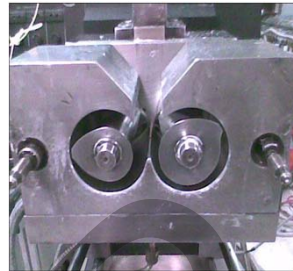
1. Mixing

Table1. Formulations					
Ingredients	Dosages (gm)				
	A	B	C1/C2/C3	D	E
Natural Rubber/ Devulcanized Rubber	200	200	200	200	200
Sulphur	1	5	3	1	5
*TBBS	1	1	3	5	5
Zinc Oxide	6	6	6	6	6
Stearic Acid	2	2	2	2	2

*TBBS- N-tert-butyl-2-benzothiazyl sulfenamide

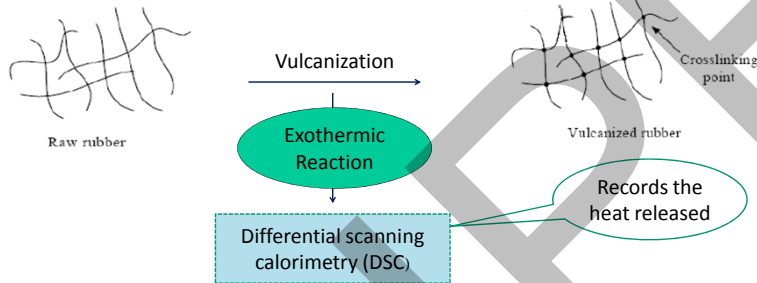


Rhinehart Tire Fire



Batch Mixer

2. Characterization; Differential Scanning Calorimetry (DSC)

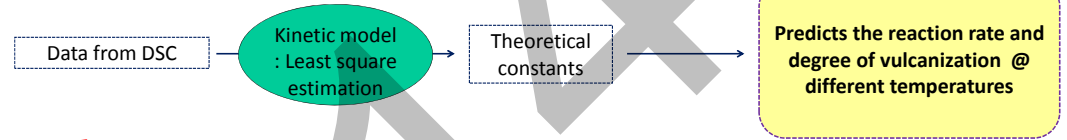


Model equations and data fitting

1. Kinetic Models

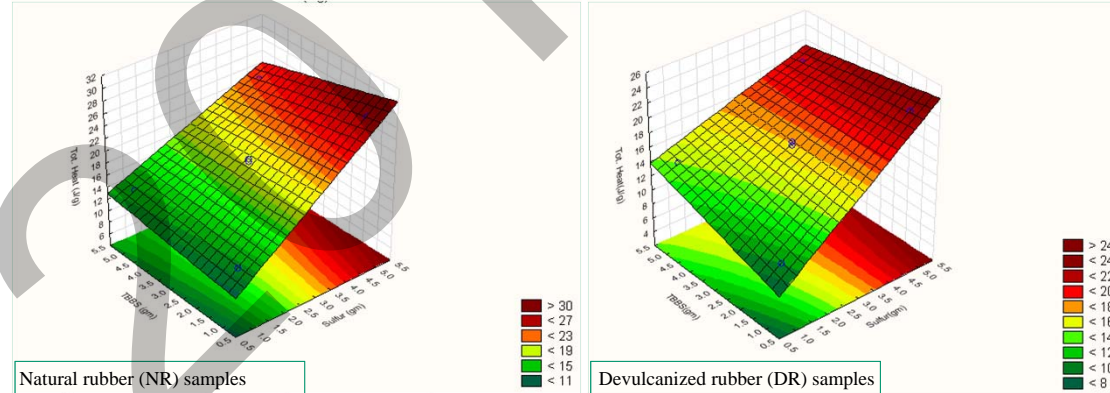
<u>Kissinger Model</u>	$dc/dt = k(1-c)^n$
<u>Arrhenius Model</u>	$k(T) = a \exp(-E/RT)$
<u>Kamal-Sourour Model</u>	$dc/dt = (k_1 + k_2 * c^m) * (1-c)^n$

2. Fitting of data

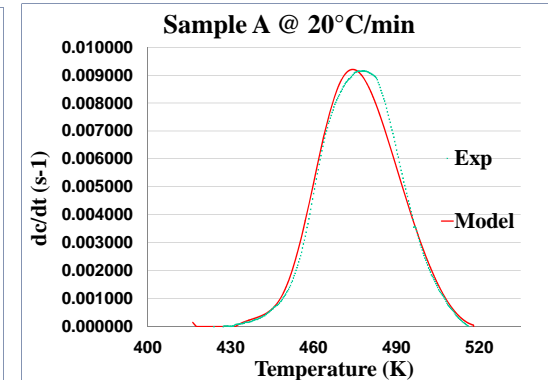
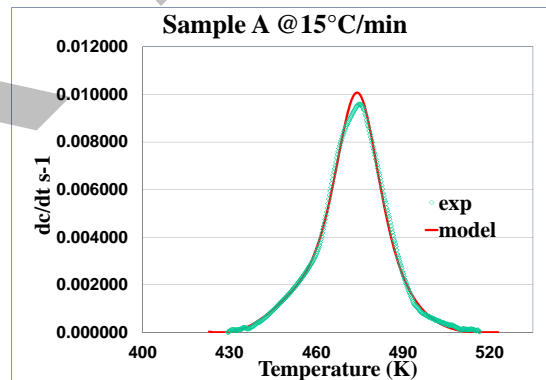


Results

- Effect of change in curative composition in total heat of reaction



- Fitted model and experimental data at different scan rates



Concluding Remarks

- The total heat of reaction is seen to be linearly proportional to the initial sulfur content;
- The total heat of reaction follows a similar trend for both natural and devulcanized rubber but the magnitude of the heat of reaction is less for devulcanized rubber samples compared to natural rubber;
- The fitted models are in good agreement with the experimental data, the constants obtained can be used to predict reaction rate and degree of vulcanization at different temperatures.

Institute for Polymer Research

Celebrating 30 years of Official Institute Status

Symposium documents for

K. M. E. Stewart

Doped Polyaniline for the Detection of Ethanol



K. M. E. Stewart and A. Penlidis

**Institute for Polymer Research, Department of Chemical Engineering
University of Waterloo**



A test system for sensing materials and sensors must be able to effectively evaluate both sensitivity and selectivity (among other response characteristics).

By testing potential sensing materials first, only the most promising sensing materials are deposited, which results in a reduction in time, effort, and cost.

Testing multiple gases at once allows for more realistic environmental conditions.

The test system below was used to identify possible sensing materials for ethanol at low concentrations.

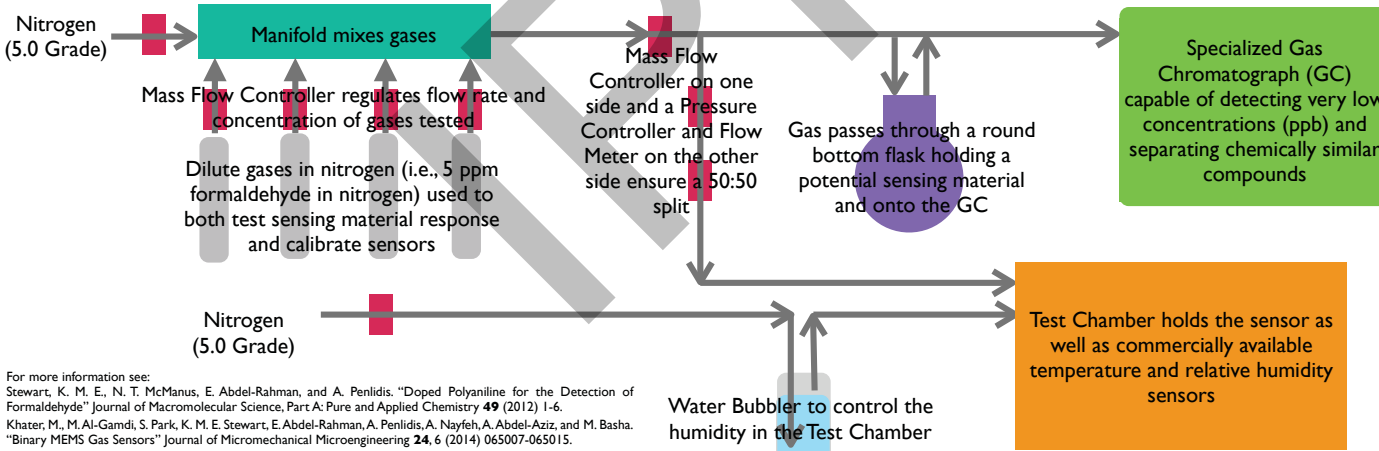
Two doped polymers were chosen from eight sensing materials tested.

A specialized gas chromatograph (GC) is used to evaluate the interaction between the gases tested for the sensing materials, as well as a standard for gas concentration when testing the full sensor.

A voltage vs. time graph is produced by the GC from which the concentration of each analyte can be determined.

The 50:50 split in gas between the GC and test chamber allows for precise and accurate verification of the concentration of multiple gases tested.

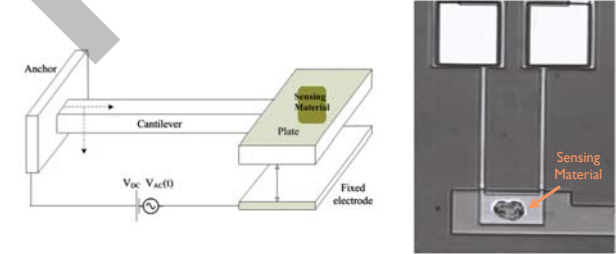
Humidity is added directly to the test chamber where a humidity sensor is placed for verification.



Polyaniline (PANI) and PANI doped with NiO and/or Al₂O₃ were tested as possible sensing materials for ethanol at low concentrations. Three replicates were run and the average response for each sensing material is listed in the Table below. The sensitivity of each sensing material was measured as ppm sorbed per gram of sensing material.

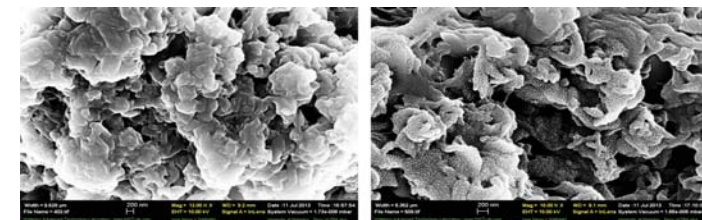
From ten potential sensing materials, PANI doped with 10% NiO was chosen to be deposited onto the MEMS-based cantilever sensor for further testing.

Sensing Material	Amount of Ethanol Sorbed (ppm/g)
PANI	13.08
PANI 5% NiO	10.20
PANI 10% NiO	13.48
PANI 15% NiO	8.55
PANI 20% NiO	11.52
PANI 5% NiO 15% Al ₂ O ₃	6.45
PANI 10% NiO 10% Al ₂ O ₃	12.40
PANI 15% NiO 5% Al ₂ O ₃	12.30



A MEMS-based cantilever sensor, shown above, was evaluated using PANI doped with 10% NiO. The sensor consists of a cantilever that ends in a plate, upon which the sensing material is placed. Ethanol sorbs onto the sensing material, increasing the weight on the plate, causing the plate to drop. When a threshold weight of ethanol is sorbed, the binary sensor triggers.

It was found that PANI doped with 10% NiO on this MEMS-based sensor had a detection limit of 50 ppm and was reponsive over the range of 50 to 1000 ppm.



Polyaniline (PANI)

PANI with 20% NiO

SEM images, above, show homogeneous dispersion of NiO throughout PANI. An even distribution of dopant increases the sensing properties of the sensing material.

For more information see:
Stewart, K. M. E., N. T. McManus, E. Abdel-Rahman, and A. Penlidis. "Doped Polyaniline for the Detection of Formaldehyde" Journal of Macromolecular Science, Part A: Pure and Applied Chemistry **49** (2012) 1-6.
Khater, M., M. Al-Gamdi, S. Park, K. M. E. Stewart, E. Abdel-Rahman, A. Penlidis, A. Nayfeh, A. Abdel-Aziz, and M. Basha. "Binary MEMS Gas Sensors" Journal of Micromechanical Microengineering **24**, 6 (2014) 065007-065015.

Institute for Polymer Research

Celebrating 30 years of Official Institute Status

Symposium documents for

Bingqing Yang

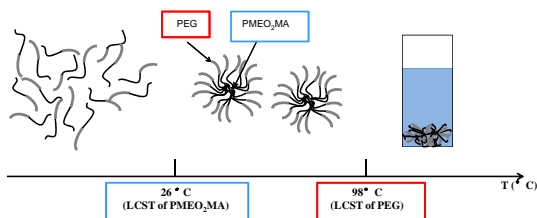
Bingqing Yang, Jean Duhamel
Department of Chemistry

Institute for Polymer
Research (IPR)

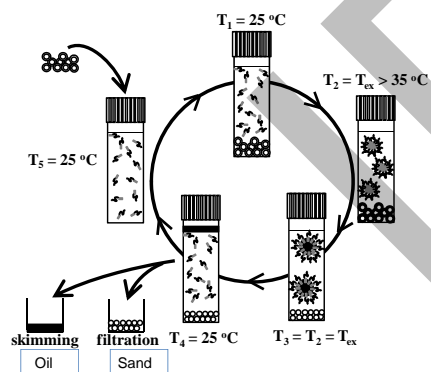
Introduction

Polymeric surfactants are among the most important additives that are used in the extraction of oil from oil sands. However, a fraction of these surfactants can enter the oil phase and are difficult to recover. The use of stimuli-responsive surfactants is one approach around this problem. This research intends to study the efficiency of temperature-responsive polymeric surfactant poly(ethylene glycol)-block-poly[2-(2-methoxyethoxy) ethyl methacrylate] (PEG-*b*-PMEO₂MA) at stabilizing oil-in-water emulsions.

Temperature-Responsive Polymer Surfactant: PEG-*b*-PMEO₂MA

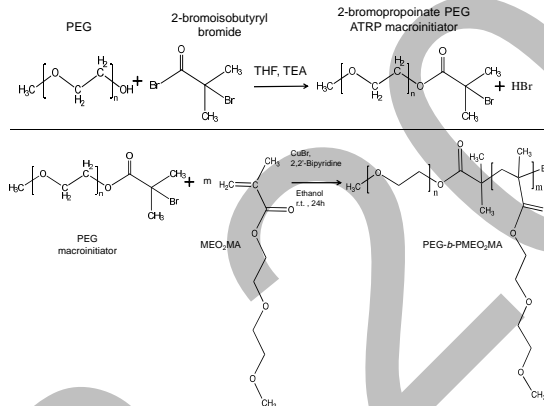


Proposed Application to Oil Extraction



Synthesis of PEG-*b*-PMEO₂MA

Atom Transfer Radical Polymerization (ATRP)



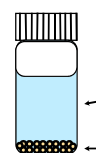
Summary of the Polymer Synthesized by ATRP

Polymer	M _n , NMR (g/mol)	PDI	LCST ¹ (°C)	Diameter ² (nm)
PMEO ₂ MA ₁₃₈	26000	1.8	26.0	-
PEG ₁₁₃ - <i>b</i> -PMEO ₂ MA ₆₄	17000	1.1	33.0	26.3 ± 0.3
PEG ₁₁₃ - <i>b</i> -PMEO ₂ MA ₈₀	20000	1.2	34.0	27.1 ± 0.4
PEG ₁₁₃ - <i>b</i> -PMEO ₂ MA ₇₇	19000	1.5	35.0	36.6 ± 0.3

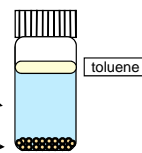
¹ Lower Critical Solution Temperature (LCST) was measured by turbidimetry.
² Measured by dynamic light scattering.

Application in Oil Extraction

Protocol #1



Protocol #2

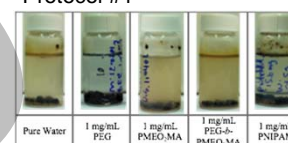


The samples were left in the shaker for 24 hrs at 45 or 50 °C.

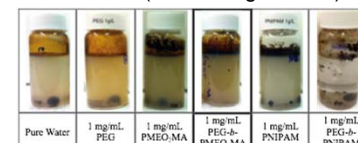
Application in Oil Extraction (Con't)

Optimal Conditions of Oil Extraction

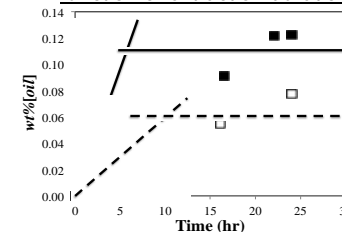
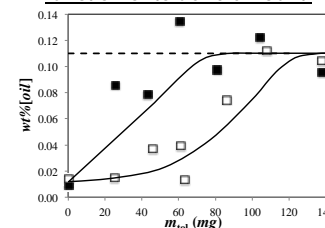
- A 1 mg/mL PEG-*b*-PMEO₂MA aqueous solution extracts extract oil efficiently.



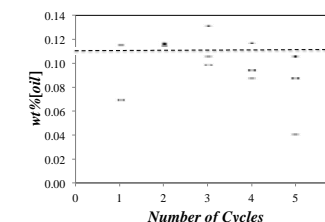
Protocol #2 (with 60 mg toluene)



- Extraction efficiency as a function of toluene amount.
- Extraction efficiency as a function of extraction duration.



Reusability of TRPS



- This TRPS was proven to be reusable for at least 5 extraction cycles.
- The recovery of the copolymer after one oil extraction cycle was found to equal 78% by using GPC instrument.

References

- Topp, M. D. D.; Dijkstra, P. J.; Talsma, H.; Feijen, J. *Macromolecules* **1997**, *30*, 8518-8520.
- Hong, J.; Wang, Q.; Lin, Y. Z.; Fan, Z. Q. *Macromolecules* **2005**, *38*, 2691.

Acknowledgements

- The authors thank Imperial Oil and NSERC for funding.

Institute for Polymer Research

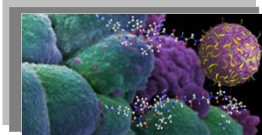
Celebrating 30 years of Official Institute Status

Symposium documents for

Wei Yi

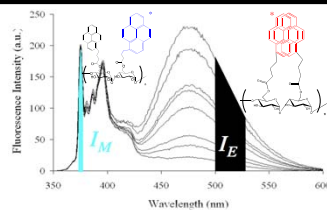
Introduction

The numerous functional groups of Starch Nanoparticles (SNPs) allow for their chemical modification, and in turn, the adjustment of their properties. Of particular interest is the hydrophobic modification of SNPs that would turn them into amphiphilic particles. This study aims to characterize how these hydrophobic modifications affect the behavior of the modified SNPs in aqueous solution. To this end,



transmission electron microscopy (TEM) and fluorescence were employed to characterize the internal dynamics and morphology of the hydrophobically modified SNPs.

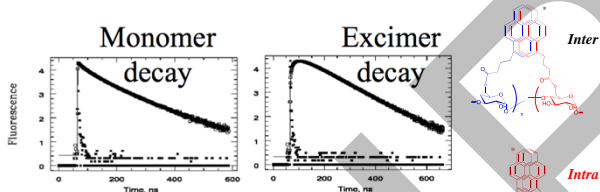
Steady-State Fluorescence Spectroscopy



$$\frac{I_E}{I_M} = Kk_d[Py]_{exc}$$

$$k_d = 4\pi N_A(D_0 + D_p)\sigma$$

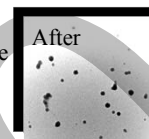
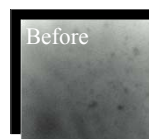
Time-Resolved Fluorescence Spectroscopy



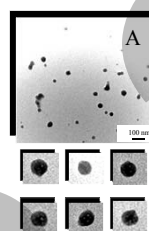
Monomer decays were acquired at 375 nm, and excimer decays were acquired at 510 nm. $\langle k \rangle$ (μs^{-1}), f_{agg} , f_{free} , and f_{diff} are determined from the life-time measurements.

Staining with Ruthenium Tetroxide (RuO₄)

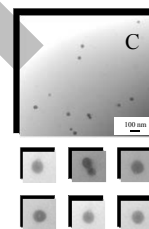
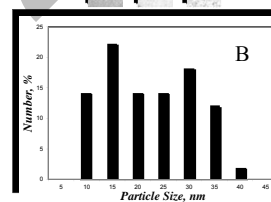
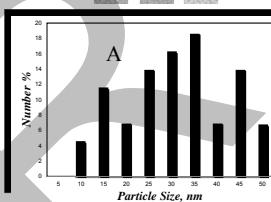
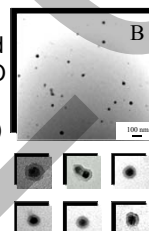
- RuO₄ (0.5 % aqueous solution)
- Stained in a petri dish (fume hood)
- The best staining time is 45 s
- Used within 2-12 hours
- Protective equipment was worn at all time
- Waste was processed separately



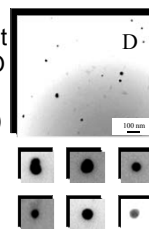
Morphology and Size Distribution from TEM



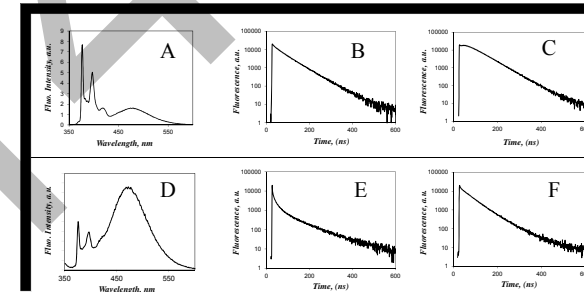
Pyrene-labeled SNPs in DMSO (A, left) and water (B, right)



Non-fluorescent SNPs in DMSO (C, left) and water (D, right)



Results from SS & TR Fluorescence



Figures above present the steady-state fluorescence spectra ($\lambda_{ex}=344$ nm) of pyrene-labeled SNPs in (A) DMSO and (B) water ($\lambda_{ex}=344$ nm, $\lambda_{em}=375$ nm) and time-resolved fluorescence decays of the pyrene monomer in (C) DMSO and (D) water and of the pyrene excimer in (E) DMSO and (F) water.

Solvent	$\eta@25^\circ C$ mPa·s	I_E/I_M	$\langle k \rangle$, μs^{-1}	$f_{diff}\%$	$f_{free}\%$	$f_{agg}\%$
DMSO	1.99	0.68	9.80	79.70	2.20	18.10
Water	0.89	5.65	52.10	5.00	0	95.00

Summary

- In water, 95% of the pyrene excimer originated from the direct excitation of pre-associated pyrene aggregate
- Only 5% of the excimer was formed diffusion in water.
- The average quenching rate constant $\langle k \rangle$ is 5 times faster in water than in DMSO
- The particle size in DMSO is 30 nm, which is 10 nm larger than in water 20 nm
- The core-shell structure was only observed by TEM for the hydrophobically modified pyrene-labeled SNPs

Reference

Zachariasse, K.; Kühnle, *Zeit. Phys. Chem.* **1976**, *101*, 267-276.
Winnik, M. A.; Redpath, T.; Richards, D. H. *Macromolecules* **1980**, *13*, 328-335.